Title
On Light Scattering from Photoexcitations: Making Movies of Nanoscale Energy Transport in Emerging Semiconductors

Author
Weaver, Hannah

Publication Date
2023

Peer reviewed|Thesis/dissertation

On Light Scattering from Photoexcitations: Making Movies of Nanoscale Energy Transport in Emerging Semiconductors

by

Hannah Leigh Weaver

A dissertation submitted in partial satisfaction of the

requirements for the degree of

Doctor of Philosophy

in

Physics

in the

Graduate Division

of the

University of California, Berkeley

Committee in charge:

Professor Naomi Ginsberg, Chair
Professor Feng Wang
Professor Kwabena Bediako

Spring 2023

On Light Scattering from Photoexcitations: Making Movies of Nanoscale Energy Transport in Emerging Semiconductors

Abstract

On Light Scattering from Photoexcitations: Making Movies of Nanoscale Energy Transport in Emerging Semiconductors

by

Hannah Leigh Weaver

Doctor of Philosophy in Physics

University of California, Berkeley

Professor Naomi Ginsberg, Chair

There are many types of excitations that may coexist and interact after light illumination in a semiconductor. In emerging semiconductors like low-dimensional and solution-processed materials, these excitations often encounter nanoscale disorder over their lifetime, including point defects, different crystalline phases, boundaries, interfaces and dielectric disorder. In addition, distinguishing between different types of excitations is vital for teasing out the intrinsic material properties so that they may be tuned and optimized for optoelectronic device applications. Optical scattering is a sensitive probe that, when incorporated into a time-resolved pump-probe microscope, correlates sample morphology to nanoscale energy transport. The unique spectrally-dependent scattering contrast from different photoexcitations and their spatiotemporal evolution together permit the distinction between coexisting excitations. We call this approach stroboscopic scattering microscopy (stroboSCAT) and demonstrate its versatility across a range of organic, organic–inorganic, and inorganic semiconductors, enabling model-free structure-function correlations with few-nanometer precision in all spatial dimensions.

Chapter 1 provides an introduction to the two classes of materials that are explored in this dissertation with an emphasis on the 2D material archetype, molybdenum disulfide (MoS_2). Next, we introduce the playing field of energy flow microscopies well-suited to study the energy transport and transduction in emerging semiconductors.

Chapter 2 explores the theoretical underpinnings and practical operation of the stroboSCAT microscope. We provide background on two approaches for understanding the optical properties of materials: scattering and frequency-dependent complex dielectric functions. We describe the photoinduced changes to the optical response and how they may be probed with transient scattering approaches in transmission or reflection. After a crash course in basic microscopy principles, the nuts and bolts of the stroboSCAT setup are described in detail, including its timing control, resolution limits, and stability.

Chapter 3 illustrates how stroboSCAT is a versatile technique that directly correlates microscopic structural motifs and macroscopic function across a broad range of materials. In TIPS-Pentacene, a molecular crystal, exciton transport is hindered by material interfaces. In a thin film halide perovskite, charge carriers find their way around resistive morphological boundaries using 3D trajectories. Finally, in silicon, oppositely signed contrast for charge carriers and heat, along with a separation in time scales, enables isolating the dynamics of each population even though they overlap.

Chapter 4 takes stroboSCAT into the 2D realm in several layered architectures and an in-depth exploration of exciton and heat transport and transduction in four-layer MoS_2. We combine near- and far-from resonant stroboSCAT measurements with temperature-dependent reflectance contrast spectroscopy to isolate overlapping exciton and heat distributions. This study demonstrates the importance of access to spatially resolved information and tunable contrast for directly discerning photoinduced heat from charge without complex models or assumptions.

As summarized in Chapter 5, this dissertation illustrates the advantages of using transient light scattering to probe photoinduced changes in the optical response of a wide range of novel semiconducting materials. With high spatiotemporal resolution and sensitivity, tunable imaging contrast and direct structure-function correlation, stroboSCAT is a powerful tool for uncovering the intricacies of energy flow on relevant length- and time scales without averaging over heterogeneous energetic landscapes or misinterpreting the emergent dynamics when different excitations coexist.

For Dad

Contents

List of Figures

List of Tables

Acknowledgments

My journey through the PhD has in many ways mirrored the heterogeneous materials that I have studied with twists and turns, sinks and obstacles, and rich and unexpected complexity. I am grateful that along my circuitous path, I was accompanied by a collection of wonderful folks who supported, inspired, and challenged me along the way.

Naomi, you were a source of steadfast encouragement and advocacy throughout the years. With your guidance and in the collaborative and curious lab community that you cultivated, I developed mastery over a tiny corner of the physical world, a gift that I deeply cherish. Thank you for fostering my growth as a physicist and for supporting my humanity in the process.

To all of my fellow dungeon-dwelling Ginsbergers – Jenna, Rebecca, Trevor, Leo, Rongfeng, Christian, Jon R., Livia, Vivian, Taz, Steph, Erin, Ahyoung, Elena, Jon K., Alex, Brendan and Lucas – thank you for the laughs and commiseration, the stimulating scientific discussions, and the solidarity. Thank you James for being my stroboSCAT teammate, especially through the pandemic. And Milan, I learned so much about rigorous, thoughtful science with your mentorship. Thank you for fielding my endless questions with patience and for believing in my ability from the very beginning. Gerd, thank you for bringing your wealth of experiences to our lab meetings. I approach scientific questions with an enriched perspective because of your probing questions.

I had the honor of working with very talented collaborators from all over the country. Thank you Aidan and Henrique in the Heinz group and Jordan in the Rand group for preparing pristine material samples for our "let's-see-what-happens-when-we-measure-this!" experimental stroboSCAT endeavors. Cora, Joeson and Dipti – the dream stroboCAT team – I learned so much from each of you. Thank you for delving into the weeds with me on what it all means and contributing so much of yourselves and your expertise to make the MoS_2 story a reality.

Thank you to all of the people at Berkeley who supported my academic learning (Professor Littlejohn), who helped me navigate the intricacies of the degree requirements and encouraged me not to give up (Joelle), who orchestrated all of the administrative operations in the group (Jessie and Shobit), who taught me the tools to enjoy the satisfaction of precision machining (Jesse), and who were friendly connections in the chemistry loading dock (Carl and Roy).

Before my time at Berkeley, I was propelled back into the physics world when the UCN_τ team at Los Alamos National Lab took a chance on a tired barista who missed working in the lab. Thank you Chris C.-W., Mark, Chris M., Andy, Deion, Wanchun, Zhaowen, Nathan, Tito, John, Robbie, Jose, and Ezra for welcoming me into a subfield that was completely unfamiliar to me. Nicole, thank you for your genuine mentorship over the years. I feel truly seen and supported by you and am grateful that our chance meeting blossomed into a beautiful connection.

I am genuinely grateful to my Lafayette physics community for introducing me to research and debunking my perception that physics was too intimidating and complex for me to ever

understand. Thank you Professor Dougherty, Lyle, David, Tony and Zoe for not only being very accessible and excellent teachers but also for encouraging a sense of community among the students. Thank you Markus for broadening my curiosity with explorations into Greek tragedy, Homer and Euripides. Rosie, thank you for being a rock in a storm that I felt so ill prepared to navigate. I would not be here without you.

Thank you Kyle for supporting me throughout the early years of my science journey, from coast-to-coast and in-between. When I doubted myself, you reminded me that I was capable of whatever I set my mind and heart to. To all of my friends who have been with me since childhood and others I met along the way, thank you for being my community.

Mom, Grandma, Jonathan and Emily and fam, Tyler and Chelle and fam, I love you all. Bekah, you remind me that I am strong and inspire me with your own strength. Dad, you were my first science role model. Thank you for being excited to witness who I was becoming, scientist or not. I miss you and can't wait to geek out with you again someday.

Chapter 1

Introduction

The energy transport and transduction processes that occur in next-generation semiconductors following photoexcitation are important to understand on a mechanistic level in order to illuminate the emergent properties of the materials of import to optimize for optoelectronic applications (e.g., light-emitting diodes, sensors and detectors, lasers, solar cells). A powerful tool to observe energy transport is time-resolved optical scattering microscopy. Imaging with high spatial resolution ensures that material heterogeneities may be explored instead of averaged over. Combining this spatial- with temporal resolution allows characterization of the nature of the transport and how it deviates from being diffusive. The first part of this Chapter introduces two classes of emergent semiconducting materials: (1) low-dimensional materials with layer-dependent properties and an optical response that is dominated by excitons in **Section 1.2**, and (2) solution-processed materials in **Section 1.3** including flexible molecular solids like pentacene derivatives and metal halide perovskites with chemically tunable optical properties and high defect tolerance. **Section 1.4** introduces the transient optical techniques that are most relevant for studying energy transport and transduction in these materials on relevant nanometer and picosecond scales. The Chapter concludes in **Section 1.5** with a summary of the remaining chapters.

1.1 The basics of semiconductor physics

Semiconducting materials are most useful when they act as highways for transporting energy stored as elementary excitations. We may alternatively refer to these excitations throughout this thesis as "photoexcitations" when they are generated via light absorption, "energy carriers" since they are the vehicles by which absorbed or injected energy in the material is transported, or just "carriers" for short. Elementary excitations are the states that emerge when a condensed matter system is not in its ground state [1]. These include quasiparticles, fermionic elementary excitations that typically look like the non-interacting real particles in the ground state material, like quasielectrons ("electrons" for short) and quasiholes ("holes" for short) with fundamental charge $+|e|$ and $-|e|$, respectively, and effective masses that

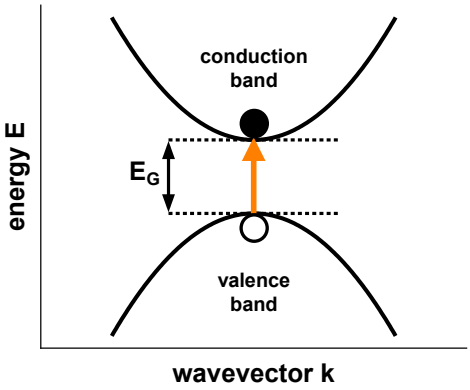

Figure 1.1: Near the band edge, the conduction and valence band may be approximated as parabolas separated by an energy gap given by E_{G}. Absorption of a photon promotes "direct" excitation of an electron from the valence band to the conduction band, leaving behind a quasiparticle "hole" in its absence.

are typically larger than the free electron mass, $m^* > m_0$, due to interactions with their environment. Although some would also consider them to be quasiparticles, the other class of elementary excitations is that of collective excitations that are bosonic and usually do not resemble their constituent particles but represent aggregate behavior of the system, including phonons (collective lattice vibrations), plasmons (collective motion of the electronic charge density), polarons (quasiparticles with an associated lattice deformation) and excitons (bound or quasibound electrons and holes). All of these elementary excitations may interact with one another when they coexist in a material and may be externally probed by photons, electrons, neutrons, and atoms, just to name a few. This thesis considers the case in which the excitations are generated and externally probed with light.

Just as electrons in an atom may occupy discrete quantum energy levels and move between them by light absorption or emission that follows optical selection rules, a macroscopic crystalline material has allowed energy bands comprised of overlapping atomic or molecular orbitals that determine the range of energy levels electrons may occupy. Energy bandgaps correspond to where no electronic states exist. Typically in a semiconductor, the bandgap ($\lesssim 2$ eV) refers to the energy difference between the top of the valence band, where the lowest-energy hole would reside, and the bottom of the conduction band, where the lowest-energy electron would reside following excitation. Vertical ($\Delta k = 0$) transitions from one band to another are optically allowed ("direct" transitions) whereas horizontal or diagonal movement between bands requires inelastic scattering with phonons or defects ("indirect" transitions). Near the band edge, the valence and conduction band are approximately parabolic with curvature inversely proportional to the effective mass [1]. An optically-allowed transition

may be excited across a direct bandgap, E_G, as shown in **Figure 1.1**, promoting an electron into the conduction band and leaving behind a positively-charged hole. Electronic band structures feature bands increasing in energy as a function of crystal wavevector, k, typically with labeled high symmetry points like "Γ" at the center of the Brillouin zone or "K" at the edge of the first Brillouin zone in a hexagonal lattice. The Brillouin zone is the real-space primitive cell mapped into reciprocal- or $k-$space instead [2]. These more intricate concepts of symmetry points and the Brillouin zone arise infrequently in the rest of the text. For our intents and purposes, it is sufficient to know that from the band structure, the nature and size of the bandgap are readily discerned.

1.2 2D materials: a glimpse into flatland

Materials with reduced dimensionality exhibit drastically different, and often tunable, properties compared to their 3D counterparts and therefore serve as test beds for understanding new physics and as building blocks for new device applications. Whereas quasi-0D and quasi-1D systems were realized experimentally in the early 1990s [3, 4], for many decades it was thought that atomically thin 2D materials could not exist due to thermodynamic instabilities at room temperature [5, 6]. Still, theorists studied toy model systems such as graphene, a single layer honeycomb network of carbon atoms, to understand carbon-based materials [7, 8] and later as an analogue for (2+1)-dimensional quantum electrodynamics [9]. The unexpected synthesis of individual crystal planes of graphene in 2004 ushered in a new era of exploration into the novel optoelectronic and transport properties of atomically thin 2D materials [10, 11].

Since graphene behaves as a zero-gap semiconductor, its applications in optoelectronic devices are limited. Fortunately, there are other layered van der Waals coupled materials that can be mechanically exfoliated down to single layers lifted from bulk crystals in the same way as graphene by using adhesive tape. One such class of materials that has stimulated broad interest across the research community is the transition metal dichalcogenides (TMDCs) [11, 13]. A single layer of the form MX_2 is composed of three atomic layers, typically formed by a transition metal layer (M=Mo, W, Ta, etc.) sandwiched between two chalcogen layers (X=S, Se, Te, etc.). The monolayer arrangement for the hexagonal lattice of molybdenum disulfide (MoS_2), an archetypal TMDC, is shown in **Figure 1.2**.

1.2.1 Excitons dominate the optical response in TMDCs

In atomically thin TMDCs, excitons or bound electron-hole pairs dominate their optical response [16]. Because their wave function extends over several lattice constants, they may be described with the Wannier-Mott exciton model. Owing to the sizable binding energy, E_B, of these quasiparticles, larger than room temperature thermal fluctuations (25 meV) even in the few-layer limit, excitons persist up to temperatures of around $T \propto E_B/k_B$ [17]. For example, the exciton binding energy in monolayer MoS_2 is $\sim$500 meV, about 20$\times$ room

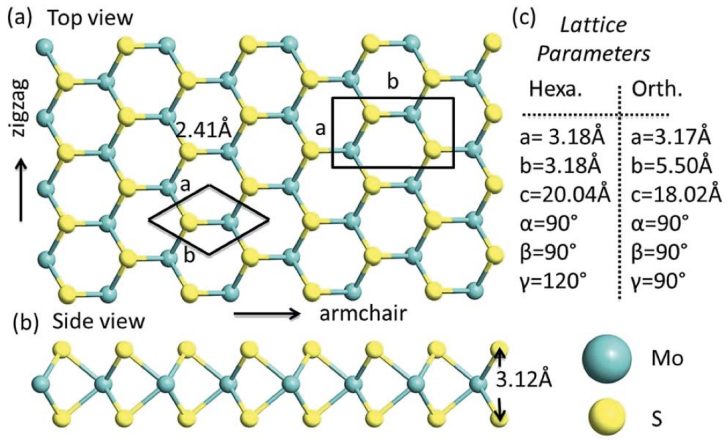

Figure 1.2: MoS_2 lattice. **(a)** Ball and stick model of the optimized geometry of single-layer MoS_2 in supercells with hexagonal and orthorhombic symmetries (top view), **(b)** side view of the layered structure and **(c)** optimized geometry parameters for orthorhombic and hexagonal supercells. Reprinted with permission from Reference [12].

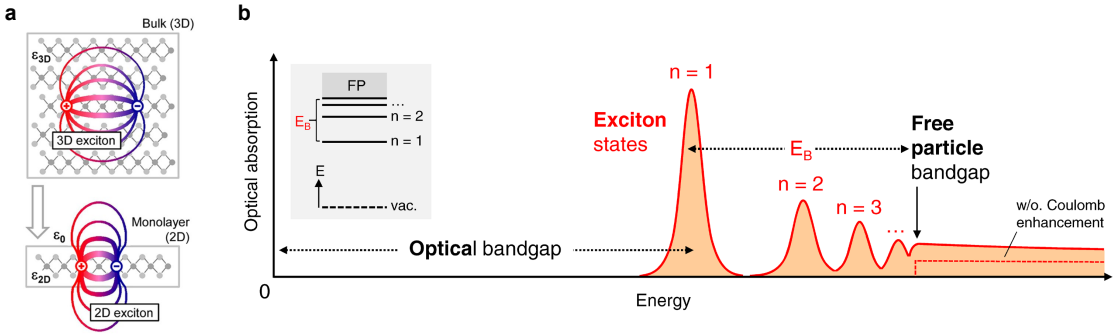

Figure 1.3: Excitons in 2D materials. **(a)** Bound electron-hole pairs form excitons in TMDCs that are well-screened in the bulk (3D) by the surrounding material with ε_{3D} but are poorly screened in the monolayer (2D) limit, where the vacuum permittivity, $\varepsilon_0 < \varepsilon_{2D}$, forms most of the dielectric environment. Reprinted with permission from Reference [14]. **(b)** Schematic of the optical absorption of an ideal 2D semiconductor with a Rydberg series of excitonic transitions below the quasiparticle bandgap, E_G. The enhanced Coulomb interaction also increases the absorption in the continuum above E_G. The inset shows the hydrogen-like energy level scheme of the exciton states labeled according to their principle quantum number $n = 1, 2, 3, ...$ with the binding energy of the ground state exciton $n = 1$ given by $E_B = E_G - E_{opt}$ where E_{opt} is the optical bandgap. Reprinted with permission from [15].

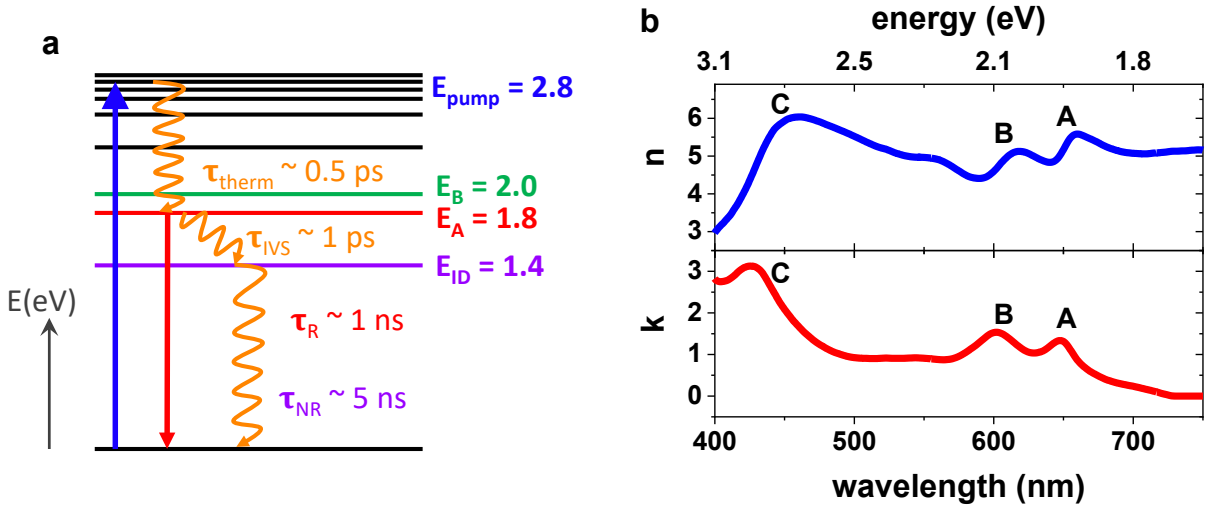

Figure 1.4: Energy level diagram and layer-dependent optical response in MoS_2. **(a)** The A and B direct intravalley excitons and the intervalley indirect (ID) exciton are the most relevant excitons in few-layer MoS_2. Time scales for thermalization, intervalley scattering (IVS), radiative (R) recombination and nonradiative (NR) recombination are labeled. The pump energy is the same as is used in the experiments in **Chapter 4**. **(b)** Real (top) and imaginary (bottom) parts of the refractive index of monolayer MoS_2. The A, B and C exciton peaks are labeled. Adapted from data in Reference [24].

temperature. The stability of these neutral quasiparticles arises for several reasons. When the electron and hole wavefunctions are confined to a dimension of only several angstroms in the 2D limit, their close proximity alone leads to a fourfold increase in the exciton binding energy compared to 3D [18]. Because the material is an effective two-dimensional sheet, most electric field lines connecting an electron and hole pass through empty space (**Figure 1.3a**). Therefore, the Coulomb interaction between the electron and hole is only weakly screened [19, 20] and also highly sensitive to the surrounding dielectric environment, including the substrate and encapsulant roughness [21]. In addition, the effective masses of the electron and hole are relatively large compared to other semiconductors ($\mu_{\mathrm{TMDC}} \approx 0.25 m_0$ compared to $\mu_{\mathrm{GaAs}} \approx 0.06 m_0$ where μ_i is the reduced mass) [15]. All of these effects taken together can be described in a 2D hydrogen-like Rydberg framework to estimate the ground state exciton binding energy [14, 22, 23]: $E_{\mathrm{B}} \propto 4\mathrm{Ry}\mu/m_0\varepsilon_{\mathrm{eff}}$ where Ry is the Rydberg constant of 13.6 eV and $\varepsilon_{\mathrm{eff}}$ is the effective dielectric constant of the TMDC and its surroundings. This model predicts a series of exciton states extending up to the quasiparticle bandgap (**Figure 1.3b**). The difference between the quasiparticle bandgap, E_{G}, and exciton resonance energy or optical bandgap, E_{opt}, defines the exciton binding energy: $E_{\mathrm{B}} = E_{\mathrm{G}} - E_{\mathrm{opt}}$.

There are a variety of excitations, interactions and decay pathways that occur after photoexcitation in TMDCs. Taking MoS_2 as an example, there are several "flavors" of

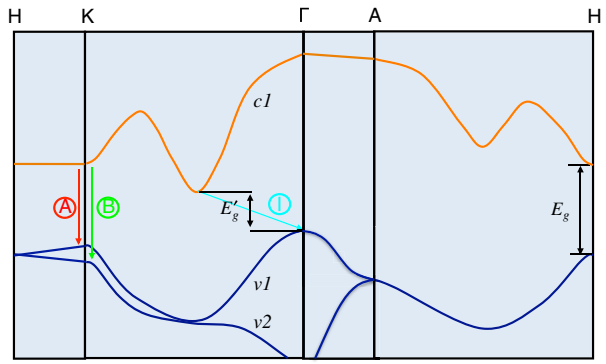

Figure 1.5: Band structure of MoS_2 showing the lowest conduction band ($c1$), direct bandgap (E_g) for the monolayer and indirect bandgap ($E_{g'}$) for the bulk, as well as the A and B excitons from the spin-orbit-split valence band ($v1, v2$). Reprinted with permission from Reference [25].

excitons that may be generated after above-bandgap excitation and subsequent relaxation processes that occur over ps-ns (**Figure 1.4a**). Each exciton generates a resonance peak in the optical response, measured in **Figure 1.4b** as variations in the complex refractive index. **Figure 1.5** shows the band structure of MoS_2 with two intravalley excitons at the K-point in the Brillouin zone that arise from the spin-orbit-split valence band. The A exciton is "bright" with radiative recombination occurring $\sim 1-3$ ns, while the B exciton, ~160 meV higher in energy, is "dark," meaning its relaxation is optically forbidden [25]. The indirect intervalley $\Gamma - K$ exciton (I in **Figure 1.5**) is also "dark" with phonon-assisted ~several ns recombination [25, 26]. If the excitation energy is high enough, a hot electron-hole pair forms the C exciton in the "band nesting" region near 3 eV, where the valence and conduction band have parallel slopes [17, 27, 28]. After sub-ps thermalization to the band edge, the electron and hole may undergo intervalley scattering to the lowest energy indirect exciton in the bilayer-to-bulk limit [29, 30]. In addition, because MoS_2 has a native doping electron background of $10^{10} - 10^{13}$ cm^{-2} from intrinsic sulfur vacancies [31], excitons may associate with free carriers, forming trions. Excitons may also interact with one another forming biexcitons. These three- and four-body states tend to have smaller binding energies, ~20-50 meV, and are short-lived, $\lesssim$ 50 ps, with nonradiative recombination being their primary relaxation pathway [32, 33]. The overall photoluminescence quantum yield (PLQY) and radiative lifetimes may be enhanced by treating the MoS_2 surface with superacid to neutralize the charged sulfur defects [34–36].

Exciton-exciton annihilation or Auger-Meitner (A-M) recombination is a nearly inescapable nonradiative channel in low-dimensional TMDCs [37]. In this diffusion-limited and density-dependent interaction, two excitons meet and one undergoes nonradiative interband recombination as its energy is transferred to the other exciton which sheds its excess energy in a cascade of optical phonons as it relaxes back to the band edge [38, 39]. The kinetics in

power-dependent transient optical absorption spectra that measure this phenomenon can be described by a bimolecular recombination model:

$$\frac{dN_x(t)}{dt} = -k_{\text{A-M}} N_x^2(t), \tag{1.1}$$

where $N_x(t)$ is the exciton density at time t and $k_{\text{A-M}}$ is the rate constant for the A-M annihilation process. The solution to Equation 1.1 is given by:

$$N_x(t) = \frac{N_0}{1 + k_{\text{A-M}} N_0(t)}, \tag{1.2}$$

and when fit to the spectroscopic data, the annihilation rate can be extracted: $k_{\text{A-M}} = 4.3 \times 10^{-2}$ cm^2/s for monolayer MoS_2 [40]. This many-body interaction is important to understand not only because it may complicate experimental interpretations, for example, when charge and lattice heating both contribute to the transient response, but also because it sets a limit on the carrier density that the material can sustain, an important parameter for device design. And yet, it is possible to reach even high carrier density regimes ($> 10^{14}$cm^{-2}) in these materials in which the excitons mutually screen one another and undergo a Mott transition from an insulating excitonic regime to an electron–hole plasma. While this effect is short lived, only manifesting for ∼ps, it drastically alters the optical response of the material [41, 42].

Since there are a host of radiative and nonradiative processes in TMDCs that occur after photoexcitation involving a range of different excitonic species, it can be difficult to intuit exciton dynamics from time-resolved spectroscopy experiments alone. Comparing results between different studies becomes especially challenging in the few- to monolayer limit where defects and dielectric environment can vary substantially from sample to sample, obscuring the intrinsic material properties. In the monolayer limit in which all of the atoms are at or very near to the surface, the number of surface and interfacial defects is enhanced, increasing the probability for defect scattering processes. The transient microscopies described below are well-suited for teasing out the intrinsic material properties from the host of coexisting excitations (see, for example, **Chapter 4**) and their excited state interactions.

1.2.2 Monolayer versus multilayer TMDCs

One of the tunable properties of TMDCs is their thickness-dependent bandgap. The lowest energy transition in bulk, few-layer and bilayer MoS_2 is indirect with weak phonon-assisted PL. In the monolayer limit, MoS_2 is a direct-gap semiconductor and exhibits high PLQY, enhanced by a factor of 10^4 compared to its bilayer counterpart, as shown in **Figure 1.6** [25, 43]. This indirect-to-direct bandgap crossover is due to an increase in the indirect gap energy as a function of decreasing layer thickness while the direct gap energy remains nearly unchanged. Neighboring layers in multilayer samples screen the delocalized orbitals at the $\Gamma - K$ transition of the indirect bandgap which becomes a higher energy transition as the layer number is reduced and confinement is increased. In comparison, the direct transition

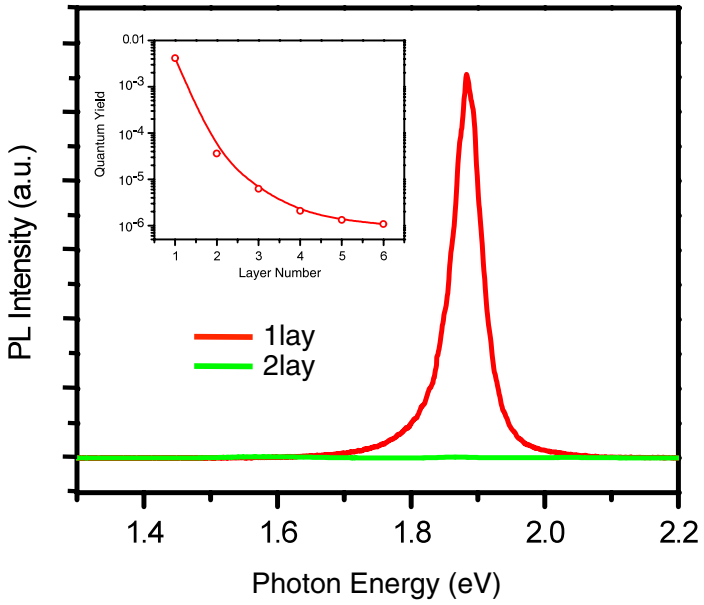

Figure 1.6: Layer-dependent photoluminescence in MoS_2. First experimental evidence of a direct bandgap in monolayer MoS_2 showing PL spectra for mono- and bilayer MoS_2 samples. Inset: Layer-dependent PLQY for layer thicknesses $N = 1 - 6$. Reprinted with permission from Reference [25].

at the zone edge (K-point), where the orbitals are very localized on the Mo atoms, is not affected by layer thickness [26].

TMDC monolayers are said to have "efficient" light-matter interactions due to their intrinsic large radiative decay rate and high oscillator strength (from an effectively reduced Böhr radius, a_0, in 2D) which leads to impressive absorption coefficients with the potential to reach 50% under optimal conditions [44]. They are therefore attractive candidates for many optoelectronic applications including in solar cells, phototransistors, photodiodes, and LEDs [45–48].

Multilayer TMDCs fill their own technological niche. They tend to have higher carrier mobilities due to interlayer screening, and their longer carrier lifetimes make them attractive candidates for fast photosensing applications [49–51]. Furthermore, the low out-of-plane thermal conductivity in multilayer TMDCs is an intrinsic design handle that may be leveraged for thermoelectric applications [50, 52].

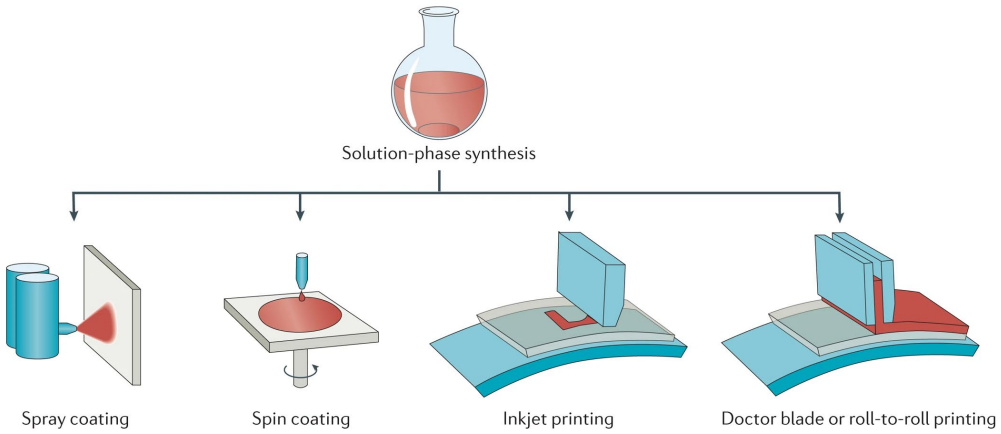

Figure 1.7: Solution-processed materials are synthesized from colloidal semiconductor "inks" that can be deposited and assembled in solid films using spray coating or spin coating, or manufacturing techniques such as inkjet printing, doctor blading or roll-to-roll printing. Reprinted with permission from Reference [56].

1.3 Solution processed semiconductors: silicon, we're coming for you!

Another class of emerging semiconductors is solution-processed semiconductors, including organic molecular crystals and metal halide perovskites. Devices made with these materials combine the ease of processing, tailored optoelectronic properties, and compatibility with flexible and comformable substrates. They may also be semi- or fully-transparent, and some organic materials are compatible with living cells, an important requirement for biomedical applications [53–55]. Their fabrication process can occur at room temperature under ambient conditions by depositing a precursor solution on a large-area substrate with readily available manufacturing techniques like spin coating, roll-to-roll printing, spray coating or doctor blading as shown in **Figure 1.7** [56]. Even a graduate student who has never held a pipette in her life can mix a few chemicals in a vial and spin coat a decent polycrystalline thin film [personal experience]!

In addition to being cost-effective, energy-efficient, and easy to fabricate, the optoelectronic properties of solution-processed semiconductors are tunable. Being able to control the bandgap, for example, is important for harnessing more of the solar spectrum in a photovoltaic cell. In organic semiconductors, the bandgap can be tuned by varying the molecular structure or by guiding the solid-sate assembly process to control the final sample morphology. Metal halide perovskite bandgaps may be tuned across the visible spectrum by changing their chemical composition [57–59].

1.3.1 Small-molecule organic semiconductors

Small-molecule organic semiconductors are considered "soft" materials. The weaker bonding between the molecules, associated by van der Waals forces as opposed to the covalent or ionic bonds found in most inorganic semiconductors, lends the solid state film its manipulatability. This means that external factors can readily influence molecular packing so that within the same film, amorphous and crystalline regions may form, sometimes with multiple crystalline polymorphs [60–62]. This variety can lead to a disordered microstructure with a tangled landscape of interfaces, defects, and regions of varying crystallinity that ultimately hinders the mobility of excitons and free carriers. That said, if the formation of nanoscale features can be controlled, they may be a design handle for directing charge transport. To understand the mechanisms by which the heterogeneity in organic semiconductors affects energy transport, it becomes necessary to perform characterizations with high spatial resolution in order to observe the impact of nanoscale structural disorder on the emergent transport properties [63–65]. We perform such a correlated structure-function measurement in **Section 3.2** in which exciton transport is impeded by domain interfaces.

Excitons in these materials are stable at room temperature because they are Frenkel-like and have a similar E_B to low-dimensional TMDCs, although the reason for their stability is due to the low dielectric constant in bulk organic semiconductors compared to inorganic ones. Because these materials are also often used for thin film transistors, it is important to also distinguish excitons from the charge carriers that are the energy currency in the transistors: excitons are photoexcited and tend to be stable over their lifetime, whereas free charge carriers occur in the same material when injected electrically, which is why they do not form excitons.

Devices made with organic semiconducting thin films will have to tolerate some level of disorder [66], however in the single crystal form, transport can be very efficient. For example, the hole mobility of a rubrene single crystal can reach 40 cm^2/Vs [67]. This efficient charge transport is due in part to the π-stacking that occurs in pentacene derivatives, where the out-of-plane delocalized p-orbitals overlap between neighboring molecules [68]. The result is a more stable crystal structure with preferred transport along the π-stacking direction [69–72].

1.3.2 Metal halide perovskites

In general, metal halide perovskites have a chemical formula of ABX_3 where A and B are cations, (A = Cs^+, methylammonium (MA^+) and/or formamidinium (FA^+) and B = Pb^{2+}, Sn^{2+} or Bi^{3+}), and X is a halide, (Br^-, Cl^-, or I^-), or halide mixture. They exhibit long charge carrier diffusion lengths [73–75], high PLQY [76, 77] and high defect tolerance [78–81], making them popular candidates for active layers in photovoltaic and light-emitting device applications. The power conversion efficiencies of perovskite solar cells have increased rapidly from 3.8% in 2009 [82] to 26% [83–87] today as fabrication protocols improve and integration with existing platforms is streamlined. Their performance is also enabled by several intrinsic

properties, including a sharp absorption onset [88] and large polaron formation, which screens carriers from defect recombination, although this is a current hot topic of debate [89].

Polycrystalline perovskite thin films exhibit a rich nanoscale structure that is important to characterize and correlate with electron and hole migration. Crystal grain sizes can range from ∼100 nm up to a few microns depending on the preparation protocol (**Section 3.3**). Within a given grain, subgrain features act as nonradiative recombination sites even though they do not appear as grooves like traditional grain boundaries in surface morphology characterization [90]. These features may be due to crystal twinning where neighboring crystal domains share lattice points at their common interface but grow in different directions. The twin domains can be quite large, similar in thickness to a typical halide perovskite layer in a photovoltaic device, ∼300 nm, although they may not ultimately impact device performance [91, 92]. In **Section 3.3**, we explore the impact of a different set of nanoscale features, morphological boundaries, that impact the lateral and axial transport of charge carriers finding the path of least resistance through a disordered energetic landscape.

The perovskite world is booming with creative scientists designing bespoke band structures by, for example, substituting the B-site cation with different metals or combinations of metals to form lead-free expanded perovskites [81, 93–95]. Perovskites have also been synthesized with reduced dimensionality as perovskite nanocrystals and quantum dots [96, 97], nanowires [98, 99], 2D sheets [100], and stacks of 2D layers [101–105]. While their instability and degradation in atmospheric conditions, especially under illumination and high temperatures, pose significant challenges for device longevity, used in combination with existing silicon-based platforms and with proper encapsulation, they are already making waves in the solar cell industry. And they will likely be light-emitting arrays in our cell phone displays before long.

Since the binding energy in metal halide perovskites is only a few millielectronvolts at room temperature [106], free charge carriers are the predominate type of energy carrier. The charge excitation is often accompanied by a stabilizing local lattice deformation, forming a polaron [107]. Due to the liquid-like polarizability of the material, a high static dielectric constant and a moderate Young's modulus lending the ionic lattice its relative softness, strong electron-phonon coupling generates quite large polarons that potentially reduce scattering with charged defects and with other charge carriers and enable photoinduced phase separation in mixed halide hybrid perovskites [89, 108, 109], though as mentioned above, the role of the polaronic nature in the defect tolerance of halide perovskites remains a topic of investigation.

1.4 Tracking nanoscale energy transport with transient scattering microscopies

We next consider the topic of tracking photoexcitations as a function of space and time both in the materials we have thus far introduced and also more broadly in new high-performance

semiconductors, where gaining a fundamental understanding of why some materials outperform others is vital for informing rational materials design. The difficulty in gaining such predictive power is compounded by nanoscale spatioenergetic disorder, manifested in defects, impurities and interfaces, that gives rise to spatiotemporally heterogeneous energy transport. Elucidating how the microscopic details of a material relate to its emergent optoelectronic properties therefore requires the ability to individually and systematically correlate nanoscale structure with energy flow across a wide range of systems.

Resolving how energy flow is affected by spatioenergetic disorder requires tracking energy carriers over a wide spatiotemporal range – nanometers to micrometers and picoseconds to milliseconds – and directly correlating the measurements with material morphology. This correlation notwithstanding, powerful spatiotemporally resolved scattering approaches have recently been developed to visualize nanoscale energy flow using photoluminescence, e.g. micro-time-resolved photoluminescence (microTRPL) which observes a carrier-specific signal due to radiative recombination [72, 110, 111], or transient absorption, e.g. transient absorption microscopy (TAM) which targets a specific excited state [112–115], as contrast mechanisms that rely on different light-matter interactions. They achieve femtosecond time resolution [114, 116], large dynamic range [72], chemical specificity [72, 110, 111, 114] and excellent spatial sensitivity [72, 110, 111]. In this thesis, we add to the toolbox of transient pump-probe microscopies stroboscopic scattering microscopy (stroboSCAT), which observes changes in the local refractive index through elastic scattering [117].

Each transient scattering technique spatiotemporally resolves photoexcited transport by using pulsed optical light to image energy flow in materials. All use a similar photoexcitation method, focusing a pump pulse through an objective to excite a small population of energy carriers (**Figure 1.8a**), and all observe the mean squared expansion of the distribution of energy carriers through what may be a heterogeneous energetic landscape using different collection methods that leverage different light-matter interactions (**Figure 1.8b**). The power of these approaches is that the observed transport behavior does not always appear diffusive. Material heterogeneity can affect electronic transport on the ∼nm-µm scale through grain boundaries, material interfaces and intergrain variation, and also on the atomic sub-nm scale through vacancies and impurities that are intrinsic to the material. Different scattering interactions – carrier-carrier, carrier-phonon, carrier-defect – also affect the way energy carriers ricochet through a material.

Transient absorption- and photoluminescence-based techniques track only a subset of energy carrier types and rely on samples that have specific optical or electronic properties, such as being absorbing yet having low optical density [114] or having large Stokes shifts [110] and appreciable emission [72, 111]. They also measure energy flow in only two dimensions, and most acquire a single image pixel at a time. These constraints limit the breadth of samples and fundamental processes that can be studied. On the other hand, stroboSCAT leverages elastic scattering, a universal optical interaction, to track evolving distributions of any type of energy carrier in three spatial dimensions, irrespective of their optical properties, as they move through any material on picosecond to millisecond time scales. This approach enables simultaneous imaging of the nano- to microscale morphological features

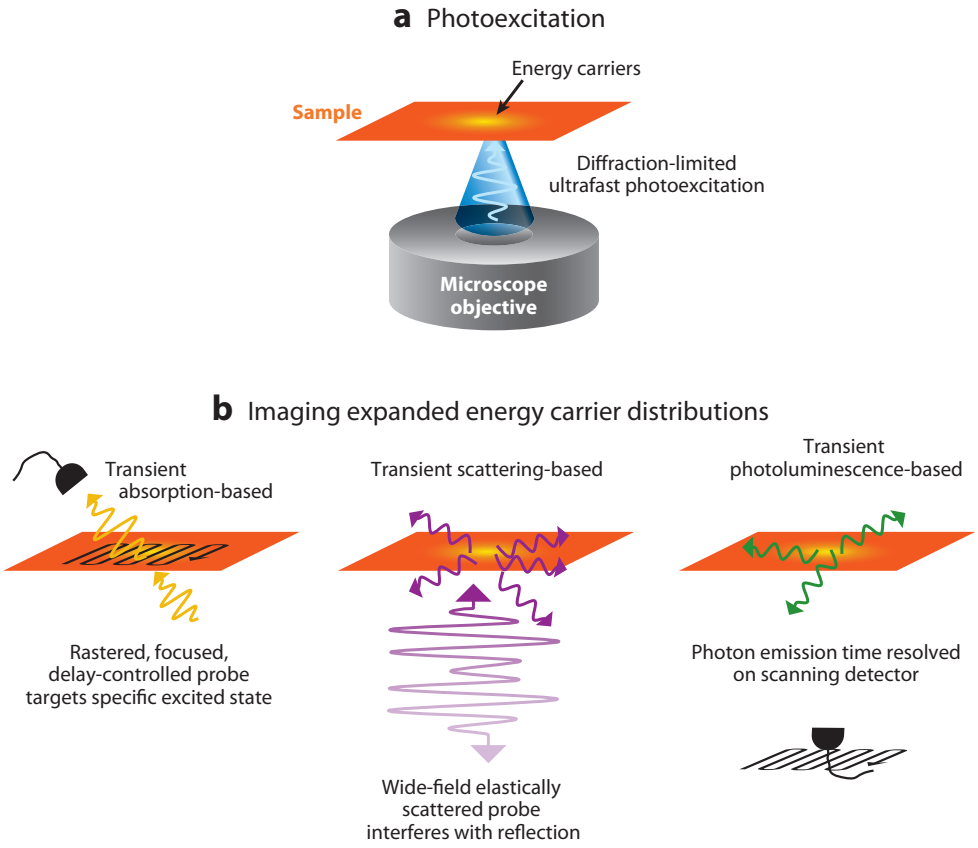

Figure 1.8: Comparison of three approaches to transient optical microscopy. **(a)** Each technique focuses a pump pulse through an objective to excite a small population of energy carriers then **(b)** leverages a light-matter interaction to produce image contrast that generates a spatial map of the photoexcited distribution. Reprinted with permission from Reference [117].

that define the spatioenergetic landscape of the material, providing much-sought-after *in situ* structure–function correlations. **Chapter 2** details the intricacies of the stroboSCAT setup in addition to the optical scattering response that underlies its contrast mechanism. In the rest of this Chapter we, however, introduce several mechanisms of diffusive and non-diffusive transport and how they might manifest in plots of the mean squared expansion as a function of time.

1.4.1 Diffusive and non-diffusive behavior

In normal isotropic diffusion, a distribution of photogenerated energy carriers undergoes a random walk driven by its concentration gradient, ∇N. The evolution of the carrier

distribution is governed by the diffusion equation:

$$\frac{\partial N(r,t)}{\partial t} = D\nabla^2 N(r,t) \tag{1.3}$$

for constant diffusion coefficient or diffusivity, D, and spatiotemporally varying carrier concentration, $N(r,t)$. When the initial carrier concentration profile is Gaussian, the solution to the diffusion equation is also Gaussian:

$$N(r,t) = \frac{1}{\sqrt{4\pi Dt}} e^{-(x-x_0)^2/4Dt}. \tag{1.4}$$

In addition to diffusing, the carriers also decay over their lifetime so the amplitude may be modified to reflect this loss, for example, by inserting a time-dependent prefactor, $A(t)$, that has some exponentially decaying behavior. The mean squared expansion (MSE) is given by:

$$\text{MSE} = \langle x(t)^2 \rangle - \langle x(0)^2 \rangle = \sigma^2(t) - \sigma^2(0) = 2Dt, \tag{1.5}$$

where $\sigma(0)$ is the initial size of the distribution, characterized by its standard deviation. Importantly, for normal diffusion, a plot of the MSE versus time is a straight line with a slope of $2D$. As a general comment, we note that the concentration gradient created by a spatially-finite excitation does not influence the intrinsic energy carrier diffusivity. The only effect of a spatially-finite excitation is to allow the observation of diffusion due to a net flux of carriers that ultimately erases the concentration gradient. Each carrier acts the same way that it would if there were only a single excitation in the material and undergoes a random walk, which over time leads to a net flux out of the initial excitation spot. This treatment assumes that the injected carrier density is in the linear regime where many particle interactions may be ignored.

After an energy carrier is photogenerated, there are several mechanisms by which it may take incremental steps that, summed up over its lifetime, yield long-range energy transport. At the one extreme is band-like coherent transport, which is common in crystalline semiconductors. The energy carrier spends most of its time in ballistic motion traveling with average velocity, $\overline{v}$, before it is interrupted by a scattering event with another carrier or phonon or the lattice that changes its momentum. The diffusivity in 1D in this case is given by:

$$D_{\text{coherent}} = 1/3\overline{v}\lambda_p, \tag{1.6}$$

where λ_p is the mean free path between collisions.

At the opposite extreme, incoherent or hopping transport occurs in systems with localized excitations that undergo energy transfer between sites, e.g., molecules, via hopping. The energy carrier spends most of its time sitting on a particular site, waiting for a thermal fluctuation that might allow it to move. The diffusivity in 1D in this case is given by:

$$D_{\text{incoherent}} = k_{\text{ET}} d^2, \tag{1.7}$$

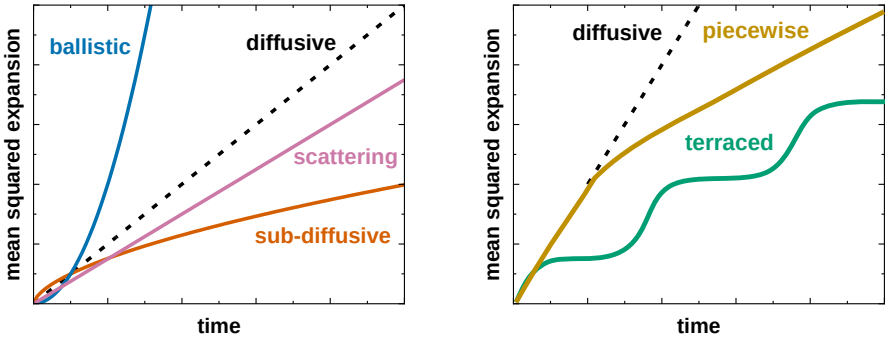

Figure 1.9: Diffusion mechanisms may be encoded in the mean squared expansion of the initial excitation distribution as a function of time. Deviations from normal diffusive behavior include (left) ballistic transport ($\propto t^2$), subdiffusive transport, (right) piecewise transport, where diffusion slows after some characteristic time and terraced transport where diffusion pauses, then resumes. Diffusive transport may also be suppressed by increased scattering, e.g., carrier-carrier or carrier-lattice scattering (left).

where k_{ET} is the transition probability per unit time to hop to a neighboring energy site and d is the distance between sites. Broadly speaking, the mechanism of transport depends on the delocalization of the excitation. In photosynthetic light harvesting systems, excitations are highly localized Frenkel excitons that reside on chromophores and hop from protein to protein [118]. (Within proteins, energy transfer is excitonic, i.e., due to wavefunction overlap rather than hopping [118–120].) In TMDCs, the excitations are excitons delocalized over many lattice sites, extending over 1 nm in real space [121]. In molecular crystals, the picture is more complicated, both for injected charge carriers and excitons, because the mean free path is short, but hopping alone cannot explain the high exciton and carrier mobilities that are observed. Other frameworks take into account the material's soft, dynamically disordered lattice that supports large fluctuations and transient exciton delocalization [122–125].

The diffusion length, L_D, characterizes the average distance that an energy carrier travels before it recombines, radiatively or nonradiatively:

$$L_D = \sqrt{2D\tau} \tag{1.8}$$

for carrier lifetime, τ. This quantity is an important device metric because if most energy carriers recombine before they reach an electrode or charge extraction layer, they cannot be used to generate work. In the literature, it is conventional to neglect the $\sqrt{2}$ and use instead $L_D \sim \sqrt{D\tau}$, however in this thesis, we will use the full definition of L_D as in Equation 1.8.

We have thus far discussed diffusion in which energy transport is due to a spatially-varying distribution of energy carriers. However, standard bulk characterizations of energy transport typically measure a drift current driven by the force of an electric field, e.g.,

Hall effect measurements. In semiconductor devices, both forms of transport are present. A helpful conversion between the two types of measurements is the Einstein relation that connects the electrical mobility, μ, to the diffusion coefficient:

$$D = \frac{\mu k_{\mathrm{B}} T}{q} \tag{1.9}$$

for charge q and temperature T.

Everything up to this point has considered normal diffusive behavior. What might non-diffusive behavior look like? Some of the possibilities are plotted in **Figure 1.9**. Equation 1.5 may be expressed more generally as:

$$\mathrm{MSE} = 2Dt^{\alpha}, \tag{1.10}$$

where $\alpha > 0$. In the case of ballistic transport, $\alpha = 2$. In general for superdiffusive transport, $\alpha > 1$, which arises due to various anomalous phenomena including hot carriers driven by pressure gradients [126], light propagation in dilute atomic vapours [127, 128] and the reduced dimensionality of 1D metals [129]. For subdiffusive transport, $0 < \alpha < 1$, which is common for systems with high energetic disorder, as energy carriers migrate energetically downhill due to spatial heterogeneity in the energetic landscape (the energy that an excitation must carry differs at different spatial locations), and hopping to subsequent sites becomes less likely. Subdiffusion may also be due to nanoscale porous interstices in disordered films where the energy flow takes a tortuous path through contiguous regions of material [130]. Increased overall scattering with other charge carriers or with lattice impurities can decrease the overall slope (diffusion coefficient) of the MSE. A host of other trends may appear in an MSE plot that deviate from straight-line normal diffusion. For example, the trend may appear piecewise when initially the charge carrier density saturates the trap state density, then at later times crosses into a regime where carriers have spread out and on average encounter more traps that slow or halt their diffusion [81]. A similar piecewise trend could appear due to partially-confined transport as in **Section 3.2**. Or, the trend may appear terraced as energy carriers encounter regions of high and low impedance in the energetic landscape as in **Section 3.3**. It may even appear to expand, stagnate, then contract over longer time scales due to the distinct energetic distribution of trapping sites in the material [131]. Clearly, the MSE plot contains a wealth of information with insights about the underlying mechanisms of energy transport that are specific to the material and its nanoscale heterogeneity.

For isotropic diffusive behavior, Gaussian functions fit to image line cuts may be used to extract MSE vs. time plots. For anisotropic diffusion, as for TIPS-Pn in **Section 3.2**, the same strategy can be used for both long and short diffusion axes. For heterogeneous, anisotropic diffusion, one possibility is to plot a radial profile averaged over all angles and fit it with a half-Gaussian to obtain an average distribution. To obtain plots like in **Figure 1.10**, discussed further in **Section 3.3.4**, the radial distribution is instead split into 10-30° slices and the intensity distribution of each slice is measured. (The intensity at any given distance from the central point is the integrated intensity of the pixels over the arc bounded

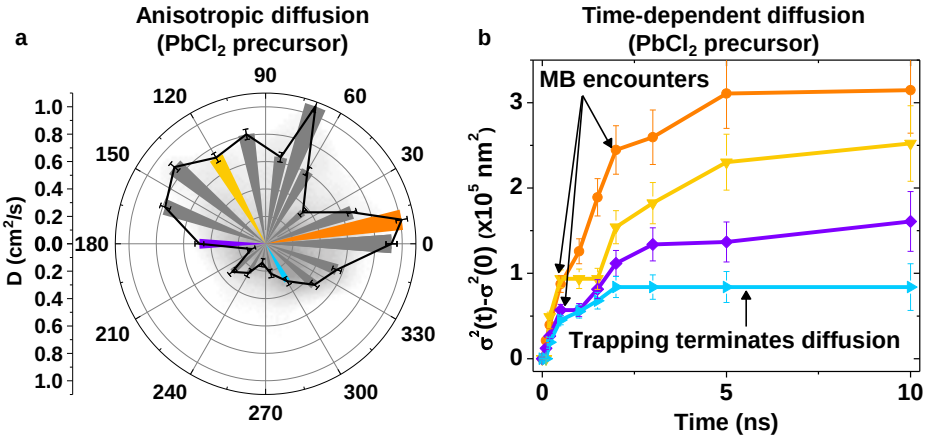

Figure 1.10: Quantifying spatial and temporal carrier transport heterogeneity in polycrystalline $MAPbI_3(Cl)$. **(a)** Angle-dependent diffusivities averaged over the first 2 ns for the $PbCl_2$ precursor data shown in **Figure 3.10a**. **(b)** Time-dependent diffusion for four representative azimuthal angles color-coded in panel (a). Error bars represent the standard deviation of the fits to several experimental datasets taken at the same location in the films. Curves represent a spline interpolation of the data points.

by the slice.) However, when trapping occurs, for example at grain boundaries, the carrier distribution is not normally distributed and thus cannot be accurately fit with a Gaussian function. In these circumstances, we measure the distance from the center of the radial distribution at which the population drops to $1/e$, then convert the extracted half-width at the $1/e$ value (w) to a Gaussian standard deviation using the relationship $\sigma = \frac{w}{\sqrt{-2\ln I_T}}$, where I_T is the chosen Gaussian intensity threshold, i.e., $1/e$ in this case, assuming a normal distribution.

1.5 Remaining chapters overview

Chapter 2 describes the inner workings of the stroboSCAT home-built microscope including its stability, resolution limits and timing control. This chapter also provides a basic introduction to optical scattering and optical properties of materials that are relevant for understanding how image contrast in transient scattering measurements are related to changes in the optical response of excitations in a material. With a connection to principles in microscopy, stroboSCAT is contextualized as a powerful interferometric, time-resolved, label-free, non-invasive, high-throughput, universal approach to visualize how energy navigates intrinsically disordered landscapes in 3D in complex semiconducting materials with high sensitivity, large dynamic range, and *in situ* correlation to underlying sample morphology.

Chapter 3 discusses three stroboSCAT case studies that demonstrate the capability to measure energy transport over four orders of magnitude in space and time, on both

neutral and charged excitations migrating through organic, organic–inorganic and inorganic semiconductors. These findings highlight the importance of moving beyond averaged metrics in disordered materials to characterize the impact, (not always detrimental, as it turns out), of nanoscale interfaces on energy transport with *in situ* structure-function correlation.

Chapter 4 investigates energy transport and transduction in several TMDC architectures with a special focus on exciton and heat dynamics in four-layer MoS_2. Temperature-dependent reflectance spectroscopy calibrates the contribution from photoinduced heating to the differential image contrast at two imaging wavelengths near- and far-from electronic resonances, enabling distinction of exciton and heat populations when they overlap.

Differential image contrast is an important player in **Chapters 3** and **4**, distinguishing between different types of energy carriers in some cases (silicon, MoS_2, black phosphorus) while, in others, reporting on the axial position of the carrier distribution (thin film perovskites and potentially a metal-contacted TMDC).

In combination, these chapters demonstrate that optical scattering is a sensitive probe of excitations in a host of emergent semiconducting materials and illuminates the intricacies of energy transport and transduction at the nanoscale, even when there is structural disorder or coexisting excitations. We envision that the fundamental insights and predictive power enabled by approaches such as stroboscopic optical scattering microscopy will continue to be an integral part of the important feedback loop between structure and emergent function in designing semiconducting materials to meet the needs of a world with a quickly expanding human population and changing climate.

Chapter 2

Stroboscopic scattering microscopy (stroboSCAT): its theoretical underpinnings and practical operation

This Chapter provides an overview of the theory behind and detailed operation of the stroboSCAT microscope. **Section 2.1** considers the phenomenon of light scattering from small particles, the fundamental light-matter interaction in any optical scattering microscopy. **Section 2.2** describes several well-understood excited-state phenomena that modify the transient optical properties of materials following light absorption and that may be applied to transient scattering microscopy and spectroscopy, both in reflection and transmission measurements. After an interlude including a microscopy crash course (**Section 2.3**) and a brief explanation of interferometric scattering microscopy (**Section 2.4**), the Chapter concludes in **Section 2.5** with a comprehensive description of the physical setup and operational details of the stroboSCAT microscope.

2.1 Light scattering from small particles and collections of small particles

Sunsets are red on Earth and blue on Mars because of elastic light scattering, a ubiquitous physical process in which the discrete electric charges that comprise matter are set into oscillatory motion by an incident electromagnetic wave [132]. The accelerated charges reradiate or scatter electromagnetic energy in all directions. Everything except vacuum scatters light. We see the world around us because of diffuse light scattering from objects illuminated by sunlight, computer screens, and candles. Scattering is often accompanied by absorption when the excited charges transform some of the incident energy into other forms of energy (e.g., thermal, chemical) [133]. For example, a sunflower appears yellow because it contains a pigment that absorbs all visible light rays except yellow ones. Absorption can also be viewed as a byproduct of scattering since it can be described as destructive interference

between incident and forward scattered light. Both scattering and absorption attenuate a light wave traveling through a medium. This attenuation is called extinction. One statement of the optical theorem is extinction = scattering + absorption [133–137]. Many phenomena may be described with a scattering treatment including diffuse reflection by rough surfaces, diffraction by slits, gratings and edges, and specular reflection and refraction at optically smooth surfaces, to name a few [132].

Mie Theory gives the exact solution for scattering of electromagnetic plane waves from a homogeneous sphere of any size embedded in a non-absorbing homogeneous infinite medium. It is the exact solution to Maxwell's equations for the boundary conditions of this geometry. In this picture, scattering naturally arises from a particle-medium dielectric mismatch due to the boundary conditions enforced by Maxwell's equations. As far as the field is concerned, a particle disappears as $n_{\text{part}}/n_{\text{med}}$ approaches 1, where n_{part} and n_{med} are the complex refractive indices of the spherical particle and surrounding medium, respectively; without a refractive index mismatch, there is no particle. When absorption is negligible, the ratio may be calculated using the real part of the refractive index, a dimensionless number that describes the speed of light in a medium with respect to the speed of light in vacuum (**Sections 2.1.1** and **2.3.1**). The incident plane wave and the scattered field are expanded into radiating vector spherical harmonics. The internal field is expanded into regular vector spherical harmonics. By enforcing the boundary condition on the spherical surface, the expansion coefficients of the scattered field can be computed. The formalism calculates the electric and magnetic fields inside and outside of an isolated spherical object and is generally used to calculate either how much light is scattered (the total optical cross section) or where it goes (the form factor). The theory predicts the relative intensity of scattered light as a function of particle size, angle of observation, and wavelength and polarization of the incident beam. It also generates the extinction, scattering, backscattering, and absorption cross sections. (See Chapter 5 in Reference [132] for complete derivations.)

Mie Theory is complete and is particularly essential for objects that have a size similar to the incident wavelength, $a \sim \lambda$, although it describes the scattering irrespective of the relationship between a and λ. It is not, however, the most insightful physical picture nor is it practical to use. Raleigh scattering is an approximation in the limit that the particle is small compared to the wavelength: $|m|a/\lambda \ll 1$ where $m \equiv n_{\text{part}}/n_{\text{med}}$ is the relative refractive index. In this limit, the scattered intensity, I_s, is given by [132]

$$I_s = I_0 \frac{8\pi^4 N a^6}{\lambda^4 r^2} \left| \frac{m^2 - 1}{m^2 + 1} \right|^2 (1 + \cos^2 \theta), \tag{2.1}$$

where I_0 is the incident intensity, N is the number density of scattering particles, r is the distance between the scatterer and the point of observation, and $0 < \theta < \pi$ is the polar angle in spherical coordinates measured from the $z-$axis. When the refractive indices depend weakly on λ, the Rayleigh limit yields the familiar $1/\lambda^4$ dependence that lends the sky its blue color [138]. The same inverse-wavelength-dependence occurs for the intensity of a radiating dipole. Mie scattering, on the other hand, is not strongly wavelength-dependent

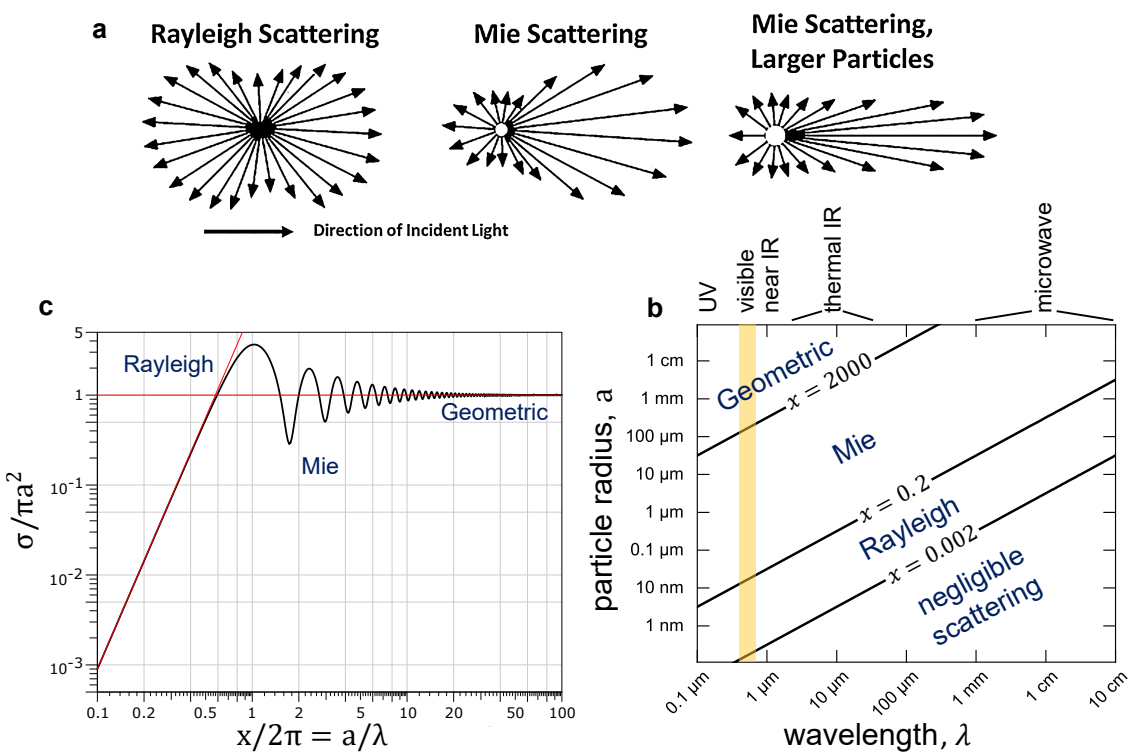

Figure 2.1: Rayleigh, Mie and geometric scattering regimes. (a) Scattered radiation patterns from particles of increasing size. Source: [139] (b) Scattering cross section as a function of size parameter, x. Adapted from Reference [140]. (c) Size parameter and scattering regime as a function of radiation wavelength and particle radius. Adapted from Reference [141].

unless it is applied in the Rayleigh limit. Averaging the intensity in Equation 2.1 over all angles θ, gives the Rayleigh scattering and absorption cross section

$$\sigma_s = \frac{8}{3}\left(\frac{2\pi a n_{\text{med}}}{\lambda}\right)^4 \frac{a^6}{\lambda^4}\left|\frac{\varepsilon_{\text{part}} - \varepsilon_{\text{med}}}{\varepsilon_{\text{part}} + 2\varepsilon_{\text{med}}}\right|^2 \tag{2.2}$$

$$\sigma_{\text{abs}} = \frac{8a\pi n_{\text{med}}}{\lambda}\,\text{Im}\left[\frac{\varepsilon_{\text{part}} - \varepsilon_{\text{med}}}{\varepsilon_{\text{part}} + 2\varepsilon_{\text{med}}}\right], \tag{2.3}$$

where $\varepsilon_{\text{part}}$ and ε_{med} are the permittivity of the particle and the surrounding medium, respectively.

Figure 2.1a shows the scattered intensity distribution as a function of particle size for a given wavelength. The intensity of scattered radiation from a Rayleigh scatterer is symmetrically distributed and behaves like a spherical wave in the far-field limit with the familiar $\cos^2\theta$ radiation pattern of an oscillating point dipole. For larger particles, there are no approximations that can be made, and Mie scattering produces a pattern like an antenna

lobe, with a sharper and more intense forward lobe but suppressed backscattering due to interference with the unscattered incident field. This effect is enhanced with increasing particle size.

One way to distinguish between scattering regimes is to define a size parameter:

$$x = \frac{2\pi a}{\lambda}. \tag{2.4}$$

The Rayleigh scattering approximation is strictly valid for $x \ll 1$ but is used in practice for $x \lesssim 0.2$. Mie scattering is valid for all x but is used in practice for $x \lesssim 2000$. For size parameters beyond this limit, geometric optics is valid (**Section 2.3**). Atmospheric scientists are well versed in mapping particle radius and regions of the electromagnetic spectrum to appropriate scattering regimes as in **Figure 2.1b**.

The scattering cross section as a function of size parameter is another way to visualize scattering regimes. The Rayleigh approximation predicts a scattering cross section that grows indefinitely with frequency (red diagonal line in **Figure 2.1c**). The scattering efficiency reaches a maximum for particles roughly equal in size to the wavelength of light, $x \sim 2\pi$. In the high-frequency limit, the scattering cross section converges to the geometric cross section, πa^2. In between these extremes, the cross section is oscillatory due to interference between the incident and scattered light waves. Mie Theory (black curve in **Figure 2.1c**) provides the correct solution across the frequency spectrum.

One very important caveat of this section on light scattering is that Mie Theory is valid for single, independent scattering events when the number of particles is sufficiently small and their separation sufficiently large that the scattered field from other particles around each particle is small compared to the external field. Under this assumption, the total scattered intensity is just the incoherent sum of the individual scattered intensities. In contrast, coherent scattering in a collection of dense particles would need to account for the interference and phase relations between the waves scattered by neighboring particles and also for 'multiple scattering' – the scattering of the scattered light. In the experiments described in this thesis, thousands to millions of excitations may by generated in a single light pulse, resulting in an average carrier separation $\lesssim 1$ nm, although this can be tuned by lowering the incoming photon density. On the one hand, the entire distribution of excitations could be treated as a single Mie scatterer with an effective $\varepsilon_{\text{part}}$, although there is the complication that the "particle" changes in size with time and does not have rigid boundaries. Alternatively, the approaches of condensed matter physics may be used to understand the photoinduced changes to the optical material properties, as we explore below in **Section 2.2**.

2.1.1 Optical properties of materials

We set aside the scattering picture for now to gain some intuition for the optical properties of solids, first at the atomic level, next zooming out to more macroscopic effects, and

finally connecting the two regimes. In the presence of a static electric field, $\mathbf{E}$, the electron distribution of an atom is displaced, giving rise to a dipole moment, $\mathbf{p}$ [142]

$$\mathbf{p} = \alpha \mathbf{E}, \tag{2.5}$$

where α, is the atomic polarizability and depends on the detailed structure of the atom in question. In bulk solids, α is a polarizability tensor, and the electric field induces a macroscopic polarization, $\mathbf{P}$, which is defined as the dipole moment per unit volume. Provided that the field is not too strong, the polarization is linearly proportional to the total field

$$\mathbf{P} = \varepsilon_0 \chi_e \mathbf{E}, \tag{2.6}$$

where χ_e is the electric susceptibility – a dimensionless quantity. Since this work concerns nonmagnetic materials, we drop the subscript moving forward. The value of χ depends on the microscopic structure of the material. Materials that obey Equation 2.6 are called linear dielectrics. Since the total field $\mathbf{E}$ may be due either to free charges in the material or to the polarization itself, it is helpful to define a new quantity called the electric displacement that can be deduced directly from the free charge distribution

$$\mathbf{D} = \varepsilon_0 \mathbf{E} + \mathbf{P} = \varepsilon_0 (1 + \chi) \mathbf{E} = \varepsilon \mathbf{E}, \tag{2.7}$$

with a new constant of proportionality, the permittivity $\varepsilon \equiv \varepsilon_0(1+\chi)$. Dividing by ε_0 leaves behind a useful dimensionless quantity called the relative permittivity: $\varepsilon_r \equiv 1 + \chi = \varepsilon/\varepsilon_0$.

Just so that we can have all of the optical constants in once place, we take a brief detour to consider light propagation in a material. For electromagnetic waves traveling through a linear, homogeneous medium, Maxwell's equations predict a propagation speed of

$$v = \frac{1}{\sqrt{\varepsilon \mu}} = \frac{c}{n}, \tag{2.8}$$

where μ is the magnetic permeability in the material, $n \equiv \sqrt{\frac{\varepsilon \mu}{\varepsilon_0 \mu_0}}$ is the refractive index, and μ_0 is the magnetic permeability in free space. In empty space, light travels unimpeded at the familiar constant $c = (\varepsilon_0 \mu_0)^{-1/2} = 3 \times 10^8$ m/s. When light travels through a material, it interacts with the particles that comprise it – mostly electrons but also nuclei. Generally speaking, the denser the material and the more electrons per unit volume it contains, the higher its refractive index, and the more it will slow light down. For most materials, $\mu \approx \mu_0$ so $n \approx \sqrt{\varepsilon_r}$.

The relationship between the atomic polarizability and the susceptibility is known as the Clausius-Mossotti formula or the Lorentz-Lorenz equation when relating the refractive index to the atomic polarizability. It can also be derived from Mie Theory or from a neat connection to the electrostatics problem of a sphere embedded in a uniform static field [132]. There are a few nuances in the derivation. First, the field in Equation 2.5 is the field due to everything except the isolated atom, $\mathbf{E}_{\text{ext}}$, whereas the field in Equation 2.6 is the total

macroscopic field in the medium, $\mathbf{E}_{\text{ext}} + \mathbf{E}_{\text{dipoles}}$. We may rewrite the polarization in terms of the atomic density, $N = \frac{1}{(4/3)\pi r^3}$, and the atomic dipole moment, $\mathbf{p}$:

$$\mathbf{P} = N\mathbf{p} = N\alpha\mathbf{E}_{\text{ext}}. \tag{2.9}$$

The total field for the atomic dipole in an external field is given by:

$$\mathbf{E}_{\text{total}} = \mathbf{E}_{\text{dipole}} + \mathbf{E}_{\text{ext}} = -\frac{1}{4\pi\varepsilon_0}\frac{\mathbf{p}}{r^3} + \mathbf{E}_{\text{ext}}. \tag{2.10}$$

Using the definition of the dipole moment in Equation 2.5 and the definition of the atomic density yields:

$$\begin{aligned}
\mathbf{E}_{\text{total}} &= -\frac{1}{4\pi r^3}\frac{\alpha}{\varepsilon_0}\mathbf{E}_{\text{ext}} + \mathbf{E}_{\text{ext}} && (2.11)\\
&= -\frac{N}{3}\frac{\alpha}{\varepsilon_0}\mathbf{E}_{\text{ext}} + \mathbf{E}_{\text{ext}} && (2.12)\\
&= (1 - \frac{N\alpha}{3\varepsilon_0})\mathbf{E}_{\text{ext}} && (2.13)\\
&\Rightarrow \mathbf{E}_{\text{ext}} = \frac{\mathbf{E}_{\text{total}}}{(1 - \frac{N\alpha}{3\varepsilon_0})}. && (2.14)
\end{aligned}$$

Substituting $\mathbf{E}_{\text{ext}}$ from Equation 2.14 into Equation 2.9, we arrive at

$$\mathbf{P} = \frac{N\alpha\mathbf{E}_{\text{total}}}{(1 - \frac{N\alpha}{3\varepsilon_0})} = \varepsilon_0\chi\mathbf{E}_{\text{total}}, \tag{2.15}$$

using the definition of χ from Equation 2.6 in the last step. By solving for α, we arrive at a result which relates α to χ, ε and n:

$$\alpha = \frac{3\varepsilon_0}{N}\frac{\chi}{\chi + 2} = \frac{3\varepsilon_0}{N}\frac{\varepsilon_r - 1}{\varepsilon_r + 1} = \frac{3\varepsilon_0}{N}\frac{n^2 - 1}{n^2 + 1}. \tag{2.16}$$

This important equation connects the microscopic properties like atomic polarizability and scattering from deeply sub-wavelength particles to the macroscopic description of continuous solid materials.

2.1.2 Light scattering near a resonance

The optical "constants" so far introduced – α, χ, ε, n – are complex-valued (indicated by '$\sim$') and take on a frequency dependence in the presence of an oscillating field: $\alpha \to \widetilde{\alpha}(\omega)$, $\chi \to \widetilde{\chi}(\omega)$, $\varepsilon \to \widetilde{\varepsilon}(\omega)$, $n \to \widetilde{n}(\omega)$. If we consider the resonant material response as a function of frequency, the polarization of the material originates from a number of sources that are active at different frequencies (**Figure 2.2**):

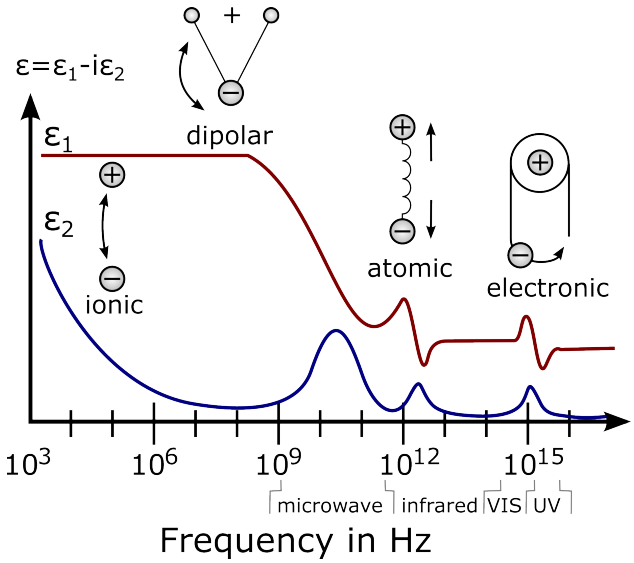

Figure 2.2: Over a wide range of frequencies, the dielectric function exhibits resonances that arise from the resonant response of different polarization processes. ε_1 and ε_2 denote the real and imaginary parts of the dielectric function, respectively. Reprinted with permission from [143].

- electronic: electron clouds displaced relative to the nucleus,
- atomic: relative displacement or reorientation of charged ion cores,
- dipolar: the alignment of permanent or induced dipoles in an electric field, and
- ionic: the movement of ionic charges, including interfacial and space charge relaxation.

The frequency of the external field determines which resonant modes will respond to the field. At the optical frequencies used in this work, electronic motion dominates the optical response. To probe the bending or stretching of bonds in an atom or molecule, lower infrared frequencies are ideal since heavier atoms have lower characteristic resonant frequencies, although collective nuclear displacements can also affect electronic resonances, as emphasized in **Section 3.4** and **Chapter 4**.

The resonance features in the imaginary part of the dielectric function, ε_2, exhibit absorptive lineshapes whereas the real part, ε_1, exhibits dispersive lineshapes where $\widetilde{\varepsilon} = \varepsilon_1 - i\varepsilon_2$. To gain some intuition for these features, we follow Feynman's treatment for the field due to oscillating charges in a material probed with optical light, also known as the Drude-Lorentz oscillator model [144]. Bound electrons in an atom can be approximated as damped springs. The equation of motion for the driven displacement of the electrons from equilibrium is

$$m\frac{\mathrm{d}^2\widetilde{x}}{\mathrm{d}t^2} + m\gamma\frac{\mathrm{d}\widetilde{x}}{\mathrm{d}t} + m\omega_0^2\widetilde{x} = qE_0e^{-i\omega t} \tag{2.17}$$

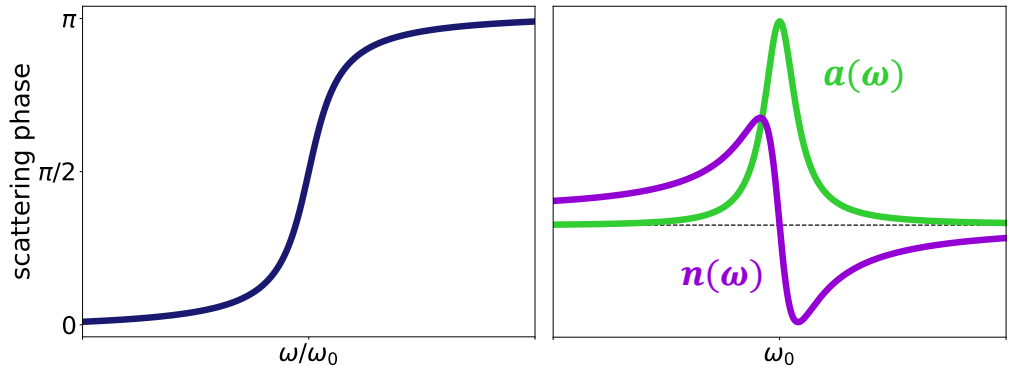

Figure 2.3: (left) An oscillator acquires a π phase lag going through its natural resonant frequency $\omega = \omega_0$. **(right)** The real and imaginary parts of the motion of an oscillator near resonance. In drawing the analogy to resonating electrons in a material, the imaginary part, $a(\omega)$, takes on an absorptive lineshape (green) while the real part, $n(\omega)$, takes on a dispersive lineshape (purple).

where m is the mass of the electron, γ is the damping coefficient, ω_0 is the natural frequency of the oscillator, q is the charge of the electron, and ω is the frequency of light driving the electron. At steady state the solution is given by

$$\widetilde{x}(t) = \widetilde{x}_0 e^{-i\omega t} \tag{2.18}$$

with

$$\widetilde{x}_0 = \frac{q}{m} \frac{E_0}{\omega_0^2 - \omega^2 - i\gamma\omega}. \tag{2.19}$$

The oscillating dipole moment created by the field is simply the real part of $\widetilde{p}(t) = q\widetilde{x}(t)$. Note that the dipole oscillates at the same frequency as the field, but has a phase lag of $\tan^{-1}[-\gamma\omega/(\omega_0^2 - \omega^2)]$, which is small when $\omega \ll \omega_0$ and rises to π when $\omega \gg \omega_0$ (left panel in **Figure 2.3**). If there are several different kinds of oscillators within a material, each electron may have a different natural frequency and damping coefficient. For j unique oscillator modes and number f_j electrons with frequency ω_j and damping coefficient γ_j, the complex polarization is given by:

$$\widetilde{\mathbf{P}}(\omega) = \frac{Nq^2}{m} \sum_j \frac{f_j}{\omega_j^2 - \omega^2 - i\gamma_j\omega} \widetilde{\mathbf{E}}. \tag{2.20}$$

Note that the physical polarization, $\mathbf{P}(\omega)$, is the real part of $\widetilde{\mathbf{P}}(\omega)$. $\widetilde{\mathbf{P}}(\omega)$ resembles the original relationship between polarization and the electric field in Equation 2.6, where we can now identify an expression for the complex susceptibility

$$\widetilde{\chi}(\omega) = \frac{Nq^2}{\varepsilon_0 m} \sum_j \frac{f_j}{\omega_j^2 - \omega^2 - i\gamma_j\omega}, \tag{2.21}$$

and a corresponding expression for the complex refractive index:

$$\widetilde{n}^2(\omega) = 1 + \frac{Nq^2}{\varepsilon_0 m} \sum_j \frac{f_j}{\omega_j^2 - \omega^2 + i\gamma_j\omega}. \tag{2.22}$$

Usually the imaginary part of $\widetilde{n}(\omega)$ is negligible except when $\omega \sim \omega_j$ and it plays a significant role, as we will now see. The electric field that propagates through a medium of driven oscillating electrons with complex refractive index is attenuated near resonance since the damping is the dissipation of absorbed energy. The wave equation in a dispersive medium is given by

$$\nabla^2 \widetilde{\mathbf{E}} = \widetilde{\varepsilon}\mu \frac{\partial^2 \widetilde{\mathbf{E}}}{\partial t^2} \tag{2.23}$$

with plane wave solutions

$$\widetilde{\mathbf{E}}(z,t) = \widetilde{\mathbf{E}}_{\mathbf{0}} e^{i(\widetilde{k}z - \omega t)} \tag{2.24}$$

and complex wave number

$$\widetilde{k} = k + i\kappa, \tag{2.25}$$

where in Equation 2.25, we separate $\widetilde{k}$ into its real and imaginary parts. The electric field in Equation 2.24 may now be written as

$$\widetilde{\mathbf{E}}(z,t) = \widetilde{\mathbf{E}}_0 e^{-\kappa z} e^{i(kz - \omega t)} \tag{2.26}$$

where $1/2\kappa$ is the attenuation length or penetration depth and the absorption coefficient is defined as $a \equiv 2\kappa$ since the intensity is proportional to $E^2 \propto e^{-2\kappa z}$. Note that an extension of Equation 2.8 is $v = \omega/k$ such that $\widetilde{k} = (\omega/c)\widetilde{n}$. Typically the second term in Equation 2.22 is small and $\widetilde{n}$ may be approximated by the first term in a binomial expansion as $\sqrt{1+x} \cong 1 + \frac{1}{2}x$ where $x = (Nq^2)/(\varepsilon_0 m) \sum \frac{f_j}{\omega_j^2 - \omega^2 + i\gamma_j\omega}$. Then,

$$\widetilde{k}(\omega) = \frac{\omega}{c}\widetilde{n} \approx \frac{\omega}{c}\left[1 + \frac{Nq^2}{2\varepsilon_0 m} \sum_j \frac{1}{\omega_0^2 - \omega^2 + i\gamma\omega}\right], \tag{2.27}$$

from which we can readily extract the real part of the refractive index and the absorption coefficient:

$$n(\omega) = \frac{c}{\omega}\mathrm{Re}[\widetilde{k}] \approx 1 + \frac{Nq^2}{2\varepsilon_0 m} \sum_j \frac{\omega_0^2 - \omega^2}{(\omega_0^2 - \omega^2)^2 + \gamma^2\omega^2} \tag{2.28}$$

$$a(\omega) = 2\mathrm{Im}[\widetilde{k}] \approx \frac{Nq^2\omega^2}{m\varepsilon_0 c} \sum_j \frac{\gamma}{(\omega_0^2 - \omega^2)^2 + \gamma^2\omega^2}. \tag{2.29}$$

These equations near one of the resonances are plotted in the right panel of **Figure 2.3** and exhibit the same absorptive ($\sim 1/\mathrm{detuning}^2$) and dispersive ($\sim 1/\mathrm{detuning}$) lineshapes that also appeared in the resonances for the dielectric function in **Figure 2.2**, where "detuning" refers to the distance between the specified frequency, ω, and the resonant frequency, ω_0. Between resonances, spectrally, the real part of the refractive index usually increases gradually with increasing frequency, but near a resonance there are rapid variations, including a large drop with increasing frequency around the peak of the absorption. This behavior is called anomalous dispersion. In terms of the damped electron-on-a-spring model, electrons are being driven at their natural frequency, so the amplitude of the oscillation is large and a large amount of energy is being dissipated by the damping mechanism. Note that contributions from other terms in the sum add a background that usually keeps $n > 1$, but even in cases where $n < 1$ it is only the phase velocity, $v_p = \omega/k$ that travels faster than c while energy travels at the group velocity, $v_g = \mathrm{d}\omega/\mathrm{d}k$.

2.2 Excited-state phenomena in semiconducting materials

There are several well-understood microscopic effects that change the optical response of a semiconductor in the excited state when it is probed by an external optical field following photoexcitation, typically quantified by changes in the absorption coefficient, a, or refractive index, n (**Figure 2.4**). (The late Millie Dresselhaus has an excellent set of lecture notes that summarize the same phenomena far more eloquently than I can [145].) The first is called Pauli blocking, band/state filling, or the Burnstein-Moss effect. After electrons are excited into the conduction band, they fill the states near the band edge, preventing further excitation into those same states, which can each only be occupied by one spin up and one spin down electron due to Pauli exclusion. With the lowest energy states in the conduction band filled, electrons from the valence band require energies greater than the nominal bandgap to be optically excited into the conduction band. This causes an apparent bandgap increase commensurate with the absorption edge being pushed to higher energies. If parabolic bands are assumed, the interband absorption coefficient is given by [146]:

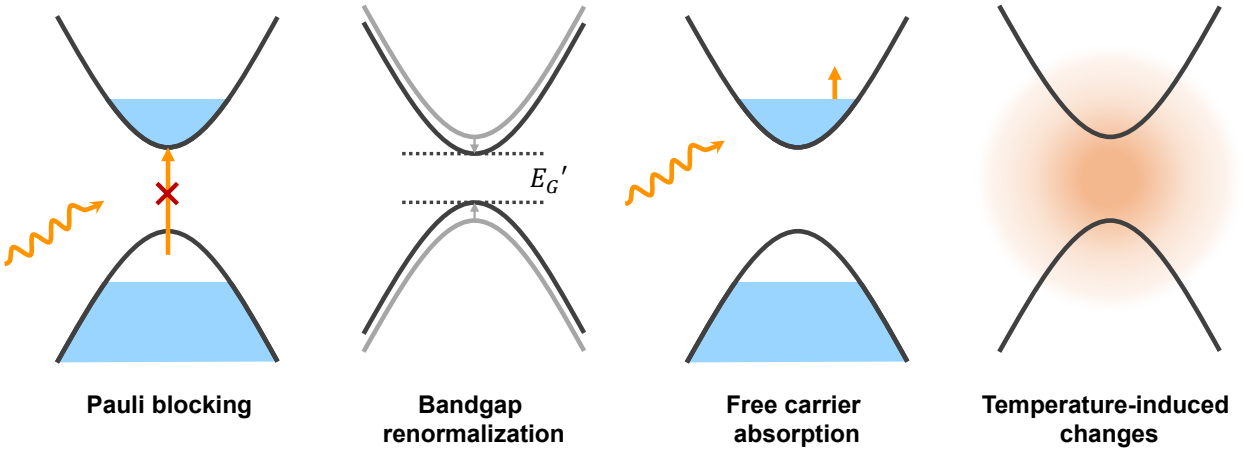

Figure 2.4: Photoinduced excited state phenomena that modify the optical response in semiconductors include Pauli blocking (also called band or state filling), bandgap renormalization (typically shrinkage), free carrier absorption, and temperature-induced changes (e.g., heating). Inspired by a presentation figure from **Cora Went**.

$$a_0(E) = 0 \qquad E < E_\mathrm{G}, \tag{2.30}$$

$$a_0(E) \propto \frac{1}{E}\sqrt{E - E_\mathrm{G}} \qquad E \geq E_\mathrm{G}, \tag{2.31}$$

where $E = \hbar\omega$ is the photon energy and E_G is the original bandgap energy. This is a standard result for direct interband transitions derived using Fermi's golden rule [147, 148]. Knowing the Fermi-Dirac distributions and densities of states for the electrons and holes, the band-filling induced change in the absorption coefficient may be calculated as $\Delta a(n_\mathrm{e}, n_\mathrm{h}, E) = a(n_\mathrm{e}, n_\mathrm{h}, E) - a_0(E)$ for free electron and hole concentrations, n_e and n_h, respectively.

The second carrier-induced change to the optical response is bandgap renormalization, typically bandgap shrinkage [149]. When electrons are injected into the conduction band at sufficiently high concentrations, their wavefunctions may overlap, forming a gas of interacting particles. The electrons repel one another because they have the same charge, and the separation between electrons with the same spin is furthermore larger than it would be if there were no Pauli exclusion due to Fermi exchange effects [150]. The net result of these electron-electron interactions is to reduce the probability of finding two electrons close to one another, which in turn decreases the Coulomb repulsion between the electrons, lowering their self-energies and therefore also lowering the conduction band energy. A similar correlation effect for holes increases the energy of the valence band edge, and overall, the bandgap shrinks in proportion to the density of the free electron-hole gas [146, 151]:

$$\Delta E_\mathrm{G} = -\left(\frac{q}{2\pi\varepsilon_0\varepsilon_\mathrm{m}}\right)\frac{3}{\pi}^{1/3} n_i^{1/3}, \tag{2.32}$$

where n_i for $i = e, h$ is the concentration of free electrons or holes and ε_{m} is the dielectric constant of the material. The estimated bandgap shrinkage is inversely proportional to the average interparticle spacing. The screening effects become significant when the interparticle spacing is on the order of the Böhr radius. Typically, bandgap shrinkage induces opposite changes in n on either side of the band edge, which may be calculated using the Kramers-Kronig relations that relate Δa to Δn (**Section 2.2.1**): $\Delta n > 0$ for $E \leq E_{\mathrm{G}}$ and $\Delta n < 0$ for $E > E_{\mathrm{G}}$.

In TMDCs, the band filling and bandgap renormalization effects roughly cancel [152–155]. In the presence of finite exciton densities, the screened Coulomb interaction between charge carriers decreases the strength of the electron-hole attraction, reducing the exciton binding energy. In addition, the photoinduced screening induces renormalization of the quasiparticle bandgap to lower energies. The decrease in exciton binding energy and bandgap shrinkage tend to be of similar magnitude but offset one another, leaving the optical bandgap relatively unchanged, shifting several tens of meV even though the underlying changes in E_{B} and E_{G} are hundreds of meV.

The third photoinduced effect on the optical response is free carrier absorption. An electron in the conduction band can absorb an incident photon and be promoted to a higher energy state within the band. This intraband absorption process may be described with the Drude model [156, 157], similar to the treatment of electrons as damped oscillators in **Section 2.1.2** but with no restoring force ($\omega_0 = 0$), yielding $n^2(\omega) \cong 1 - \frac{Nq^2}{m\varepsilon_0}\frac{1}{\omega^2 - i\omega\gamma}$ [158, 159]. The free carrier absorption coefficient for $\omega \gg \gamma$ is given by [160–164]:

$$a_{\mathrm{FCA}}(\omega) = \frac{q^2}{c\varepsilon_0}\frac{1}{n(\omega)\omega^2}\left(\frac{\Delta N_{\mathrm{e}}}{m_{\mathrm{e}}\tau_{\mathrm{e}}} + \frac{\Delta N_{\mathrm{h}}}{m_{\mathrm{h}}\tau_{\mathrm{h}}}\right), \tag{2.33}$$

where $n(\omega)$ is the refractive index at photon frequency ω, N_{e} and N_{h} are the number density of electrons or holes, respectively, m_{e} and m_{h} are the effective electron or hole mass, respectively, and $1/\gamma_i = \tau_i$ for $i = e, h$ are the mean free time between collisions for electrons or holes, respectively. The Drude model treats conducting electrons as particles on a damped spring driven by an optical field without a restoring force since the electrons are "free." It assumes that between collisions with the lattice, electrons move in straight lines and do not interact with one another. Because of the $1/\omega^2$ dependence, the free-carrier absorption increases as the probe photon energy is decreased, producing a broad absorption spectrum that extends from the band-to-band absorption edge into the infrared spectral region [159], although when γ is frequency-dependent, it may exhibit a different scaling, (e.g., in InAs, $a_{\mathrm{FCA}} \propto \omega^{-3}$) [157]. In contrast, both Pauli blocking and bandgap renormalization effects are largest near the bandgap and approach zero for $E \ll E_{\mathrm{G}}$.

The last photoinduced effect is a change in temperature, which has a more complicated effect on the optical response that results from thermal expansion, shear strain from thermal expansion against the substrate, broadening of the Fermi level, electron-phonon interactions, and Fermi level shifts [165]. The Varshni relation is an empirical expression for the temperature dependence of the bandgap [166, 167]:

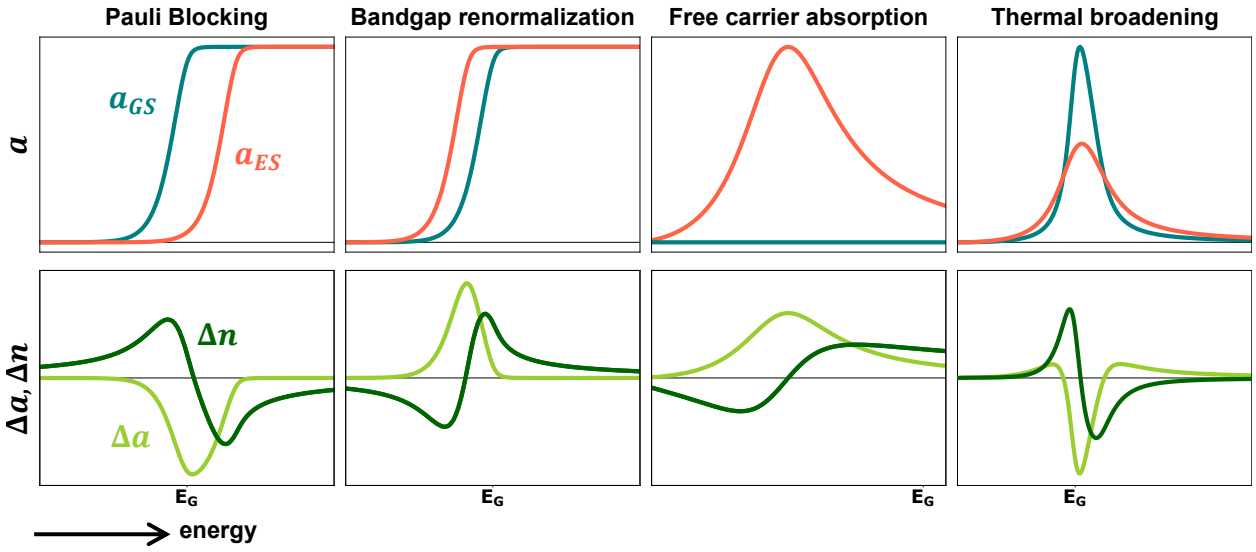

Figure 2.5: Modeled changes in the absorption coefficient and refractive index in the excited state near the bandgap energy, E_G, for the four often implicated phenomena discussed in this section. In the top row, the ground state (blue) and photoinduced or excited state (salmon) absorption coefficients are plotted as a function of energy. In the bottom row, the change in absorption coefficient, Δa (light green), is shown with the change in refractive index, Δn (dark green), calculated using a Kramers-Kronig transformation. Plots generated with code adapted from **Cora Went** [168].

$$E_{\mathrm{G}}(T) = E_0 - \frac{\zeta T^2}{T + \psi}, \tag{2.34}$$

where ζ and ψ are fitting parameters characteristic of a given material. For small changes in temperature, it is reasonable to assume that changes in the refractive index are linear with changes in temperature [162]:

$$\Delta n = \frac{\mathrm{d}n}{\mathrm{d}T_L}\Delta T_L, \tag{2.35}$$

where T_L is the lattice temperature.

The ground- and excited state absorption coefficient and changes in the real and imaginary parts of the refractive index for each of these effects are summarized in **Figure 2.5**, with thermal broadening representing one common temperature-induced effect. Changes in the absorption coefficient can be calculated from changes in the real part of the refractive index and vice versa using the Kramers-Kronig relations that we explore next.

2.2.1 Connection between the real and imaginary parts of the refractive index

The Kramers–Kronig relations are bidirectional mathematical relations, connecting the real and imaginary parts of any complex function that satisfies causality, linear response, and conservation of energy. These relations are often used to calculate the real part from the imaginary part (or vice versa) of response functions in physical systems. The complex refractive index is one such response function that satisfies these criteria. Lorentz derived the following expression for the real and imaginary parts of the refractive index, similar to Equations 2.28 and 2.29 [169]:

$$\mathrm{Re}[\widetilde{n}(\omega)] = 1 + \frac{2\pi c^2}{\omega^2} N \mathrm{Re}[f(\omega)] \tag{2.36}$$

$$\mathrm{Im}[\widetilde{n}(\omega)] = \frac{2\pi c^2}{\omega^2} N \mathrm{Im}[f(\omega)] \tag{2.37}$$

where $f(\omega)$ is the forward scattering amplitude and N is the density of scatterers. Kramers and Kronig inferred from this formula that the real part of the refractive index approaches unity in the high-frequency limit and then applied a Hilbert Transform [170]:

$$\mathrm{Re}[\widetilde{n}(\omega)] = 1 + \frac{2}{\pi} P \int_0^\infty \frac{\omega' \,\mathrm{Im}[\widetilde{n}(\omega')]}{\omega'^2 - \omega^2} \,\mathrm{d}\omega' \tag{2.38}$$

$$\mathrm{Im}[\widetilde{n}(\omega)] = \frac{-2\omega}{\pi} P \int_0^\infty \frac{\omega' \,\mathrm{Re}[\widetilde{n}(\omega')] - 1}{\omega'^2 - \omega^2} \,\mathrm{d}\omega' \tag{2.39}$$

where P denotes the Cauchy principal value of the integral. Further, if one invokes the optical theorem [133–137], $\sigma_{\mathrm{tot}} = \frac{4\pi c}{\omega}\mathrm{Im}[f(\omega)]$, then the real part of the forward scattering amplitude and the total cross section are related by:

$$\mathrm{Re}[f(\omega)] = \frac{\omega^2}{2\pi^2 c} P \int_0^\infty \frac{\sigma_{\mathrm{tot}}(\omega')}{\omega'^2 - \omega^2} \,\mathrm{d}\omega'. \tag{2.40}$$

Even though the upper integral limit goes to infinity, it turns out that these transformations work on a finite frequency range on actual measured data [171]. For example, taking a known change in refractive index, the transient absorption spectrum can be calculated. This connection is important because scattering can also induce changes in the transient transmission that are separate from changes in absorption, as explored further below in **Section 2.2.3**. For the work discussed in this thesis, the Kramers-Kronig relations are mostly useful for comparing spectra collected in reflection in the stroboSCAT microscope to those collected in transmission, which, depending on the material, may be more common in the literature.

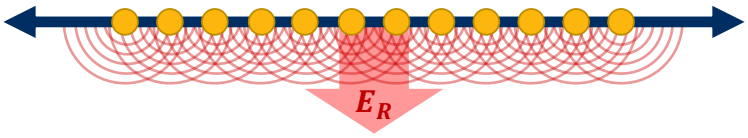

Figure 2.6: Spherical wavelets from scatterers at an interface interfere to create an overall normally reflected field.

2.2.2 Transient transmission and reflection measure changes in the excited state optical response

One way to experimentally measure the change in the absorption coefficient or refractive index is to measure the change in reflectivity, R, or transmittance, T, in the excited state (ES) compared to the ground state (GS) and to construct differential signals $\Delta R/R = (R_{\mathrm{ES}} - R_{\mathrm{GS}})/R_{\mathrm{GS}}$ and $\Delta T/T = (T_{\mathrm{ES}} - T_{\mathrm{GS}})/T_{\mathrm{GS}}$. These are commonly called "pump-probe" experiments (e.g., the transient scattering microscopies introduced in **Section 1.4**) since an impulsive pump pulse generates excitations in the material that are probed by a second, temporally delayed pulse. To find an expression for $\Delta R/R$ or the transient reflectance, we invoke a geometric scattering approach (**Section 2.3**) to describe normal reflection from an interface between two index-mismatched materials. This approximation is connected to the small-particle scattering picture described in **Section 2.1**. An interface is made up of closely-spaced small scatterers, which according to Huygens, act as point sources for spherical wavelets. The wavelets interfere with one another, canceling out in the transverse direction, except for at the edges, and coherently summing in the normal direction, yielding a net reflected field (**Figure 2.6**). Although the scattering picture is more complete, the geometric optics approximation for the reflected field is a decent one, especially when the density of scatterers is high, such as in a solid state material. The Fresnel equation for normal reflection from an interface between two materials with different refractive indices is given by [172]:

$$R \equiv |r|^2 = \left| \frac{\widetilde{n}_i - \widetilde{n}_t}{\widetilde{n}_i + \widetilde{n}_t} \right|^2 = \left(\frac{\widetilde{n}_i - \widetilde{n}_t}{\widetilde{n}_i + \widetilde{n}_t} \right) \left(\frac{\widetilde{n}_i - \widetilde{n}_t}{\widetilde{n}_i + \widetilde{n}_t} \right)^* \tag{2.41}$$

where $\widetilde{n}_i = n_i + ik_i$, $\widetilde{n}_t = n_t + ik_t$ are the complex refractive indices of the incident medium and transmitting medium, respectively. After cranking through some algebra and using the definition of the complex conjugate, (for $z = a + ib$, $z^* = a - ib$), the reflectance may be expressed as:

$$R = \frac{(n_i - n_t)^2 + (k_i - k_t)^2}{(n_i + n_t)^2 + (k_i + k_t)^2} \tag{2.42}$$

Let's assume that the substrate or incident medium is transparent, $k_i = 0$, and that it does not respond to the pump light, n_i = constant. The pump may, however, induce changes

in the complex refractive index of the transmitting material: $n_t \to n_t'$, $k_t \to k_t'$. For small changes in n_t and k_t ($\Delta n_t \ll n_t$ and $\Delta k_t \ll k_t$), the transient reflectance response may be approximated by a first order Taylor expansion:

$$\frac{\Delta R}{R} \approxeq \frac{1}{R}\left[\left(\frac{\partial R}{\partial n_t}\right)_{k_t} \Delta n_t + \left(\frac{\partial R}{\partial k_t}\right)_{n_t} \Delta k_t\right] \tag{2.43}$$

with

$$\frac{1}{R}\left(\frac{\partial R}{\partial n_t}\right)_{k_t} = \frac{-4n_i\left(n_i^2 - n_t^2 + k_t^2\right)}{\left[\left(n_i + n_t\right)^2 + k_t^2\right]\ \left[\left(n_i - n_t\right)^2 + k_t^2\right]} \text{ and} \tag{2.44}$$

$$\frac{1}{R}\left(\frac{\partial R}{\partial k_t}\right)_{n_t} = \frac{8n_i n_t k_t}{\left[\left(n_i + n_t\right)^2 + k_t^2\right]\left[\left(n_i - n_t\right)^2 + k_t^2\right]}. \tag{2.45}$$

For off-resonant probing conditions, $\Delta k_t \approx 0$ and $k_t \approx 0$, Equation 2.43 simplifies to:

$$\frac{\Delta R}{R} \approx \frac{4n_i}{n_t^2 - n_i^2}\Delta n_t. \tag{2.46}$$

It might be tempting to use a similar procedure to estimate $\Delta T/T$ from the transmittance. The Fresnel equations, however, only describe the reflected or transmitted field amplitudes or power right at either side of the interface. The incident light is further attenuated as it transmits through the material, being scattered and absorbed as it goes along. It is customary to relate the change in optical density, OD, (**Appendix B**) to the change in transmission:

$$-\Delta OD = \frac{\Delta T}{T} \tag{2.47}$$

where the transmittance is defined using the Beer-Lambert law as

$$T \equiv \frac{I}{I_0} = e^{-OD} \tag{2.48}$$

Techniques that measure $\Delta T/T$ are commonly called transient "absorption" since the absorbance, A, is given by $A = 1 - T$. In practice, scattering (Δn) also contributes to the attenuation of the probe light as it transmits through the material, so this is really an approximation and a misnomer. Transient "extinction" would be a more descriptive label. There are ways to model photoinduced refractive index changes in thin films measured in transmission to account for Δn using, e.g., the Fresnel equations or a full transfer-matrix calculation [173–175].

2.2.3 Additional thoughts on transient scattering in reflection versus transmission

Although both absorption and reflection share a common origin in the scattered probe field, absorption is associated with the imaginary part of the refractive index (k), whereas reflection arises from changes to both k and the real part of the refractive index n. For high-index materials, such as metal halide perovskites and the vast majority of inorganic semiconductors, n is typically ∼10-20 times larger than k across the visible spectrum, so that to a good approximation, reflectivity is dominated by n [173, 174]. In the high n/k limit, excited state reflectance is also dominated by changes to n [173, 174, 176, 177]. The pure transient absorption spectrum (not transient transmission, which contains contributions from both absorption and reflectance) then corresponds to the Kramers-Kronig transform of the transient reflectance spectrum [178–180].

There are several advantages to probing in a reflection geometry. It is more generalizable than measurements in transmissive geometries since it does not require thin or optically transparent samples. The reference field, sometimes called the local oscillator, refers to the unscattered part of the field that interferes with the scattered field to give rise to absorption or reflection. The reference field is much weaker in reflection than in transmission, since only a small fraction, typically 1-10%, of the forward propagating field is reflected. This results in a higher signal-to-background ratio, i.e., higher contrast, at the expense of lower photon counts, i.e., higher shot noise. Nevertheless, photoinduced changes to n (Δn) display a relatively weak dependence on spectral detuning from the main absorption change at the band edge ($\Delta n \sim 1/\text{detuning}$, $\Delta k \sim 1/\text{detuning}^2$). The probe field can therefore be tuned away from absorptive wavelengths and into the transparency region of the semiconductor. Large probe powers at non-absorptive wavelengths are relatively benign and allow filling the well depth of the detector used, thus simultaneously maximizing contrast and minimizing relative fluctuations due to shot noise.

In transmission-based geometries such as transient absorption, the co-propagating reference and signal fields that traverse the entire sample preclude extracting phase (depth) information over axial distances much smaller than the Rayleigh range without more sophisticated interferometric techniques such as off-axis holography or models that take into account changes to the complex refractive index in combination with experimental access to imaging different axial sample planes [181]. In contrast, a reflection-based geometry uses a spatially well-defined interfacial reflection as the reference field, which can provide up to ∼20-nm sensitivity to depth, depending on the refractive index of the material.

When measuring in dense samples with appreciable dispersion and absorption, forward-scattered light may undergo multiple scattering or re-absorption events prior to interfering with the local oscillator, quickly scrambling phase information. In transient reflectance, by focusing on back-scattered light near the refractive index interface on the illuminated side, and remaining spectrally far away from large photoinduced absorption changes, phase scrambling is minimized.

Deeply subwavelength-sized objects have equal backscattering and forward-scattering

contributions, whereas larger objects have much larger forward-scattering contributions [182, 183]. In collinear pump-probe experiments, where the signal field is necessarily emitted in the same direction as the reference field, detecting in an backscattering geometry significantly enhances the ratio of signals arising from small objects near the refractive index interface, the signal of interest in transient reflectance, versus bulk contributions that can arise from birefringence, bulk heating, or sample inhomogeneities.

Taken together, these fundamental differences give transient reflectance a set of unique capabilities that are highly complementary to those of transient absorption: (1) the ability to apply the same instrument to a vast range of different materials and track energy flow in a rapid, benign fashion in dense or opaque environments without changing wavelengths or detection geometry, (2) the unique opportunity to extract 3D information through preserved phase sensitivity and (3) the potential to extract the full dielectric response of a material to photoexcitation without propagating assumptions through Kramers-Kronig transformations.

2.3 Microscopy crash course

In order to probe dynamics in heterogeneous, microstructured materials with diffraction-limited spatial resolution, it is essential to couple the pump and probe light sources into a microscope. We now introduce a few basic microscopy concepts that are relevant for understanding the imaging process involved in transient scattering microscopies including stroboSCAT.

2.3.1 Ray tracing in geometric optics

The simplest treatment of light wave propagation is called geometric optics. It defines a ray of light as any path for which the total optical path length (OPL) is minimized, where $\mathrm{OPL} = \int_{\mathrm{path}} n(r)\mathrm{d}s$ for spatially varying index of refraction n along spatial coordinate s (**Figure 2.7a**). This definition is based on Fermat's Principle that states that to get from point 'a' to point 'b,' a light ray travels the path of least time, $t_{a\to b} = \mathrm{OPL}/c$, where c is the speed of light in vacuum. An immediate consequence of this premise is that in a homogeneous medium, light travels in a straight line. Rays are normal to the local wavefront and point along the direction of energy flow. Rays can be absorbed and reflected and even bend at interfaces between two materials. But at this level of abstraction, phenomena such as diffraction and interference cannot be explained. (These effects are treated in wave optics.)

The equation that governs ray tracing is Snell's Law, $n_1 \sin\theta_1 = n_2 \sin\theta_2$, which describes how the direction of a light ray changes as it travels across an interface between two materials with different refractive indices where the propagation angle is measured relative to the surface normal (**Figure 2.7b**). The larger the angle when the ray hits the index mismatched interface, the more the ray will be deflected. This principle explains why lenses with curved surfaces can focus incident collimated, or, plane wave, light to a point since every ray in the wavefront hits the curved surface at a different incident angle relative to the normal (**Figure**

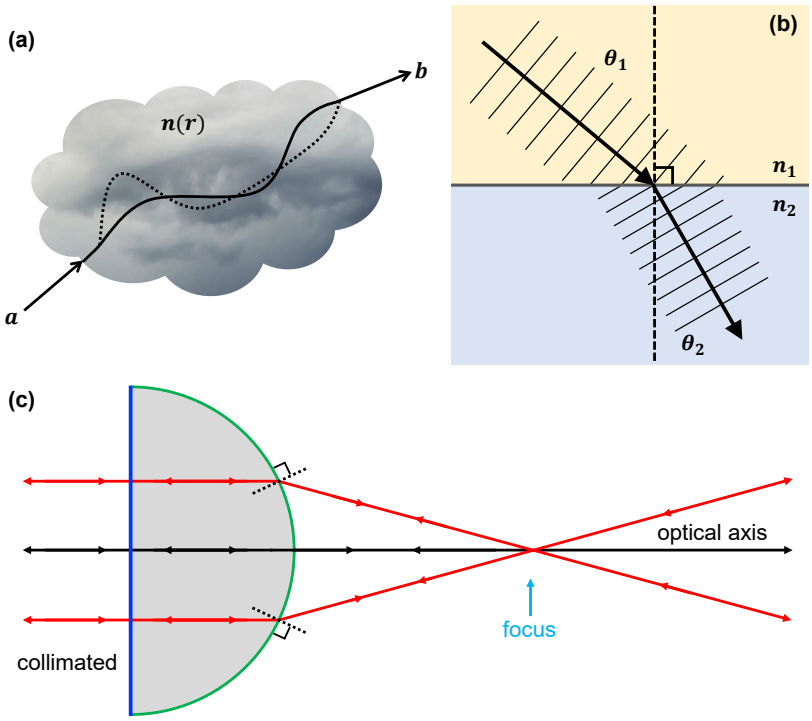

Figure 2.7: **(a)** A light ray travels through a material with variable optical density or refractive index, $n(r)$, by taking the path of least time (solid line) over other paths (dashed line). **(b)** A light ray travels through homogeneous material 1 with n_1 at angle of incidence θ_1 and bends towards the surface normal traveling at θ_2 through homogeneous material 2 with $n_2 > n_1$. The indices of refraction and angles are related by Snell's Law. **(c)** Snell's Law applied when ray tracing an incident plane wave through a plano-convex lens. The curvature of the lens bends the incident light rays to a focal point.

2.7c). The optical axis of a lens is the line that passes through its center of curvature. Out of Snell's Law falls a few useful ray tracing rules for imaging objects through lenses:

- A ray parallel to the optical axis, normally incident on a lens, passes through the focus.
- A ray that passes through the center of a lens is not diverted.
- A ray that passes through the focus emerges parallel to the optical axis.
- A ray will follow the same path if its direction of travel is reversed.

Images form where rays that emerge from the same point in the object plane cross again. With these rules, one can trace rays emerging from an object through a convex lens to its image formation on the other side as in the top of **Figure 2.8**. Taking these all together, it seems as though lenses map lines (collimated light) to points (focused light) and vice versa,

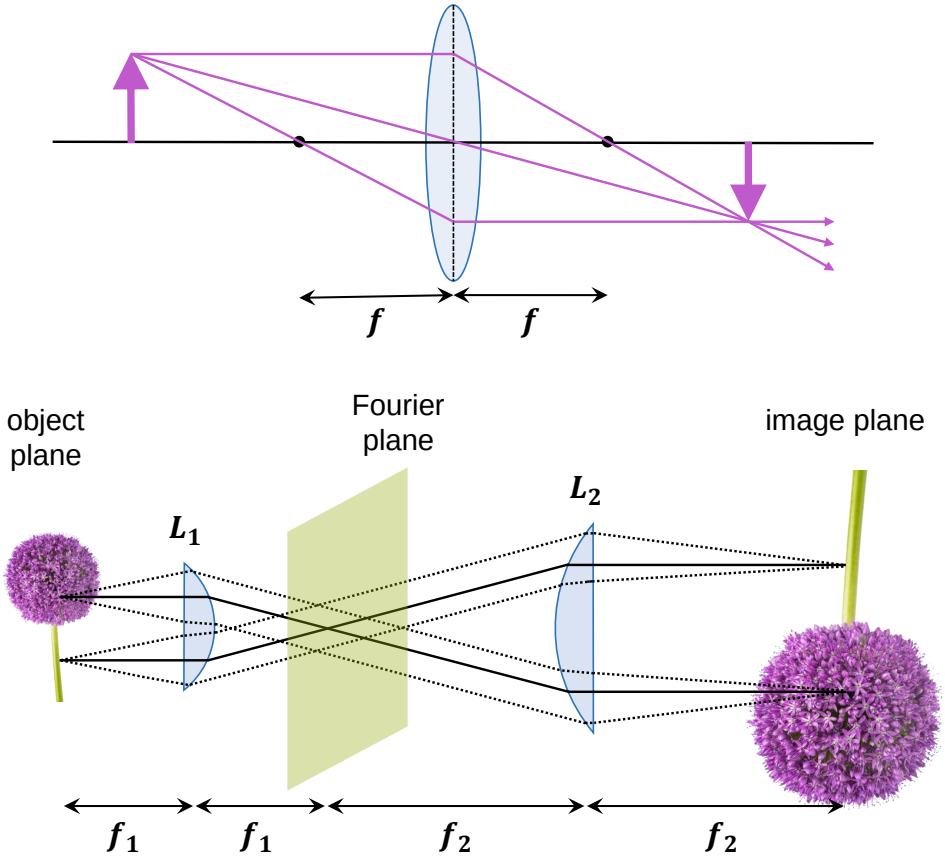

Figure 2.8: (top) 2f imaging through a single lens, like a magnifying glass. Using ray tracing rules, the rays emerging from one point on an object cross again on the other side of the converging lenses, forming an inverted image. **(bottom)** A 4f imaging system consists of two lens separated by the sum of their focal lengths. An object placed one focal length in front of L_1 is imaged onto the conjugate image plane one focal length away on the other side of L_2 with a magnification of f_2/f_1. The Fourier plane of both lenses sits between the lenses, shown in green.

which sounds suspiciously like a Fourier transform. And indeed it is! In the far-field, or Fraunhofer regime, a lens performs an optical Fourier transform on its input. This property is utilized in Fourier-plane imaging to measure momentum-resolved dispersion relations [184] and transition dipole moment orientations [185], for example.

2.3.2 4f imaging systems

The heart of a real-space imaging system is a 4f lens arrangement that performs two Fourier transforms, mapping the plane a distance f_1 in front of the first lens to a plane "4f" away (or more generally "$2(f_1+f_2)$" away) with adjustable (de-)magnification as shown in the bottom

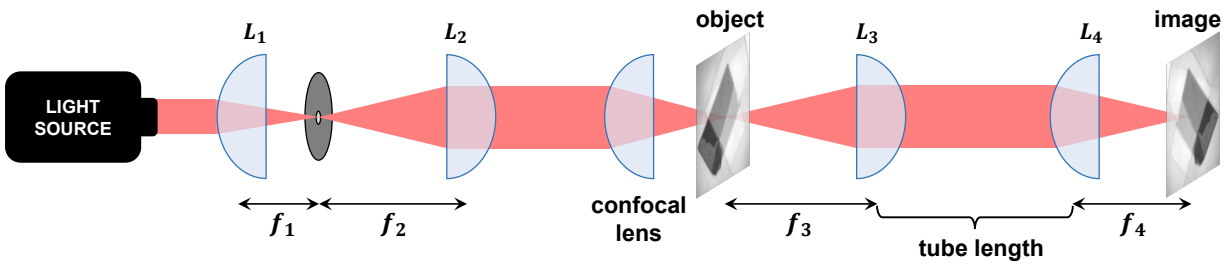

Figure 2.9: An illumination source is expanded through a 4f lens arrangement consisting of L_1 and L_2 with spatial filtering through a pinhole in the Fourier plane. A confocal lens focuses the light onto the sample plane, which is imaged through a second 4f system. When L_3 is an objective, the tube lens, L_4, is placed one tube length away from the back focal plane of the objective to mitigate aberrations from vignetting.

of **Figure 2.8.** It consists of two lenses separated by the sum of their focal lengths. Lenses in this configuration are said to be confocal since they share the same focus. The ratio of the focal length of the downstream lens to that of the upstream lens sets the (de-)magnification of the imaging system: $M = f_2/f_1$. Planes in the imaging system that are simultaneously in focus are called "conjugate planes," in this case the object and image plane. In between the lenses, one focal length away from each, is the Fourier, or pupil, plane. The second lens brings the image back to real space, although it is inverted. 4f imaging systems are useful because they are telecentric: their magnification does not depend on defocus, i.e., an object or detector displaced from focus will produce a blurred image, but the image magnification will not change. This property has several associated advantages including reduced paraxial error and large depth of field with symmetrical blurring on either side of the focus that result in overall lower image distortions.

Consider an example of an imaging system that includes an illumination source that must be spatially filtered and enlarged before imaging a single point of a sample onto a detector (**Figure 2.9**). Spatial filtering refers to removal of selected "spatial frequencies" from an optical beam. If a beam mode is Fourier transformed, (which is accomplished in optics by appropriate use of a lens, in this case, L_1 of **Figure 2.9**), the frequencies of amplitude fluctuations that create the beam's original transverse profile are explicitly displayed. In the context of homogenizing what are intended to be transverse Gaussian beams, blocking light further away from the beam axis in this Fourier plane, for example with a pinhole of appropriate diameter, allows one to remove undesired imperfections in the spatial beam profile to produce a smooth, transverse intensity profile once the beam has passed through another, Fourier transforming, lens (L_2 in **Figure 2.9**). The resulting low-pass-filtered beam also has increased spatial coherence, meaning that the phases of a given wavefront at different points in space are correlated with one another. The light source, let's say a laser, first passes through a 4f lens arrangement to enlarge the beam size by a factor of f_2/f_1. The first lens, L_1, focuses the beam onto a pinhole to clean up the beam

mode using the spatial filtering approach described above. At the focus where the pinhole is placed, the incident beam's transverse intensity distribution is Fourier-transformed such that only the lowest order spatial frequency corresponding to the desired Gaussian mode is transmitted, resulting in a (more) spatially coherent Gaussian beam mode. The second lens, L_2, recollimates the beam. Another way to improve the beam mode is to couple the light into a single-mode optical fiber, however, this strategy tends to result in more power losses than using a pinhole, depending on the size of the pinhole. In the stroboSCAT microscope, we use 25 µm and 50 µm pinholes for the pump and probe beams, respectively. A smaller pinhole diameter produces a cleaner beam mode since more of the higher spatial Fourier components are removed but at the expense of power throughput. Therefore, a diameter is chosen to balance the competing requirements for photon densities exciting or imaging the sample and spatial filtering. Next, the light is focused onto the object plane with a focusing or confocal lens to illuminate a single spot. (Without this lens, the object could be imaged all at once with widefield illumination, as is done with our stroboSCAT probe beam – see **Section 2.5**.) The light that scatters from this point in the object is imaged through a second 4f lens arrangement, where the image is magnified by f_4/f_3. By scanning the light over the object plane, a full image may be reconstructed at the image plane. When L_3 is an objective lens, L_4 is called the "tube lens" since it is placed one "tube length" away from the back focal plane of the objective, (the plane located behind the objective which, in general, is not the same as the front focal plane), to minimize vignetting, where slightly off-axis rays from imperfectly collimated light are clipped and result in a distorted image that is darker at the periphery. While the diagram in **Figure 2.9** seems specific to transmission imaging, it is also an unfolded diagram of a reflectance microscope. In this case, the confocal lens and L_3 would be the same focusing element, often an objective.

2.3.3 Spatial resolution

The spatial resolution of an imaging system is an important metric that depends on the numerical aperture (NA $\equiv n \sin\theta$, where n is the refractive index between the objective and sample, not of the objective itself) and illumination wavelength. The NA describes the range of angles that can be collected in an imaging system at the limiting aperture, the diameter that most severely restricts the collected angular range, typically the objective lens (**Figure 2.10a**). The NA defines the resolving power of a microscope since collecting light that scatters at high angles corresponds to high spatial frequency information and therefore the ability to resolve finer details. Air objectives ($n = 1$) can have an NA as high as 0.95, while oil-immersion objectives ($n = 1.5$) can reach an NA of up to 1.4. The depth of field (DOF), the range of object distances for which the object is in focus in the image plane, is inversely related to the NA: DOF $\propto \frac{1}{\mathrm{NA}^2}$. Therefore, high-NA objectives integrate over less sample depth (are more sensitive to the surface of the sample) than low-NA objectives. Optical microscopes have a spatial resolution that is limited physically by the wavelength of the imaging or imaged light in what is known as the diffraction limit, $\sim \lambda/2$, analogous to a Nyquist frequency. Ernst Abbe and Lord Rayleigh derived more rigorous definitions for the

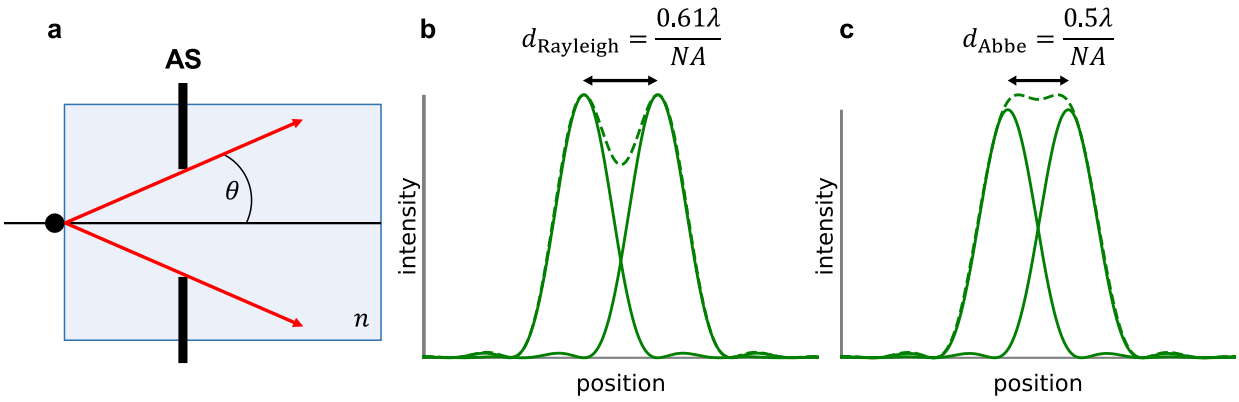

Figure 2.10: (a) The numerical aperture ($\text{NA} = n \sin\theta$) is the range of angles (2θ) that can be collected by an imaging system at the aperture stop (AS). **(b,c)** The optical diffraction limit can be defined in two ways: by the Rayleigh criterion (b) and the Abbe criterion (c), where point objects are represented by Airy functions with solid curves and the sum of their intensity patterns by a dashed line.

diffraciton limit that take into account the interference of Airy disk wavefronts emanating from an intricate structure of point sources in the object plane. Abbe declared two objects "resolved" when they are separated by a minimum distance, d, equal to the radius of the diffraction Airy disk [186]:

$$d_{\text{Abbe}} = \frac{\lambda}{2\text{NA}}. \tag{2.49}$$

Rayleigh's modification was to say that two point sources are readily distinguished when the principal diffraction maximum of one coincides with the first minimum of the other, a slightly more stringent criterion [187]:

$$d_{\text{Rayleigh}} = \frac{0.61\lambda}{\text{NA}}. \tag{2.50}$$

The two definitions are compared in **Figure 2.10b,c**.

The property that ultimately sets a microscope's spatial resolution is the width of its point spread function (PSF), also known as the impulse response because it characterizes the microscope's response to a spatially impulsive input like a point source or a deeply sub-wavelength particle. The PSF maps points in the object plane to blurred points in the image plane. The PSF in a diffraction-limited system is well approximated by a Gaussian function with a full width at half maximum (FWHM) given by the Abbe criterion. (See **Sections 2.5.4** and **4.3.4**.) Although light rays are subject to many operations as they propagate through an imaging system, the entire process of imaging an input object through a "black box" imaging system may be reduced to a convolution operation (**Figure 2.11**). This result falls out of a Fourier optics treatment [188–190]. Briefly, an imaging system may be treated

Figure 2.11: A microscope can be described as a linear system with object inputs (like two points, g_{in}) that are transformed into image outputs by convolution with the microscope point spread function (PSF) that blurs every point in the input plane to a blob when imaged or mapped to the output plane, as in g_{out}.

as a linear shift-invariant system in which any linear combination of "solutions" (outputs) is also a solution and every point in the input object has the same impulse response (PSF). If we know how the system responds to a delta function impulse (a point source input object), then we know its response to any arbitrary input (spinach leaf, butterfly wing, silicon wafer) which may be constructed from a linear superposition of impulse responses across the input object plane. The overall response, a sum of scaled and shifted copies of the system's impulse response or PSF, turns out, in the continuous limit, to be a convolution.

iBiology, MicroscopyU from Nikon, ThorLabs and the MIT course on Optics taught by Barbastathis, Sheppard and Oh (available on MIT OpenCourseWare) are all great places to learn more about microscopy basics.

2.4 Interferometric scattering microscopy

Interferometric scattering microscopy (iSCAT) is an ultrasensitive label-free probe of nano-objects [191–193]. In a typical inverted microscope setup, a focused or plane wave laser beam is coupled into a high-NA objective and undergoes reflection at the interface between the sample (e.g., metal nanoparticles, dye molecules, or proteins each in a medium with a different refractive index than glass) and glass substrate. The reflected field also acquires a π phase shift when the material has a higher refractive index than glass. Some of the incident light elastically scatters from the sample and, for deeply sub-wavelength objects, propagates as a spherical wave (**Section 2.1**) that is collimated by the objective. The reflected and scattered fields interfere (left panel in **Figure 2.12**), and the light intensity reaching the detector can be described as [194]:

$$I_{\text{iSCAT}} = \frac{cn\varepsilon_0}{2}|E_r + E_s|^2 \propto |E_r + E_s|^2 = |E_i|^2[r^2 + s^2 + 2rs\cos\phi], \tag{2.51}$$

where n is the refractive index, c is the speed of light in vacuum, ε_0 is the vacuum permittivity, E_i is the incident electric field, $E_r = E_i r e^{i\phi_r}$ is the reflected field with reflection coefficient r, $E_s = E_i s e^{i\phi_s}$ is the scattered field with real scattering amplitude s, and $\phi = \phi_r - \phi_s$ is

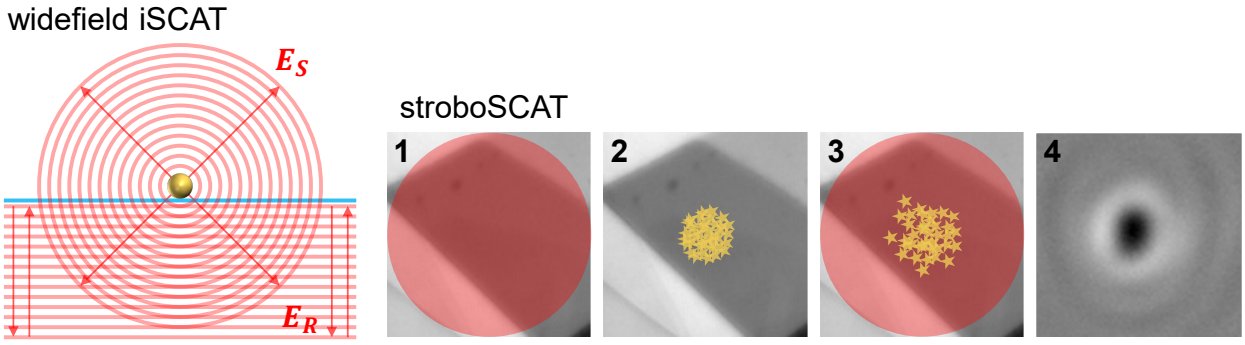

Figure 2.12: (left) In iSCAT, plane wave light incident on a nano-object is reflected at the substrate-sample interface and scattered by the nano-object. The interference between the backscattered and reflected field dominates the image contrast. **(right)** iSCAT is used as a widefield probe in stroboSCAT. The experimental sequence involves (1) collecting a ground state iSCAT image, (2) photoexciting the material with a focused pump pulse, (3) collecting an excited state iSCAT image after a controllable time delay and (4) calculating the differential image with contrast induced by the presence of photoexcitations.

the phase difference between the scattered and reflected field. The scattering amplitude is proportional to the polarizability [132] which, from the Clausius-Mossotti relation (Equation 2.16), scales with the particle volume:

$$s \propto \alpha = \varepsilon_{\text{med}} \frac{\pi D^3}{2} \frac{\varepsilon_{\text{part}} - \varepsilon_{\text{med}}}{\varepsilon_{\text{part}} + 2\varepsilon_{\text{med}}} \tag{2.52}$$

for particle diameter, D. The term of Equation 2.51 proportional to s^2 is the pure scattering signal, which drops as D^6. The scattering from a 5-nm particle is one million times smaller than the scattering from a 50 nm particle. This term dominates the signal reaching the detector in darkfield microscopy. Even with excellent background suppression, scattering due to sample imperfections sets a lower bound of about 40 nm on the smallest observable particle from pure scattering alone [195]. The interferometric cross term, however, scales with s rather than s^2, and is amplified by the reflected field amplitude r. If the reflected background field is explicitly collected, as in iSCAT, this interferometric crossterm dominates for small particles and allows for extremely high sensitivity measurements to be made by simply increasing the incident electric field strength. Note that when imaging macroscale materials and objects like solutions, thin films or crystals, as opposed to nano-objects like localized excitations or gold beads, the modality is referred to as interference reflection microscopy (IRM), where imaging contrast arises from the change in reflectance at a refractive index boundary [196, 197].

The overall phase ϕ can be expanded into [195, 198]:

$$\phi = \phi_{\text{Gouy}} + \phi_{\text{scat}} + 4\pi n z/\lambda, \tag{2.53}$$

where ϕ_{Gouy} is the Gouy focusing phase difference between the scattered and reflected light, which is constant for a fixed objective-sample distance (and typically tuned to $-\pi \leq \phi_{\text{Gouy}} < -\pi/2$ for maximum contrast [199]), ϕ_{scat} is the scattering phase (related to the material's complex refractive index; $\phi_{\text{scat}} \simeq 0$ for off-resonant probing), z is the object-interface distance, n is the refractive index of the medium, and λ is the illumination wavelength. Each time a beam propagates into or out of a focus, it acquires a $-\pi/2$ phase shift. Gouy made the first experimental observation of this effect in 1890 when he interfered two plane waves reflected from a planar and concave mirror. He noticed that the central disk in the interference pattern changed from dark to bright or vice versa if he moved the observation plane to just before or after the focus. A modern version of Gouy's experiment in a Mach-Zehnder interferometer is shown in **Figure 2.13a,b** [200]. The on-axis phase shift is given by (**Figure 2.13c**):

$$\psi(z) = \tan^{-1}(z/z_0) \tag{2.54}$$

where z is the propagation direction and z_0 is the Rayleigh range, the distance from the beam waist at which the area of the beam doubles. This principle thus far applies to the focusing phase of the reflected field, but what about the scattered field? Babinet's principle states that if plane wave light passes over an object and diffracts, then the accumulated phase must be opposite to the same beam's accumulated phase passing through an aperture of similar profile because the sum of the waves passing through these opposite profiles must add to that of a plane wave [201]. Therefore the phase shift acquired by diverging light from a point source that is collimated is $+\pi/2$. Since Gouy's original experiment, there have been many theoretical descriptions and experiments demonstrating this phase anomaly with origin stories ranging from Heisenberg's uncertainty relations [202] to geometrical properties of Gaussian beams [203]. For me, it is one of many optics magic tricks I may never fully grasp.

The relationship $\phi \propto z$ in Equation 2.53 allows for three dimensional image contrast that converts phase delays into amplitude contrast with complete signal inversion observed for scatterers that are $z = \lambda/4n$ above the interface. For the $MAPbI_3$ films in **Figure 3.10**, $n(635\text{ nm}) = 2.6$, leading to a π phase flip every 60 nm, which is similar to the pump and probe $1/e$ penetration depths (50-70 nm), as further illustrated in **Section 3.3**.

The iSCAT signal contrast, or signal-to-background ratio, can be expressed as:

$$\begin{aligned} \text{contrast} &= \frac{\text{iSCAT signal}}{\text{background}} = \frac{I_{\text{particle}} - I_{\text{background}}}{I_{\text{background}}} \\ &= \frac{|E_r + E_s|^2}{|E_r|^2} - 1 = \frac{|E_i|^2[r^2 + s^2 + 2rs\cos\phi]}{|E_i|^2 r^2} - 1 \\ &\approx 1 + \frac{2rs\cos\phi}{r^2} - 1 = \frac{2s\cos\phi}{r}, \end{aligned} \tag{2.55}$$

where we assume that s^2 is negligible for $s \ll r$, as for small particles, the cross term, $2|E_i|^2 rs\cos\phi$, dominates over the second pure scattering term. Note that the image contrast

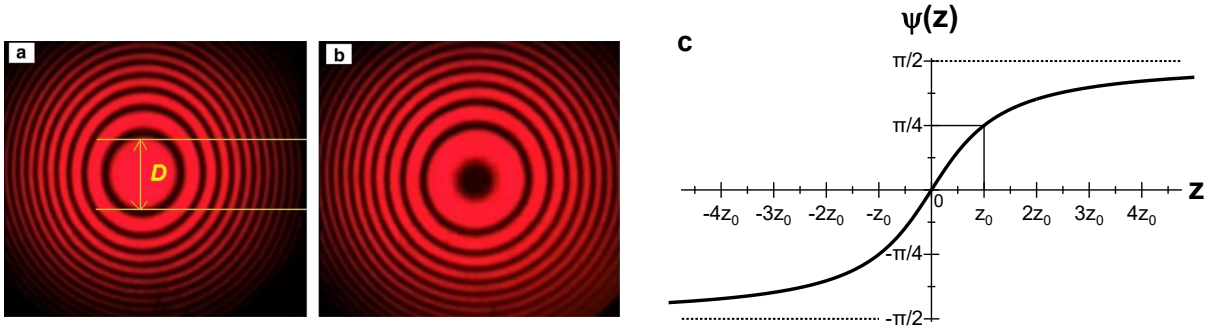

Figure 2.13: (a,b) A collimated beam interferes with a focusing beam in a Mach-Zehnder interferometer. On one side of the focus, the central lobe is bright (a) while on the other side it is dark (b), exhibiting a full π phase shift through the focus. Reprinted with permission from [200]. **(c)** The Gouy focusing phase $\psi(z)$ represents the phase delay of a Gaussian beam through focus (at $z = 0$) along the the beam axis. At the Rayleigh range, z_0, the accumulated phase shift is $\pi/4$.

scales *linearly* with the scattering amplitude, and therefore also with particle volume, making it possible to detect <5 nm particles [204, 205] and to track proteins very sensitively, even performing quantitative mass imaging on proteins as small as 20 kDa [206–210].

Next, we explore the signal-to-noise ratio (SNR) in the detection scheme. Laser intensity fluctuations (shot noise) and beam pointing instability are the most prominent sources of noise in iSCAT. For the ideal shot-noise-limited case, the SNR may be expressed as [195]:

$$\begin{aligned} \text{SNR} &= \frac{\text{iSCAT signal}}{\text{background}} \times \frac{\text{background}}{\text{background fluctuations}} \\ &= \text{iSCAT contrast} \times \frac{\text{background}}{\text{background fluctuations}} \\ &= \frac{2s\cos\phi}{r} \times \frac{N}{\sqrt{N}} \propto \sqrt{N} \end{aligned} \tag{2.56}$$

where $N \propto r^2$ is the number of photoelectrons detected by the camera (**Section 2.5.4**). Note that since N scales with the incident intensity, the SNR for a given exposure time can be improved at will, one of the characteristic features of sensitive shot-noise limited measurements. In practice, the photon flux is limited by the amount of power from the illumination source.

2.4.1 Extension of iSCAT into the pump-probe domain: stroboSCAT

We employ iSCAT as a probe in a time-resolved pump-probe experiment (right panel in **Figure 2.12**). In our approach, we first introduce a diffraction-limited, short pump light pulse to generate a localized collection of energy carriers. These carriers act as point scatterers in the sample by modifying the local material electric polarizability, although due to the small inter-particle spacing, typically <1 nm, the entire distribution of scatterers may be thought of as one sub-wavelength scattering object, as discussed at the end of **Section 2.1** and further below in this Section. We subsequently probe the pump-induced changes to the elastic scattering profile of the material at controllable time delays over a large sample area in which the energy carriers diffuse, thus imaging the evolving carrier distribution in space and time. In principle, any photoexcitation – e.g., charge carriers, excitons, phonons – may be detected in this way since the measurement observable, elastically backscattered light, does not rely on the material absorbing or emitting light at a particular frequency. A large probe area considerably reduces acquisition time by acquiring a snapshot of the sample's scattering profile in a single image exposure, obviating the need for sample, beam, or detector scanning and providing morphological correlation with diffraction-limited resolution. The signal can also be spectrally resolved in the same instrument (see **Sections 2.5.5** and **3.3.2**), a technique known as spectral interferometry [211–213].

Inspired by advances in scattering-based interferometric and photothermal microscopies [194, 195, 204, 209, 214–217] that achieve extremely sensitive detection of tiny scatterers down to single molecules, we call our approach stroboscopic scattering microscopy (stroboSCAT), where "stroboscopic" refers to the use of strobing or flashing laser pulses to capture rapid and precisely-timed image exposures that are not possible with electronically-controlled camera shutters. Whereas iSCAT allows single-particle tracking of nanoparticles and biomolecules, stroboSCAT opens a new range of possibilities for tracking the spatiotemporal evolution of distributions of photogenerated energy carriers. We use iSCAT's formalism to treat the pump-induced contrast changes; a similar formalism based on the optical theorem has been used for transient spectral interferometry of quantum dots [211, 212]. All of the treatment we have thus far developed in this chapter for light scattering and photoinduced changes to optical properties applies. Microscopically, both absorption and reflection originate from scattering. Macroscopically, however, most semiconductors possess refractive indices in the visible range that are dominated by their relatively wavelength-independent real part (n) rather than by their imaginary part (k), which is responsible for absorption. For these high n/k ratios, stroboSCAT is primarily sensitive to changes in n [173, 174, 176]. The physical process is similar to transient reflectance spectroscopy, except that it takes place in a microscope with a high-NA objective that collects the light scattered at oblique angles from the distribution of photoexcitations. Overall, stroboSCAT is a high-throughput method to track time-evolving carrier distributions in 3D with high spatiotemporal resolution and *in situ* morphological correlation in a wide range of materials (for example, opaque or transparent, emissive or not emissive, composite or uniform). We show in **Chapter 3** that

these distinctive attributes enable detailed and model-free structure–function correlations in a broad range of materials, precisely pinpointing the origin of functional heterogeneity in disordered semiconductors.

Similar to in other differential pump-probe measurements, in stroboSCAT, the pump-probe differential contrast is defined as:

$$I_{\text{stroboSCAT}} = \frac{I_{\text{pumpON}} - I_{\text{pumpOFF}}}{I_{\text{pumpON}}} \tag{2.57}$$

$$= \frac{|E_i|^2[(r^2 + s^2 + 2rs\cos\phi)_{\text{pumpON}} - (r^2 + s^2 + 2rs\cos\phi)_{\text{pumpOFF}}]}{|E_i|^2[(r^2 + s^2 + 2rs\cos\phi)_{\text{pumpOFF}}]}. \tag{2.58}$$

We make the following assumptions to simplify the equation further: (1) $s \ll r$, which is valid for deeply sub-wavelength scatterers, certainly applicable for each individual excitation but also for particles – or in this case, a collection of particles – with a diameter up to ∼50 nm [195], (2) r does not change significantly between pump-on and pump-off images (confirmed using a variable aperture in **Section 2.5.6**) and (3) the $\sim -\pi$ Gouy phase difference between the scattered and reflected field dominates the phase contribution to ϕ such that the $\cos\phi$ term is virtually identical for the pump-on and pump-off measurements and is approximately equal to -1 for scatterers at the substrate-sample interface (**Figure 2.14**). With these assumptions, Equation 2.58 becomes

$$I_{\text{stroboSCAT}} \cong \frac{2\cos\phi(s_{\text{pumpON}} - s_{\text{pumpOFF}})}{r + 2s_{\text{pumpOFF}}\cos\phi} \approx \frac{2\cos\phi(s_{\text{pumpON}} - s_{\text{pumpOFF}})}{r}. \tag{2.59}$$

When carriers channel deeper into the sample, however, the depth-dependent pump-on contribution to the relative phase, $\cos(4\pi nz/\lambda)$, modulates the first term in the differential contrast expression in Equation 2.58, enabling retrieval of depth-dependent information. As shown, the denominator can further be simplified to r, since $r \gg s_{\text{pumpOFF}}\cos\phi$. Thus, the contrast is proportional to the change in the scattering amplitude between the material in the presence versus absence of excited state species, which, in turn, is directly proportional to the change in polarizability (or, equivalently, susceptibility, dielectric function, or refractive index) of the material between unpumped and pumped states. Overall, stroboSCAT benefits from the elegance, sensitivity and 3-dimensional contrast achievable with iSCAT, but expands it to the entirely different realm of ultrafast energy flow.

Optical scattering from a localized collection of photoexcitations is the most general description of the differential observable in stroboSCAT measurements. The presence of excitons, charge carriers, lattice heating and their combinations modifies the local complex refractive index such that the photoexcited material scatters the probe differently than the ground state material. In a real experiment, we inject thousands to millions of photoexcitations distributed over a few hundred thousand square nanometers. Zooming out from this single excitation picture, the ground state material can be described by an average refractive index. Upon photoexcitation, the pump pulse generates a Gaussian spatial distribution

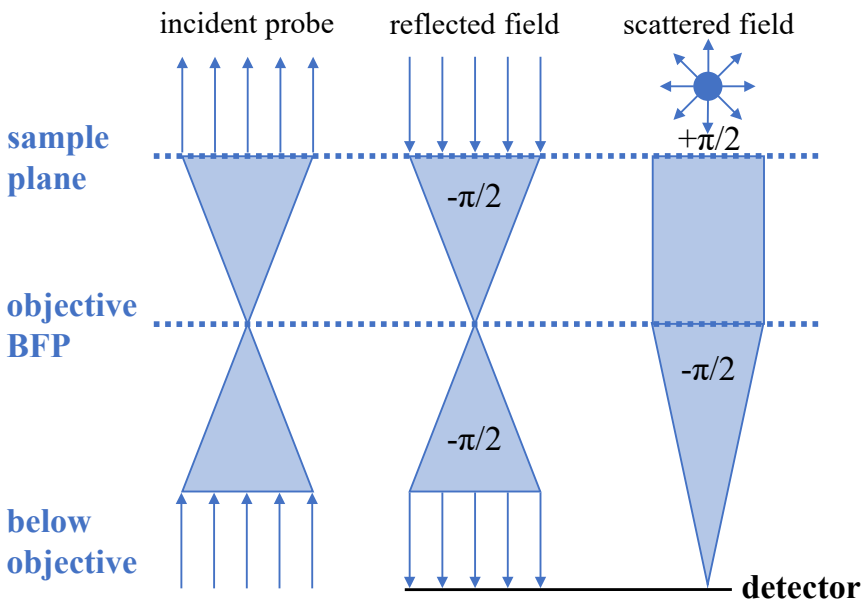

Figure 2.14: The Gouy focusing phase for widefield stroboSCAT measured from the sample plane. The reflected field, focused through the back focal plane (BFP) of the objective, acquires $\phi_{\mathrm{r,Gouy}} = -\pi$ while the scattered field, collimated by the objective before being focused onto the detector by the tube lens, acquires $\phi_{\mathrm{s,Gouy}} = 0$. The overall Gouy contribution to the interferometric phase is the difference between the two contributions: $\phi_{\mathrm{Gouy}} = \phi_{\mathrm{r,Gouy}} - \phi_{\mathrm{s,Gouy}} = -\pi$. See **Section 2.4** for the explanation of the focusing phase for propagating plane waves and diverging light from a point source.

of photoexcitations with a local refractive index that varies radially, following the carrier concentration gradient. This quasiparticle field ultimately alters the polarization associated with the oscillating bound charges in the surrounding material (and also redistributes charge), making it easier or more difficult for the external field of the probe pulse to couple to the excited material (compared to the ground state material). This competition results in a difference in scattering amplitude (or optical polarizability) due to this underlying microscopic perturbation in the presence of quasiparticles, the sign of which depends on the nature of the quasiparticle field, local transition dipole/polarization response, and the probe frequency. Considering the entire photoexcited distribution as a single "object" comparable to the imaging wavelength, the optical response of the sample may instead be described in terms of transient reflectance as in **Section 2.2.2**.

2.5 Detailed description of the stroboSCAT setup

Our original implementation of stroboSCAT is illustrated in **Figure 2.15**. (See also **Sections 3.4** and **4.4**, which mention use of an ultrafast laser setup.) The pump and probe

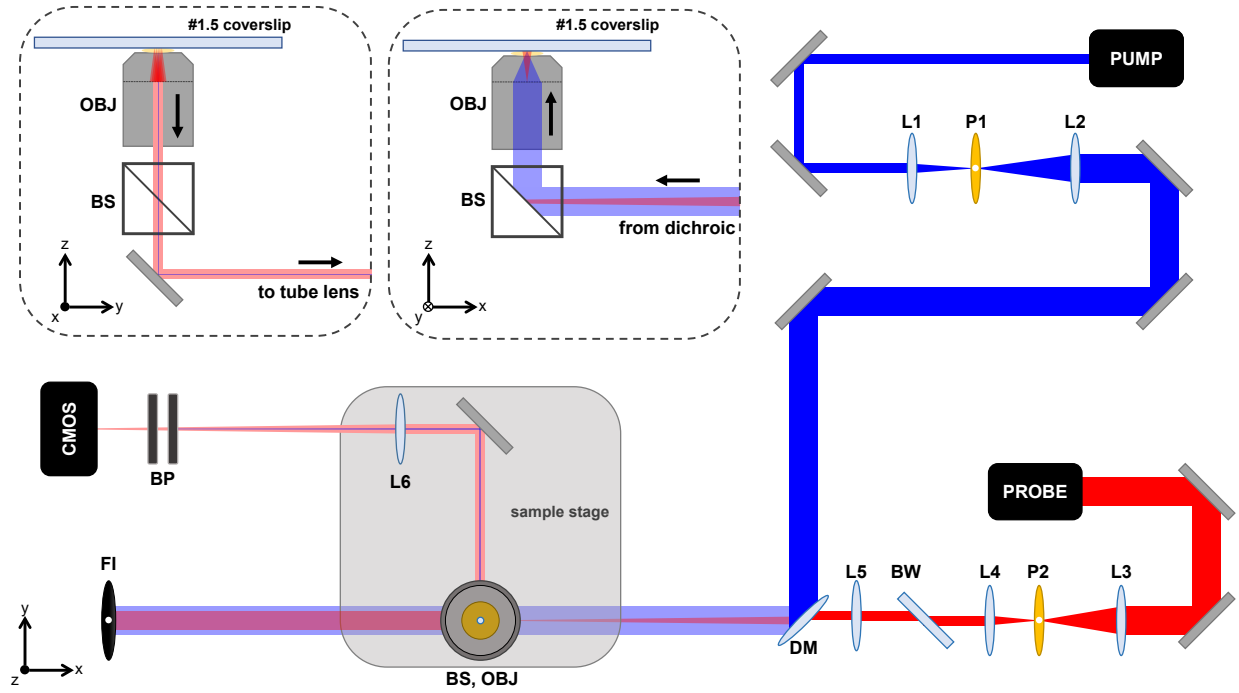

Figure 2.15: Schematic of the stroboSCAT setup. Laser diodes synchronized through a single oscillator/laser driver are used for the pump and probe. After passing through spatial filters, the beams are combined with a dichroic mirror before reflecting off a 50/50 beamsplitter into the objective. The pump is sent collimated into the objective while the probe is focused in the back focal plane of the objective to result in confocal and widefield illumination spots, respectively. Both light reflected from the sample-substrate interface and scattered from the sample are collected, spectrally filtered, and focused onto a CMOS detector for imaging.

BP	bandpass filter(s)
BS	beamsplitter
BW	“beam walker”
DM	dichroic mirror
FI	final alignment iris
L1	LA 1131-A-50 mm lens
L2	LA 1433-A 150 mm lens
L3	LA 1509-A 100 mm lens
L4	LA 1131-A 50 mm lens
L5	AC-254-300-A “widefield” lens
L6	AC-254-500-A “tube” lens
OBJ	Leica HC PL APO 63x/1.40 NA oil-immersion objective
P1	25 µm pinhole
P2	50 µm pinhole

diodes are spatially-filtered through 25 and 50 µm pinholes (P1 and P2) and telescoped to ∼6 mm and 1 mm beam diameters, respectively, before entering the microscope. The two beams are combined using a dichroic mirror (DM) and directed to a home-built microscope stage of very similar design to the microscope body detailed in Ortega-Arroyo et al. [218]. The probe beam is deflected by transmission through the DM, so that a "beam walker" (BW), a piece of glass of the same thickness as the DM oriented at 90° relative to the DM, is placed in the probe path to pre-compensate the beam deflection. An $f = 300$ mm widefield lens (L5) is also inserted in the probe beam path upstream of the DM to focus the beam in the back focal plane of the objective, resulting in widefield illumination (∼5-60 µm depending on the beam size prior to L5) of the sample. A 50/50 beamsplitter (BS) reflects the pump and probe light into a high numerical aperture (1.4 NA) oil-immersion objective (Leica HC PL APO 63x/1.40NA) and onto the sample, resulting in overlapped confocal and widefield illumination, respectively. Probe light reflected from the sample-substrate interface as well as scattered from the sample are collected through the same objective. The light transmitted through the beamsplitter is focused onto a complementary charged metal-oxide semiconductor (CMOS) detector (PixeLINK PL-D752, equipped with the Sony IMX 174 global shutter sensor) using an $f = 500$ mm lens (L6) placed one tube length (200 mm) away from the back focal plane of the objective. Bandpass filters (BP) just in front of the camera filter out the pump light in the usual stroboSCAT configuration or, when measuring widefield emission, other appropriate emission filter arrangements are used for any given sample. The total magnification is given by the magnification of the objective times the tube lens focal length divided by the objective's tube length: $63 \times 500/200 = 157.5\times$. On square pixels of 5.86 µm, this magnification corresponds to 37.2 nm/pixel. Optional half- or quarter-waveplates are used to control the polarization of pump and probe beams in polarization-sensitive measurements, such as for TIPS-pentacene described in **Chapter 3**.

2.5.1 The quirks of working with pulsed diode lasers

For all data shown in the text, the light sources used are linearly polarized PicoQuant laser diodes from the LDH series with dual pulsed and continuous wave modes and thermoelectric coolers. Current available wavelengths are 408, 440, 465, 515, 635, 700, 725, and 778 nm. Typical pulse widths are ∼100 ps with spectral widths ∼2-8 nm. The diodes are driven by the same laser driver with a base oscillator frequency of 80 MHz (PDL828-S "SEPIA II" equipped with two SLM 828 driver modules and a SOM 828-D oscillator, PicoQuant). For the experiments shown in **Chapters 3** and **4**, we use a laser repetition rate of 2 MHz and 10 MHz, respectively, with the pump modulated at 660 Hz (every 3030 or 15151 pulses, respectively). The pump-probe delay times are controlled using the electronic delay capabilities of the driver to delay the probe with 20 ps resolution. Time "zero," when the pump and probe temporally overlap typically occurs around a -4 ns delay setting on the driver, giving the pump light a head start to cover its longer optical path up to the DM. We verified the calibration of the 'coarse' and 'fine' adjustments of the diode driver electronic delays using a computer-controlled mechanical translation stage (Newport) in a standard pump-probe

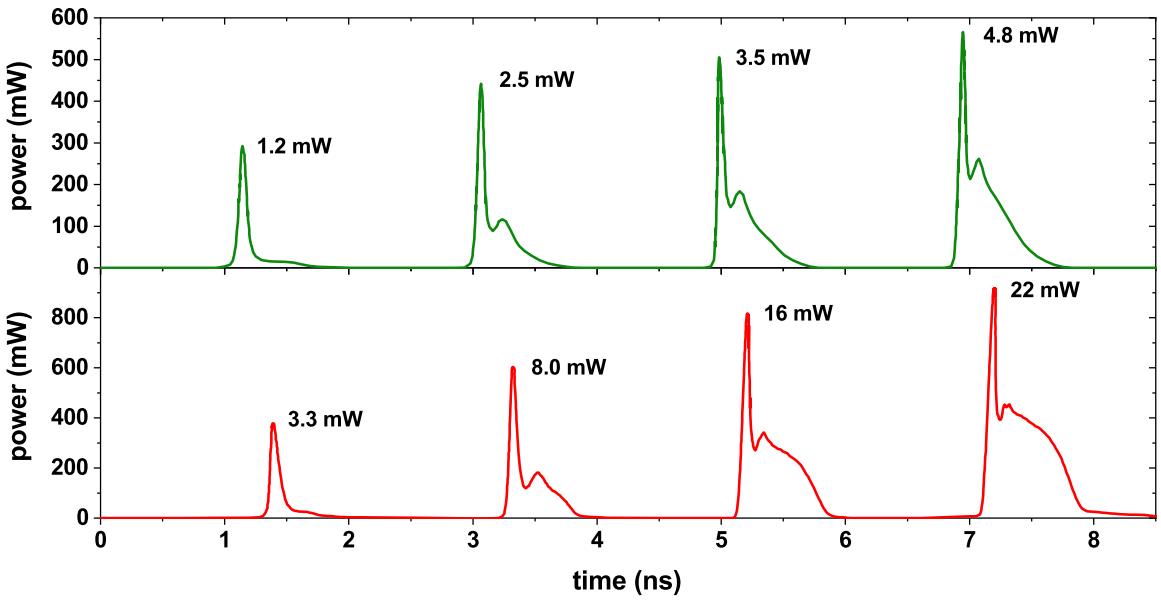

Figure 2.16: Diode laser pulse profiles for the 440 (green) and 635 (red) nm diode sources. For increasing diode currents or, equivalently, average output powers, the relative proportion of an afterpulse shoulder also grows in.

geometry for delay times < 2 ns, and using an oscilloscope for delay times > 2 ns. We note that diodes and repetition rates are easily interchangeable for different experimental configurations.

There are several considerations to keep in mind when selecting pump and probe wavelengths. The pump source must have enough energy to photoexcite the material, i.e., must be higher in energy than the bandgap. The higher above bandgap the pump excitation, the more heat will be generated due to thermalization. In selecting a probe wavelength, it is helpful to identify the material's band edge and any other electronic resonances, near which the transient signal will be enhanced. For many bulk materials, however, probing far detuned from any electronic resonance provides enough elastic scattering contrast to achieve good SNR (**Chapter 3**). In the simplified case where a single resonance feature dominates the transient optical response, the transient reflectance contrast may be tuned across the resonant zero crossing, as above-baseline (positive) contrast will then flip towards below-baseline (negative) differential contrast. In the case where multiple electronic resonances coexist, the probe energy may be selected to be more sensitive to a certain type of energy carrier (e.g., exciton, free carrier, heat). (See **Chapter 4** for an example where a near-resonant probe energy is sensitive to all forms of photoexcited energy, whereas a far-from resonant probe energy is sensitive only to heating.)

For short-time dynamics (<500 ps), diode afterpulsing can affect the accuracy of the measurements when using high diode powers (**Figure 2.16**). Therefore, care must be taken

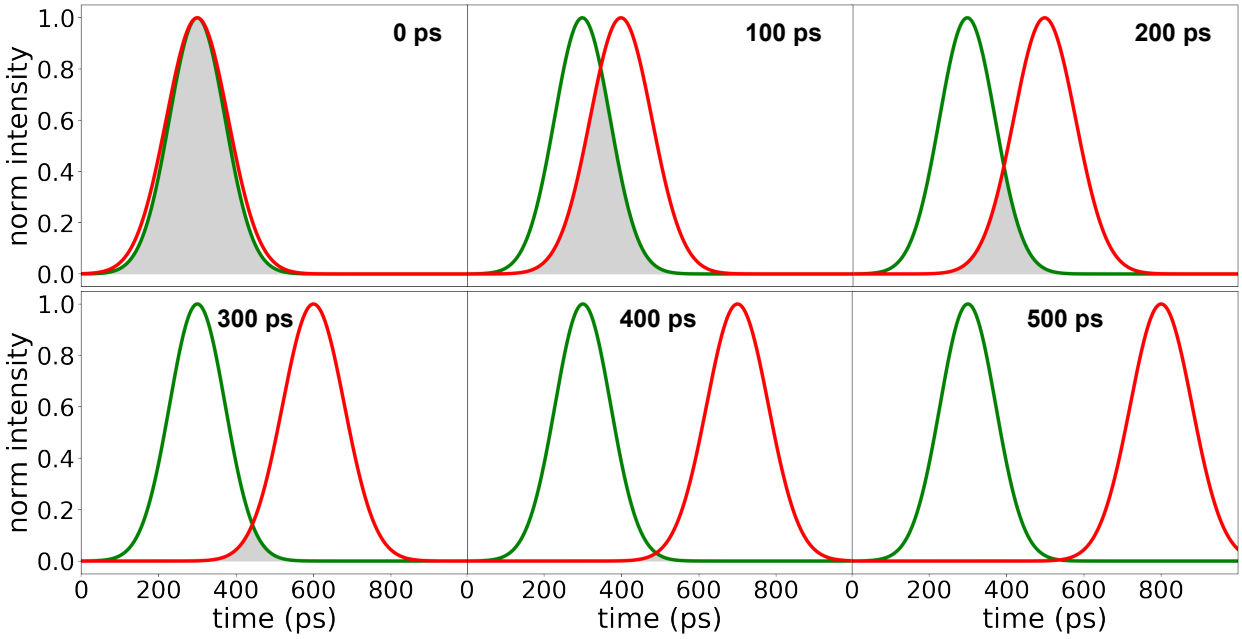

Figure 2.17: Diode laser temporal pulse overlap for the standard pump-probe configuration and relative pump-probe time delays from 0 to 500 ps: 440 nm pump (green, $\sigma = 72$ ps) and 635 nm probe (red, $\sigma = 80$ ps). Significant pump-probe overlap persists up to ∼200 ps.

to minimize diode powers at the source, i.e., by reducing the diode current, rather than using neutral density filters in the beam paths. In other words, the leftmost pulses in **Figure 2.16** are closest to Gaussian in time and are most sought after. Typical measurements in **Chapter 3** and **4** use powers whose pulses look like the first (first or second) pulse from the left for the pump (probe). Even at sufficiently low diode powers, however, care must be taken in interpreting results of time delays within the first ∼200 ps due to the finite pulse width and lingering temporal overlap between the pump and the probe (**Figure 2.17**). Technically anytime the pump and probe are overlapped temporally on the sample, the probe can measure whatever is photogenerated immediately after pump excitation (e.g., hot carriers, higher-energy excitons, trions), even though the dynamics of such short-lived carriers would be smeared out over the instrument response function (see **Figure 2.25c** below).

When using pump and probe wavelengths that are within $\lesssim$100 nm, it is important to use tight bandpass or sharp long- or short-pass filters to completely reject the pump light before the camera. As a word of caution, we learned this the hard way when using a 440-520 nm pump-probe configuration with a FBH520-40 bandpass camera filter. In the stroboSCAT data, we were puzzled by a weak, bright signal that persisted over all time delays, including the -5 ns time delay. When we dispersed the pump and probe light through a prism to spectrally resolve them, it became clear that some of the 440 nm pump light was leaking

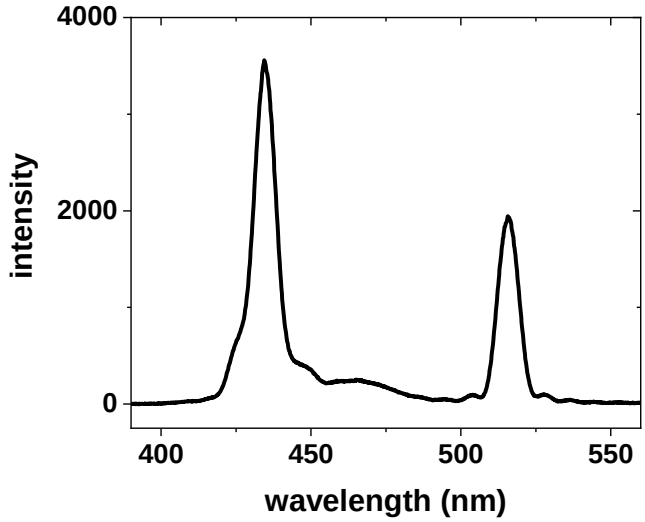

Figure 2.18: The output of two diode sources may spectrally overlap when they are close together, as shown here for the 440 and 520 nm diodes. Even if the overlap is small, the pump light may leak through the chosen camera filters and appear as "bright" contrast in all stroboSCAT time-delayed images. In cases where the pump and probe wavelengths are within ∼100 nm of each other, it is essential to choose a camera filter that sufficiently rejects the pump light.

through the bandpass filter above 500 nm (**Figure 2.18**). Using a filter with a smaller bandwidth (FBH520-10), however, successfully eliminated the pump light signal.

For accurate carrier density calculations, as described in **Appendix B.1**, the diode laser power exiting the objective must be measured after every realignment for a given diode current ("Intensity %" in the laser driver software) and pulse repetition rate using a large area power meter like the Thorlabs microscope slide power meter sensor S175C. Every diode head has a different threshold current for lasing and the output power follows a nonlinear trend thereafter (**Figure 2.19**). Measuring the power at two or three diode currents and extrapolating the trend with a line is not a good approximation of the actual trend.

2.5.2 Experimental timing control

To trigger and synchronize the CMOS camera to the 660 Hz pump modulation rate, we convert the synchronization output of the laser driver to a TTL pulse with an MPD NIM to TTL converter. A trigger pulse is sent to the camera at the beginning of every probe laser pulse burst. At 660 Hz, each image has an exposure time of 1.3 ms with a 0.2 ms buffer to allow for overhead processing. The pulse burst length that yields the appropriately spaced 660 Hz camera trigger is given by the ratio of the laser repetition rate and the camera trigger

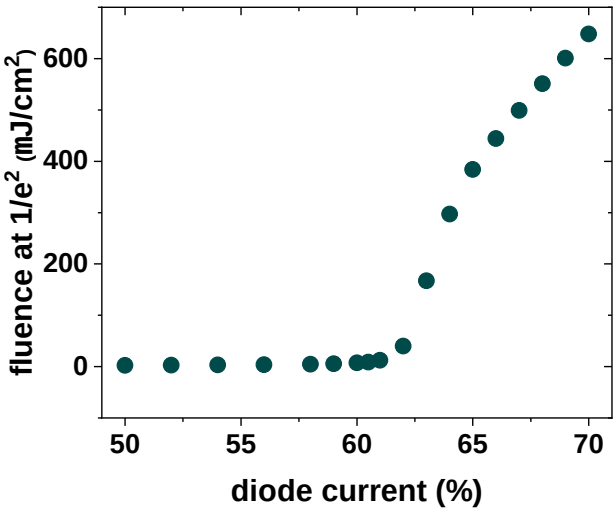

Figure 2.19: 440 nm diode laser power output at 40 MHz repetition rate measured just after the objective as a function of diode current, in units of %, which are used to set the diode current in practice. The laser has zero output until the diode current reaches a threshold value, after which the power increases nonlinearly with a trend that depends on the diode source and repetition rate.

rate. For example, for a laser repetition rate of 2 MHz, the laser driver should trigger the camera after each burst of $2 \times 10^6/660 = 3030$ pulses. This timing sequence is detailed in **Figure 2.20**.

In the data acquisition, consecutive images correspond to (1) probe with pump on and (2) probe with pump off. The ratio pump-on/pump-off for each consecutive pair is computed, and the ratio is averaged over 1000-3500 image pairs for a total collection time, including LabVIEW program overheads, of ∼4-15 seconds to generate a single pump-on/pump-off pair for a single stroboSCAT image. To collect and gather sufficient statistics on a time series, we perform a time delay scan (often referred to simply as a scan) comprised of one sweep through the specified pump-probe time delays. Averaged pump-off images (iSCAT) are simultaneously recorded at each time delay to track any changes in sample morphology over the measurement, such as photoinduced damage or drift. After scanning through a full set of pump-probe delay times, the experiment's time delay sequence is repeated N times, with N ranging from 3-20, depending on the signal-to-noise ratio of the measurement, with the final image for each delay corresponding to an average of images taken over N time delay scans. For materials with good SNR, a measurement of 10 time delays scanned twice might take about 10 minutes to acquire. For materials that require longer averaging as in **Section 4.3**, a measurement of 12 time delays scanned 15 times takes 80 minutes. A -5 ns time delay image is collected to be used for background subtraction and also to check for

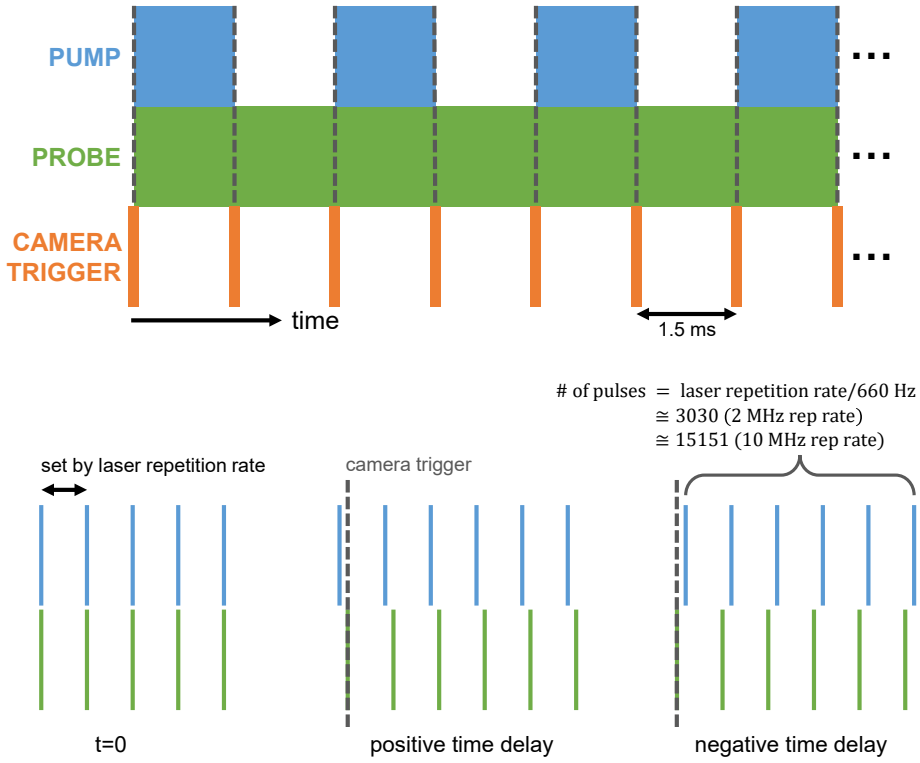

Figure 2.20: Timing sequence for stroboSCAT measurements. The camera is triggered at 660 Hz at the beginning of each probe pulse burst, the length of which depends on the laser repetition rate. Positive and negative time delays correspond to the probe arriving after and before the pump in one exposure, respectively.

any emission or steady state signal build up if the laser repetition rate is so high that the carriers (including heat) do not fully decay between pulses. To be able to record images at 660 Hz we reduce the region of interest from the full 1200×1920 pixel sensor to 192×192 pixels, i.e., ∼7×7 µm, although different aspect ratio configurations may be used [219], and a faster camera could allow for even larger fields of view. A paper shutter controlled with a stepper motor is used to block pump and probe light (if desired) during program overheads to minimize sample exposure.

2.5.3 Instrument stability

Although autofocusing capabilities as detailed in reference [218] were incorporated in the instrument, we found that for stroboSCAT measurements <20 minutes, our microscope is stable enough that autofocusing is not necessary, provided temperature fluctuations are minimal. In the laser lab, the temperature is stable to within ±0.5°F of the set point, with oscillations occurring over $T = 4$ hours. Over the coarse of a single measurement, fluctuations

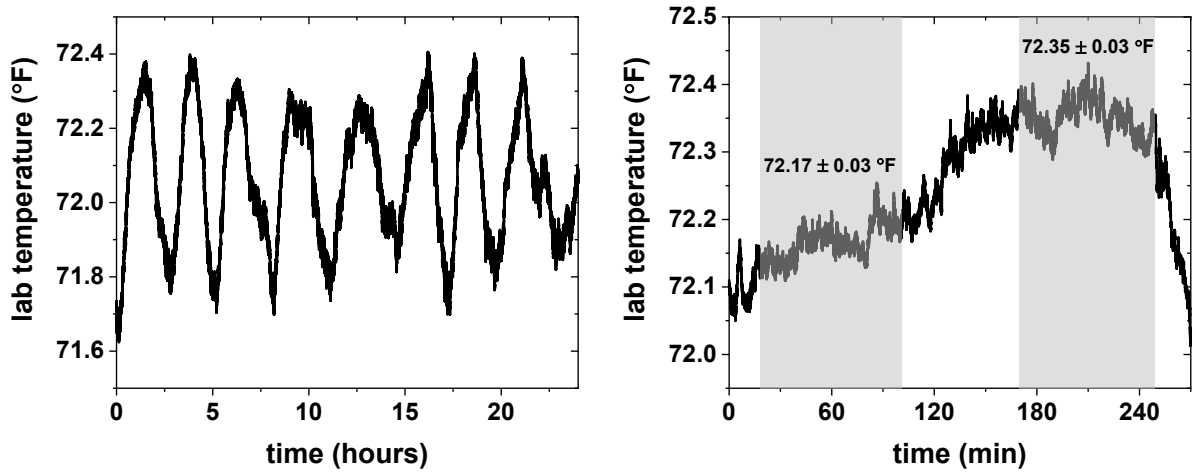

Figure 2.21: (left) Typical room temperature fluctuations over 24 hours in the laser lab. The temperature stays well within ±0.5°F of the 72°F set point with an oscillatory period of about 4 hours. **(right)** Laser lab temperature fluctuations for the near- and far-from resonant probe measurements in encapsulated 4L MoS_2 described in **Chapter 4**. Gray regions indicate the two data collection periods labeled with the average laser lab temperature and its standard deviation over the course of the measurement.

are much smaller (**Figure 2.21**). For measurements requiring longer averaging, such as for most of the experiments in **Chapter 4**, we manually refocus the differential time-zero image every ∼20 min. The change in the time-zero differential profile over this time is barely noticeable by eye, but the focal drift does suppress and broaden the measured differential profile as the entire setup drifts with the room temperature fluctuations (**Figure 2.22**). Placing the microscope stage in a thermally insulated enclosure is one passive option that could be implemented, as opposed to the active autofocusing mentioned above, for mitigating focal drift when longer averaging is required. We also found that heavier samples, such as a silicon wafer cut into the form factor of a typical sample coverslip ($\sim 20 \times 50$ mm), tend to maintain a stable focus over longer periods of time, up to a few hours.

One other source of variability between measurements is the tilt of the cantilevered sample stage, which can be adjusted with two knobs bolted to the aluminum sample holder (**Figure 2.23**). Depending on how the sample is fabricated and mounted, leveling the sample holder with respect to the optical table does not necessarily ensure that locally the crystal face, or smaller coverslip that the sample was deposited onto, is orthogonal to the optical axis. To level the sample with respect to the optical axis of the incoming probe light, one strategy is the following:

- Focus the image in one area of the sample by adjusting the $z-$axis micrometer.

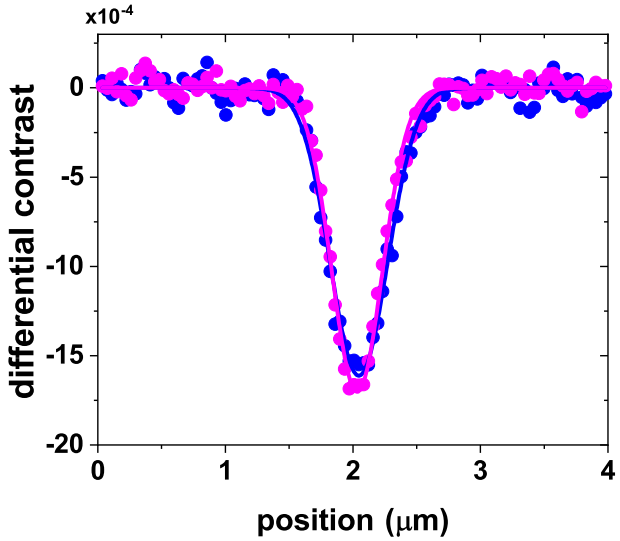

Figure 2.22: Focal drift in the time-zero differential image profile right after focusing (pink) and after 20 min of data collection (blue). In the de-focused profile, the amplitude is suppressed by 5% and the width broadened by 14%.

- Translate the stage in x or y several tens of μm away.
- Refocus the image by tuning the corresponding sample tilt knob.
- Continue to iterate along each axis separately, refocusing with the corresponding sample tilt knob, until the image stays in focus even after translating over many tens of μm in either direction.

If the sample tilt is way off of normal, it can make the pump beam profile look astigmatic and also impart asymmetry to the probe PSF so that differential images acquire an asymmetrical wonkiness as well, an effect that is especially pronounced in dual-contrast images (**Figure 2.24**).

The laser diodes provide high stability (<0.1% RMS) and modularity in terms of repetition rates (single shot – 80 MHz), electronic delays (20 ps – 2 ms) and pulse sequencing, and fast warm-up times (<10 minutes from turning on, although see **Section 4.3.5** for long-time drift characterization) at the expense of time resolution compared to ultrafast lasers. The use of electronic delays and modulation, as well as a widefield probe, results in no moving parts in the setup (apart from optional shutters), leading to an extremely stable and compact (<1 m^2) setup, with system realignment needed only once every 2 months with daily use. We note that for interferometric contrast, the temporal coherence length of the light source must be greater than the path difference between the scattered and reflected fields [218]. Laser illumination is, however, not necessarily required. Nanoparticles close to the substrate

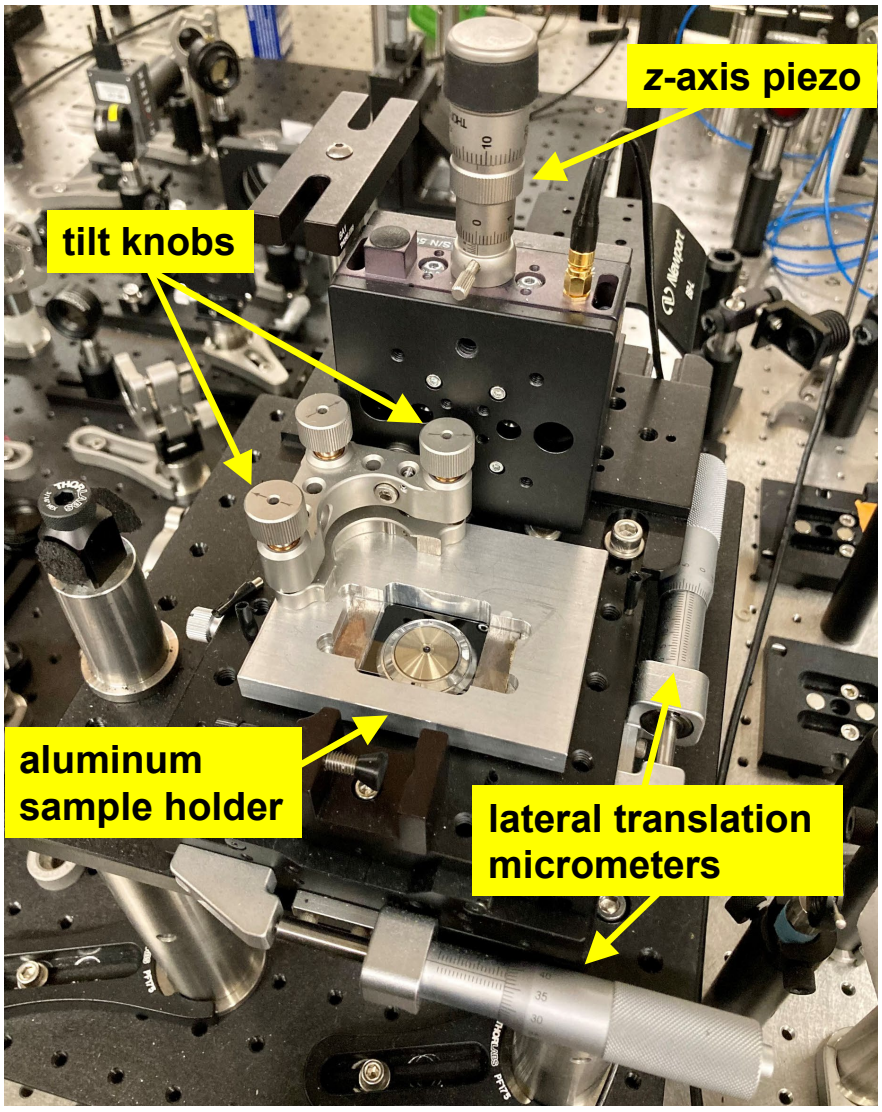

Figure 2.23: Labeled picture of the microscope stage showing the lateral translation micrometers, sample tilt knobs, and aluminum sample holder cantilevered from the $z-$axis focusing piezo.

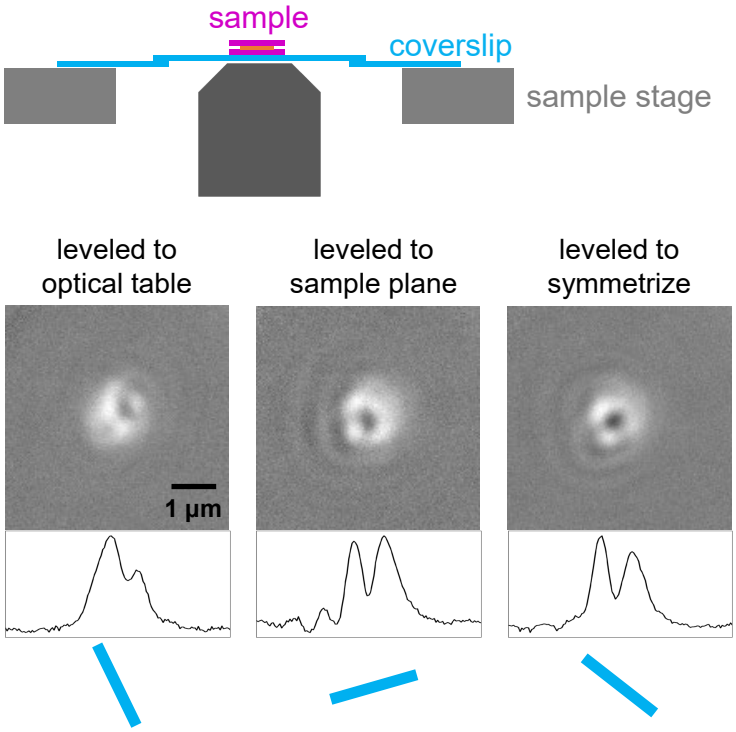

Figure 2.24: Sample tilt has a marked effect on the symmetry of stroboSCAT images, shown here as an example in bare 4L MoS_2. This sample was prepared on a 22×22 mm coverslip with added glass "wings" to span the sample stage. The differential images and line cuts show the time-zero signal after leveling the sample stage to the optics table (left), leveling the sample to maintain focus over a large area as described in the text (center) and tweaking that level to symmetrize the differential signal (right). Lingering asymmetry at this point is likely due to laser misalignment.

surface can be imaged with iSCAT using more incoherent sources such as LEDs [220]. Very large coherence lengths are undesirable as they can lead to interference among many optical elements, thus degrading image quality [221]. With a probe FWHM spectral width of 2-3 nm, we estimate a coherence length of $L = \frac{c}{\pi\Delta\nu}$ =∼40-60 µm for the diode lasers, depending on the medium's refractive index – much longer than the path difference for any films or crystals deposited on the substrate, but not long enough to lead to much interference from optical elements in the beam path. Ultrafast lasers with >30 nm spectral bandwidths (<2 µm coherence length) are still coherent enough, thus providing the opportunity to extend stroboSCAT experiments to the femtosecond realm [184, 222]. (In fact, even LEDs can maintain sufficient coherent lengths of tens of µm [219] and, depending on the temporal constraints of the dynamics, it can be beneficial to image with less temporally coherent light to mitigate imaging artifacts from drifting background interference patterns.) The use of ultrashort pulses for pump excitation is not affected by coherence length constraints. Nevertheless,

another advantage of using pulsed diodes is the low peak powers needed compared to highly impulsive (<100 fs) excitation for the same amount of overall excited state population. For short-pulse excitations, multi-photon effects, sample damage and heating must be carefully taken into consideration. For example, at the typical GW/cm^2 peak powers used in many ultrafast pump-probe experiments, carrier temperatures in semiconductors can reach $\sim 10^2$ K [126, 223], leading to the observation of hot-carrier dynamics [126] over several hundred picoseconds that we did not observe in our experiments using peak powers that are three orders of magnitude lower. Observing these hot-carrier dynamics in tandem with heat on ultrafast time scales, however, could be useful in understanding electron-phonon coupling or ultrafast energy transduction to heating, for example. Still, it is valuable to be able to characterize longer time scale dynamics using diode lasers with variable repetition rates in order to follow thermal dynamics explicitly. The tradeoffs between temporal resolution, temporal dynamic range, and temporal coherence must be carefully considered and tailored to each material system.

2.5.4 System resolution and sensitivity

As shown in **Figure 2.25a**, the 440 nm pump beam profile has a FWHM of 306 nm, which is ∼twice the diameter of a diffraction-limited spot. The total system spatial resolution according to the convolution theorem is the square root of the sum of the squares of the theoretical resolution limit and the object size. With the standard 440-635 nm pump-probe configuration, this formula yields a maximum spatial resolution of $\sqrt{(635/2.8)^2 + 306^2} = 381$ nm, where the pump profile represents the profile of the photoexcited object, and we use the probe's theoretical resolution using the Abbe convention. Using a diffraction-limited pump could improve the resolution to a best-case scenario (with these wavelengths) of ∼276 nm. We opted for a non-diffraction-limited beam by underfilling the objective in order to avoid polarization scrambling in the focal plane. The probe PSF is measured by imaging 40 nm gold beads on a clean glass substrate. The full 635 nm probe PSF (black curve in **Figure 2.25b**) fits well to a first-order Bessel function of the first kind, $2J_1(x)/x$ with $x = \frac{2\pi}{\lambda} r\mathrm{NA}$ for spatial coordinate r (blue dashed curve in **Figure 2.25b**). The central lobe is approximately diffraction-limited, as shown by the expected Abbe diffraction-limited Gaussian with $\sigma = \frac{\lambda}{2\mathrm{NA}(2\sqrt{2\ln 2})}$ (red dashed curve in **Figure 2.25b**). The measured probe PSF is used in the simulations in **Section 3.3.3**. The system temporal instrument response function (IRF) is determined to be ∼240 ps using a half-Gaussian to fit the signal rise-time in a stroboSCAT experiment on TIPS-pentacene (**Figure 2.25c**).

In terms of achievable sensitivity, a typical <10-minute experiment consists of averaging 3,500 (pump-on/pump-off) image pairs per delay time. Given a camera well depth of ∼30,000 electrons, taking 8-pixel-wide line cuts, the total photoelectron count per image per 8-pixel-wide area is $\sim 5 \times 10^9$. In a shot-noise-limited measurement, these figures provide a $1/\sqrt{N}$ sensitivity floor of 1.4×10^{-5}. In the differential image, taking the ratio of pump-on and pump-off images yields background fluctuations of 2×10^{-5}, in agreement with the

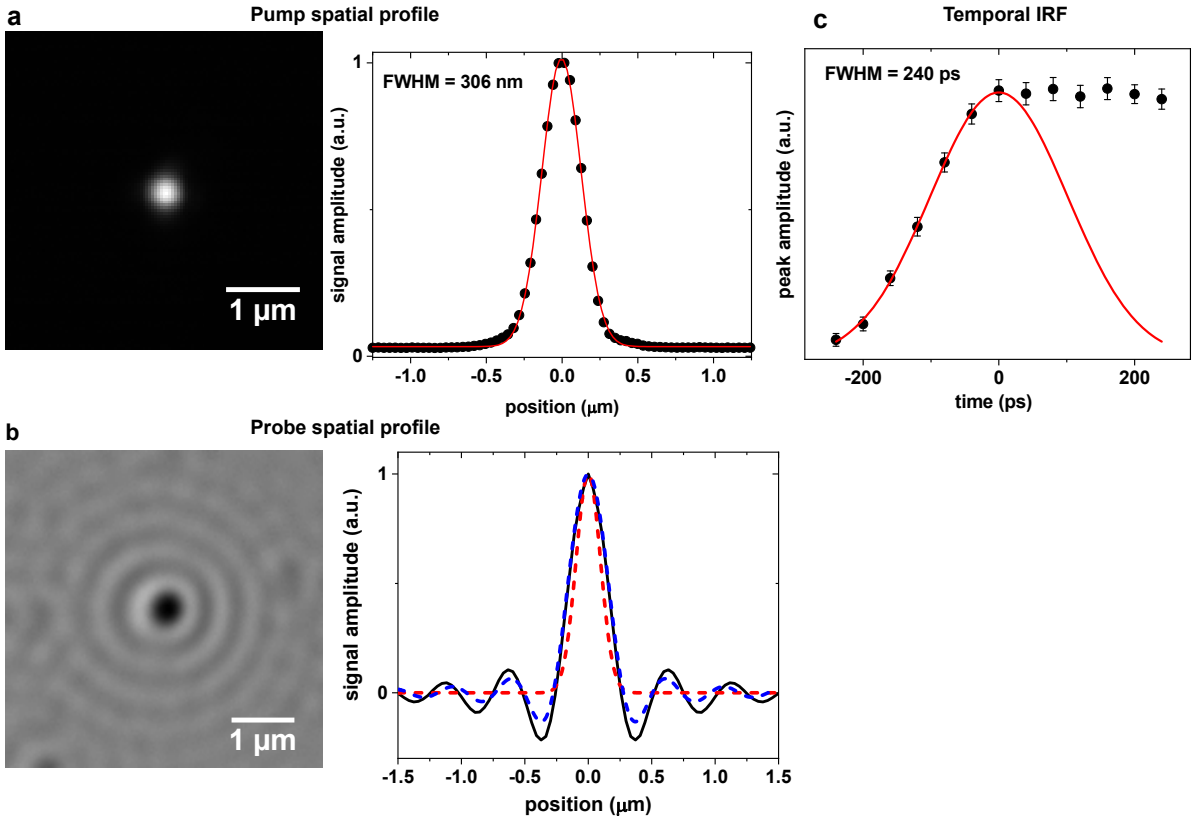

Figure 2.25: **(a)** Pump reflection from a glass substrate imaged on the CMOS camera, exhibiting a Gaussian profile with a FWHM of 306 nm. **(b)** Widefield probe PSF imaged using a 40 nm gold nanoparticle. The central lobe of the PSF corresponds closely to the expected diffraction-limited Gaussian (red dashed curve), while a first order Bessel function of the first kind is a better approximation of the entire PSF profile (blue dashed curve). **(c)** Gaussian peak amplitude as a function of pump-probe time delay at early times for a stroboSCAT experiment on TIPS-Pentacene. The instrument response function (IRF) of the system is estimated to be ∼240 ps.

above calculation based on the camera well depth. Achieving shot-noise-limited measurements is enabled in large part by current CMOS technology that utilizes high speed line scanning with low bandwidth amplifiers, resulting in characteristically lower read noise compared to electron multiplying charge-coupled device (EMCCD) detectors. For low-contrast samples, such as silicon and low-SNR samples such as few-layer TMDCs, longer averaging was used (10-15 scans), improving the sensitivity to $\sim 10^{-5}$, although at a certain point, this approach has diminishing returns as other sources of noise – such as laser, thermal or vibrational fluctuations or drift – begin to dominate over the shot noise. Averaging over more pixels or integrating azimuthally can also be done for isotropically expanding signals like charge carriers in silicon and excitons and heat in 4L MoS_2, further improving the sensitivity. Near-shot-noise limited measurements were easily attained for homogeneous samples, while strongly scattering samples might include slightly higher noise levels due to imperfect background subtraction.

2.5.5 *In situ* spectrally resolved stroboSCAT (spectroSCAT)

Several research groups have shown that spectrally resolving a signal near an absorption resonance can be used to detect both the phase and amplitude response of deeply subwavelength nano-objects (e.g., single molecules and quantum dots) [211, 212, 224, 225]. Indeed, with spectral resolution, small phase shifts between the signal and reference fields result in dramatic changes to the spectral profile of the object under study near its absorption resonance. As such, using the available phase information, several studies reproduced with high certainty and accuracy the known depth at which these single nano-objects were located above the focal plane [211, 212, 225]. Building on these studies, we incorporated the ability to obtain spectral measurements into the stroboSCAT microscope setup. Whereas stroboSCAT provides the ability to track carrier motion in 3D, spectral resolution taking over one of our spatial axes provides complementary phase-sensitive information on the sample's spectral response to photoexcitation in localized regions of its heterogeneous landscape within the same field of view. The latter allows benchmarking stroboSCAT's phase sensitivity and helps reinforce our interpretation of depth-dependent transport across morphological boundaries in perovskite thin films **(Chapter 3**). It is also useful for locating the excited state electronic resonances in a material, which can inform the choice of probe wavelength (**Chapter 4**).

For spectrally resolved measurements, the same event sequence, camera model, and pump pulse excitation are used, but instead of a narrowband probe, we use a broadband white light (WL) probe. The WL probe is generated by focusing the fundamental output (1030 nm, 200 kHz) of a Light Conversion PHAROS ultrafast regeneratively amplified laser system into a 3 mm yttrium aluminum garnet (YAG) or sapphire crystal. For the spectral data on $MAPbI_3$ (**Section 3.3**), the WL output is filtered with a 675 nm longpass filter to reduce sample exposure to above-bandgap light. The WL is sent collimated into the objective to obtain near-diffraction-limited probe pulses on the sample, in contrast to using the widefield probe elsewhere in this thesis. The reflected and backscattered light is then coupled into a home-

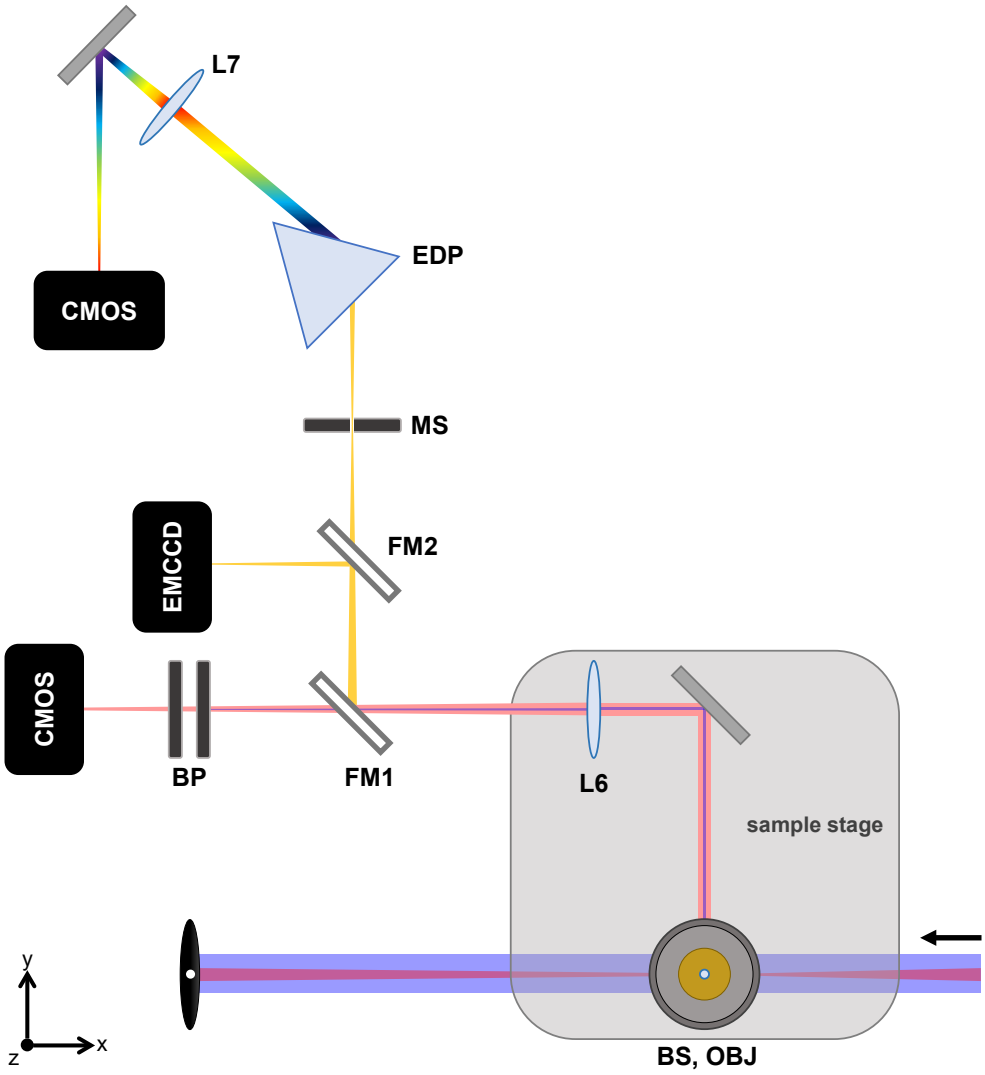

Figure 2.26: Spectrally resolved stroboSCAT and fluorescence imaging capabilities in the stroboSCAT microscope. For fluorescence imaging, two flip mirrors (FM1 and FM2) direct the microscope output to a sensitive EMCCD. For spectrally resolved stroboSCAT, the microscope output is filtered through a mechanical slit (MS) before being dispersed through an equilateral dispersive prism (EDP) and then imaged onto a CMOS camera with a focusing lens (L7, AC254-150-B).

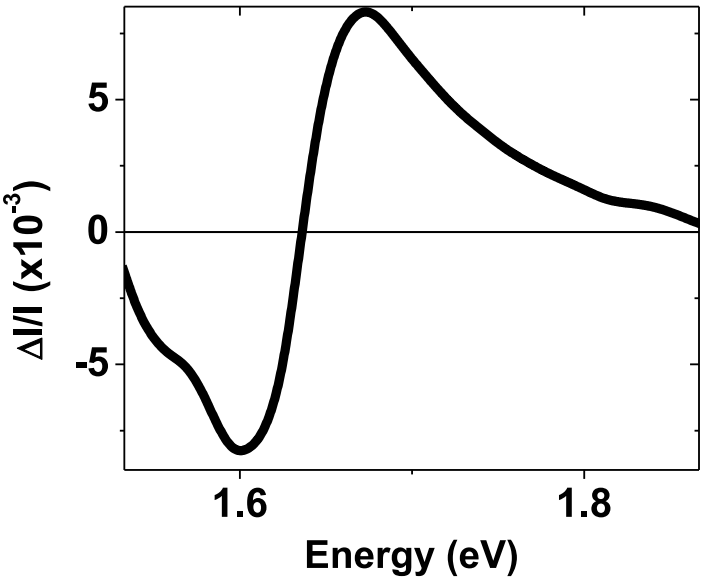

Figure 2.27: Spectrally resolved stroboSCAT signal near the $MAPbI_3$ band edge.

built prism spectrometer and dispersed onto a CMOS camera (PixeLINK PL-D752, the same as is used in stroboSCAT) as shown in **Figure 2.26**. The entrance slit of the spectrometer (MS) is placed in the image plane. This dual imaging/spectroscopy mode is similar to that recently implemented for widefield transient absorption microscopy [226, 227]. The electronic delays between pump and probe are controlled using an external delay generator, (DG645, Stanford Research Systems), triggered with the pulse output of the ultrafast laser and feeding a user-delayed signal to the diode driver. The spectrum is calibrated using the known transmission spectrum of a Thorlabs FGB67 filter. For more sensitive fluorescence imaging, the output of the microscope may also be sent to a separate EMCCD (Andor Luca) with appropriate filtering to isolate the expected emission.

Using spectrally resolved stroboSCAT, we observe a characteristic dispersive spectral profile around the band edge (**Figure 2.27**, discussed further in **Section 3.3**). This profile reproduces the transient absorption spectrum through a Hilbert transform. These data confirm that the signals we observe in reflection-based stroboSCAT for lead halide perovskites originate from changes to n, not k. In general, all of the data shown in this thesis (except for TIPS-Pentacene and the near-resonant measurement in four-layer MoS_2) are taken with a probe that is spectrally detuned from band edge resonances, i.e., away from where the largest photoinduced resonance changes occur in semiconductors. Macroscopically, stroboSCAT in these cases reports on changes to the real part of the refractive index. Microscopically, the signal arises from non-resonant Mie scattering of the probe field with closely-spaced deeply subwavelength particles and their modified surroundings.

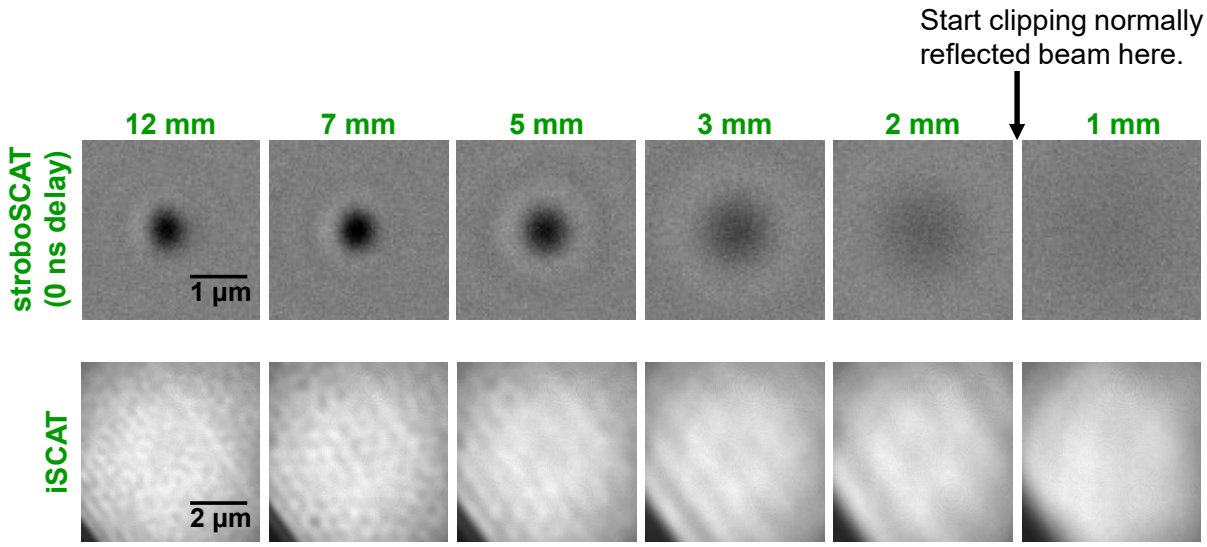

Figure 2.28: Distinguishing scattering from normal reflection in stroboSCAT. stroboSCAT contrast for TIPS-pentacene at 0 ns time delay (top row). The images show how the differential contrast changes as high spatial frequencies of the scattering field are progressively filtered out using a variable aperture placed between the objective and beamsplitter. The bottom row shows the corresponding ground state iSCAT images for comparison.

2.5.6 Distinguishing scattering from normal reflection

It is possible to separate light scattered from the sample and unscattered light simply participating in specular reflection at the sample-substrate interface near the back focal plane of the objective by making use of the fact that small scatterers (e.g., individual energy carriers, quantum dots, nanoparticles, etc.) near a refractive index interface radiate the majority of photons at the critical angle determined by the interface, due to interference between the dipole emission and the reflected field [208, 228, 229]. This directionality applies not only to elastic scattering but also to other light-matter interactions such as absorption, photoluminescence, and inelastic scattering from deeply subwavelength particles near the refractive index interface. Here, we assume that the light traveling at the critical angle is due to elastic scattering. This phenomenon results in the scattered field being directed at oblique or high angles relative to the optical axis [228]. Since widefield illumination only requires a very low numerical aperture, the spatial frequencies of the scattered light and illumination beam are well separated near the back aperture of the objective. Indeed, it has been shown in iSCAT experiments that the illumination beam can be attenuated with an appropriate partial reflector while transmitting the vast majority of the scattered field in order to increase the iSCAT contrast significantly [208, 228]. Similarly, the normally-reflected light can be entirely blocked, resulting in a sensitive darkfield backscattering microscope [230].

To verify that the same separation of spatial frequencies is present in stroboSCAT, and

to confirm the signal source is scattering from a collection of small particles (and not just a change in the reflection coefficient, r, of the interface), we introduced an aperture between the objective and beamsplitter in **Figure 2.15** to be able to interchange between stroboSCAT and normal reflectance modes of imaging.

Figure 2.28 shows the effect of spatially filtering the scattered field only while the normally-reflected illumination field is fully transmitted. The stroboSCAT signal magnitude reduces and the spatial extent of the signal on the detector plane increases as high spatial frequencies are filtered out. These experiments indicate that the scattered field emitted toward high-NA associated directions (predominantly from the edges of a localized distribution of photoexcitations) is indeed responsible for the observed signal.

Furthermore, a 3 mm beam stop attached to a thin wire was inserted to block the normally-reflected beam while transmitting the scattered field only [230]. Using the same experimental conditions, we were unable to observe any signal above noise on the detector, presumably because the stroboSCAT signal requires mixing reflected light with the scattered light in order to be detectable. In contrast, images of dust particles or other strongly-scattering objects, upon placement of this beam stop, switch from having dark contrast on a bright background to having bright contrast on dark background, as expected for darkfield microscopy.

The same control measurements were performed on all samples, giving identical results. Taken together, these observations indicate that the interferometric cross-term dominates the differential signal magnitude, i.e., $s^2 \ll rs\cos\phi$, and the reflection coefficient, r, does not change significantly between pumped and unpumped states. Thus, darkfield microscopy or the typical relative waist sizes of probe lesser than pump in transient reflectance microscopy are not able to achieve the same sensitivities as stroboSCAT.

2.6 Conclusion

In this Chapter, we laid the foundation for understanding the physical principles that govern the observables in a stroboSCAT measurement: optical scattering, characterized on the atomic or molecular scale by the polarizability and on the macroscopic scale by complex frequency-dependent optical functions including the refractive index, dielectric function or susceptibility, with the connection between the two regimes given by the Clausius-Mossotti relation. We described several ways in which photoexcitations in a material locally change these optical functions through modifications to the material absorption coefficient or, equivalently, scattering since the two are causally related through the Kramers-Kronig relations. Although not exhaustive, this brief introduction of concepts in optical scattering, excited state phenomena, microscopy, and iSCAT, the imaging probe in stroboSCAT, provides the necessary context for the remaining thesis Chapters and, hopefully, points the curious reader towards helpful resources for more in-depth exploration. Finally, we detailed the ins and outs of the experimental operation of the stroboSCAT instrument, which we hope will be valuable for future stroboSCAT enthusiasts.

Chapter 3

Imaging material functionality through three-dimensional nanoscale tracking of energy flow

3.1 Introduction

As we have developed in the preceding chapters, the ability of energy carriers to move between atoms and molecules underlies biochemical and material function. Understanding and controlling energy flow, however, requires observing it on ultrasmall and ultrafast spatiotemporal scales, where energetic and structural roadblocks dictate the fate of energy carriers. Here, we implement a non-invasive optical scheme that leverages non-resonant interferometric scattering to track tiny changes in material polarizability created by energy carriers. We thus map evolving energy carrier distributions in four dimensions of spacetime with few-nanometer lateral precision and directly correlate them with material morphology. We visualize exciton, charge and heat transport in polyacene, silicon and halide perovskite semiconductors and elucidate how disorder affects energy flow in three dimensions. For example, we show that morphological boundaries in polycrystalline metal halide perovskites possess lateral- and depth-dependent resistivities, blocking lateral transport for surface but not bulk carriers. We also reveal strategies for interpreting energy transport in disordered environments that will direct the design of defect-tolerant materials for the semiconductor industry of tomorrow.

3.1.1 Visualizing energy flow over four orders of magnitude in space and time

We use stroboSCAT to visualize energy flow in a wide range of semiconductors, demonstrating its capability over four orders of magnitude in space and time, on both neutral and charged excitations migrating through organic, organic–inorganic and inorganic semiconductors. Before focusing on disordered semiconductors, we illustrate stroboSCAT imaging of carrier diffusion in an ordered semiconductor: **Figure 3.1a,b** displays the spatial profile of charge carriers as a function of pump–probe time delay in a methylammonium lead bromide ($MAPbBr_3$) perovskite single crystal. At 635 nm, the probe is spectrally far from the band edge (570 nm), primarily detecting changes in n. Using ultra-stable picosecond pulsed laser diodes, we achieve shot-noise-limited differential contrast with sensitivities approaching 10^{-5} and a signal-to-noise ratio averaging 40 for up to a 1 ns pump–probe time delay with less than 1 min integration per time delay. In this simple example, the diffusivity D for the charge carriers can be modeled from the Gaussian distribution variance σ^2 of the scattering profile with time t: $2Dt = \sigma^2(t) - \sigma^2(0)$ (**Section 1.4.1**). The achievable sample-dependent spatial precision, $\Delta\sigma(t) = \pm 2 - 10$ nm for a <1 min measurement per time delay (or $\Delta\sqrt{2Dt} = \pm 4 - 20$ nm), is not limited by diffraction but rather by fitting precision, which depends on the signal-to-noise ratio [72, 114]. **Figure 1d,e** summarizes similar analyses on a variety of semiconductors using the same experimental setup to image heat, neutral bound pairs of charges (excitons) and free charge carrier diffusion. For data shown in this Chapter, the light sources used are two laser diodes for the pump and probe with center wavelengths of 440 and 635 nm, respectively, and a base laser repetition rate of 2 MHz, with the exception of measurements in silicon in **Section 3.4**, where other pump and probe wavelengths are indicated. Additional laser wavelengths are also possible and detailed in **Section 2.5**. Sample preparation protocols are detailed in **Appendix A.2**.

All reported injected energy carrier densities, n_0, are calculated as $n_0 = ja$, where j is the peak pump fluence in photons/cm^2, and a is the absorption coefficient reported in the literature. Peak photon fluence is calculated from peak energy fluence, which is defined here as $2E/\pi r^2$, with E being the pulse energy and r being the beam radius at $1/e^2$. For each sample, a pump-power dependence over several time delays is performed in order to ensure that the rate of decay of the stroboSCAT signal peak amplitude is power-independent over the range of powers used. In this way we ensure that many-body effects such as Auger-Meitner recombination do not contribute significantly to the determined diffusivities. Using higher powers may lead to incorrect estimations of the diffusion coefficient as the population distributions approach flat-top profiles rather than Gaussian profiles, which, if fit with a Gaussian function, will appear as erroneously large distribution widths [114]. For TIPS-Pentacene and silicon, power-dependent behavior is non-trivial and discussed in further detail below (**Section 3.2** and **Section 3.4**, respectively).

Our results closely match other published values for materials whose energy diffusivities were previously determined [232–235], confirming stroboSCAT's viability. One notable observation in **Figure 3.1c,d** is that carrier diffusivities in $MAPbBr_3$ are reduced more than

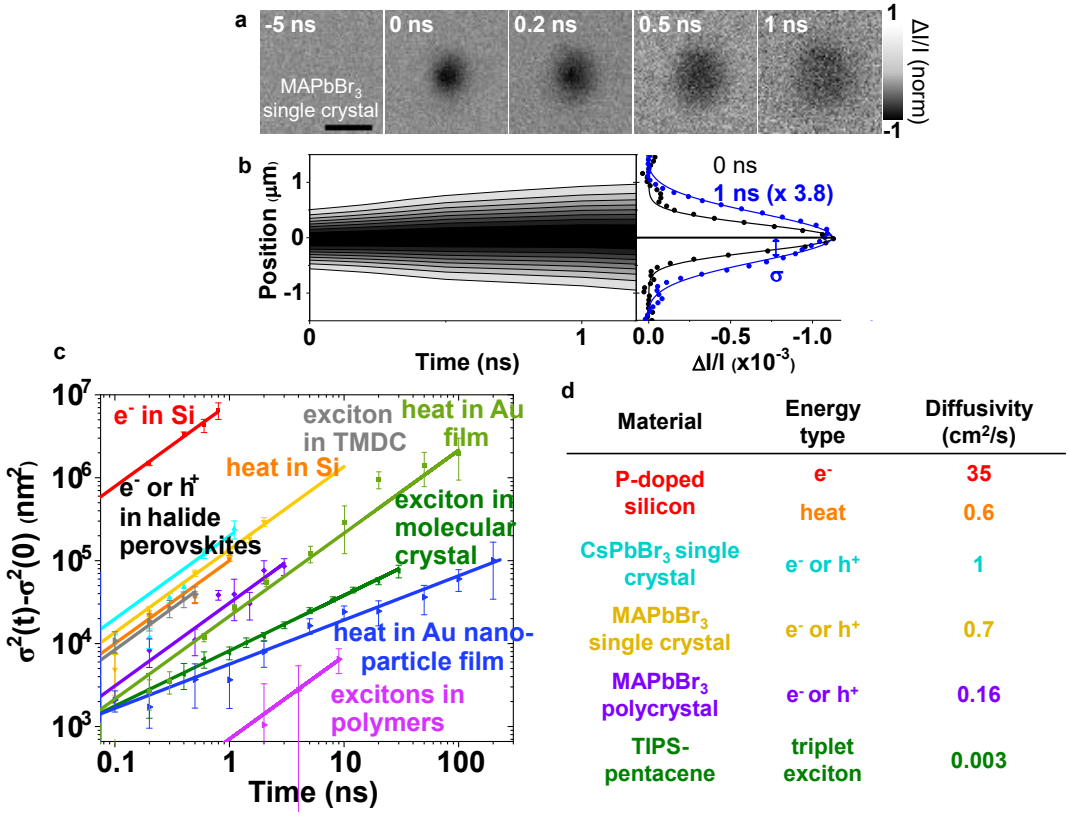

Figure 3.1: Visualizing semiconductor exciton, charge and heat transport across four orders of magnitude in space and time. **(a)** Example stroboSCAT dataset for a $MAPbBr_3$ single crystal, showing charge carriers diffusing as a function of pump–probe time delay. The peak pump-injected carrier density is 2×10^{18} cm^{-3}, and the probe is spectrally far from the band edge (570 nm). The peak power densities at the sample are on the order of 0.2 MW cm^{-2}, far below the onset of nonlinear optical effects. All stroboSCAT plots are generated by taking the difference between pump-on and pump-off raw pixel intensities (I), normalized to the raw pump-off intensities, yielding $\Delta I/I$ contrast images. Scale bars are 1 μm. **(b)** The spatiotemporal population distribution along the horizontal spatial axis is plotted, along with 1D Gaussian profiles extracted at 0 and 1 ns pump-probe delay. **(c)** Charge, exciton or heat distributions versus time measured for a range of semiconductors. See panel (d) for color coding. Error bars represent the 95% confidence intervals from Gaussian fits. All experiments are performed in a linear excitation regime, as confirmed by a lack of power dependence to extracted diffusivities. **(d)** Diffusivities extracted from linear fits of the data in (c).

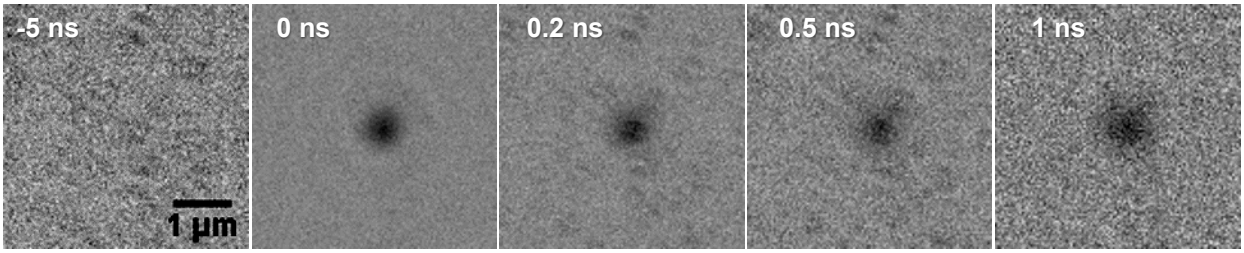

Figure 3.2: stroboSCAT time series on a $MAPbBr_3$ polycrystalline film. Note that background contributions due to sample vibrations/drift during acquisition are larger for heterogeneous samples than for samples that scatter homogeneously. The extracted diffusivity from this dataset is 0.15 ± 0.02 cm^2/s. The average and standard deviation across 5 datasets is 0.16 ± 0.05 cm^2/s. Fluence is 10 µJ/cm^2 ($n_0 \approx 2 \times 10^{18}$ cm^{-3}) [231]. The pump at 440 nm is above bandgap, while the probe at 635 nm is non-resonant with both ground and excited state absorption.

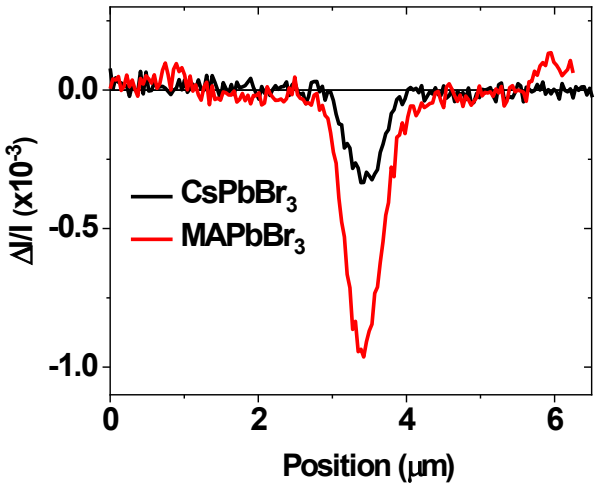

Figure 3.3: stroboSCAT contrast difference at 0 ns pump-probe time delay at a fluence of 10 µJ/cm^2 for $MAPbBr_3$ vs. $CsPbBr_3$ single crystals. The contrast magnitude is lower by a factor of 2.7 in $CsPbBr_3$ despite both systems having similar absorption coefficients and both being probed with below-bandgap, off-resonant light. The extent to which contrast magnitude can be used to gain information on electron-phonon coupling in these different systems will be the subject of future investigations.

fourfold in disordered polycrystalline films compared with those in single crystals (**Figure 3.2**). Nevertheless, the impact of domain interfaces on energy flow can be nontrivial, depending greatly on their type, size, distribution and composition. Furthermore, the magnitude of the stroboSCAT contrast can change as a function of chemical composition in single crystals even when they have similar absorption coefficients (**Figure 3.3**). We use stroboSCAT to track and morphologically correlate energy flow up to, within, and across energetic obstacles, using two classes of emerging semiconductors as case studies in **Sections 3.2** and **3.3** below. We also demonstrate a case where heat and charge flow, even when they overlap, may be readily distinguished by distinct differential contrast when their diffusivities and dynamics are substantially dissimilar (**Section 3.4**). Our results and corroborating simulations reveal that carrier trajectories are governed by highly anisotropic paths of least resistance, precluding the viability of diffusive models extracted from bulk or averaged measurements and calling for new ways to interpret and quantify energy flow in disordered environments.

3.2 Exciton transport is impeded by grain boundaries in TIPS-Pentacene

We first explore the effect of low-curvature domain interfaces on exciton migration in polycrystalline 6,13-bis(triisopropylsilylethynyl)pentacene (TIPS-Pn) [236] films. TIPS-Pn is a promising singlet-fission sensitizer for hybrid solar panels and represents an archetypal system in which to study energy transport in π-stacked molecular crystals (**Figure 3.4a**) [237, 238]. In **Figure 3.4b**, iSCAT images at two different probe field polarizations display two orthogonally oriented crystalline domains (light versus dark) separated by straight interfaces. The images are filtered using a Fourier bandpass that removes interference fringes from the probe field diffracting off of crystalline interfaces in the sample, a consequence of using wide-field illumination (**Figure 3.5**). Exciton migration imaged by stroboSCAT within a domain (**Figure 3.4c–e**) shows that at early time delays, the migration is nonlinear, lending support to previous reports that attribute this behavior to the interchange between fast-diffusing singlet and slow-diffusing triplet pair excitations [239]. Early-time dynamics are dictated by singlet fission into two triplets and the reverse process of triplet fusion into a singlet, which affects the rate of exciton migration since singlets diffuse faster than triplet excitons [240, 241]. The combination of this interplay with singlet-singlet annihilation gives rise to nonlinear diffusive dynamics for as long as triplets are strongly bound – up to nanoseconds (**Figure 3.6b**) [242]. To eliminate singlet-singlet and free triplet-triplet annihilation and concentrate on intrinsic singlet-triplet interchange, our measurements are taken at 147 fJ (140 µJ/cm^2 peak fluence), as we detect no significant changes in the peak amplitude decay between 74 and 147 fJ (**Figure 3.6a**). At higher fluences, faster decay of the peak amplitudes at early times is observed, resulting in faster apparent diffusion. Beyond 5 ns, we observe linear diffusion for all fluences at $D = 0.003$ cm^2/s, consistent with the common interpretation of free triplet migration (**Figure 3.6c**) [72, 239]. Furthermore, intradomain diffusion along

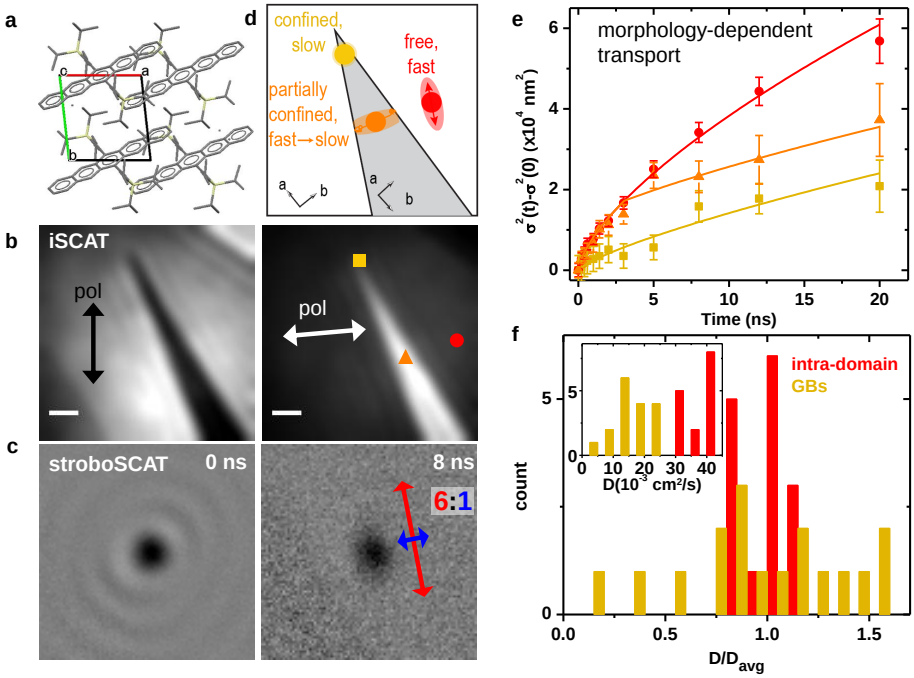

Figure 3.4: Morphology-dependent exciton transport in TIPS-Pentacene. **(a)** Crystal structure of TIPS-Pn [236], displaying the orientation of the crystallographic a and b axes. Carbon atoms are grey, silicon atoms are yellow. **(b)** iSCAT images at different polarizations (pol) showing two orthogonally oriented crystal domains. These images are bandpass-filtered to remove diffraction fringes near interfaces (**Figure 3.5**). Mean squared displacement curves measured at the positions depicted by the red circle, orange triangle and yellow square are displayed in panel (e). **(c)** stroboSCAT images at 0 and 8 ns time delay in a crystalline domain (red spot in (b)), displaying anisotropic diffusion with sixfold faster transport along the π-stacked (red) axis of the crystal (**Figure 3.7**). The lab frame anisotropy directionality changes in different domains in relation to their crystal orientations. Both the pump (440 nm) and probe (635 nm) are resonant with ground-state absorption in this example. **(d)** Schematic of exciton diffusion behavior at three different spots: intradomain (red), confined (yellow) and intermediate transport scenarios (orange). **(e)** Corresponding population expansion dynamics along the fast-diffusion axes. The pump is circularly polarized and the probe polarization is chosen to avoid contrast bias across domains. Error bars represent the 95% confidence intervals from Gaussian fits. **(f)** Spot-to-spot variability of initial diffusivity D_0, determined from the fitting function $f(t) = 2D_0t^{\alpha}$ where α is a free parameter, for intradomain and grain boundary-confined scenarios. Peak fluence is 140 µJ cm^{-2}. Scale bars are all 1 µm.

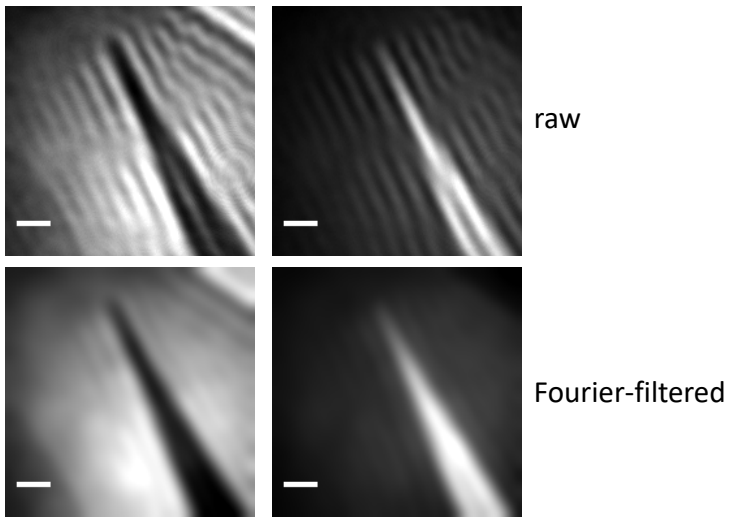

Figure 3.5: iSCAT images of TIPS-Pentacene crystalline domains at orthogonal probe polarizations shown in **Figure 3.4b**. Raw (Fourier-filtered) images are shown at the top (bottom). Scale bars are 1 µm.

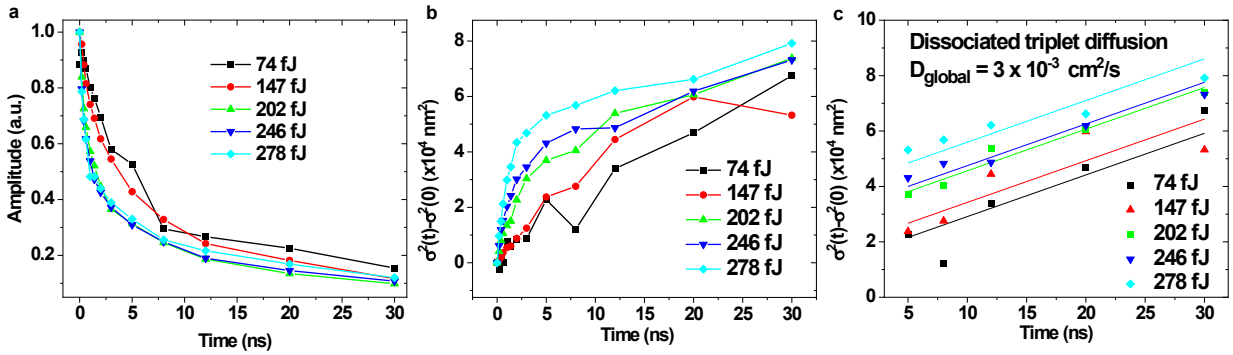

Figure 3.6: TIPS-Pentacene power-dependent early and late time dynamics. **(a)** Peak amplitude decay from normalized peak Gaussian amplitudes of the stroboSCAT signal for different pump fluences. **(b)** Nonlinear diffusive dynamics due to the interplay between singlet-fission, triplet fusion and singlet-singlet annihilation gives way to linear diffusive behavior **(c)** at long times.

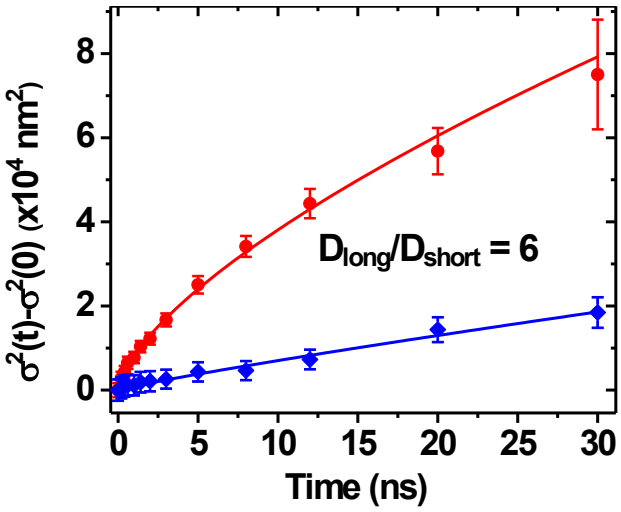

Figure 3.7: Anisotropic diffusion in TIPS-Pentacene. Diffusivity along the long π-stacked axis (red) is approximately 6 times larger than along the short axis (blue). Diffusivities are determined from fits to a sub-diffusive model, $f(t) = 2D_0t^\alpha$, where D_0 is the initial diffusivity and α is a free parameter.

the π-stacked axis is approximately 6 times larger than along the short axis, as expected for these intrinsically anisotropic systems when fit to a sub-diffusive model (**Figure 3.7**) [71, 72].

The key finding enabled by stroboSCAT is the degree to which individual grain boundaries hinder exciton transport in molecular crystals and that the extent of this hindrance varies widely. The narrow wedge-shaped central domain in this example provides an opportunity to systematically quantify the effect of domain confinement by interfaces on exciton migration (**Figure 3.4d**). Population distribution expansion along the fast migration axis at red, orange and yellow spots highlighted in **Figure 3.4b,d** are plotted in **Figure 3.4e**. Comparing the bulk crystalline domain (red) and the most confined spot (yellow), we find that interfaces severely hinder exciton transport, slowing it approximately fourfold. Transport at the partially confined area (orange) can be accurately modeled piecewise, with free migration up to 3 ns (overlapping orange and red curves) and confined migration thereafter (where the orange curve parallels the yellow curve), indicating a transition from bulk-like to slower transport at an interface.

We measured exciton migration in 15 different domains and at 17 different grain boundaries, all of whose results are summarized in **Figure 3.4f**. In **Figure 3.8**, we provide several more detailed examples. stroboSCAT images are shown on the left at 0 and 8 ns time delays. In the middle column, corresponding iSCAT (pump-off) images at the probe polarizations used for each dataset are shown. On the right, a larger field-of-view image is used to capture the three domains in a single image at a given polarization. Note that the contrast for each crystalline domain in iSCAT (pump-off) images switches between bright and dark depending

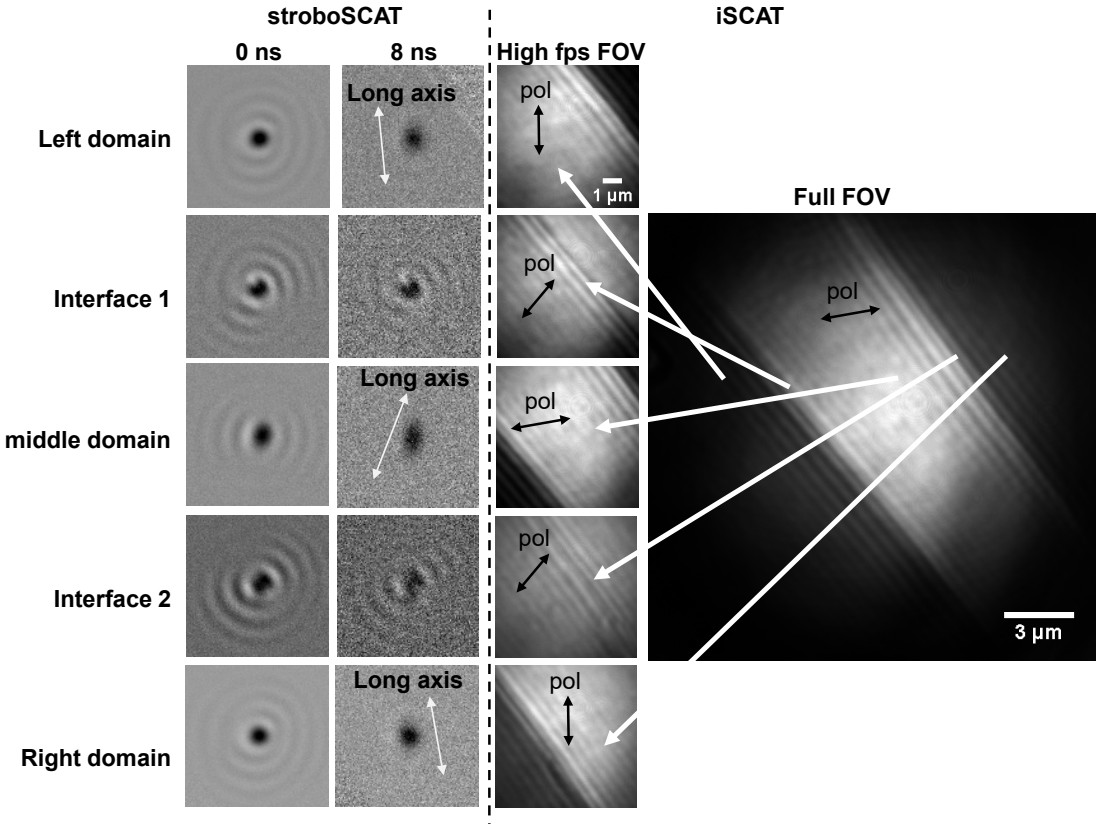

Figure 3.8: Additional datasets in TIPS-Pentacene within three crystalline domains and at two grain boundaries in the same field of view (FOV) using stroboSCAT and iSCAT.

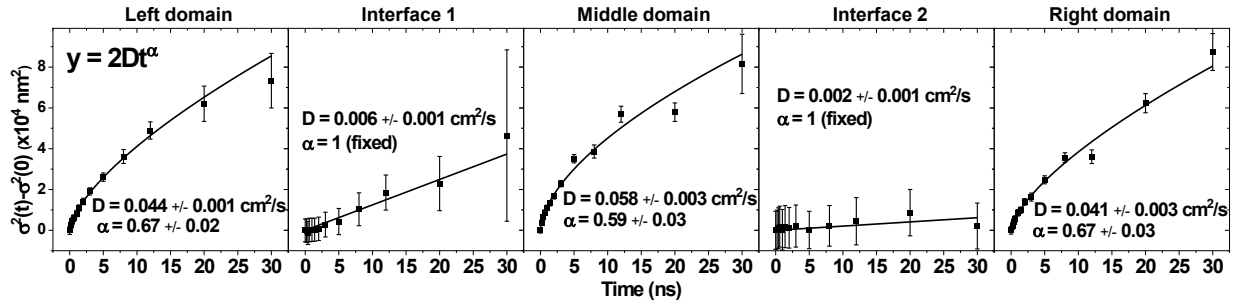

Figure 3.9: Population expansion plots for domains and grain boundaries in TIPS-Pentacene. To extract the exciton dynamics, a subdiffusive model is used to fit the mean squared expansion curves and extract an effective D_0 to compare among domains and grain boundaries. Due to the larger noise at grain boundaries and apparently linear diffusive behavior, we used a linear model to avoid over-fitting.

on the probe polarization used. The middle domain appears somewhat out-of-plane (i.e. the *c*-axis is not perpendicular to the substrate plane), as evidenced by a non-circular profile of the excitation spot at 0 ns in the stroboSCAT image, which we attribute to projection distortion. This non-planar orientation of the crystalline domain was observed in around 20% of the domains investigated in these films. For all datasets, the pump was circularly polarized. When investigating grain boundaries, the probe polarization was set to equalize contrast across domains, as shown explicitly in the iSCAT images of Interface 1 and 2 in **Figure 3.8**. We tested the validity of this approach by verifying that similar results were obtained with a circularly-polarized probe both in domains and at grain boundaries, although the signal-to-noise ratio was poorer when using a circularly, instead of linearly polarized, probe beam. The exciton migration in the domains and interfaces in **Figure 3.8** is summarized in **Figure 3.9**.

Across the range of domains and grain boundaries explored, we found that (1) exciton transport is always slower at grain boundaries than in domains (**Figure 3.4f** inset) and (2) transport speed is consistent in all measured domains, whereas transport at grain boundaries is highly variable, as indicated by the normalized distribution of initial ($t = 0$) diffusivities in **Figure 3.4f**. Indeed, interface formation kinetics, degree of lattice misorientations, and void and impurity concentrations will give rise to a wide range of transport behavior at different interfaces. Thus, high-throughput and correlative measurements of exciton migration over nanometer length scales provide the crucial ability to investigate energy transport properties *in situ* for individual interfaces and surrounding crystal domains and to correlate these with their specific morphologies.

3.3 Navigating morphological boundaries in polycrystalline thin film lead halide perovskites

Although large crystalline domains separated by abrupt interfaces provide a systematic environment for testing the effects of crystalline mismatch on energy transport, a more commonly encountered morphology in polycrystalline semiconductors consists of sub- to few-micrometer-sized domains. In these materials, energy carriers almost inevitably encounter domain boundaries during their lifetimes. Grain boundaries and, more generally, morphological boundaries (MBs) between domains (which are most typically crystal grains) thus significantly impact bulk-averaged measures of energy flow such as charge mobility and recombination [243, 244]. There is, however, little consensus on the effect of MBs on the functional properties of a wide range of semiconductors. Nowhere is the debate currently more salient than with metal halide perovskites [226, 245–252]. For example, despite numerous studies suggesting that MBs in perovskites have large trap densities, act as recombination centers and impede carrier transport, photovoltaic efficiencies for polycrystalline films have reached 26% and do not necessarily scale favorably with grain size [83, 87, 253, 254]. The primary difficulty in resolving these paradoxes lies in elucidating how the functional impacts

of MBs locally deviate from bulk-averaged metrics. This challenge is exacerbated by the vast diversity of preparation protocols for polycrystalline metal halide perovskites, which lead to radically different material properties [255]. We show that visualizing carrier distributions in 3D as they trace the paths of least resistance through different halide perovskite films provides systematic and individualized detail on the effect of traps, the lateral- and depth-dependent conductive properties of MBs and the resulting spatiotemporal anisotropy of charge transport as a function of material morphology.

The stroboSCAT time series in **Figure 3.10a** illustrates differences in charge carrier transport for three polycrystalline methylammonium lead iodide ($MAPbI_3$) films prepared using common protocols that lead to different domain sizes (**Appendix A.2**). Each protocol uses different precursors – lead acetate ($PbAC_2$), lead iodide (PbI_2), or lead chloride ($PbCl_2$) – which are indicated on the left of the corresponding datasets in **Figure 3.10a**. We characterized the absorption and emission properties of each $MAPbI_3$ film as a benchmark for proper film preparation (**Figure 3.11)**. The decay lifetimes correspond closely to those reported for related preparation protocols [247, 256, 257]. Each precursor-specific preparation generates a $MAPbI_3$ polycrystalline film with different characteristic domain sizes. We extract approximate domain sizes for each sample with AFM and confocal images (**Figure 3.12**). On average, films with smaller domains exhibit slower lateral carrier transport, confirming that MBs negatively affect interdomain carrier transport. From the data in **Figure 3.10a** we extract lateral diffusion lengths (**Section 1.4.1**), $L_{D,\text{avg}} = \sqrt{4D\tau}$ where τ is the carrier lifetime, by azimuthally averaging and time-averaging over the first 2 ns only, during which D is approximately constant. We find $L_{D,\text{avg}}$ values of 180 nm, 200 nm and 700 nm for films made respectively with $PbAC_2$, PbI_2 and $PbCl_2$ precursors. As these samples are emissive, we also display the correlated steady-state widefield emission pattern arising from carrier recombination [248] in **Figure 3.10b**. The close correspondence between widefield emission and stroboSCAT images at late time delays confirms that the full extent of carrier migration is captured by stroboSCAT.

3.3.1 Contrast phase flips coincide with morphological boundaries

In the largest-domain $MAPbI_3$(Cl) film in **Figure 3.10a**, the sign of the stroboSCAT contrast can reverse from negative to positive. By correlating stroboSCAT measurements with structural maps in the same field of view (**Section 3.3.2**), we show that these contrast flips occur only at MBs. We rule out the possibility that the contrast flips arise from a change in carrier density, scattering amplitude or heat, as we do not observe these sign flips in any other region when varying the pump fluence over four orders of magnitude. We therefore attribute these contrast flips to a change in the phase of the interferometric cross-term combining the reflected and scattered fields (**Section 2.4**). The cross-term phase depends linearly on the depth of the scattering objects with respect to the sample–substrate interface, providing a measure of the distribution of scatterers along the optical axis [198, 258]. The resulting

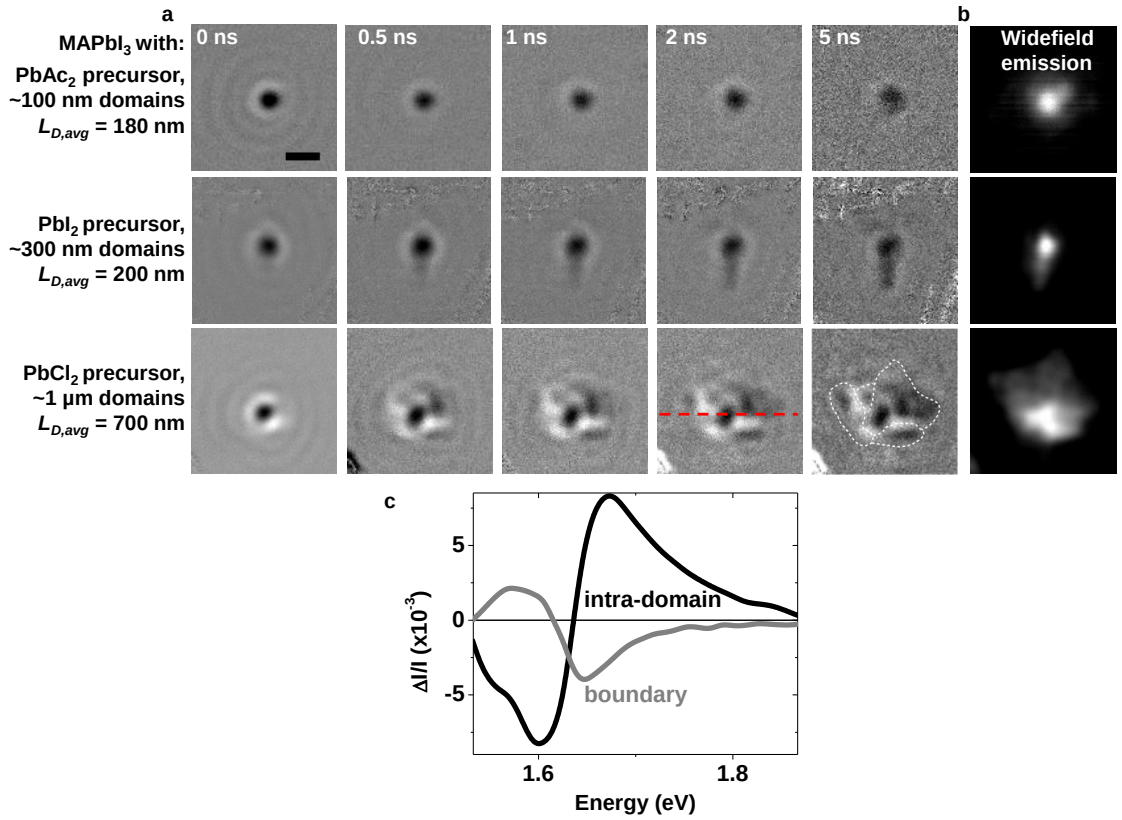

Figure 3.10: Heterogeneous charge carrier transport in polycrystalline $MAPbI_3$ thin films. **(a)** stroboSCAT time series on three $MAPbI_3$ samples prepared from different precursors. **(b)** Corresponding widefield emission images from confocal excitation. Normalized stroboSCAT contrast is represented in grayscale with black (white) representing the most negative (positive) value. The MB positions for the large-domain film are depicted using dashed white lines. The signals do not depend on pump or probe polarization. The scale bar is 1 µm and applies to all panels in (a). Peak carrier density is 1.5×10^{18} cm^{-3}. The probe at 635 nm is above the bandgap of $MAPbI_3$ but away from the band edge (760 nm) where the largest photoinduced absorption change occurs. **(c)** Spectrally resolved interferometric signal near the $MAPbI_3$ band edge using the same excitation conditions but probing using broadband white light, showing a phase-flipped signal at MBs compared to the signal within domains.

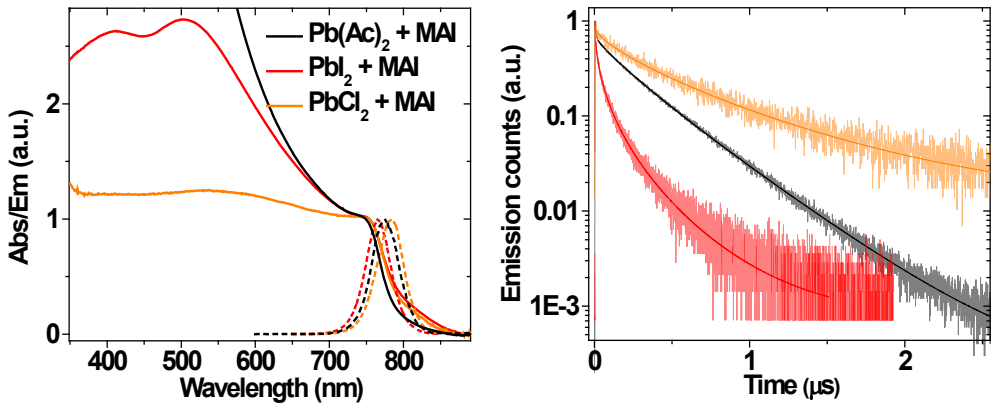

Figure 3.11: Absorption and emission spectra for $MAPbI_3$ films prepared from $Pb(Ac)_2$ (black), PbI_2 (red) and $PbCl_2$ (orange) precursors. **(left)** The absorption spectra are baselined by subtracting the transmission changes due to scattering and reflectance to facilitate comparison between films. **(right)** Emission spectra and lifetimes are measured using 470 nm excitation at ~ 0.1 µJ/cm^2 on a FluoTime 300 instrument (PicoQuant). The curves overlaid on emission decay traces correspond to stretched exponential tail fits $A \times \exp(-t/\tau)^\beta$ with parameters $\tau = 276, 24, 379$ ns and $\beta = 0.88, 0.48, 0.74$ for films made from $Pb(Ac)_2$, PbI_2 and $PbCl_2$ precursors, respectively.

stroboSCAT contrast is strongly negative for carriers located within ~30 nm of the interface and weakly positive for carriers located at depths of ~50 ± 20 nm (**Section 3.3.3**). Thus, the localized regions of positive contrast in these films indicate that, at MBs, the density of carriers at depths around 50 nm is significantly larger than the density within 30 nm of the surface. This observation suggests that when a carrier encounters a MB near the surface of the film, the path of least resistance leads deeper into the film rather than across the feature, resulting in a very low density of surface carriers at MBs. In contrast, subsurface carriers appear to cross MBs almost unimpeded. Our findings provide important mechanistic insight as to why conductive AFM on $MAPbI_3$ films indicates infinite MB resistance at the film surface but carriers still somehow migrate to adjacent domains [251].

3.3.2 *In situ* spectral interferometry on $MAPbI_3(Cl)$ films

We corroborate our interpretation of the contrast flips using spectral interferometry (**Section 2.5.5**): using near-diffraction-limited pump and probe beams, we measure the pump-induced spectral changes around the band edge of $MAPbI_3$ in diffraction-limited volumes that allow distinguishing intradomain vs. MB signals. **Figure 3.10c** shows representative spectral response profiles within a domain (black trace) versus at a boundary (grey trace) at $t = 0$

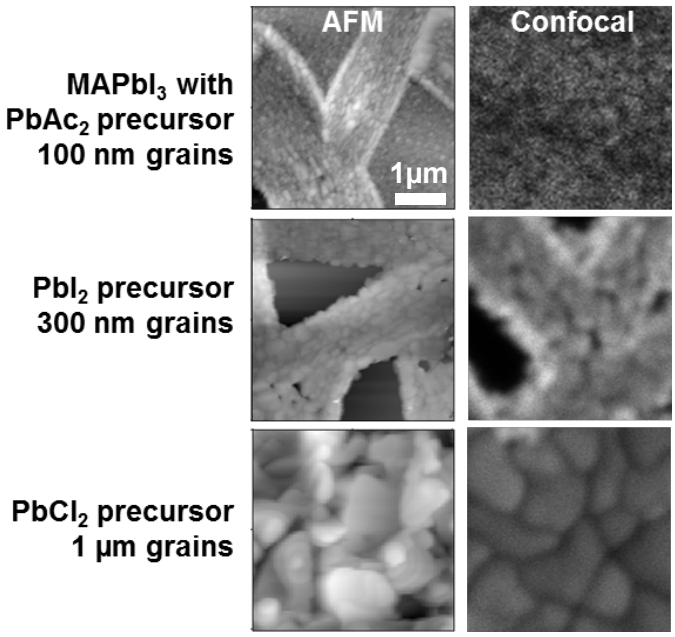

Figure 3.12: Example AFM and confocal images for all three $MAPbI_3$ films studied. Images are not correlated to the same sample areas studied in **Figure 3.10a**.

for the large-domain $MAPbI_3$(Cl) film. Previous spectral interferometry studies on single quantum dots or molecules showed that, depending on the depth of the object with respect to the reflective interface, the band edge spectral profile shows distinctive features with positive, negative or dispersive line shapes [211–213]. Similarly, the transient reflectance spectral response at the band edge of $MAPbI_3$ should show such distinct features if the photoinduced changes emanate from surface vs. subsurface free carriers. The dispersive line shape that we observe within the domain corresponds closely to that reported in the literature from bulk transient reflectance spectroscopy of $MAPbI_3$ single crystals [174]. In contrast, the response from MBs occurs at the same spectral position but is inverted, indicating a $\sim \pi$ phase shift of the signal at the MB relative to within the domain. The conserved spectral position shows that the primary difference between the intradomain and MB response is the phase, not the presence of another excited state species or the chemical composition at the MB.

Additional datasets (**Figures 3.13** and **3.14**) show that intradomain signals always show the same dispersive line shape, and that phase shifts between $\pi/2$ and π always occur at MBs. This trend, which persists across $\sim$50 measured regions, confirms that charge carriers cross MBs only below the film surface in our samples. **Figure 3.13** shows representative spectral interferometry data from within $MAPbI_3$(Cl) domains vs. at MBs. The spectral response at MBs (red traces) occurs at the same spectral positions as in domains but is inverted.

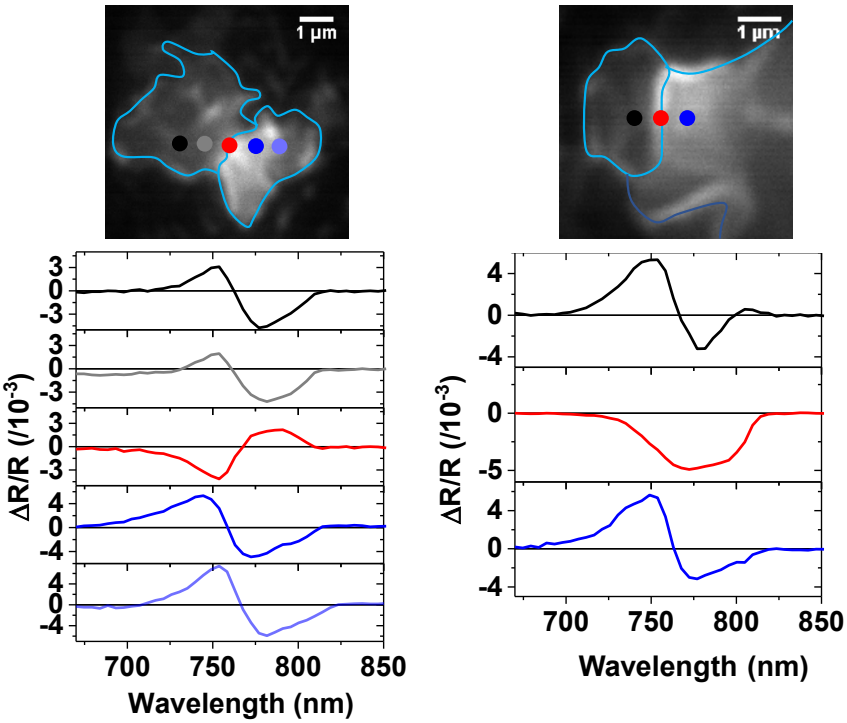

Figure 3.13: Spectral interferometry of intradomain vs. MB photoinduced signals in a $MAPbI_3(Cl)$ film at a pump-probe time delay of ∼0 ns. The images at the top are widefield emission images indicating the domains and boundaries being probed. The colored dots represent the overlapped pump and probe positions, with corresponding spectral profiles displayed below for each of these positions. Approximately 80% of measured MBs show dispersive line shapes like that found in the left panel, while the rest display line shapes between dispersive and negative, like that shown in the right panel.

The exact spectral profile at the MB can vary somewhat from MB to MB, though it always displays a phase shift with respect to the intradomain signal. Out of ∼50 MBs we measured in two different films, ∼40 of the spectra at MBs possess an inverted dispersive line shape like the red trace shown in the left panel of **Figure 3.13**; others exhibit line shapes that are halfway between negative and dispersive (**Figure 3.13** right panel, red trace), indicating phase shifts between $\pi/2$ and π. These different MB profiles suggest that each MB has slightly different depth-dependent resistive properties, but that all MBs appear to be highly resistive at the film surface, one of the key scientific findings of our work. We also note that the small probe volumes employed here allow us to confirm that our interpretation of stroboSCAT results (which employ a widefield probe) is not compromised by interference effects arising from a more complex point spread function (PSF) (i.e., from scatterers at different locations).

The pump and probe spots can also be displaced with respect to one another to follow

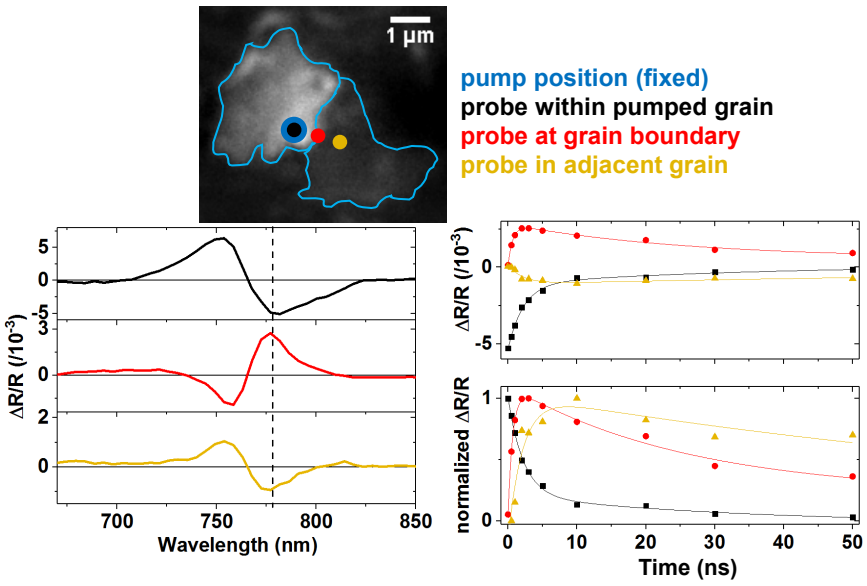

Figure 3.14: Spectral and temporal dependence of the transient scattering signal in a $MAPbI_3(Cl)$ film for three probe positions: one overlapped with the pump within a domain (black), one away from the pump in an adjacent domain (gold), and one at the domain boundary separating the two domains (red). The kinetic traces shown are taken at the spectral position indicated by the dashed line in the bottom left panel. The widefield emission image at the top indicates the domains and boundary being probed.

the migration of carriers from one domain to another through a MB. **Figure 3.14** displays the spectral and temporal dependence of the signal for three probe positions: one spatially overlapped with the pump (position represented by the blue dot) within a domain (black), one away from the pump in an adjacent domain (gold), and one at the domain boundary separating the two domains (red). The spectral phase within the two domains is identical, but the signature spectral phase flip is again observed at the MB, confirming that the transport pathway between the two domains is below the MB surface. The temporal dependence of the signal follows the expected kinetic behavior: the arrival time of the signal (i.e., the carriers) is delayed at the MB (red) and even further delayed in the adjacent domain (yellow), confirming that a significant population of carriers from the pumped domain does cross through the MB into the adjacent domain, but is somewhat slowed down by the MB. The recovery of the original intradomain phase once carriers cross into the adjacent domain indicates that carriers rapidly diffuse in 3D once away from the MB. Overall, by relating these phase-sensitive spectrotemporal data at key specific locations to what we have observed in spatiotemporal stroboSCAT, we not only confirm our original interpretation that transport through MBs occurs through sub-surface pathways, but also rule out potential artifacts in both spectral interferometry and stroboSCAT that could arise due to strong pump scattering off of the MB (avoided here because the pump is spatially separated from the MB), probe interference

effects from back-surface reflections (avoided here because our probe is tightly focused on the front surface of the film), or spectral changes as carriers transport through the material that could give rise to fluke signals at our original probe wavelength of 635 nm.

3.3.3 Simulations of depth-dependent carrier diffusion in $MAPbI_3(Cl)$ films using the finite element method

We characterize depth-dependent MB resistivities by time-propagating finite element simulations of carrier diffusion in heterogeneous $MAPbI_3(Cl)$ films with a simple model implemented in the MATLAB PDE toolbox (**Figure 3.15**). The simulations quantitatively reproduce the observed diffusion behavior and associated stroboSCAT contrast (**Figure 3.15a**). The parabolic diffusion equation is solved in a heterogeneous environment consisting of domains separated by abrupt domain boundaries. We simulate the carrier distribution evolution in a 2D $x-z$ (lateral-axial) film slice following an initial localized excitation (**Figure 3.15b**). To obtain reasonable agreement with experiments, the MBs must be parametrized by resistivities that are infinite at the film surface, concurring with results from AFM experiments [251], but that rapidly drop as a function of depth, approaching nearly intradomain resistivity within ∼50 nm of the film surface (**Figure 3.16a**).

Simulation parameters and assumptions

To carry out the finite element simulations, the $MAPbI_3(Cl)$ film thickness is 300 nm as measured by AFM. MBs are assumed to lie approximately perpendicular to the substrate plane. The films are assumed to be 1 domain thick (i.e., no MBs parallel to the substrate plane), as illustrated in **Figure 3.15b**. These assumptions are reasonable based on cross-sectional SEM measurements taken on $MAPbI_3(Cl)$ films prepared using the same protocol [256]. The MBs are simulated as 200 nm thick. We choose 200 nm based on confocal fluorescence microscopy measurements that show occasionally completely dark MBs even though the image is convolved with a ∼200-300 nm PSF, implying that the effect of MBs is felt over a >150 nm region despite the fact that they may be far thinner. For simulations with correlated structural measurements (**Figures 3.17** and **3.18**), slight adjustments to the MB thickness are made in the simulation if they are determined to be larger than the diffraction limit in the confocal measurement. Since simulations are performed in the $x-z$ plane, MBs that are not perfectly in the $y-z$ plane are also simulated with larger thicknesses. Von Neumann boundary conditions are assumed at all film edges, though the proportion of carriers reaching the lateral edges are negligible over the simulation time. Interparticle interactions are ignored, supported by the fluence-dependent measurements shown in **Section 3.3.4**. A first-order rate constant for recombination is included (see below). The starting condition is an injected carrier density profile from the pump with a FWHM of 306 nm and exponentially decaying as a function of depth with a $1/e$ penetration depth of 60 nm.

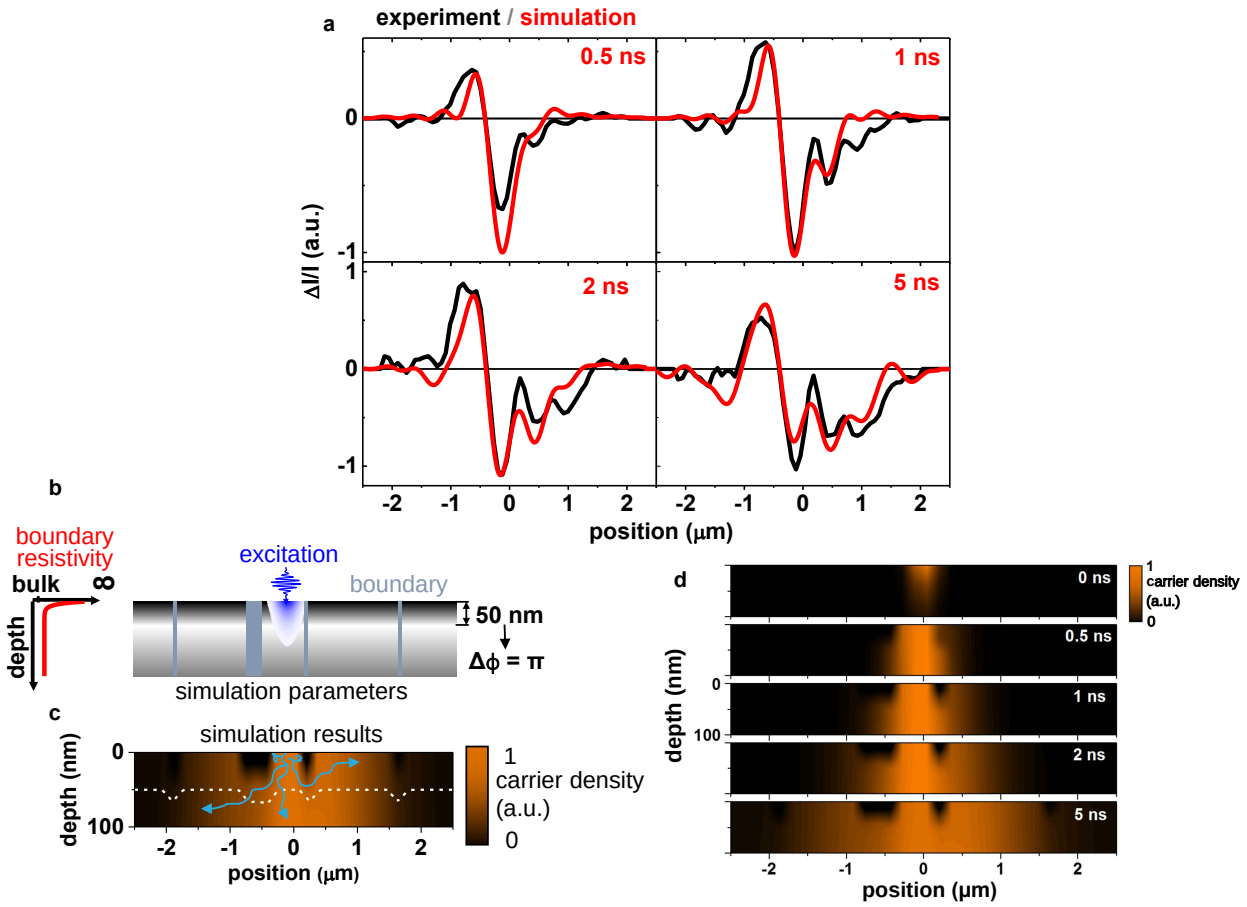

Figure 3.15: Finite element simulations in a polycrystalline $MAPbI_3(Cl)$ film. **(a)** Quantitative agreement of experimental stroboSCAT data with simulation results after the simulation results have undergone appropriate contrast scaling and convolution with the apparatus' PSF. **(b)** A sketch of a film cross-section used in simulations in which MB positions were derived by comparing the simulations in (a) to the phase-sensitive stroboSCAT images for the $PbCl_2$ precursor film in **Figure 3.10a**. Grayscale shading represents the depth-dependent contrast expected from stroboSCAT measurements in $MAPbI_3(Cl)$, resulting from an interferometric phase change of $\Delta\phi = \pi$ for scatterers located at a depth of 50 nm (**Figure 3.16c**). **(c)** Results of simulations using time-propagated finite element analysis of carrier migration along the line cut indicated by the horizontal red line in **Figure 3.10a**, displaying the carrier distribution (orange shading) of the film 5 ns after excitation. The dashed white trace is the average axial position of the carrier distribution. The light-blue traces are hypothetical carrier trajectories that are consistent with the observed carrier distributions. **(d)** Calculated carrier distributions for other time delays. The simulations use a 300 nm thick film, as measured by AFM; only the top 100 nm is displayed here, which is more representative of the actual probing depth in our experiments.

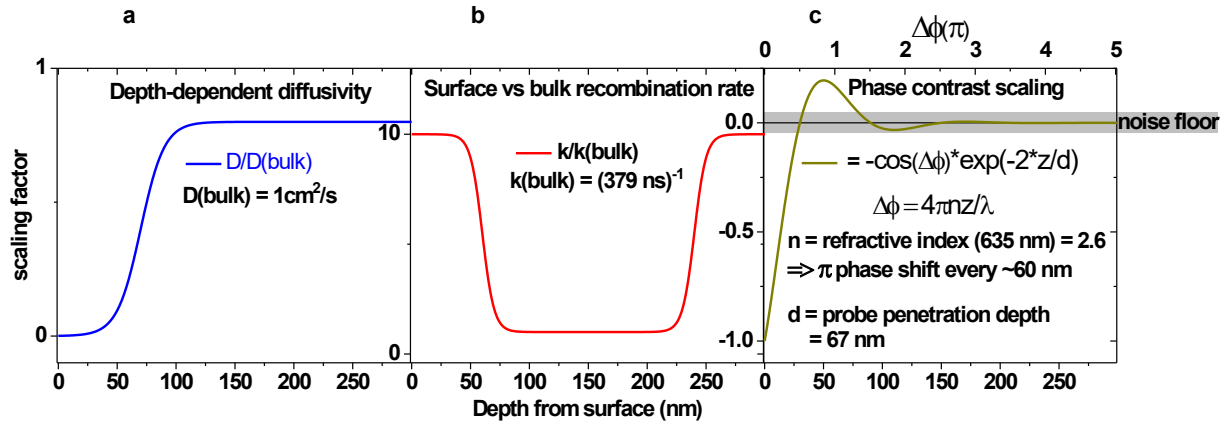

Figure 3.16: Depth-dependent simulation parameters: diffusivity **(a)**, recombination rate **(b)**, and contrast scaling for a probe wavelength of 635 nm in $MAPbI_3(Cl)$ due to interferometric phase sensitivity **(c)**. The noise floor for the modeled experiments is indicated by the grey box in (c).

The key simulation parameters are shown in **Figure 3.16**. First, the MBs are assumed to have depth-dependent resistive properties. This assumption is based on conductive-probe AFM measurements that show that the surface of MBs in $MAPbI_3$ films are infinitely resistive, but that carriers do cross domain boundaries, leading the authors to postulate that the resistivity of MBs decreases as a function of depth [251]. While the depth-dependent resistive profiles can adopt many forms, and may be MB-dependent and film-dependent, we adopt the simple form shown in **Figure 3.16a**: an infinitely-resistive surface as previously measured using AFM, with a rapid drop-off to a value similar to the bulk resistivity. Note that the value that is varied in the simulations is the diffusion coefficient, related to resistivity, ρ, through the Einstein equation, $D = kT/(q^2 N\rho)$, for charge q and charge number density N. The simulations qualitatively reproduce the data over a wide range of drop-off rate and final value for the diffusivity, but the onset of the drop-off is well-constrained: carriers need to pass through the MB in the region of 40-80 nm below the surface to reproduce the signals we observe. Importantly, including depth-dependent resistive profiles at MBs is crucial to reproducing stroboSCAT data for every simulated dataset – the phase flips cannot be reproduced with any other parameters described herein, and, as mentioned earlier, we have never observed phase flips due to changes in the carrier density in these materials over 4 orders of magnitude in pump fluence.

Second, the recombination rate at the top and bottom surface of the films is assumed to be 10 times larger than in the bulk, based on multiple studies showing that surface recombination dictates carrier lifetimes in $MAPbI_3$ perovskites [174, 259]. The recombination rate profile shown in **Figure 3.16b** is determined based on the knowledge that surface contributions dominate photoluminescence decay with 400 nm excitation (∼40-60 nm pene-

tration depth) [259]. The simulation reproduces the experimental results over a wide range of parameters for the recombination rate profile vs. depth.

Finally, after simulating carrier diffusion, the stroboSCAT contrast is reproduced by applying an exponentially-modified contrast scaling term based on the phase sensitivity of iSCAT (**Section 2.4**): $-\cos(\Delta\phi) \times e^{(-2z/d)}$ where $\Delta\phi = 4\pi nz/\lambda$ is the depth-dependent phase, z is the height above the substrate-sample interface ($z = 0$), and $d = 1/a$ is the probe penetration depth for absorption coefficient a (**Figure 3.16c**). A π phase shift, which occurs every $\lambda/4n \approx 60$ nm, corresponds to a contrast flip from negative to positive when the population distribution shifts to being centered around a depth of $d \gtrsim 50$ nm above the substrate-sample interface. To account for the finite probe penetration depth of $d = 67$ nm, and the fact that probe photons that reach the detector upon scattering at a sample depth z pass through $2z$ of the material and may also be absorbed, we attenuate the simulated incident probe light using a damped cosine function. The negative sign accounts for the fact that the phase at the surface is $-\pi$ due to the Gouy phase (**Section 2.4**). Finally, once this scaling is applied, the contrast is integrated across the depth of the film to simulate the stroboSCAT signal, which is then convolved with the probe PSF (**Section 2.5.4**).

The resulting carrier distributions of the simulation are shown in **Figure 3.15**. The dashed white trace in **Figure 3.15c** represents the average axial position of the carrier distribution, indicating how the carrier density peaks further beneath the surface at the MBs. **Figure 3.15a** plots the resulting traces for four time delays, showing excellent agreement for these data and for additional structurally correlated datasets shown in **Figure 3.18**. The combination of experiments and simulations thus enables a semi-quantitative description of the 3D evolution of carrier distributions in these films: MBs act as impassable walls at the film surface, removing a lateral transport pathway for surface carriers. Carriers at depths below ~50 nm, however, cross almost unhindered into neighboring domains. Within domains, unimpeded 3D migration quickly leads to uniform carrier distributions. Since stroboSCAT is most sensitive to carriers located near the surface where the contrast is negative (**Figure 3.16c**), we clearly distinguish domains (negative contrast) from MBs (positive contrast). This unique axial sensitivity afforded by phase contrast therefore provides a comprehensive 3D picture of both the morphological and functional properties of these materials.

MB mapping to confirm stroboSCAT contrast flips at MBs

To confirm that tracking carriers in 3D using stroboSCAT provides structural information, we undertook correlated measurements on a well-defined region in a $MAPbI_3(Cl)$ film with domains that are clearly visible and separated in confocal emission microscopy images collected with an Olympus IX83 microscope (**Figure 3.17a**). The MB features are on the order of the diffraction limit or smaller, therefore they are not resolved in the ground state iSCAT image (**Figure 3.18b**). Correlative measurements between the two microscopes are enabled by scratching a fiducial marker into the film. The use of an optical method (rather than AFM or SEM) for structural correlation is necessary, as the films need to be imaged at the same face as the probe is incident, i.e., through the sample substrate, and in oxygen- and

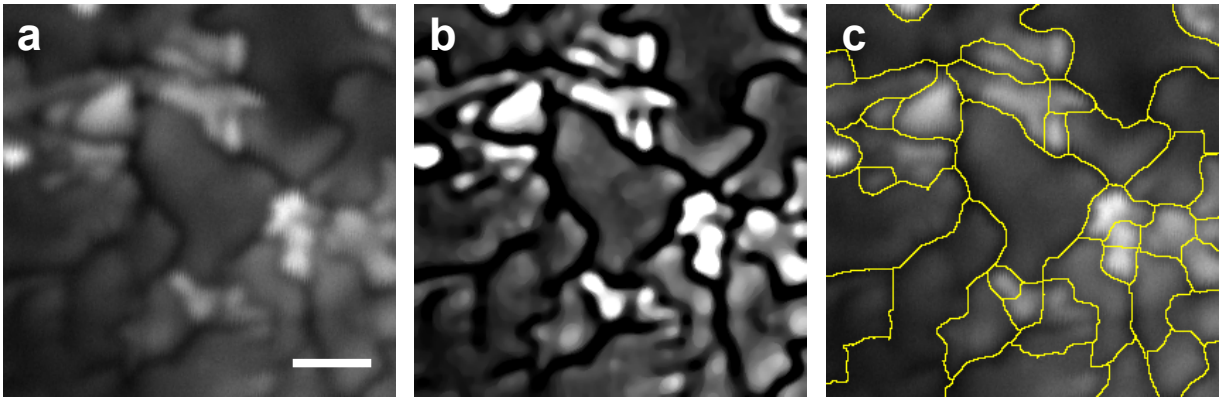

Figure 3.17: Region in a $MAPbI_3(Cl)$ film used for structurally-correlated stroboSCAT measurements. **(a)** Scanning-beam confocal fluorescence image. **(b)** Pre-processed image used as the input for watershed segmentation. **(c)** Resulting watershed boundaries (yellow) overlaid onto the raw confocal image in (a). Scale bar is 1 µm.

moisture-free conditions. Domain boundaries in these films are dark in confocal emission microscopy, as has been previously observed [247]. Surface cracks would not give rise to large contrast changes in confocal emission unless they extend to depths comparable to or greater than the microscope's depth of field, ∼150-200 nm. We use a watershed algorithm in ImageJ [260, 261] to delimit the location of MBs. A watershed algorithm is commonly called a "segmentation" image processing method because it treats grayscale pixel intensities like a topographic map, dividing the image into a series of catchment basins separated by watershed lines by gradually "flooding" the image "surface" starting from local extrema [262–264]. It provides a reproducible and systematic way to draw boundaries in an image. We found the ImageJ plugin "Interactive H Watershed" [265] worked best, after the following pre-processing procedure in ImageJ. First, the image is blurred with a median blur filter ($r = 3$), then an unsharp mask is applied to enhance the edges ($r = 4, \text{weight} = 0.9$), then another median blur filter is applied ($r = 3$). This procedure enhances the dark MB features so the watershed process is not misguided by noise. The result is show in **Figure 3.17b** after starting with the raw confocal image acquired in **Figure 3.17a**. Next, to run the watershed algorithm on the pre-processed image in **Figure 3.17b**, a few parameters must be defined. The **Intensity Threshold** parameter is set to zero so that the "flooding" stops when the entire image is covered. For the same reason, the **Peak Flooding** parameter is set to 100%. The **Seed Dynamics** parameter may be tuned to change the initial number of local maxima from which to propagate the watershed segmentation, which ultimately determines how segmented the final image is. A higher (lower) value selects fewer (more) local maxima which tend to be more (less) robust to noise. For the result shown in **Figure 3.17c**, a seed parameter of 1015 was used.

For fluorescent samples with larger domain features, such as in the film in **Figures**

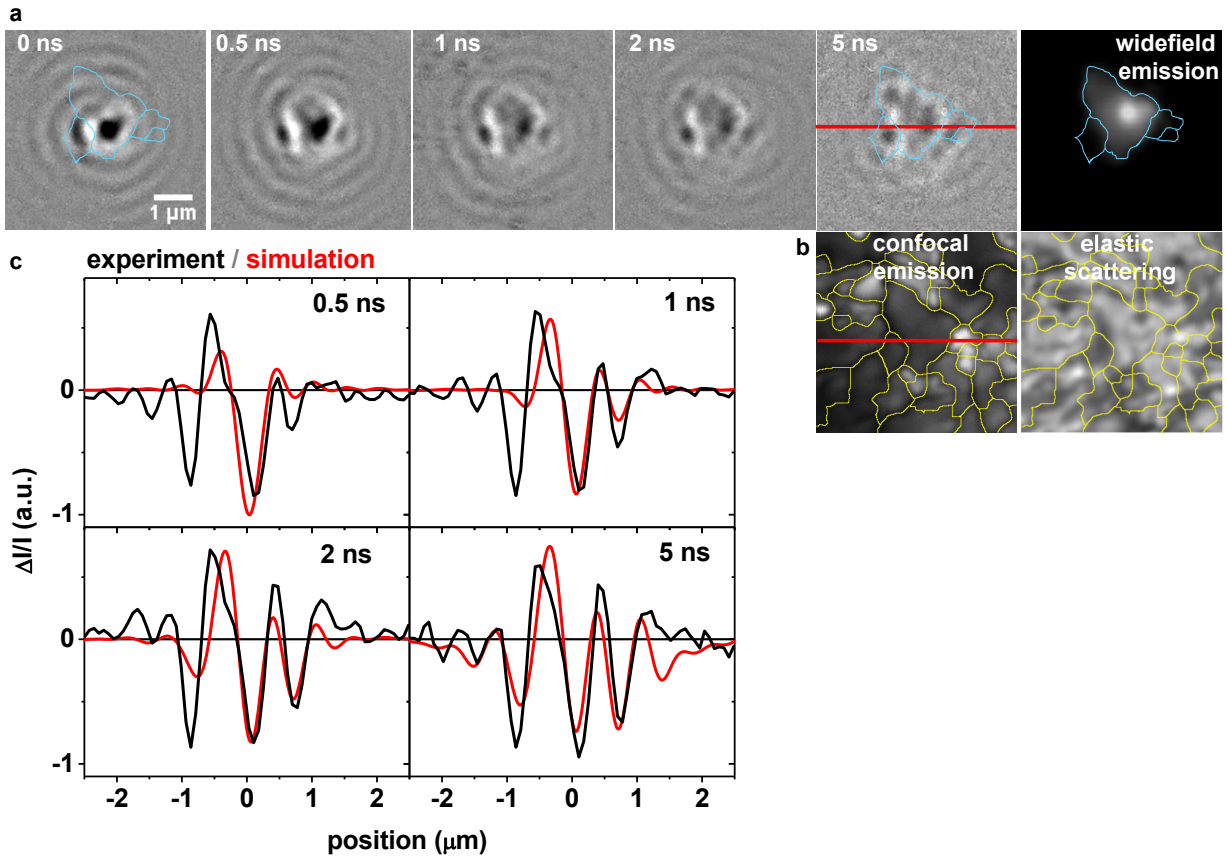

Figure 3.18: Structurally-correlated stroboSCAT-confocal fluorescence measurements in a $MAPbI_3(Cl)$ film. **(a)** stroboSCAT time series with correlated widefield emission from confocal excitation. The overlaid cyan curves show the 4 most relevant domains taken from **Figure 3.17c**. **(b)** Correlated scanning-beam confocal fluorescence and elastic scattering at 635 nm. **(c)** Experimental and simulated stroboSCAT data for different time delays through the line cut indicated by the horizontal red line in (a) and (b). The simulations use the MB positions through the line determined from the confocal image in (b).

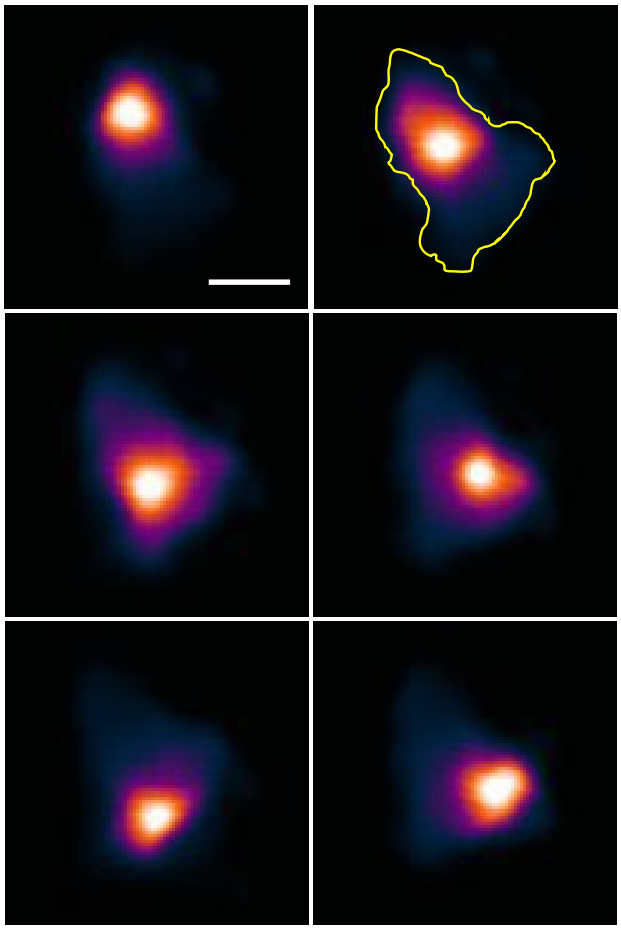

Figure 3.19: Widefield fluorescent images collected in the stroboSCAT microscope with an EMCCD following confocal excitation at different spots within the same domain. In principle, large domains and the MBs that define them could be mapped out by overlapping such images. The overlaid yellow curve shows the largest domain taken from **Figure 3.17c**. Scale bar is 1 µm.

3.17 and **3.18**, it might be possible to map out polycrystalline domains in the stroboSCAT microscope instead. After collecting multiple widefield emission images following confocal excitation at different spots in the domain (**Figure 3.19**) and overlaying the resulting images, MBs may be delineated. This requires a simple change in the detection path to direct the reflected fluorescence to an EMCCD camera and the addition of a filter to block the pump light (**Figure 2.26**). In the future, this might obviate the need for correlative measurements across different instruments.

Although most of the literature refers to MBs as grain boundaries, confocal emission microscopy or AFM in principle do not provide direct proof that the observed features are indeed grain boundaries, which would require a microstructural crystalline-phase sensitive

technique like electron backscattering diffraction (EBSD). **Figure 3.18a** shows the corresponding stroboSCAT data when exciting the large central domain. By overlaying the MB positions determined from confocal microscopy (**Figure 3.18b**) on the 0 ns and 5 ns frames, it is clear that the light contrast in stroboSCAT arises at the MB locations and dark contrast arises within domains, clearly delineating the structure of these polycrystalline films. These deductions are confirmed with the finite element diffusion simulations shown in **Figure 3.18c** and **Figure 3.15a**, which reproduce the signal almost quantitatively despite using a relatively simple model. In the simulations shown in **Figure 3.18c**, the positions of the MBs are constrained to those determined in confocal microscopy.

3.3.4 Spatial and temporal carrier transport heterogeneity in polycrystalline $MAPbI_3(Cl)$ films

By measuring multiple regions and different films, we reveal that each MB has its own conductivity profile, leading to interdomain energy carrier flow patterns that are highly anisotropic both axially and laterally. Within the same film, both the stroboSCAT time series and widefield emission show vastly different interdomain connectivity patterns at each probed spot (**Figure 3.20**). Trapping times differ too, with some spots exhibiting population expansion up until 5 ns while others display expansion up until 50 ns. While there is generally good correspondence between widefield emission and late-time stroboSCAT images, some differences can arise if electron and hole transport are substantially different, for example due to preferential trapping of one species at MBs, since excess free carriers of one species will not give rise to photoluminescence, but will still change the polarizability of the medium. Within a single large domain, specific intra- and interdomain connectivity patterns determine carrier diffusion pathways. **Figure 3.21** shows a stroboSCAT time series and widefield emission emission when pumping at two slightly offset spots in the same region of a large-domain $MAPbI_3(Cl)$ film. The final carrier population distribution and contrast flips correspond almost perfectly, confirming that fast intradomain transport and preferential interdomain connectivities across depth- and lateral-dependent paths of least resistance through MBs define overall carrier transport pathways. Note that even though carriers can cross MBs more readily below the film surface, MBs still act as bottlenecks to carrier transport due to their average resistivities being higher than intradomain resistivities. Note also that some MBs clearly possess larger average resistivities than others, acting as more effective bottlenecks to carrier transport.

We confirm that our measurements are performed within a linear excitation regime by examining widefield photoluminescence profiles after excitation with a low, 0.3 $\mu J/cm^2$, and high, 10 $\mu J/cm^2$, pump fluence (**Figure 3.22**). Results show a small, $\sim$10% variation of carrier population distribution on average despite a 30-fold reduction in peak fluence. Lower excitation powers display slightly broader distribution profiles, likely an indication that slightly fewer carrier-carrier scattering events impede diffusion at early times in the low-fluence measurements. The small deviation confirms that high-order recombination terms

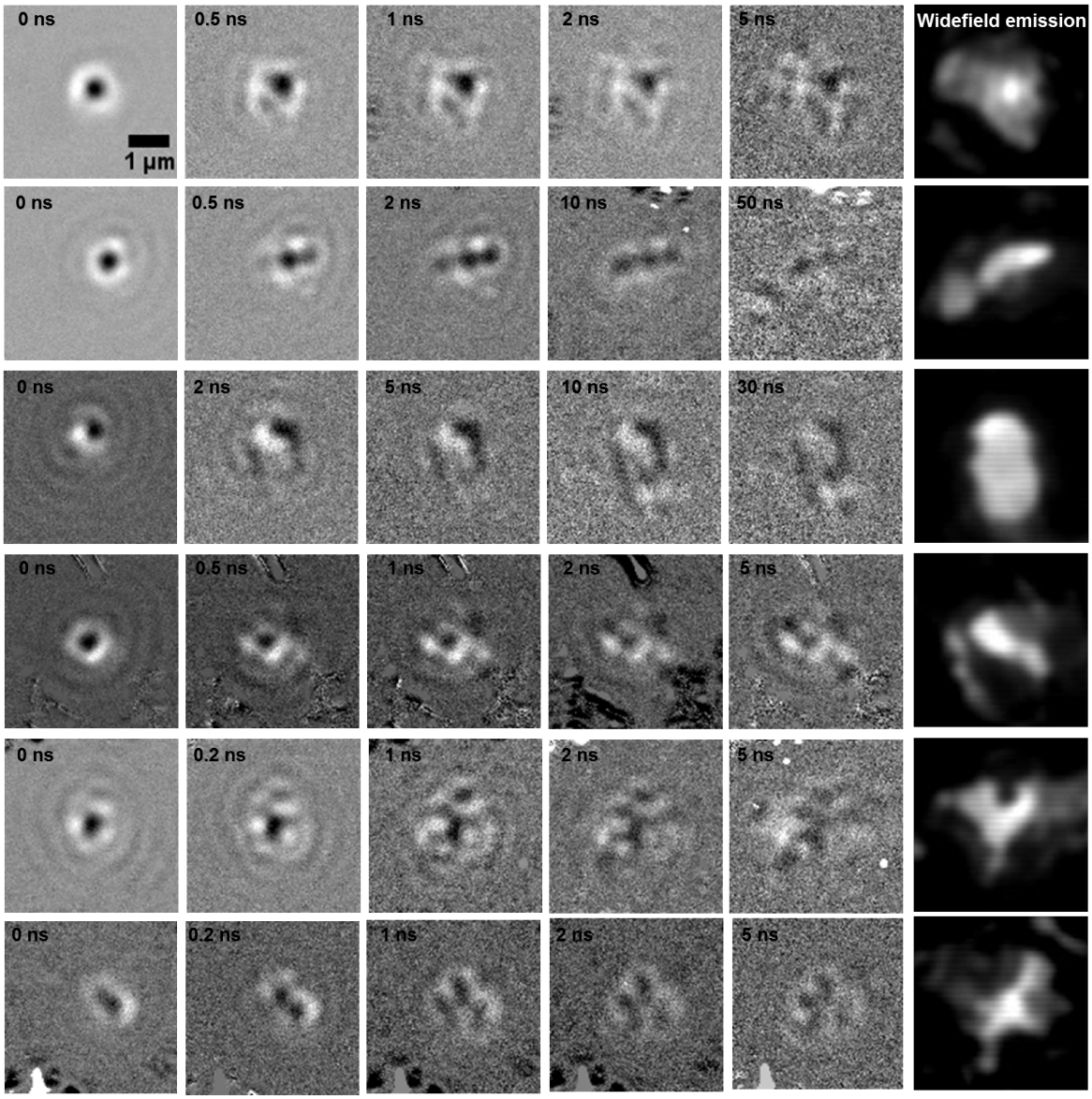

Figure 3.20: Illustration of spot-to-spot heterogeneity within a single film of $MAPbI_3$ made with $PbCl_2$ precursor. All excitation fluences are 10 µJ/cm^2 ($n_0 \approx 1.5 \times 10^{18}$ cm^{-3}) [266].

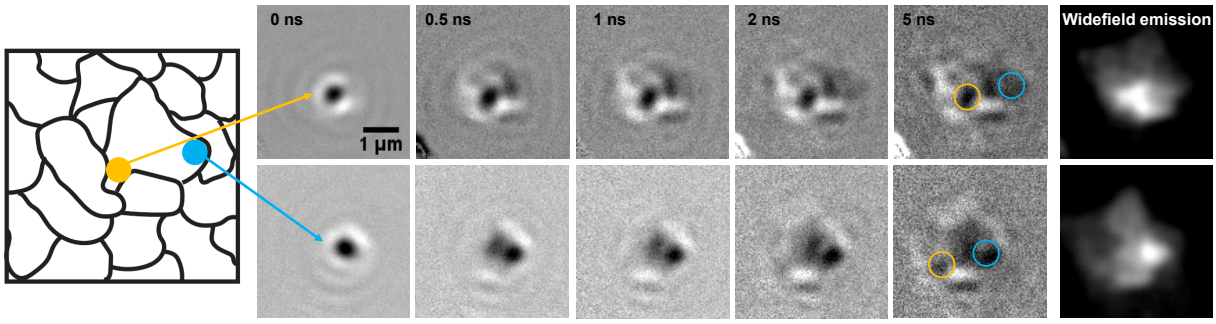

Figure 3.21: Intra- and interdomain connectivity patterns in a large-domain $MAPbI_3(Cl)$ film determines carrier diffusion pathways. The gold and blue circles show where the initial distribution of free carriers are injected. The same circles are overlaid on the 5 ns images to allow spatially correlating the two images.

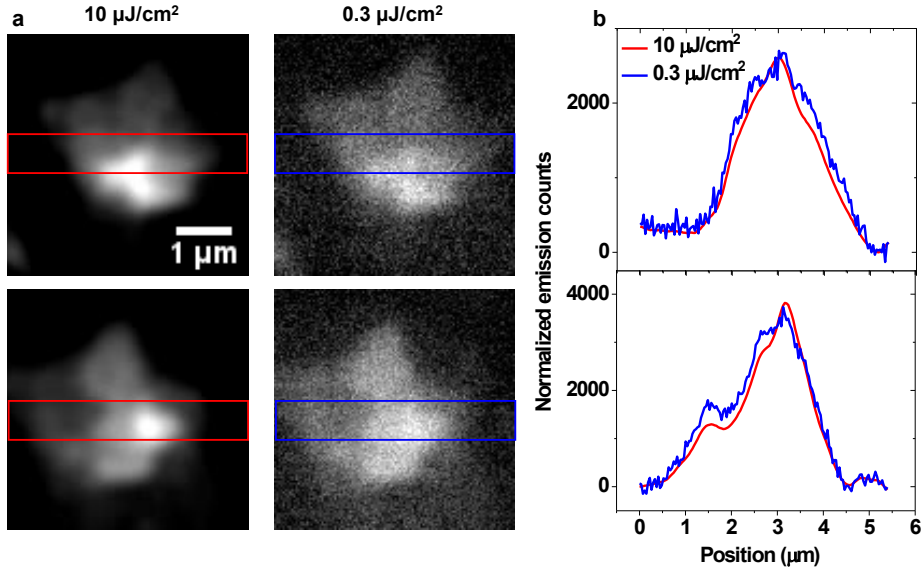

Figure 3.22: Pump-power-dependent widefield photoluminescence profiles in a $MAPbI_3(Cl)$ film, excited at the same spots from **Figure 3.21**. Red and blue curves in **(b)** correspond to fluence-normalized, integrated photoluminescence intensity profiles delimited by the rectangles in **(a)**.

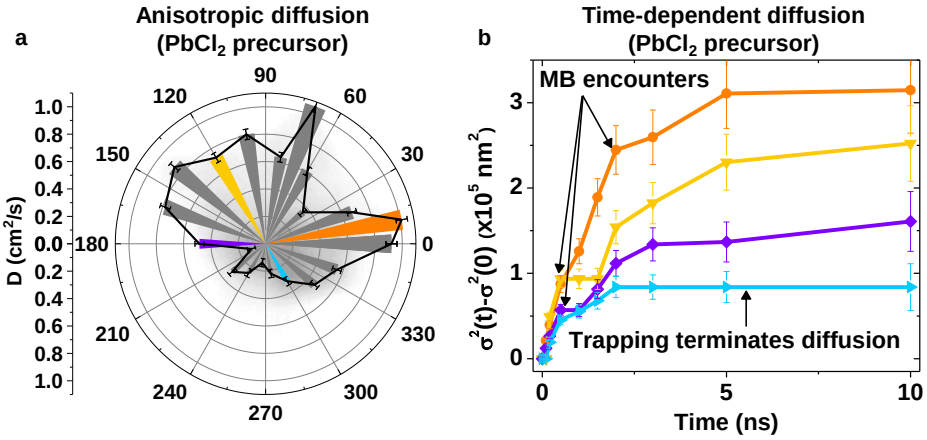

Figure 3.23: Quantifying spatial and temporal carrier transport heterogeneity in polycrystalline $MAPbI_3(Cl)$. **(a)** Angle-dependent diffusivities averaged over the first 2 ns for the $PbCl_2$ precursor data shown in **Figure 3.10a**. **(b)** Time-dependent diffusion for four representative azimuthal angles color-coded in panel (a). Error bars represent the standard deviation of the fits to several experimental datasets taken at the same location in the films. Curves represent a spline interpolation of the data points. Further analyses for films prepared from different precursors are presented in **Figure 3.24**.

do not contribute substantially to the stroboSCAT measurements at the fluences used, and thus that the measurements are performed within a linear excitation regime.

To generalize our findings, we systematically quantify the degree of functional heterogeneity in these samples with further analyses. **Figure 3.23a** plots the initial angle-resolved charge carrier lateral diffusivity for $MAPbI_3(Cl)$, which ranges from 0.1 cm^2/s to 1.1 cm^2/s. The time dependence of lateral carrier motion along each of the four color-coded directions in **Figure 3.23a** is depicted in **Figure 3.23b**. Although intradomain transport both before and after passing through a MB can be as high as 1.3 cm^2/s, the terraces between the higher-slope portions of the curves observed in the time dependence in **Figure 3.23b** illustrate how MB encounters seem to temporarily halt lateral energy flow. The final plateau in population expansion occurs within several nanoseconds, indicating that a large fraction of carriers stop migrating on time scales much shorter than the average carrier recombination time (379 ns, **Figure 3.11**). This termination indicates that at these fluences the carrier density decreases on a few-nanosecond time scale to below the material's trap-state density. Furthermore, it suggests that some traps do not act as recombination centers but may instead be hole- and/or electron-selective. This analysis emphasizes the importance of tracking carriers until diffusion terminates rather than extrapolating from the early-time constant diffusion through to the carrier lifetimes, which would falsely imply an average diffusion length in this sample of $\sim$ 10 µm instead of $\sim$ 1 µm. We perform similar measurements across $MAPbI_3$ films prepared with $Pb(Ac)_2$ and PbI_2 precursors and analyze the mean squared

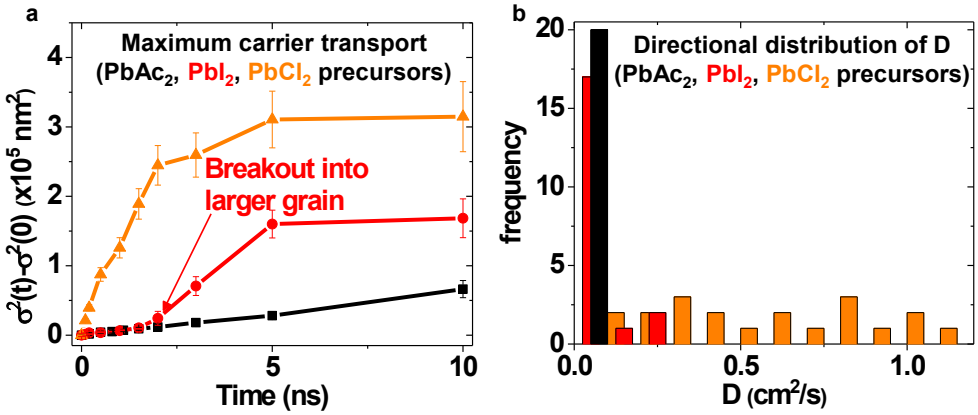

Figure 3.24: **(a)** Population expansion for the fastest azimuthal trajectory for each dataset from **Figure 3.10a**. Error bars represent the standard deviation of the fits to several experimental datasets taken at the same location in the films. **(b)** Distribution of diffusivities over 20 radial trajectories for thin film perovskite samples prepared from three different precursor solutions.

expansion along the fastest azimuthal trajectory for comparison. The evident functional heterogeneity across synthetic routes is shown in **Figure 3.24**. In summary, we show that moving beyond averaged metrics in all spatiotemporal dimensions is essential to answering multiple prominent questions surrounding these materials and to addressing the functional impacts of structural and electronic disorder. For example, we find that in our large-domain $MAPbI_3(Cl)$ films, MBs (in many cases, grain boundaries) do not act as recombination centers and only substantially affect lateral transport for surface carriers, not bulk carriers. For charge extraction in planar photovoltaic architectures, surface carriers are axially extracted and should therefore be minimally affected by MBs that are oriented perpendicular to the charge extraction layers.

3.4 Distinguishing heat from charge in p-doped silicon

The following unpublished stroboSCAT experiments in silicon were performed in collaboration with ***Leo Hamerlynck, Rongfeng Yuan*** *and* ***Stephanie Hart****.*

As each type of energy carrier changes the local material optical polarizability differently, the sign and magnitude of the stroboSCAT contrast can differentiate coexisting types of energy carriers. For example, at certain probe conditions, heat can generate opposite contrast to that of free charge carriers, as we observe in p-doped silicon with a doping density of 7×10^{19} cm^{-3} (**Figure 3.25a**). Here, datasets were collected using a 4 MHz laser repetition rate with

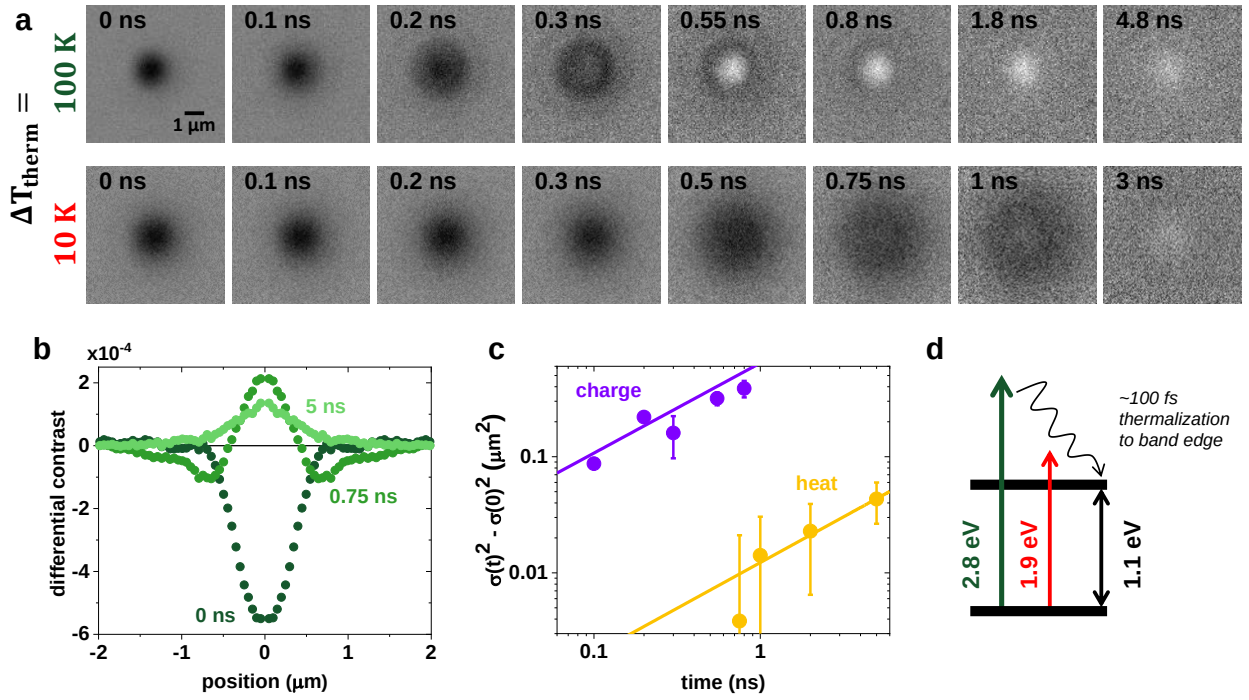

Figure 3.25: **(a)** stroboSCAT time series on a p-doped silicon wafer probed at 1.6 eV following 2.8 eV (top) and 1.9 eV (bottom) excitation, showing decreased heating (positive contrast) in the case where the thermalization energy is lower (bottom). The pump fluences were 1.6 mJ/cm^2 ($n_0 \sim 8.1\times10^{19}$ cm^{-3}) and 2.0 mJ/cm^2 ($n_0 \sim 1.6\times10^{19}$ cm^{-3}), respectively. **(b)** Separation of time scales in the evolution of the positive and negative contrast, with negative contrast dominating at early time delays (darkest green), followed by a stage of coexistence (lighter green), with positive contrast alone observed at late time delays (lightest green). **(c)** Extracted charge and heat dynamics for the top data series in (a), with $D_{\text{charge}} \sim 4$ cm^2/s and $D_{\text{heat}} \sim 0.2$ cm^2/s. **(d)** Energy diagram showing the above-bandgap pump energies (2.8 eV and 1.9 eV) in relation to the indirect bandgap energy (1.1 eV). Both pump and probe are far above the silicon bandgap and distinct from pump-induced absorption changes at the band edge.

the same probe energy (1.6 eV), but carriers were generated in the top row with a 2.8 eV pump (with a fluence of 1.6 mJ/cm^2, $n_0 \sim 8.1 \times 10^{19}$ cm^{-3}) and in the bottom row with a 1.9 eV pump (with a fluence of 2.0 mJ/cm^2, $n_0 \sim 1.6 \times 10^{19}$ cm^{-3}), producing different amounts of heating due to thermalization to the band edge (1.1 eV). Over the rise of the pump-probe temporal overlap, the signal exhibits negative (dark) contrast, which rapidly expands and quickly decays with a $1/e$ time of 0.6 ns. At an intermediate ($\sim 0.3 - 1$ ns) pump-probe time delay, a positive (bright) contrast feature appears in the center, indicating a different species is formed rapidly. After $\sim 2 - 4$ ns, the signal is dominated by positive contrast that decays over tens of ns.

Although there is a region of positive and negative contrast coexistence, the overall separation of time scales in the population dynamics and transport permits distinction between the two types of energy carriers, as seen in the azimuthally-averaged cross-sections plotted in **Figure 3.25b**. By fitting to the sum of two Gaussians when there is overlap and to a single Gaussian when there is not, (i.e., the negative contrast is subsumed by the noise floor), we extract the diffusivities for each species. A negative-amplitude Gaussian expands at a rate of 4 cm^2/s and a positive-amplitude Gaussian expands at a rate of 0.2 cm^2/s (**Figure 3.25c**). The expansion of the positive signal is on the order of previous reports of silicon's temperature-dependent thermal diffusivity [233, 267], and heat and free charge carriers are expected to produce opposite changes to the refractive index of silicon at optical wavelengths, as lattice heating increases the refractive index, while dispersive changes to the refractive index due to absorption are negative above the bandgap [161, 268]. We therefore attribute the negative (dark) contrast to photogenerated electrons and holes and the positive (bright) contrast to heat deposited in the lattice through relaxation of excess energy from above-bandgap excitation as well as electron-electron, electron-hole, and especially electron-phonon scattering that happen most in the center of the carrier distribution, where the carrier density is largest.

The commonly referenced charge carrier diffusivities for silicon are $D_{\text{electrons}} = 39$ cm^2/s and $D_{\text{holes}} = 13$ cm^2/s [232], an order of magnitude faster than what we observe. These values are typically obtained from bulk Hall effect measurements on doped silicon that characterize the drift velocity of the majority carrier by applying electric and magnetic fields that are orthogonal to each other and an applied current. There are several key differences to keep in mind for comparison to our additionally photodoped measurements. First, the incident pump laser pulse generates a bath of electrons and holes that move in a correlated manner on account of electrostatics tending to enforce charge neutrality. Therefore, the relevant dynamical quantity to compare to is the ambipolar diffusion coefficient that represents the net effect of the electron and hole motions when they are co-occurring, weighted by their respective concentrations and transport properties [269–271]:

$$D_{\text{a}} = \frac{kT}{q} \frac{n_e + n_h}{(n_e/\mu_{\text{h}}) + (n_h/\mu_{\text{e}})} = \frac{D_{\text{e}} D_{\text{h}} (n_e + n_h)}{D_{\text{e}} n_e + D_{\text{h}} n_h}, \tag{3.1}$$

where n_e and n_h are the electron and hole concentrations, respectively, μ_{e} and μ_{h} are the electron and hole mobilities, respectively, and D_{e} and D_{h} are the electron and hole diffusivi-

ties, respectively, related to the drift mobility by the Einstein relation [272, 273]. Typically, the variables n_e and n_h in Equation 3.1 represent dopant densities that are correlated to conducting electron and hole densities, however here, we use them to describe both dopant and photoinduced electron and hole densities. In the high carrier injection limit ($> 10^{18}$ cm^{-3}), Equation 3.1 simplifies to:

$$D_{\mathrm{a}} = \frac{2D_{\mathrm{e}}D_{\mathrm{h}}}{D_{\mathrm{e}} + D_{\mathrm{h}}}. \tag{3.2}$$

This expression predicts an ambipolar diffusivity of $D_{\mathrm{a}} = 19$ cm^2/s, which has been confirmed with optical pump-probe measurements [271] but that is still much larger than the diffusivity associated with the expansion we measure for the negative contrast in **Figure 3.25**. There are two additional considerations when comparing transport quantities in silicon: (1) the injected carrier density [270, 274] and (2) the dopant density [275] both increase carrier-carrier scattering, thereby reducing the rate of charge transport. Dopants also introduce carrier-lattice scattering. The photogenerated carrier densities in our measurements ($\sim 10^{20}$ cm^{-3}) are high compared to those in Hall effect measurements, where doping concentrations are orders of magnitude lower (typically $10^{13} - 10^{18}$ cm^{-3}; compare, for example, to intrinsic silicon with 5×10^{22} atoms/cm^3). With all of these additional factors taken into account, the expansion of the negative contrast that we observe is in agreement with other comparable measurements. The stroboSCAT team was stumped with our seemingly low charge carrier diffusivities until **Stephanie Hart** tracked down these important considerations and contextualized them within our experiments [274, 276]. Ongoing efforts on the stroboSCAT team aim to further characterize these impurity- and carrier-density-dependent scattering effects in p-doped, n-doped and intrinsic silicon, and with sub-ps time resolution in order to benchmark stroboSCAT's ability to mechanistically characterize these different scattering processes and how they affect transport more generally.

To bolster our contrast assignments and benchmark the temperature sensitivity of the setup, we decrease the overall temperature elevation in the silicon following photoexcitation by lowering the pump photon energy (**Figure 3.25a,d**), keeping the probe energy (1.6 eV) and measurement averaging the same. Within the pump-probe pulse overlap, the hot electrons relax to the band edge, transferring their excess energy to the lattice. This fast thermalization process increases the local sample temperature in proportion to the above-bandgap excitation and photogenerated carrier density. Using a calorimetry calculation (**Appendix B.2** with $a(2.8\ \mathrm{eV}) = 3.11 \times 10^4\ \mathrm{cm}^{-1}$ and $a(1.9\ \mathrm{eV}) = 3.04 \times 10^3\ \mathrm{cm}^{-1}$ from [277]), we estimate that the temperature increases from bandgap thermalization, $\Delta T_{\mathrm{therm}}$, are 100 K and 10 K using a 2.8 eV pump ($n_{\mathrm{peak}} = 6.0 \times 10^{20}\ \mathrm{cm}^{-3}$) and 1.9 eV pump ($n_{\mathrm{peak}} = 1.2 \times 10^{20}\ \mathrm{cm}^{-3}$), respectively. Due to silicon's high refractive index, 20-30% of the incident light is reflected at the index mismatch between the glass substrate and the silicon wafer surface and must be accounted for in this calculation. Additionally, the spot size of the pump on the sample is wavelength-dependent and must be accurately included. The higher temperature in the $\Delta T_{\mathrm{therm}} = 100$ K case clearly generates more positive contrast or heat (**Figure 3.25a**, top row) as compared to the lower temperature $\Delta T_{\mathrm{therm}} = 10$ K measurement (**Figure**

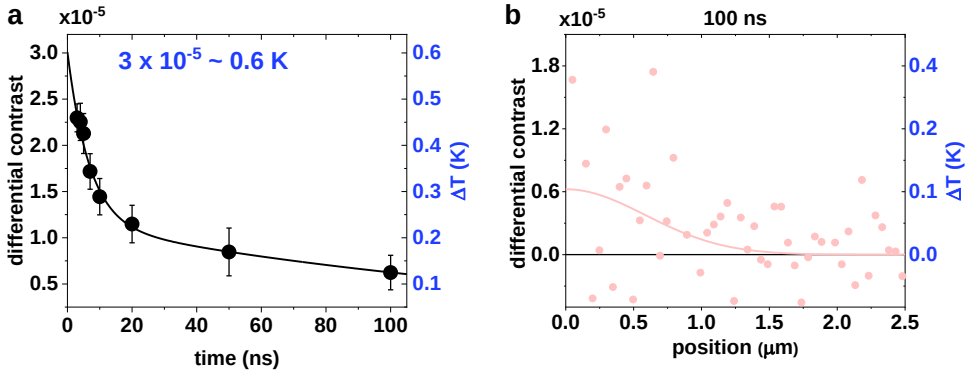

Figure 3.26: Temperature calibration and sensitivity in silicon with 1.9 eV pump excitation ($\Delta T_{\text{therm}} = 0.6$ K, $n_{\text{peak}} = 5.5 \times 10^{18}$ cm^{-3}). **(a)** Amplitude decay from fits to single positive Gaussians. The vertical intercept of the fit yields the conversion factor from differential heat contrast to temperature elevation. **(b)** Azimuthally averaged data for the 100 ns time delay with a temperature axis calibrated with the same conversion factor as in (a).

3.25a, bottom row), corroborating our contrast assignment. In a separate measurement, we decrease the 1.9 eV pump fluence from 2.0 mJ/cm^2 to 0.12 mJ/cm^2 to achieve lower elevated temperatures. Since the heating due to thermalization scales linearly with carrier density (**Appendix B.2**), the temperature increase due to thermalization at the reduced pump fluence is given by $\Delta T_{\text{therm}} = (0.12/2.0) \times 10$ K $= 0.6$ K. We calculate a conversion factor between differential contrast and temperature elevation by using $\Delta T_{\text{therm}} = 0.6$ K as the time zero temperature and fitting the heat amplitude in the time delay range when heat alone is detectable to a decaying exponential function (**Figure 3.26a**). The vertical intercept of the fit yields the conversion factor. We estimate that, even for these averaging conditions of ∼2 minutes per time-delayed image, we can reliably measure temperature differences of $\sim 100 - 200$ mK (**Figure 3.26b**). The temperature sensitivity ultimately depends on the signal-to-noise ratio, which may be increased with more averaging. It also depends on the proximity of the probe to electronic resonances in the material and the achievable imaging contrast, which for silicon is lower due to its high reflectivity (**Section 2.4.1**). We explore the coexistence of heat and charge further in the next Chapter.

We note that we were not able to reproduce the values of carrier and thermal diffusivity obtained previously in our group (**Figure 3.27**), but work is underway to reconcile our results with these and more broadly with the literature, based on the effects of carrier-carrier and carrier-lattice scattering.

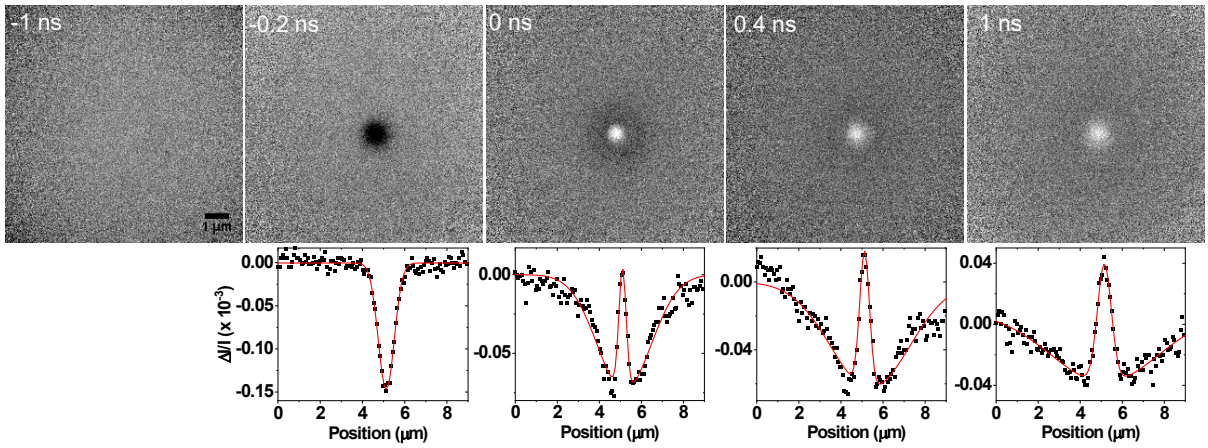

Figure 3.27: stroboSCAT time series on a p-doped silicon wafer as reported in Reference [278] using a 440 nm pump and 635 nm probe. Fits are to a sum of two Gaussians. Fluence is 0.5 mJ/cm^2 ($n_0 \sim 2 \times 10^{19}$ cm^{-3}) [277]. 10-scan averaging and 8-pixel wide integration are used for the plots shown.

3.5 Conclusion

Establishing the fundamental relationship between microscopic structural motifs and macroscopic function has been a long-standing multiscale challenge. In response, we devised a highly accessible and high-throughput strategy for measuring energy flow *in situ* that is universally applicable to different energy forms and material properties. Benefitting from the high spatiotemporal resolution, sensitivity and dynamic range of stroboSCAT, we demonstrated 3D measurement of energy flow through heterogeneous environments on pertinent scales, enabling direct correlation of the structure and functional connectivity in a broad range of semiconductors. We envision that stroboSCAT will impact the study of energy materials well beyond the scope of this present work and will eventually reach the ultimate sensitivity limit of tracking single energy carriers [279], permitting nanometric functional mapping using single-particle localization with few-nanometer precision in all spatial dimensions. As examples since this original work was published [278], our group has gone on to employ stroboSCAT to study longitudinal transport along and transverse transport between bundled ultrathin inorganic halide perovskite nanowires [98], trap-limited transport in halide double perovskites [81], and subdiffusive heat transport in disordered films of gold nanocrystals [130]. Finally, using scattering as a contrast mechanism enables a comprehensive range of processes—not only energy flow but also the transport of chemical species or ions—to be studied with the same level of detail and could shed light on catalytic cycles and chemical energy storage. Very recently, first steps have also been accomplished *in operando* in this direction, both in battery electrodes [280] and in a stroboSCAT-compatible electrochemical cell in our lab [219].

Chapter 4

Exciton transport in 2D architectures with an emphasis on co-measuring and discerning charge and heat in a few-layer TMDC

4.1 Introduction

Heat and charge coexist in many semiconducting materials following photoexcitation or electrical injection. Here "heat" refers to heating induced lattice fluctuations, and "charge" to excited state electrons, holes and their correlated combinations, e.g., excitons. In low-dimensional materials, Auger-Meitner (A-M) processes, density-dependent heat-generating exciton annihilation events, are prevalent even at modest exciton densities due to enhanced Coulomb interactions [281], and nonradiative pathways often dominate due to defects and natural background doping [32, 282] (**Section 1.2.1**). The combination of these effects can lead to a significant fraction of absorbed light energy undergoing transduction to lattice heating, which coexists with other charge excitations like excitons. Similarly, in nanoscale electronic devices, charge carrier scattering with phonons leads to Joule heating and elevated device temperatures that impair efficient electronic dynamics, including transport, due to increased scattering with the lattice [283]. As device dimensions and volume for heat dissipation continue to decrease, material interfaces increase, and carrier-boundary scattering also plays a key role in self-heating, limiting thermal and electrical conductivity [284–288]. Each of these dissipative effects in optoelectronic devices is important to discern so that metrics such as photoluminescent quantum yield (PLQY) and carrier diffusion length might be optimized. Additionally, thermal management strategies often leverage inherent material anisotropies in energy flow which give rise to thermoelectric capabilities, the ability to reversibly convert an electric potential, V, to a temperature gradient, ∇T, or vice versa [289]. In either case, distinguishing heat from charge when they coexist in a material and

discerning their unique photoinduced dynamics is vital not only for informing design principles for directing heat and charge in emerging materials but also for drawing well-informed conclusions about intrinsic material properties.

Distinguishing between heat and charge with optical measurements is, however, challenging. For example, both ground state and transient excited state optical spectroscopy manifest complex perturbations to the location, amplitude, and width of electronic resonances [166, 290, 291]. Even if signatures of unique excitations are quantitatively observed, because their signatures can overlap spectrally and temporally, they remain difficult to quantitate despite judicious choices in excitation and probing wavelengths, time-dependent signatures, measuring as a function of voltage bias, and measuring a pump fluence- or temperature dependence. In particular, local heating could influence or masquerade as electronic excitations in semiconducting materials, and because it is spectrally ubiquitous, isolating the electronic dynamics is especially challenging. Physically, heating leads to increased lattice fluctuations, which change the mass density, an effect measured by the thermo-optic coefficient and which may be observed as a frequency-independent change in the dielectric function [292–294]. Near an electronic resonance, however, heating broadens and shifts the resonance feature, an effect that adds to or cancels any transient photoinduced changes from the electronic carriers themselves [290, 291]. This behavior is especially complicated in transition metal dichalcogenides (TMDCs) where heat dissipation following photoexcitation is prevalent and different exciton resonance features may spectrally overlap [152, 295].

The growing collection of spatiotemporally resolved optical microscopies are excellent candidates for characterizing photogenerated energy and its transport in semiconducting materials because they provide spatial dynamics in addition to the information provided by more traditional time-resolved spectroscopy (**Section 1.4**). These techniques, e.g., micro-time-resolved photoluminescence (microTRPL) [72, 110, 111, 296–299], transient absorption microscopy (TAM) [30, 112–114, 300], variations of transient reflectance microscopy [301–303], including stroboscopic scattering microscopy (stroboSCAT) [278], directly measure the progressive expansion of initially localized populations of impulsively photogenerated energy carriers with nanoscale sensitivity and down to ultrafast time resolution. TRPL is, however, restricted to detecting electron-hole radiative recombination, and, to our knowledge, there are no reports of TAM separately resolving heat directly in addition to charge [304]. Fortunately, due to its sensitivity to changes in the real part of the dielectric function, stroboSCAT has investigated heat flow in metallic composite films [130, 305] and has distinguished heat and charge flow in p-doped silicon based on different signs of imaging contrast, a substantial separation in time scales, and corroboration with commonly cited respective diffusivities (**Section 3.4**) [278]. To address the additional challenges associated with characterizing electronic dynamics and transport in ultrathin semiconductors, especially when heat and electronic diffusivities are not as dissimilar as in silicon and where photogenerated heat is prominent, additional strategies must be developed.

In this Chapter, we employ stroboSCAT to observe energy transport in several TMDC architectures: first, in a TMDC heterobilayer (**Section 4.2.1**), second in a metal-contacted TMDC heterostructure (**Section 4.2.2**), and finally in an encapsulated few-layer TMDC

(**Section 4.3**). Briefly at the end of the Chapter, we discuss preliminary results in a layered intrinsic thermoelectric material (**Section 4.4**). The bulk of the Chapter concerns an in-depth study in the final TMDC architecture where we directly co-measure both heat and excitons in few-layer molybdenum disulfide (MoS_2) on relevant nanometer and picosecond length- and time scales. Through a combination of near- and far-from resonant stroboSCAT probing conditions, one of which isolates heat alone, and calibration with steady state temperature-dependent reflectance contrast spectroscopy, we observe and quantitatively discern transient thermal and electronic contributions to the photogenerated dynamics. This new strategy enables isolation and characterization of the excitonic dynamics without concern for mistaking thermal contributions for electronic ones.

This capability with few-layer MoS_2 complements the capabilities of microTRPL, which is largely restricted to monolayer TMDC measurements [111, 297, 298] because additional layers lead to very low PLQY due to the emergence of an indirect bandgap. Furthermore, we corroborate our results with a spatiotemporal model for heat and exciton populations. With the ability to detect temperature elevations as low as 100 mK, our study suggests that even a modest temperature elevation has a substantial effect on the optical response in few-layer MoS_2. More broadly, this Chapter establishes a strategy for isolating electronic dynamics and transport in a wide range of conventional and emerging semiconductors that offers great potential for more incisively investigating thermal management and thermoelectric energy conversion.

4.2 stroboSCAT with interfaces

4.2.1 TMDC heterostructure

In Richard Feynman's lecture "There's Plenty of Room at the Bottom," he poses the following questions: What could we do with layered structures with just the right layers? What would the properties of materials be if we could really arrange the atoms the way we want them? We can now begin to explore the answers to these questions as synthesis techniques in the "Lego land" of 2D materials continue to improve, and bottom-up materials design – making designer stacks of atomically thin insulators, semiconductors, metals and superconductors – enables the construction of a huge variety of layered structures with an unprecedented level of control over material properties and device functionalities [306, 307]. Heterobilayers are one such TMDC heterostructure in this 2D playground with exciting applications in spin- and valleytronics and excitonic devices. When tungsten and molybdenum dichalcogenides are stacked on top of one another, a type-II band alignment forms (**Figure 4.1a**). Following photoexcitation of one layer, rapid (sub-ps) charge transfer occurs so that the electron and hole are localized to different layers. Then, owing to the large Coulomb interaction ($E_b \sim 150$ meV), the spatially separated electron and hole form an interlayer exciton (ILE) that persists at room temperature (**Figure 4.1b**). ILEs are both spatially and momentum indirect due to their spatial separation in different layers and the lattice

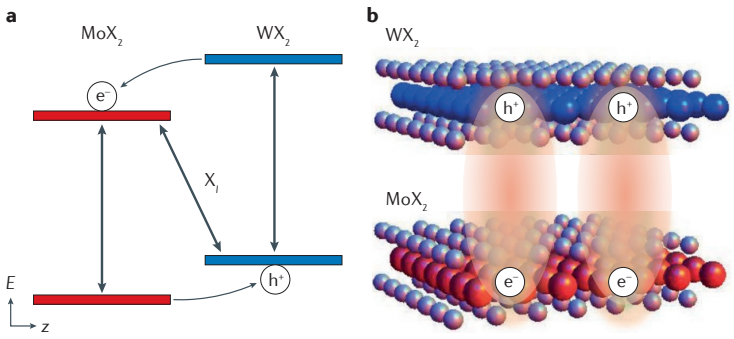

Figure 4.1: Interlayer excitons in 2D semiconductor heterostructures. **(a)** Energy-level diagram showing type-II band alignment for a typical MoX_2-WX_2 heterostructure. Ultrafast interlayer electron transfer to the MoX_2 or hole transfer to the WX_2 results in the formation of interlayer excitons. **(b)** Illustration depicting spatially indirect, interlayer excitons in a MoX_2-WX_2 heterostructure. Reprinted with permission from Reference [313].

mismatch between the two layers. Therefore, the lifetime of ILEs (∼µs) tends to be orders of magnitude longer than that of intralayer excitons (<ns) [47, 308–312]. While the phonon-assisted relaxation process for ILEs allows them to diffuse long distances over their lifetime (>µm), their radiative recombination is strongly quenched, making PL a difficult observable to measure ILE dynamics. With stroboSCAT's universal scattering approach, however, we can directly map ILE dynamics. We were also curious to explore the following questions: (1) Can differential scattering contrast distinguish between different "flavors" of excitons (intralayer vs. interlayer, optically bright vs. dark)? (2) Can we measure ILE dissociation rates at charge transfer interfaces? (3) Can we characterize how altering the energy landscape (mechanical strain, dielectric disorder) impacts energy migration?

With our sights set high on these challenging scientific questions, we teamed up with **Cora Went** and **Joeson Wong**, expert TMDC fabricators in the **Harry Atwater** group at Caltech, who prepared a MoS_2-WSe_2 heterostructure by exfoliation onto a glass substrate (**Figure 4.2**) [314]. iSCAT imaging, technically interference reflection microscopy, in the stroboSCAT microscope readily identifies the ∼3×3 µm heterostructure boundary (yellow box in **Figure 4.2**) and the constituent few-layer MoS_2 and WSe_2 flakes that overlap to form the vertical junction. stroboSCAT measurements at low 440 nm pump fluence (15 µJ/cm^2) in the few-layer MoS_2 show a moderately expanding (∼0.3 cm^2/s) positive contrast profile (first row in **Figure 4.2**). Under identical experimental conditions, differential contrast in the few-layer WSe_2 is negative and expands slightly faster (∼0.4 cm^2/s) (second row in **Figure 4.2**). Although we had trouble reproducing the positive-only contrast measurement in MoS_2 at correspondingly lower fluences, we still suspect that it represents excitons in MoS_2, based on further study of MoS_2 discussed in **Section 4.3**. In this heterostructure sample, it is possible that the pump was at an optimal defocus to observe this effect since the time zero signal is wider than that in WSe_2, even though we measured a higher diffusivity in WSe_2

than in MoS_2. It is also possible that, since we were probing very close to a resonance feature, heterogeneity in the sample's optical response shifted the relative position of the probe with respect to the exciton resonances at different sample locations within the same few-layer MoS_2 region. In the same sample regions, we also perform measurements with a higher pump fluence (330 $\mu J/cm^2$) and observe negative contrast only in both materials, although with a much slower diffusivity ($\sim$0.03 cm^2/s). This was our first clue that lattice heating is a prevalent transduction pathway for the absorbed light energy in TMDCs, especially when generated via nonlinear A-M processes (**Section 1.2.1**). Due to the different dynamics measured in the low- and high-pump fluence regimes, we hypothesize that the differential contrast is dominated by excitons in the low-fluence measurements (bright for MoS_2, dark for WSe_2) and by heat in the high-fluence measurements since excitons tend to diffuse faster than heat in TMDCs, up to several cm^2/s depending on sample quality and preparation method [111, 298, 300, 315–318]. The probe wavelength (635 nm) is between the A and B exciton resonances in both materials, but closer to both resonances in MoS_2, based on previous measurements of the dielectric function of monolayer MoS_2 and WSe_2 [295]. We can make informed guesses about the contrast assignment based on the measured dynamics and power-dependent trends, but without in-house measurements of the steady state dielectric function (with ellipsometry or reflectance contrast spectroscopy, for example) or, better yet, the excited-state spectral response (transient absorption or reflectance, for example) on this particular sample, we cannot definitively state exactly what gives rise to the oppositely-signed contrast in the two materials. It is, however, likely related to the relative position of the probe energy and material electronic resonances as we find in few-layer MoS_2 below (**Section 4.3**).

stroboSCAT measurements in the heterostructure region exhibit faster diffusion (>3 cm^2/s) than in either of the constituent layers, with transport proceeding all the way up to the edges of the heterostructure (third row in **Figure 4.2**). Although interference from the heterostructure edges in the ground state iSCAT image modulates the otherwise flat, featureless sample, the uniform background in the differential images suggests that the "bubbly" differential contrast features are not an imaging artifact but the result of real sub-diffraction contrast flips occurring in the interferometric detection. Small deformations in the top WSe_2 layer caused by residue from the PDMS transfer (stuck to the top of the MoS_2 flake) could be the culprit. Similar contrast flips from dielectric inhomogeneities have been observed in WSe_2, for example [319]. The heterostructure is too thin to account for a depth-dependent phase flip from the spatially separated electrons and holes, which would require an extra optical path length of $z \sim 40$ nm and, in any case, the Böhr radius for the ILE is at most a few nm. In sum, it was exciting to directly observe the ILE transport and to measure dynamics that were distinct from the constituent layers, but we decided that in order to understand the complicated differential contrast in the heterostructure, we should characterize its components separately and in a uniform dielectric environment provided by hexagonal boron nitride (hBN) encapsulation (**Section 4.3**).

Before we abandoned this first TMDC structure for more homogeneous pastures, we explored one additional area of interest: a one-layer—few-layer lateral interface in WSe_2

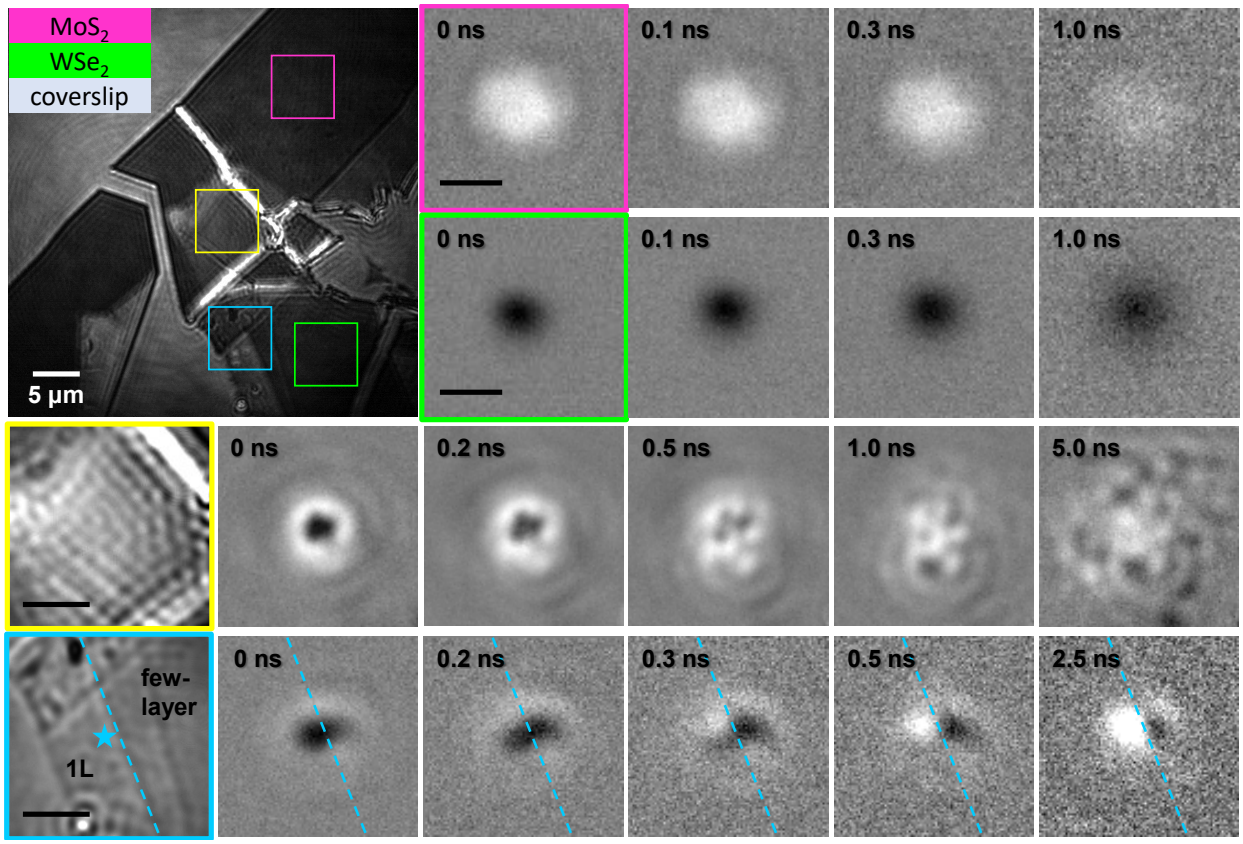

Figure 4.2: iSCAT/IRM image of the MoS_2-WSe_2 heterostructure where MoS_2 was first deposited and then partially covered with WSe_2 (top left) with boxes showing the areas measured with stroboSCAT (440 nm pump, 635 nm probe). (pink) few-layer MoS_2 and (green) few-layer WSe_2, exhibiting moderate diffusivity (0.3-0.4 cm^2/s) that we attribute to excitons. (yellow): fast expansion (> 3 cm^2/s) of IDEs in the heterostructure region. (blue): transfer of excitons across a lateral monolayer—few-layer WSe_2 boundary (blue dashed line) following excitation in the monolayer (blue star) with PL dominating the signal at later times in the monolayer.

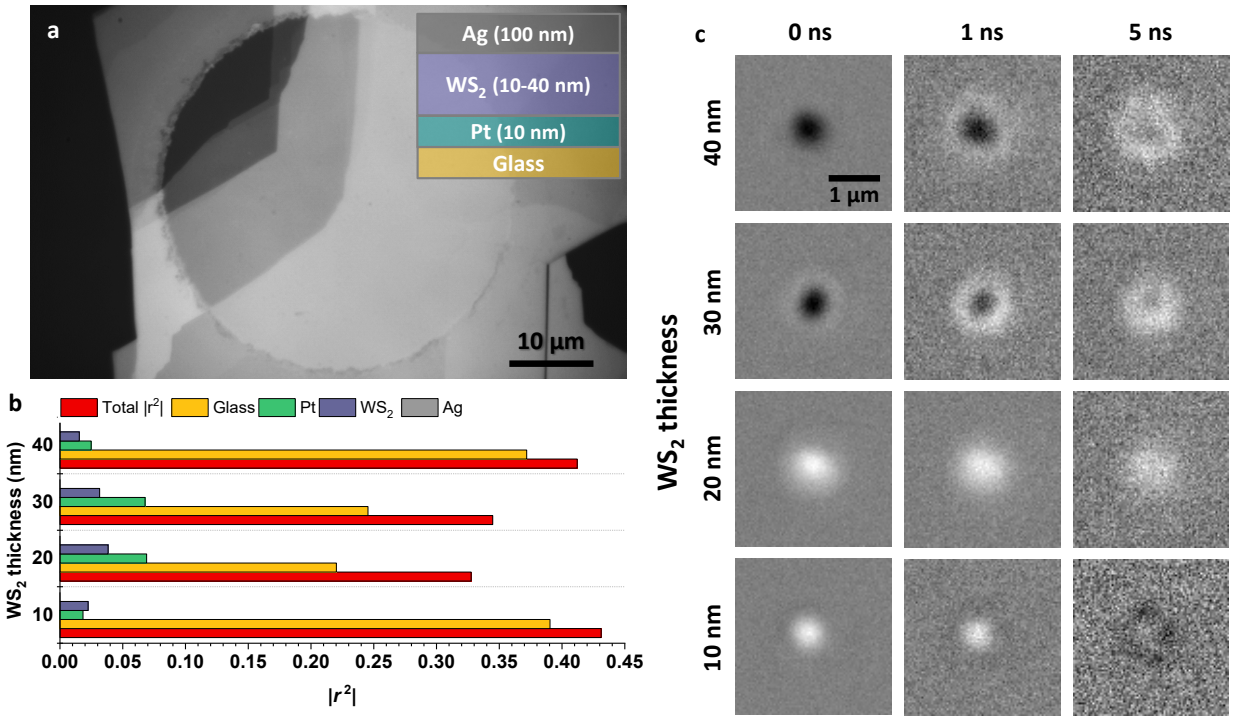

Figure 4.3: **(a)** iSCAT/IRM image of the metal-contacted WS_2 heterostructure where grayscale shades within the circular feature indicate different WS_2 thicknesses. The stack is imaged through the platinum layer that covers the entire substrate. **(b)** Reflected field intensities within each of the layers in the vertical stack as a function of WS_2 thickness, calculated with the transfer-matrix method. The reflected field at the glass-Pt interface is strongest, indicating that the glass-Pt interface is a good reference plane. **(c)** WS_2-thickness-dependent stroboSCAT measurements with contrast that can be explained with depth-dependent phase flips (or lack thereof) in all except the thinnest (10 nm WS_2) stack.

(fourth row in **Figure 4.2**). Pumping in the monolayer region, we observe transfer of the initial population across the interface into the few-layer region, although PL from the highly luminescent monolayer overwhelms the signal on the monolayer side at late times. Even though the nature of the monolayer and few-layer exciton is very different, (direct and highly localized in the former, indirect and more delocalized in the latter), the exciton seems to convert readily across the interface. In future studies (with more spectral filters and a judiciously chosen probe!), it could be interesting to explore the rate of this process as a function of layer thickness on the few-layer side. stroboSCAT is a well-poised tool for such a study since PL is suppressed on the few-layer side, even for just a bilayer.

4.2.2 Vertical metal-contacted TMDC

Eager to utilize the depth-dependent phase sensitivity of stroboSCAT, we measured one final TMDC stack, or "sandwich," in this case, to explore exciton dissociation, a prerequisite for current generation in a TMDC-based solar cell. **Cora** designed a sample geometry consisting of a thin WS_2 flake (10-100 nm) surrounded by metal contacts (Pt and Ag) with different work functions to drive exciton dissociation. The glass substrate is coated with 10 nm of sputtered Pt before the WS_2 is transferred. To cap the WS_2 with Ag, **Cora** used a new method she developed to transfer nanoscale 3D metal contacts onto TMDC flakes that preserves the pristine TMDC surface with a gentle, nondamaging van der Waals contact [320]. The fabricated Pt-WS_2-Ag sandwich imaged with iSCAT/IRM is shown in **Figure 4.3a** where different grayscale shades indicate the WS_2 thickness under the Ag cap (circular feature), which is verified with optical reflectance contrast (**Section 4.3.5**) before the Ag transfer [321, 322]. In the open-circuit case, excitons are generated by the pump pulse with a concentration profile that exponentially decays into the thickness of the WS_2 so that initially, the exciton profile center-of-mass along the z-axis is concentrated near the Pt-WS_2 interface. Then, holes move toward the Ag contact while electrons transfer to the nearby Pt contact until a field, $-E$, is established that completely counteracts the built-in field due to the different metal work functions, E, resulting in a net zero field:

$$E = \frac{W_{\mathrm{Pt}} - W_{\mathrm{Ag}}}{d} \sim 200 \text{ meV}, \tag{4.1}$$

where W_i is the metal work function and d is the WS_2 thickness.

Based on the refractive index of WS_2 at the 635 nm probe wavelength ($n_{WS_2} \sim 5$), we estimate that the interferometric stroboSCAT signal for holes accrues a π phase flip when they are at least 30 nm above the MoS_2-Pt interface. With additional interfaces beyond the usual substrate-sample interface, however, the interpretation of the interferometric contrast, and which plane in the stack serves as the "reference" from which carrier height, z, should be measured, is more complex. We turn to the transfer-matrix method (TMM) to calculate the reflected field amplitudes, r, within each layer following coherent propagation of an incident plane wave onto a multilayer planar stack [323]. The model assumes that everything is uniform in the transverse directions with interfaces and layers perpendicular to the normal, $\hat{\mathbf{z}}$, and incident plane wave light traveling in $+\hat{\mathbf{z}}$. The only required inputs are the thickness and complex refractive index over the range of relevant wavelengths for each layer in the stack. See **Appendix B.4** for more details. With this analysis, it is possible to determine which interface, if any, dominates the overall reflection and if the reflected field amplitude acquires a π phase flip with respect to the incident field. The results of the transfer-matrix analysis for different WS_2 thicknesses are shown in **Figure 4.3b**. The reflected field within the glass layer (yellow bars in **Figure 4.3b**) is strongest in all cases, indicating that the glass-Pt interface above it is a good proxy for the dominant reference field reflection plane. Light that scatters from carriers at the Pt-WS_2 interface, 10 nm above the dominant reflection interface, accrues an additional phase of $\phi = 0.46$, 15% of the way to a π phase flip. In

order to accumulate the full phase flip, the holes must travel vertically at least 27 nm in the WS_2, which means phase flips due to vertical hole transport should only occur in the 30 and 40 nm thick WS_2 regions. Indeed, over several ns we do observe dark contrast in the center of the distribution give way to light contrast in these regions, and no phase flip in the 20 nm thick region, however, the 5-ns results from the thinnest 10 nm region are not consistent with the trend because dark contrast emerges (**Figure 4.3c**). Other explanations might consider heating effects, (the 2.8 eV pump is nearly 1.5 eV above the bandgap), how to account for interferometric contrast contributions from electrons and holes that may have different axial profile distributions, or even whether electrons and holes might exhibit differently signed contrast at this probe energy (2 eV). While the TMM formalism is useful for establishing the dominant reflection interface in a multilayer stack and for estimating the enhanced absorption from multiple reflections (**Appendix B.4**), it is totally blind to the volume of photogenerated carriers that scatter light at all angles and to how their out-of-plane distribution evolves, which is vital for understanding phase contrast due to vertical transport in stroboSCAT, (see **Section 3.3**, for example). We considered constructing our experimental sample and detection geometry in Lumerical, a powerful photonic simulation software, to explore the mechanism of the phase contrast. In a future iteration of this experiment, it would also be useful to actively gate the sample to study exciton dissociation as a function of applied field, especially since it is unclear whether the different work functions of the metal contacts actually do establish a built-in voltage or if photoinduced carriers can readily screen the field from each metal by localizing near the metal surfaces.

4.3 Co-measuring and discerning photoinduced heat from charge and their transport in few-layer MoS_2

Since dissipative processes are ubiquitous in semiconductors, characterizing how electronic and thermal energy transduce and transport at the nanoscale is vital for understanding and leveraging their fundamental properties. For example, in low-dimensional TMDCs, excess heat generation upon photoexcitation is difficult to avoid since even with modest injected exciton densities, exciton-exciton annihilation still occurs. Both heat and photoexcited electronic species imprint transient changes in the optical response of a semiconductor, yet the unique signatures of each are difficult to disentangle in typical spectra due to overlapping resonances. In response, we employ stroboSCAT to simultaneously map both heat and exciton populations in few-layer MoS_2 on relevant nanometer and picosecond length- and time scales and with 100-mK temperature sensitivity. We discern excitonic contributions to the signal from heat by combining observations close to and far from exciton resonances, characterizing photoinduced dynamics for each. Our approach is general and can be applied to any electronic material, including thermoelectrics, where heat and electronic observables spatially interplay, and lays the groundwork for direct and quantitative discernment of different types of coexisting energy without recourse to complex models or underlying assumptions.

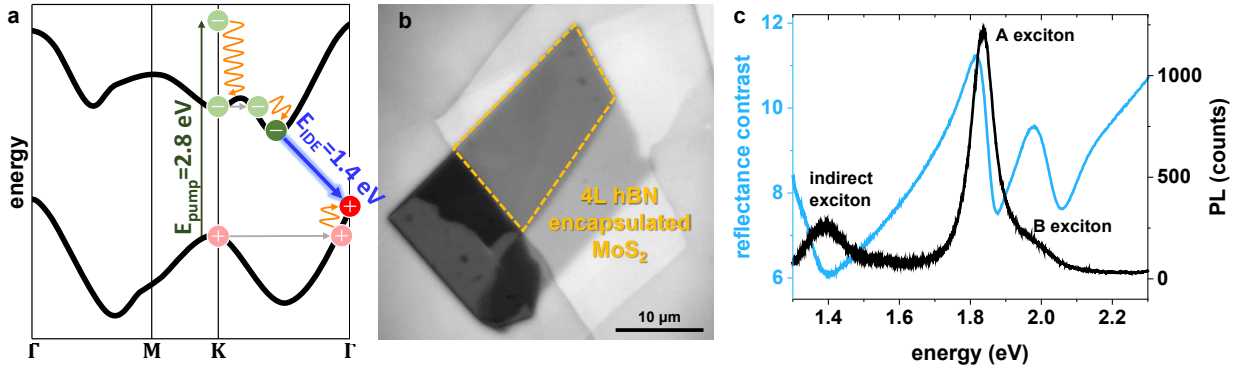

Figure 4.4: **(a)** Calculated single particle band structure for 4L MoS_2 from Reference [26] showing the above-bandgap pump excitation (green arrow) at the K-point of the Brillouin zone followed by fast thermalization (orange) and intervalley scattering (gray) to the lowest energy indirect exciton (blue arrow). **(b)** Optical reflectance image of the entire MoS_2 flake with the measured 4L hBN-encapsulated region outlined in yellow. **(c)** Steady state photoluminescence (PL) spectrum (black) showing strong emission from the direct A exciton near 1.8 eV with a blue shoulder corresponding to emission from the direct B exciton. Emission from the indirect exciton (1.4 eV) is comparatively weaker. The reflectance contrast spectrum (blue) exhibits dispersive resonance features near the PL peaks.

To demonstrate the capability of identifying and simultaneously tracking electronic and thermal energy evolution, we focus on an hBN-encapsulated four-layer (4L) MoS_2 flake fabricated using the hot pick-up technique and supported by a glass substrate [314]. Before proceeding with spatiotemporally resolved transport measurements, we pre-characterize the sample. The relevant portion of the electronic structure is shown schematically in **Figure 4.4a** [26]. Optical reflectance microscopy readily identifies the encapsulated 4L region outlined in yellow in **Figure 4.4b**. Sample thickness characterization is found in **Figure A.2**. The steady state photoluminescence spectrum in **Figure 4.4c** shows characteristic strong emission from the spin-orbit split A (∼1.8 eV) and B (∼2 eV) direct excitons, with a strong B:A photoluminescence intensity and dispersive resonance amplitude ratio in the blue reflectance contrast spectrum indicative of good sample quality [324]. Photoluminescence due to recombination of the lowest-energy indirect exciton (IDE) in the near-infrared (∼1.4 eV), indicated by the blue arrow in **Figure 4.4a**, is comparatively weak.

We use stroboSCAT to directly visualize heat and exciton transport in the 4L MoS_2. These particular experiments employ a 2.82 eV (440 nm) diode laser pump (green arrow in **Figure 4.4a**) that generates excitations at the K-point of the Brillouin zone [25]. Efficient sub-ps intervalley scattering (horizontal gray lines in **Figure 4.4a**) and ∼fs phonon-assisted relaxation to the band edge (orange in **Figure 4.4a**) occur within the ∼200 ps experimental instrument response function (IRF), and we therefore expect the IDE to be the dominant electronic excitation on the time scale of our measurements [29, 30]. Despite the fact that the

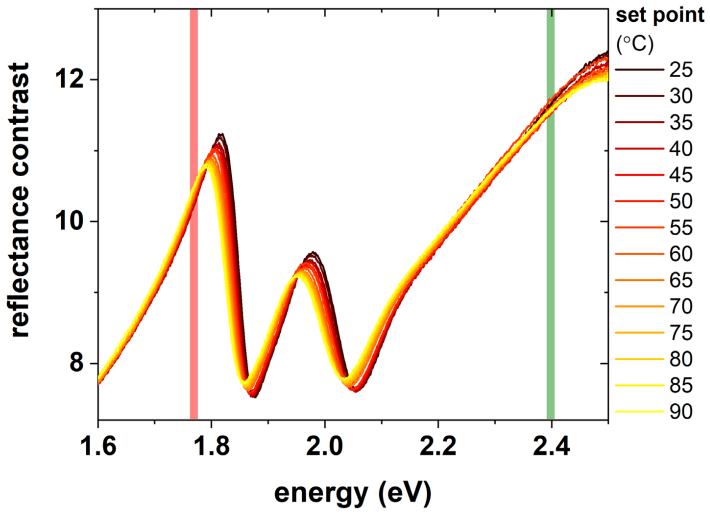

Figure 4.5: Temperature-dependent reflectance contrast spectra over a range of temperature set points near the A and B exciton resonances. The near- and far-from-resonant probe energies are indicated with the red and green lines, respectively.

4L MoS_2 is not luminescent, the presence of photoexcitations modifies the material's local dielectric function, generating transient scattering contrast that evolves as a function of space and time according to the quantity and location of decaying and diffusing photoexcitations. Near an absorption resonance, the sign of the differential contrast can be tuned above (bright) or below (dark) the baseline (gray) background. For a dispersive optical resonance, the transient response leads to oppositely signed $\Delta R/R$ on either side of the resonance [174, 212, 325] (**Section 2.1.2**). Heat, which also modulates electronic resonances, may also modify $\Delta R/R$.

To isolate the effect of heating on the optical response, steady state reflectance contrast (RC) spectra [295, 321] are measured at a range of temperatures from room temperature to 90°C, as described below in **Section 4.3.5**. RC spectra are obtained by measuring reflected spectra from the sample atop of the substrate (R) and separately under the bare glass substrate (R_0) and calculating $RC = (R - R_0)/R_0$. RC spectra over the measured temperature range are presented in **Figure 4.5**, showing the characteristic A and B exciton resonance peaks redshifting and broadening with increasing temperature. From these spectra, we identify two spectral regimes, near- and far-from resonance, which tune the relative contribution to the stroboSCAT signal from heat and excitons, enabling distinction between the two, as developed below in **Section 4.3.7**. We select probe energies for spatiotemporal imaging from available discrete diode laser sources indicated by the red (near resonant, 700 nm or 1.77 eV) and green (far-from resonant, 515 nm or 2.41 eV) vertical lines in **Figure 4.5**.

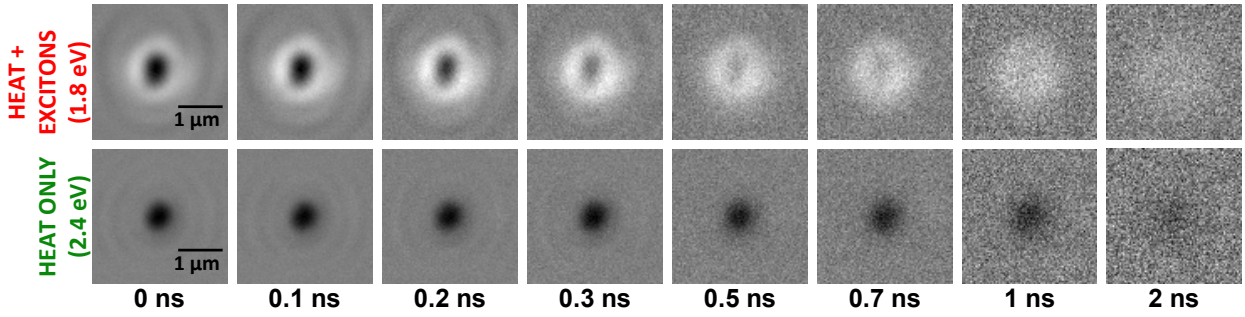

Figure 4.6: stroboSCAT time series captured with a near-resonant (top) and far-from-resonant (bottom) probe. The focused 2.82 eV pump generates a peak initial exciton density of 3.5×10^{13} cm^{-2}.

4.3.1 Complementary stroboSCAT measurements directly image heat and charge dynamics

In the same sample region, we collect two complementary stroboSCAT measurements over a 7 ns time window by probing at the near- and far-from resonant energies (**Figure 4.6**). In both measurements, the same applied pump pulse fluence of 35 µJ/cm^2 generates an estimated peak exciton density of 3.5×10^{13} cm^{-2}, falling in an intermediate density regime where A-M interactions play a significant role but still being an order of magnitude below the Mott transition at which excitons would dissociate [15, 41, 42]. We use transfer-matrix calculations executed with the "tmm" Python software package [323, 326] to estimate the total absorption over the four layers of material in the sample, which is enhanced by multiple internal reflections and interference at the two hBN-MoS_2 interfaces (**Appendix B.4**). We input complex refractive index values from the literature for 4L MoS_2 [327] and a flat dispersion for hBN ($n_{\mathrm{hBN}} = 2.2$) with no absorption in the visible ($k_{\mathrm{hBN}} = 0$) [328]. The input layer thickness of MoS_2 is 0.65 nm [329], while the hBN thicknesses are experimentally estimated with AFM (5 and 19 nm for the bottom and top layers, respectively). The calculation predicts that 6% of incident photons are absorbed per layer, resulting in an overall $1/e^2$ carrier density of $4.8{\times}10^{12}$ cm^{-2}, or a peak carrier density of $3.5{\times}10^{13}$ cm^{-2}. By contrast, a simple absorption calculation (**Appendix B.1**) using $a(2.8\ \mathrm{eV}) = 7.2 \times 10^5$ cm^{-1} yields an estimated $1/e^2$ carrier density of $1.5{\times}10^{12}$ cm^{-2}, or a peak carrier density of $9.3{\times}10^{12}$ cm^{-2}, an underestimate by more than a factor of 3 since it does not account for multiple internal reflections that enhance the absorption. The spatiotemporal model we describe below in **Section 4.3.8** predicts a maximum exciton density at time zero of $\sim 8{\times}10^{12}$ cm^{-2}, lower than that predicted by the transfer-matrix calculation because it takes into account a finite pump pulse duration (72 ps) over which appreciable exciton-exciton annihilation occurs. The most realistic characterization of the exciton density is the spatiotemporal model with the peak exciton density from the transfer-matrix calculation as the initial condition, $N(0,0)$. Furthermore, a binding energy of $\sim 4k_{\mathrm{B}}T$ (at room temperature) suggests that dissociated

free carriers make up $< 2\%$ of the total photoexcited electronic population.

Hot excitons thermalize and scatter to the indirect band edge within the IRF, transferring their excess energy to the lattice via efficient phonon emission. We therefore expect to observe both long-lived (several ns) IDEs and lattice heating simultaneously on our measurement time scales. In the far-from resonant stroboSCAT measurement, we observe negative (dark) contrast alone that decays and expands over several nanoseconds (**Figure 4.6**, bottom), whereas in the near-resonant stroboSCAT measurement at the top of **Figure 4.6**, we observe bright positive contrast beyond a dark, negative-contrast center that similarly decays over several nanoseconds, with positive contrast dominating after 1 ns. We assume that each sign of contrast, positive or negative, in each measurement is generated by either heat or excitons, the two dominant forms of energy in the material following photoexcitation. Temperature-dependent RC spectra predict negative differential contrast due strictly to heating in the near-resonant measurement (**Section 4.3.5**), therefore we deduce that positive contrast in the same measurement must be due to the presence of excitons. Using these assignments, we observe that excitons diffuse faster than heat, giving rise to positive amplitude extending beyond the heat-dominated negative contrast. This assignment is consistent with previous reports of exciton and heat diffusivity in MoS_2, in which exciton diffusivities are up to a few cm^2/s [298, 330, 331] while reported heat diffusivities are slower at $\sim$0.2 cm^2/s [332, 333].

4.3.2 Data analysis methods: azimuthal profile averaging

To utilize the full 2D information about energy transport obtained in stroboSCAT, we azimuthally average the roughly cylindrically symmetric differential images in **Figure 4.6** about the same center pixel for all time delays in a given measurement. We use the `numpy.ravel` and `numpy.bincount` functions in Python to flatten the image from a 2D to 1D array before binning the data by radial position (see **Appendix B.5**). We discard the center pixel since it tends to be quite noisy and fit the data beginning at pixel 1. A better center pixel value may be reconstructed from Gaussian fits to the data.

To investigate the sensitivity to which pixel is designated as the central one, we explore the effect of mislocalizing the center pixel on a simulated 2D Gaussian population isotropically expanding with a diffusivity of 1 cm^2/s. The result of the azimuthally averaged profiles for the time zero distribution using the true center pixel (blue) up to a center pixel mislocalized by $r^2 = 50$ are shown in **Figure 4.7a**. Mislocalizing the center pixel smears out the extracted Gaussian profiles and ultimately suppresses the calculated mean squared expansion by up to 25% for this particular diffusivity as shown in **Figure 4.7b**. The effect is less pronounced for a more slowly expanding population. To be more quantitative and to automate the center pixel localization on a real dataset, we define a grid of possible center pixels around the geometric center of the time zero image in the near-resonant probe measurement (**Figure 4.7c**). At each of these pixels, we extract an azimuthally averaged profile after squaring the pixel intensities in the raw image. Two examples are shown in **Figure 4.7d**, one averaged about the geometric center (blue) and another about a slightly displaced center pixel (red). For each profile, we calculate a "focal score" given by the ratio of the maximum

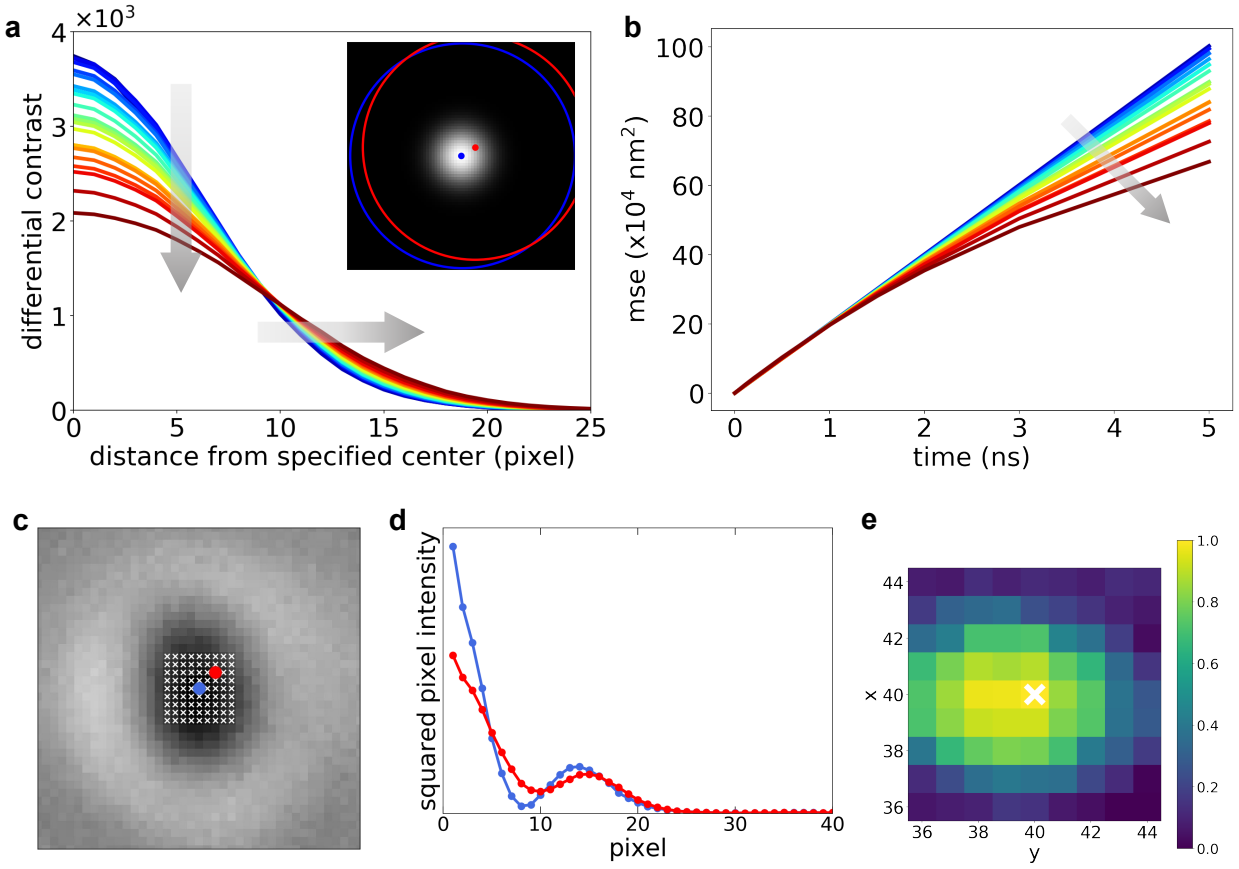

Figure 4.7: Center pixel localization for azimuthal averaging. **(a)** Azimuthal averages of a time zero simulated 2D Gaussian image (inset) averaged about the true center (blue) and increasingly mislocalized centers up to $r^2 = 50$ (maroon). **(b)** Resulting mean squared expansion from azimuthal averaging about an increasingly mislocalized center pixel for the same simulated dataset as in (a). The extracted diffusivity ranges from the defined diffusivity of 1 cm^2/s (blue) to 0.75 cm^2/s (maroon). **(c,d)** On a real dataset, we extract azimuthally averaged profiles from a grid of possible center pixel values defined around the geometric image center (c). The squared pixel intensity as a function of radial distance from a given center is shown in (d) after azimuthally averaging about the geometric center (blue) and an offset pixel (red). **(e)** For each profile, a "focal score" is calculated by taking the ratio of the profile maximum to its FWHM. The highest scored profile (white x) defines the best center pixel for azimuthal averaging.

squared pixel intensity divided by the FWHM. The result is shown in **Figure 4.7d** with the maximum score, and therefore best center pixel, marked with a white x, which also happens to correspond to the geometric center in this case. In practice, we found that selecting the center pixel by eye in the time-zero image is usually more than sufficiently accurate.

4.3.3 Data analysis methods: Simpson's rule

To calculate the integrated population at each time delay, we use Simpson's rule on each azimuthally-averaged profile. Simpson's rule is a numerical method to approximate the integrand under a set of $N+1$ equally spaced points between $[a, b]$ using a quadratic interpolant in order to estimate the area under a discrete function or data array. This approximation is generally more accurate than a Riemann sum or the trapezoid rule which uses a linear interpolant. It is especially useful for calculating the area under a carrier distribution that does not fit well to a simple function like a Gaussian, (like the low-η early-time exciton distributions described in **Section 4.3.11**). The formula for Simpson's rule is given by

$$\int_a^b f(x)\mathrm{d}x \approx S_N(f) = \frac{\Delta x}{3}\sum_{i=1}^{N/2} f(x_{2i-2}) + 4f(x_{2i-1}) + f(x_{2i}), \tag{4.2}$$

where N is an even number, f is a discrete data array, $\Delta x = (b-a)/N$ is the spacing between adjacent array elements and $x_i = a + i\Delta x$ for integer index, i.

Or, in terms of the first, last, even and odd elements of the data array:

$$S_N(f) = \frac{\Delta x}{3}(\text{first} + 4(\text{sum of odds}) + 2(\text{sum of evens}) + \text{last}). \tag{4.3}$$

Equation 4.3 is also known as "Simpson's One-Third Rule." In practice, this calculation is implemented with the `scipy.integrate.simpson` function in `Python`. Note that for azimuthally averaged profiles, the integrand becomes $rf(r)$.

To find the error introduced by this calculation, we use the standard error propagation formula for a function that is a sum of (scaled) variables:

$$f_1 = x + y \rightarrow \delta f_1 = \sqrt{\delta x^2 + \delta y^2} \tag{4.4}$$

$$f_2 = Cx \rightarrow \delta f_2 = C\delta x. \tag{4.5}$$

Therefore, the error on the area/integrand calculated with Simpson's rule is given by

$$\delta S_N(f) = \Delta x\sqrt{\left(\frac{\delta\text{first}}{3}\right)^2 + \sum\left(\frac{4}{3}\delta\text{odd}\right)^2 + \sum\left(\frac{2}{3}\delta\text{even}\right)^2 + \left(\frac{\delta\text{last}}{3}\right)^2}, \tag{4.6}$$

where the error on each element is the standard error of the mean from azimuthal averaging.

When the carrier distributions fit well to a Gaussian function, as is the case with the heat-dominated far-from resonant measurements in **Figure 4.6**, the integrated area under

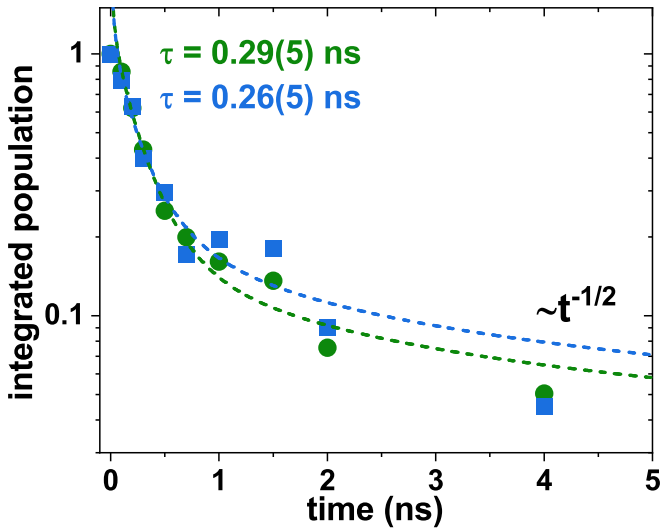

Figure 4.8: Integrated areas representing carrier populations calculated with Simpson's rule (blue) are similar to those calculated from Gaussian fits to the heat-dominated data in **Figure 4.6** (green), yielding kinetic fit parameters that agree within error.

the distribution that represents the total carrier population is easy to calculate from the Gaussian fit parameters as Area $= A\sigma^2$ for a 2D population, where A is the (unnormalized) fit amplitude and σ is the fit width. This yields very similar results to the area calculated with Simpson's rule (**Figure 4.8**).

4.3.4 Data analysis methods: point spread function correction

The goal with the 4L MoS_2 experiments is to isolate and characterize the excitonic contribution to the near-resonant stroboSCAT measurement (top row in **Figure 4.6**). We determined that a way to do so is by subtracting away the heat-only contribution (bottom row in **Figure 4.6**) from the near-resonant dataset. To quantitatively compare and subtract the datasets at the two imaging wavelengths, however, we must apply a pixel size correction to account for their different point spread functions (PSFs). A diffraction-limited PSF is well-approximated by a normalized Gaussian function (**Section 2.3.3**)

$$\mathrm{PSF}_\lambda(r) = \frac{1}{2\pi\sigma_\lambda^2}\, e^{-r^2/2\sigma_\lambda}, \tag{4.7}$$

where $r^2 = x^2 + y^2$ and σ_λ is given by the Abbe diffraction limit:

$$\sigma_\lambda = \frac{\lambda}{2\ \mathrm{NA}\ 2\sqrt{2\ln 2}}. \tag{4.8}$$

In these experiments, excitons are generated by a nearly diffraction-limited 440 nm pump pulse and then efficiently convert to lattice heating, resulting in an initial Gaussian heat distribution

$$G_{\mathrm{pop}}(r) = N_{\mathrm{pop}}\, e^{-r^2/2\sigma^2_{\mathrm{pop}}}, \tag{4.9}$$

where σ_{pop} is the width of the actual heat population (temperature profile). This distribution is imaged in one set of experiments by a widefield 515 nm probe with a PSF given by

$$\mathrm{PSF}_{515}(r) = \frac{1}{2\pi\sigma^2_{515}}\, e^{-r^2/2\sigma^2_{515}}, \tag{4.10}$$

where σ_{515} is defined by Equation 4.8. This imaging operation yields a measured Gaussian distribution, $G_{\mathrm{meas},515}(r)$, and may be represented by a 2D convolution (see **Appendix B.3**):

$$G_{\mathrm{meas},515}(r) = G_{\mathrm{pop}}(r) \otimes \mathrm{PSF}_{515}(r) = \frac{N_{\mathrm{pop}}\sigma^2_{\mathrm{pop}}}{\sigma^2_{\mathrm{pop}} + \sigma^2_{515}}\, e^{-r^2/2(\sigma^2_{\mathrm{pop}}+\sigma^2_{515})} = \frac{N_{\mathrm{pop}}\sigma^2_{\mathrm{pop}}}{\sigma^2_{\mathrm{meas},515}}\, e^{-r^2/2\sigma^2_{\mathrm{meas},515}} \tag{4.11}$$

where

$$\sigma^2_{\mathrm{meas},515} = \sigma^2_{\mathrm{pop}} + \sigma^2_{515}. \tag{4.12}$$

From experimentally measured data at time zero, $\sigma_{\mathrm{meas},515} = 180$ nm, so for a diffraction-limited microscope, the initial heat distribution, from Equations 4.8 and 4.12, has a width of $\sigma_{\mathrm{pop}} = \sqrt{\sigma^2_{\mathrm{meas},515} - \sigma^2_{515}} \approx 160$ nm, which is slightly larger than the pump width of $\sigma_{\mathrm{pump}} \approx 130$ nm, to be expected since the heat distribution may expand slightly during the temporal overlap of the ∼100 ps pump and probe pulses.

If it were possible to measure only heat with a 700 nm probe, the measured Gaussian distribution, $G_{\mathrm{meas},700}(r)$, would be represented by a different convolution:

$$G_{\mathrm{meas},700}(r) = G_{\mathrm{pop}}(r) \otimes \mathrm{PSF}_{700}(r) = \frac{N_{\mathrm{pop}}\sigma^2_{\mathrm{pop}}}{\sigma^2_{\mathrm{meas},700}}\, e^{-r^2/2\sigma^2_{\mathrm{meas},700}} \tag{4.13}$$

where

$$\sigma^2_{\mathrm{meas},700} = \sigma^2_{\mathrm{pop}} + \sigma^2_{700}, \tag{4.14}$$

and again, σ_{pop} is the width of the actual generated heat population which, under identical excitation conditions, does not change with probe wavelength. The Gaussians defined in Equations 4.9, 4.10, 4.11 and 4.13 are plotted for comparison in **Figure 4.9**.

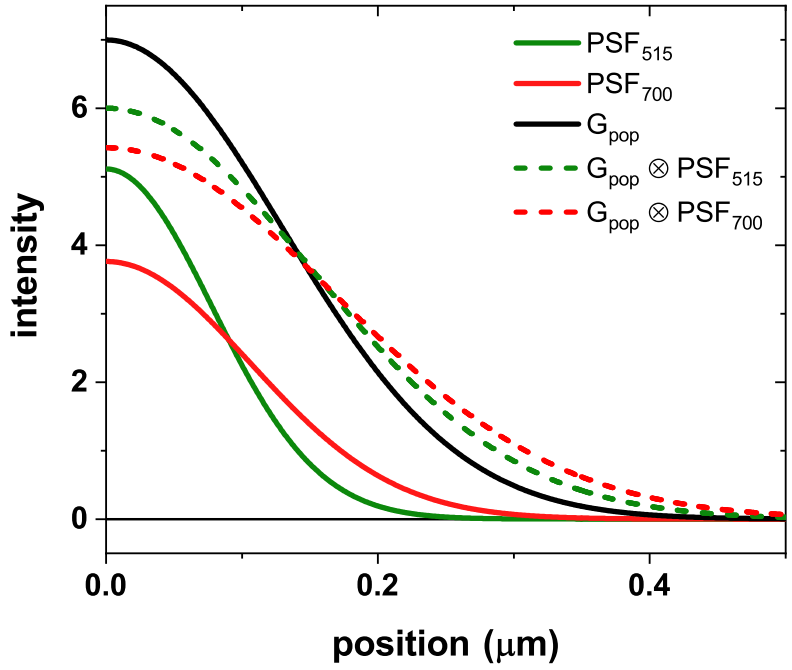

Figure 4.9: Gaussians and convolutions of Gaussians. For a given Gaussian distribution of arbitrary amplitude representing a photogenerated heat population (black), convolution with an imaging probe PSF represented by a normalized Gaussian function (solid red and green curves for a 515 and 700 nm imaging probe, respectively) yields a blurred (suppressed and broadened) measured distribution (dashed red and green curves).

The goal is to transform the measured 515 nm heat distribution data to what would have been measured with a 700 nm probe in order to perform an accurate subtraction of the heat distribution from the total measured differential signal measured with 700 nm, which includes heat and excitonic contributions. The transformation of the measured 515 nm data for this purpose requires suppressing the amplitude and stretching the width of $G_{\mathrm{meas},515}(r)$, as shown in **Figure 4.9** comparing the dashed red and green curves, to represent the additional "smoothing" that would occur with a broader imaging PSF. To make this transformation more concrete, we define a correction factor, κ:

$$\kappa \equiv \frac{\sqrt{\sigma_{\mathrm{pop}}^2 + \sigma_{700}^2}}{\sqrt{\sigma_{\mathrm{pop}}^2 + \sigma_{515}^2}} = \frac{\sigma_{\mathrm{meas},700}}{\sigma_{\mathrm{meas},515}} \tag{4.15}$$

where $\kappa > 1$. We express Equation 4.13 in terms of κ and known variables. The amplitude of $G_{\mathrm{meas},700}(r)$ may be expressed as

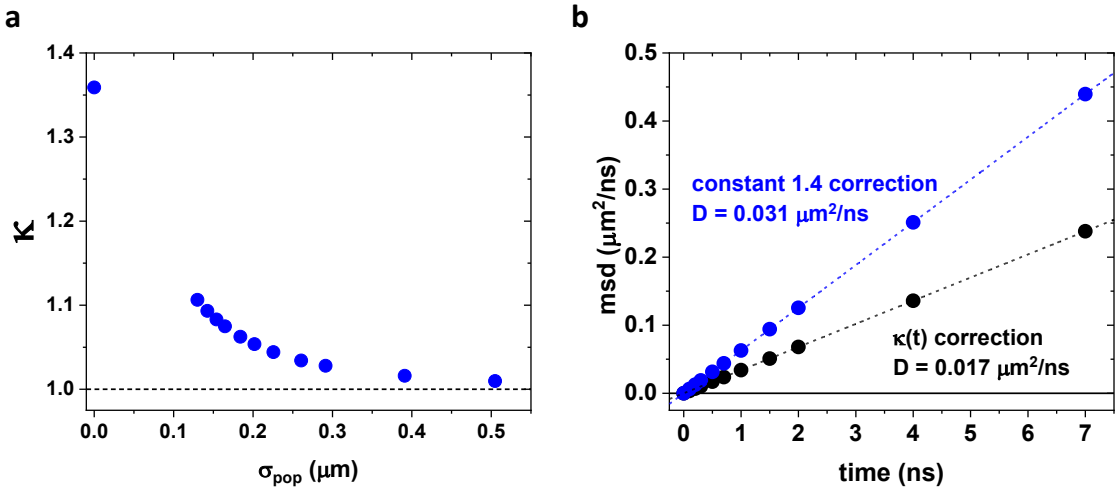

Figure 4.10: PSF correction. **(a)** Correction factor, κ, as a function of the actual population width, σ_{pop}. The maximum correction factor occurs for a delta function population and asymptotes to 1 (no correction) for increasingly broader populations, as expected. **(b)** Data transformation with a time-dependent correction factor $\kappa(t)$ (black) preserves the dynamics of the raw 515 nm data whereas a constant correction (blue) factor inflates the extracted diffusivity.

$$\frac{N_{\text{pop}}\sigma_{\text{pop}}^2}{\sigma_{\text{meas},700}^2} = \frac{1}{\kappa^2}\frac{N_{\text{pop}}\sigma_{\text{pop}}^2}{\sigma_{\text{meas},515}^2}, \tag{4.16}$$

and the Gaussian exponent of $G_{\text{meas},700}(r)$ may be expressed as

$$-\frac{r^2}{2\sigma_{\text{meas},700}^2} = -\frac{1}{\kappa^2}\frac{r^2}{2\sigma_{\text{meas},515}^2} = -\frac{(r/\kappa)^2}{2\sigma_{\text{meas},515}^2} = -\frac{r'^2}{2\sigma_{\text{meas},515}^2} \tag{4.17}$$

where $r = \kappa r'$ represents the "contracted" r-axis when imaging with 515 nm light, which must be multiplied by κ in order to reproduce the effectively "stretched" r-dimension when imaging with 700 nm light. Therefore, to transform the measured 515 nm heat distribution to what would have been measured with 700 nm light requires dividing the measured 515 nm data everywhere by κ^2 and stretching the radial position axis by a factor of κ.

Because the heat distribution expands over time, the correction factor κ is time-dependent:

$$\kappa(t) = \frac{\sigma_{\text{meas},700}(t)}{\sigma_{\text{meas},515}(t)} = \frac{\sqrt{\sigma_{\text{pop}}^2(t) + \sigma_{700}^2}}{\sqrt{\sigma_{\text{pop}}^2(t) + \sigma_{515}^2}} \tag{4.18}$$

so that every time point must be amplitude- and width-corrected by a different (diminishing) factor (**Figure 4.10a**). $\kappa(t)$ is calculated by: (1) extracting $\sigma_{\text{meas},515}(t)$ from the Gaussian

time (ns)	κ
0.0	1.078
0.1	1.071
0.2	1.065
0.3	1.060
0.5	1.052
0.7	1.045
1.0	1.038
1.5	1.031
2.0	1.026
4.0	1.015
7.0	1.010

Table 4.1: Time-dependent PSF correction values

fit to the raw data at each time delay, (2) calculating $\sigma_{\text{pop}}(t)$ using (1) and Equation 4.12, and (3) calculating $\sigma_{\text{meas,700}}(t)$ using the result of (2) in Equation 4.14. The time-dependent correction factors applied to the raw azimuthally averaged 515 nm data before subtracting from the raw azimuthally averaged 700 nm data are listed in **Table 4.1**.

Without accounting for the finite size of the imaged excited population, one may be tempted to use the ratio of the resolution limits at the two imaging wavelengths ($700/515 \approx 1.4$) as a global correction factor. However, the more complete picture described here demonstrates the importance of including the generated population's finite width and its time evolution in our analysis (**Figure 4.10a**). We confirm that the time-dependent correction factor preserves the measured dynamical information in the raw far-from resonant data in **Figure 4.6**, including the mean squared expansion of the heat distribution, which should be invariant to imaging wavelength under identical excitation conditions (**Figure 4.10b**).

Another way to think about transforming the measured 515 nm heat distribution into what would have been measured at 700 nm is to think of a 700 nm PSF as the convolution of a 515 nm PSF with a small adjustment PSF:

$$\text{PSF}_{700} = \text{PSF}_{515} \otimes \text{PSF}_{\text{adj}} \tag{4.19}$$

such that, from the convolution theorem (**Appendix B.3**)

$$\sigma_{700}^2 = \sigma_{515}^2 + \sigma_{\text{adj}}^2. \tag{4.20}$$

For diffraction-limited PSFs with widths defined by Equation 4.8, $\sigma_{\text{adj}} \approx 70$ nm. The actual heat population would then be convolved with this broader PSF:

$$G_{\text{pop}} \otimes \text{PSF}_{700} = G_{\text{pop}} \otimes \text{PSF}_{515} \otimes \text{PSF}_{\text{adj}} = G_{\text{meas,515}} \otimes \text{PSF}_{\text{adj}}. \tag{4.21}$$

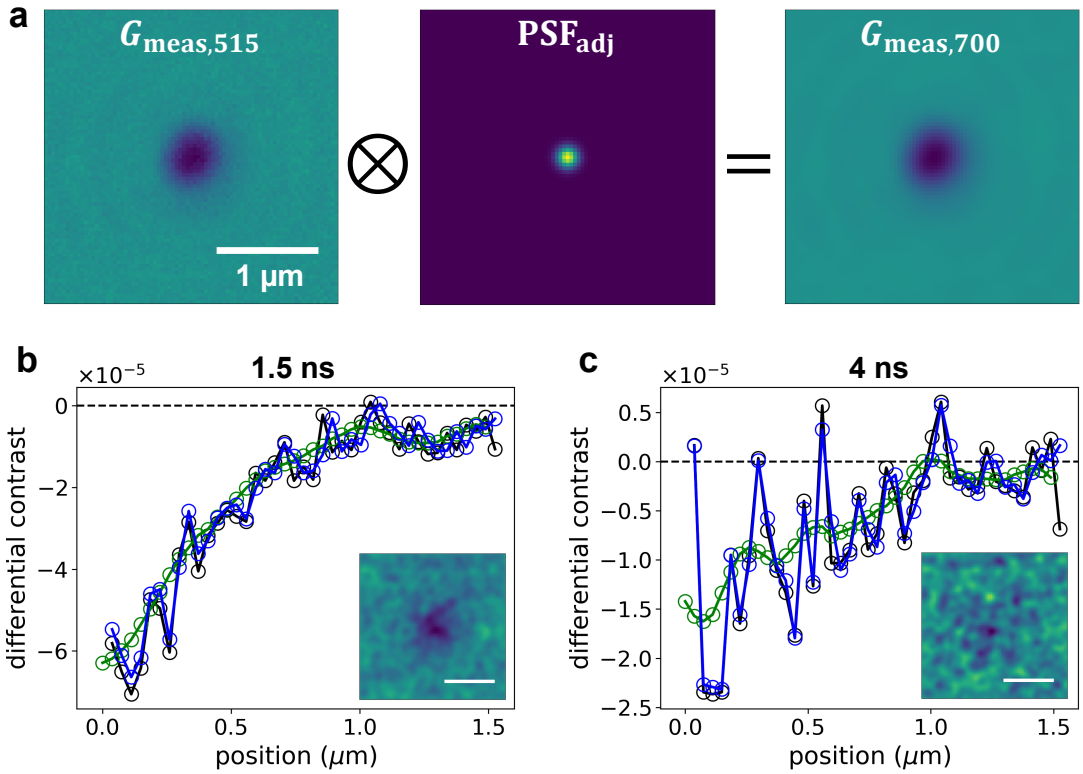

Figure 4.11: 2D convolution correction with an adjustment PSF. **(a)** Measured heat distribution at time zero convolved with adjustment PSF. **(b,c)** Comparison between raw measured heat distribution (black), "kappa" corrected data (blue) and 2D convolved data as in Equation 4.21 (green) for 1.5 (b) and 4 (c) ns time delays, respectively, with inset images showing the result of the 2D "adjustment" convolution. Scale bars are all 1 μm.

Therefore, convolving the measured 515 nm data with this adjustment PSF should accomplish the same task of transforming the 515 nm data to what would have been measured with a 700 nm probe if only heat were detectable at this imaging wavelength. Note that all PSF functions are normalized Gaussians, therefore the area under G_{pop} is preserved in this operation (**Appendix B.3**):

$$2\pi N_{\text{pop}}\sigma^2_{\text{pop}} = 2\pi N_{\text{meas,515}}\sigma^2_{\text{meas,515}} = 2\pi N_{\text{meas,700}}\sigma^2_{\text{meas,700}}. \tag{4.22}$$

While in theory, this correction method should be equivalent to the tabulated "κ" correction described above, in practice the convolution with the adjustment PSF smooths over the noise in the data, and for later time delays when the signal-to-noise ratio is worse, the blurring ultimately distorts the data. The tabulated "κ" correction preserves the raw "noisiness" in the transformation (**Figure 4.11**). In any case, some kind of PSF correction is required

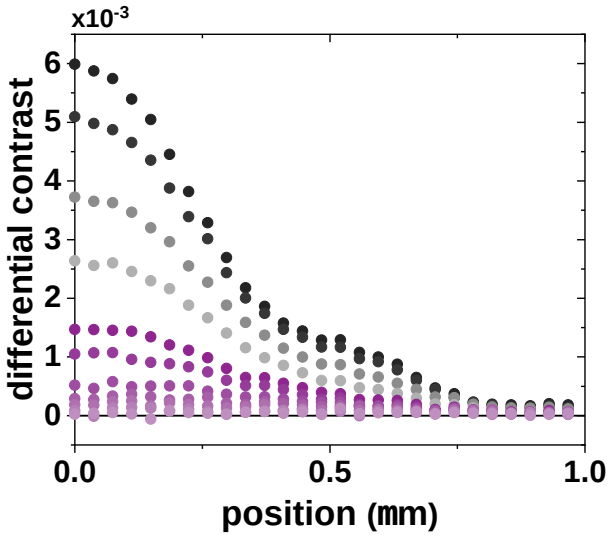

Figure 4.12: Exciton profiles extracted after subtracting the raw far-from resonant heat-dominated profiles (*without PSF correction*) have an extra "bump" near 0.5 µm.

for accurate subtraction of data collected at different imaging wavelengths. Without it, the extracted exciton profiles acquire artifacts like the extra "bump" shown in **Figure 4.12**.

It should be noted that performing a deconvolution of each collected image (pump on and pump off) would obviate the need for any of the PSF correction calculations described here and would be especially valuable in cases where there are overlapping Gaussian populations at multiple imaging wavelengths or inherent anisotropies or heterogeneities that lead to non-isotropic population expansion. In practice, deconvolution over many collected images may become computationally expensive and would require properly flatfield-corrected images and precise knowledge of the imaging PSF. Deconvolutions can also introduce artifacts into the recovered data if not implemented with care. Still, being able to compare directly across any datasets collected at different imaging wavelengths would be very valuable, perhaps a project for future stroboSCAT-ers.

With this PSF correction, the spatial extent of the positive time-zero signal measured with the near-resonant probe (and also the extracted exciton profile at time zero, described below in **Section 4.3.7**) is obviously larger than the corrected negative time-zero signal measured with the far-from resonant probe (**Figure 4.13**). This observation suggests that different imaging PSFs at the two probe wavelengths are not sufficient to explain the discrepancy. Instead, unique dynamics give rise to the differing spatial extent of the positive and negative contrast signals respectively probed near- and far-from resonance, confirming that they represent distinct photoexcited species. As the positive contrast has already been assigned to an exciton population (**Section 4.3.1**), we deduce that the negative contrast far-from resonance must be generated by heat. A single Gaussian function fits all far-from

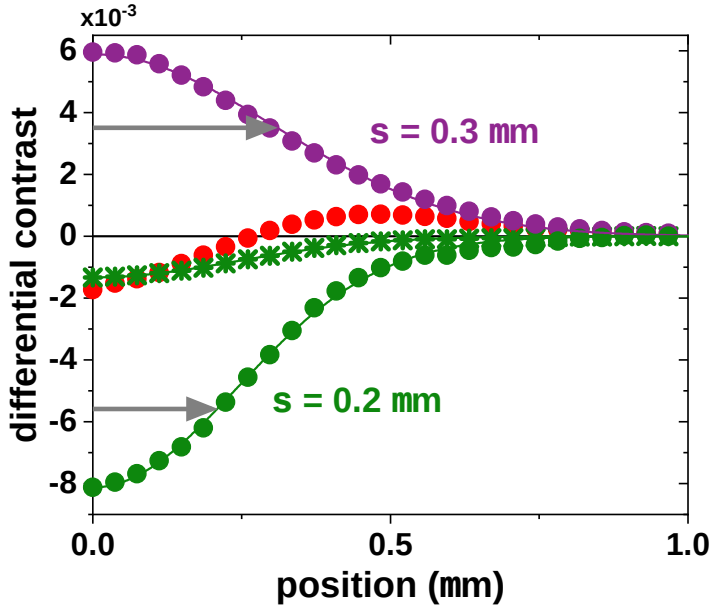

Figure 4.13: Time zero radial profiles of the 2.4 eV probe heat-dominated signal (green stars) following PSF correction, 1.8 eV probe raw signal (red), exciton profile (purple), and 1.8 eV heat profile (green circles).

resonant data well, therefore we deduce that the measurement is dominated by the optical response due to heating, and any potential contribution from excitons (positive or negative) is below our detection limit.

4.3.5 Steady state temperature-dependent reflectance contrast spectroscopy

It is possible to isolate the positive exciton contribution to the near-resonant dataset despite its spatial overlap with the negative heat contribution by using the far-from resonant heat-dominated measurement as a proxy for the heat spatiotemporal evolution, which may be subtracted out. This strategy requires quantitative knowledge of the difference in strength of the optical response due to heating at the two probe energies, the magnitude of which depends on the proximity to exciton resonances. We introduce a scaling factor, η, into this image subtraction to account for this difference: $\eta = \frac{\text{strength of optical response due to heat at 1.8 eV}}{\text{strength of optical response due to heat at 2.4 eV}}$. The far-from resonant stroboSCAT measurement characterizes the optical response due to heating at 2.4 eV. To quantitate the optical response due only to heating near resonance at 1.8 eV, we refer to the temperature-dependent reflectance contrast spectra in **Figure 4.5** which we now describe in more detail.

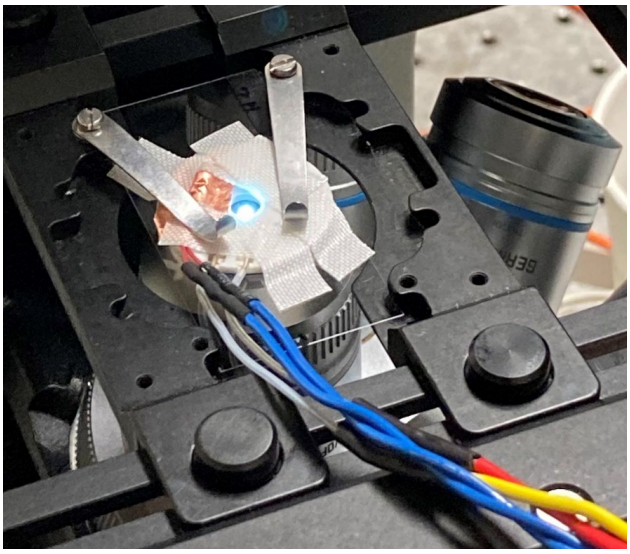

Figure 4.14: Ceramic heater centered and mounted onto the 4L MoS_2 sample in an inverted reflectance contrast microscope in the Harry Atwater lab at Caltech.

We transport the 4L MoS_2 sample to Caltech to visit **Joeson** and **Cora** and perform reflectance contrast spectroscopy measurements in their lab. Broadband emission from a stabilized tungsten-halogen lamp source (ThorLabs SLS201L) is spatially filtered through an optical fiber then focused into a 0.9 NA air objective in a Leica DMi8 inverted microscope, illuminating the sample within a ∼1 µm spot size. The reflected light output is fiber-coupled to a calibrated Princeton Instruments Spectrometer (HRS300) with ∼1.5 nm spectral resolution. Spectra are collected by averaging 500 frames (10 ms exposure per frame) together for each temperature-dependent spectrum after heating and equilibrating the sample for 5 minutes. We also use a hefty ceramic heater (HT19R) with a small opening (4 mm diameter) to decrease the distance between the heater and the sample to lower both the thermal equilibration time and the temperature gradient between the heater and sample. To provide a precise but macroscopic indicator of the sample location in order to center the small heater opening over the sample directly, we mark a separate, clean glass coverslip with a small Sharpie spot and align the mark underneath the sample flake in a high-power optical microscope. Then, we add thermal paste to the underside of the heater, center its opening over the marker spot, press it onto the 4L MoS_2 substrate, and secure it with fiberglass tape (**Figure 4.14**). To characterize the temperature-dependent reflectance contrast, we follow this general procedure:

1. allow the system to equilibrate for 5 min at the new temperature set point
2. image and align the field of view by jogging the $x-y$ sample stage to the bare substrate

3. send the output to the spectrometer and focus the live spectrum to the R_0 room temperature spectrum collected before ramping up the heater temperature
4. acquire 500 spectra under the substrate to characterize R_0
5. immediately, without changing the focus, jog back to the center of the sample and acquire 500 spectra to characterize R
6. increment the temperature set point by 5°C
7. repeat steps 1-6 for all temperature set points from $25 - 90$°C

One nice feature of this setup is that we could repeatably jog back and forth between the same location on the bare substrate and the encapsulated 4L MoS_2 by stepping the $x - y$ piezo sample stage, enabling very reproducible measurements. We should, however, have inserted a step after #2 above to collect a background spectrum before each set of R and R_0 spectra in order to increase the signal-to-noise ratio, especially in the spectral region near 2.4 eV where the lamp intensity is low. In addition, we never measured the room temperature in the Caltech lab and it may not have been as well controlled as the stroboSCAT laser lab (~ 22°C $\pm$ 0.3°C as in **Figure 2.21**). The use of an air objective in the Atwater reflectance contrast microscope adds an additional index-mismatched interface that enhances the overall reflection compared to what would be measured with an oil immersion objective. We use transfer-matrix simulations (**Appendix B.4**) to estimate a correction factor to convert between the air and oil immersion objective cases: $R_{\text{oil}} \backsimeq R_{\text{air}} - \frac{R_{0,\text{air}}}{2}$ where R is the reflectance under the sample and substrate and R_0 is the reflectance under the substrate only. The reflectance contrast, $RC = R/R_0$, may then be converted as $RC_{\text{oil}} = 2RC_{\text{air}} - 1$.

To estimate the temperature-dependent contribution to the stroboSCAT contrast at the near-resonant 1.8 eV probe, we first extrapolate the temperature-dependent reflectance contrast, binned over the 4 nm laser line, to room temperature (22°C in the temperature-controlled stroboSCAT laser lab) to extract $RC_{\text{room temp}}$, the y-intercept in **Figure 4.15a**. Next, we reframe the RC in units of differential stroboSCAT contrast by calculating the difference between the reflectance contrast at 1.8 eV found at each given elevated temperature and the value measured at room temperature and then normalizing it to the room-temperature response: $(\Delta R/R)_{\text{heating}} = \frac{RC_{\text{hot}} - RC_{\text{room temp}}}{RC_{\text{room temp}}}$. Finally, for direct comparison to stroboSCAT contrast, the result is multiplied by -1 to account for a relative difference of π in the Gouy focusing phase of the focused and widefield probes used in the reflectance contrast and stroboSCAT measurements, respectively. The result is plotted in **Figure 4.15b** for each heater set point up to 90°C ($\Delta T = 70$ K) with a linear fit that goes through the origin, the slope of which, -0.00042(5)/K, quantifies the predicted differential stroboSCAT contrast associated with a given temperature increase. To estimate the temperature at which to compare to η, we use a spatiotemporal kinetic model (**Section 4.3.8**) to iteratively fit exciton and heat experimental profiles until the predicted maximum achieved temperature in the MoS_2 matches

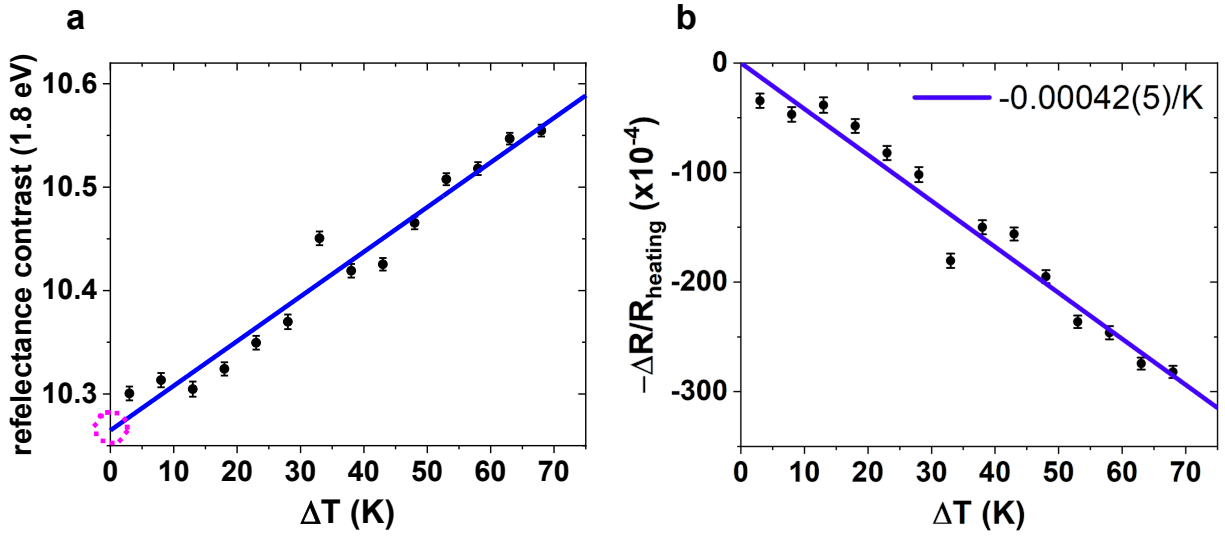

Figure 4.15: Temperature-dependent reflectance contrast spectroscopy. **(a)** Reflectance contrast at 1.8 eV as a function of sample temperature elevation. The trend is extrapolated to room temperature ($\Delta T = 0$, pink dashed circle) using a linear fit (blue line). **(b)** Expected differential contrast due to heating, $\left(\frac{\Delta R}{R}\right)_{\text{heating}} = \frac{RC_{\text{hot}} - RC_{\text{room temp}}}{RC_{\text{room temp}}}$, at 1.8 eV. The vertical axis is multiplied by -1 for direct comparison to widefield stroboSCAT measurements. The linear fit (blue line) has a fixed intercept through the origin.

the value of η used in the fit. With this method we estimate that the sample reaches a maximum temperature of 18 K above room temperature after accounting for fast interfacial heat transfer to surrounding hBN, a reasonable estimate that is close to the predicted temperature increase from thermalization to the band edge. We perform a simple calorimetry calculation to estimate the maximum temperature in the sample if all absorbed photons were converted to heat (**Appendix B.2**). Using a peak carrier density in the center of the excitation spot of $N_{\text{peak}} = 3.5 \times 10^{13}$ cm^{-2}, a pump energy of $E_{\text{pump}} = 2.8$ eV, and a specific heat capacity [332] of $c = 15.22$ cal/(mol·K) $= 3.27 \times 10^{12}$ eV·cm^{-2}K^{-2}, the maximum sample temperature increase is given by $\Delta T_{\text{max}} = N_{\text{peak}} E_{\text{pump}} c = 30$ K. Roughly half of this heat is due to thermalization to the indirect bandgap: $\Delta T_{\text{therm}} = N_{\text{peak}}(E_{\text{pump}} - 1.4 \text{ eV})c = 15$ K. The scaling factor η is therefore given by the ratio between the predicted maximum stroboSCAT contrast due to heat near resonance divided by the maximum stroboSCAT contrast at time zero in the far-from resonant measurement:

$$\eta = \frac{-0.00042(5)/\text{K} \times \Delta T_{\text{max}}}{-0.00124(2)} = \frac{-0.00042(5)/\text{K} \times 18 \text{ K}}{-0.00124(2)} = 6.1(5). \tag{4.23}$$

We assume that the sample reaches the temperature set point. We estimate that even if the sample at the highest temperature set point was 5°C cooler than the heater, the effect on the extracted slope in **Figure 4.15b** would be negligible; η would increase to $\eta = 6.7(4)$

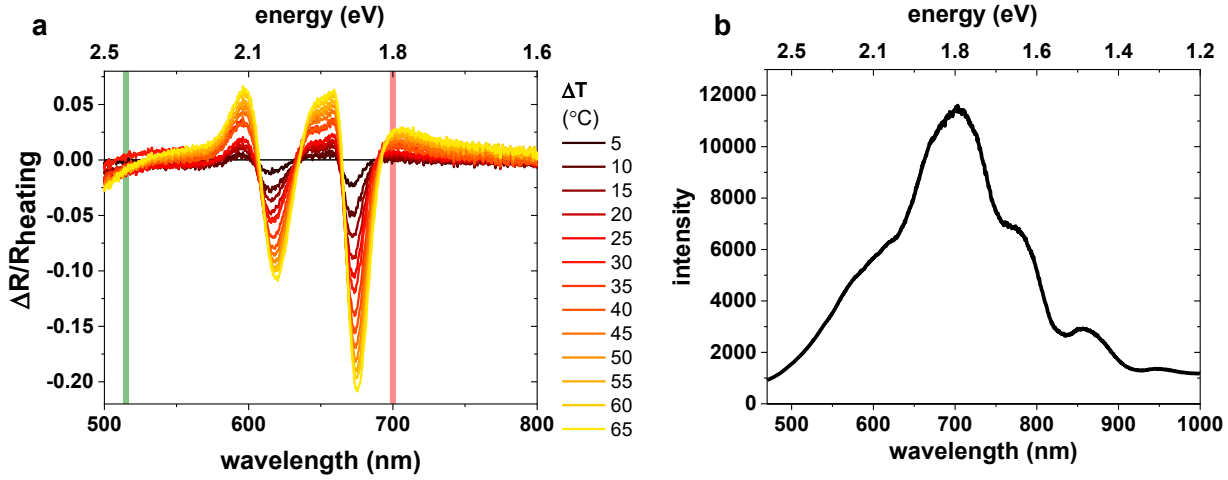

Figure 4.16: Obstacles to measuring the response due to heating at the far-from resonant probe energy. **(a)** Constructed differential reflectance spectra due to steady state heating normalized to the lowest controlled temperature set point spectrum (25°C). A zero-crossing near 2.4 eV (green line) further complicates reliable quantification of the optical response due to heating at this energy, while the trend near 1.8 eV (red line) is clear and monotonic (**Figure 4.15b**). **(b)** The spectral power distribution of the stabilized tungsten-halogen light source has relatively low intensity near 2.4 eV.

from $\eta = 6.1(5)$.

The lowest controlled heater set point (25°C) was used as a proxy for room temperature to normalize higher temperature set points in the construction of a differential reflectance spectrum due to sample heating:

$$\Delta R/R_{\text{heat}} = \frac{RC_{\text{hot}} - RC_{25°\text{C}}}{RC_{25°\text{C}}}, \tag{4.24}$$

yielding a qualitative representation of the optical material response due solely to heating (**Figure 4.16a**). A zero crossing in the differential spectrum, in addition to poor lamp spectral power above 2.2 eV (**Figure 4.16b**), adds significantly to the uncertainty near 2.4 eV and precludes quantitative analysis of the expected $\Delta R/R$ contrast due to heating in this spectral regime.

We initially set out to measure the temperature-dependent reflectance contrast in the stroboSCAT microscope by mounting a ceramic heater (ThorLabs HT10KR2 shown in **Figure 4.17a**) onto the 4L MoS_2 sample with fiberglass tape and measuring the reflected probe profile under the sample and under the neighboring bare substrate as a function of temperature, up to a 75°C temperature set point, the maximum temperature we felt comfortable heating a slide in close contact with the oil immersion objective. We first characterized the heater and substrate response by simultaneously measuring the actual heater temperature

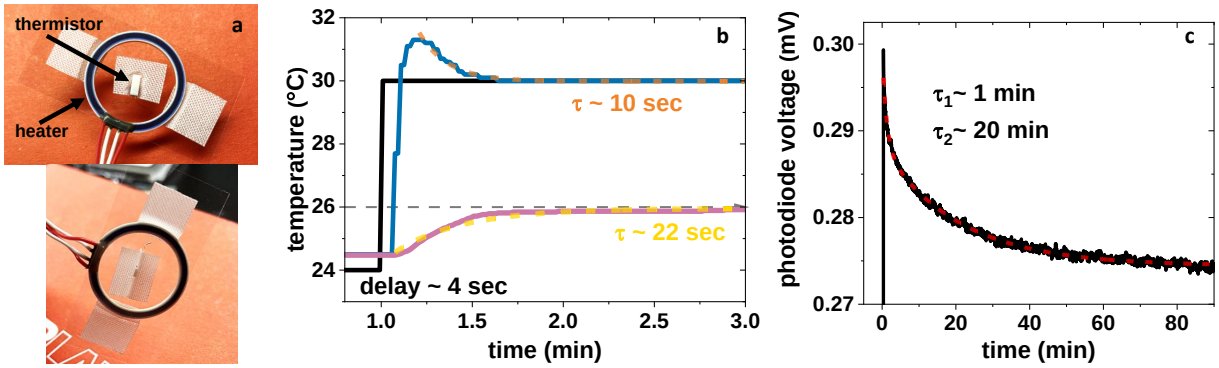

Figure 4.17: Ceramic ring heater characterization. **(a)** Ceramic heater (20 mm inner diameter ring) and thermistor mounted on a glass substrate with fiberglass tape using the full thermistor face (top) compared to the smaller top edge (bottom). **(b)** Temperature set point (black), heater temperature (blue) and thermistor temperature (pink) after changing the temperature set point from below room temperature (no heating) to 30°C. Time constants are from single exponential fits (dashed lines) to the rise or fall of the substrate or heater temperature, respectively. **(c)** Photodiode voltage monitoring the intensity of the probe diode laser right after the laser interlock is disabled. A fit to a biexponential decay (red dashed line) reveals a fast time component that could be associated with electronic optimization of the diode laser current for lasing followed by a longer component that may be from thermal drift, even though the diode laser heads have integrated Peltier cooling.

(blue curve in **Figure 4.17b**) using its integrated thermistor and the substrate temperature in the center of the heater (pink curve in **Figure 4.17b**) using a platinum thermistor (ThorLabs TH100PT shown in **Figure 4.17a**) as a function of temperature set point (black curve in **Figure 4.17b**). After a short delay between the input of a new temperature set point, the ceramic heater temperature overshot, then fully stabilized to the 30°C set point in ∼40 seconds using feedback control parameters $P = 125$, $I = 0$ and $D = 0$. The substrate temperature ramped up more slowly, reaching a steady state temperature of 26°C in ∼90 seconds. The offset between the steady state temperature of the heater and the center of the substrate would generate a temperature gradient across the 4L MoS_2 encapsulated region of at most 0.02°C. Note that when using the smaller top edge of the thermistor to measure the center substrate temperature instead, (2.6 mm^2 compared to 10 mm^2 full-face area), the steady state temperatures were $\sim 0.5 - 1$°C cooler compared to using the full thermistor face. From these characterizations, we set a generous equilibration time of at least 5 minutes for all of the components to reach a steady state after incrementing the temperature set point by $\Delta T = 5$°C.

The reproducibility of the focus and imaging field of view were major challenges for these $RC(T)$ measurements. We tried several approaches to eliminate sources of drift and other measurement variability: measuring with a widefield probe, measuring with a fo-

cused probe, correcting for the laser lab temperature fluctuations, carefully registering image stacks in post-processing, looking at image histograms after thresholding, blurring images with Gaussian filters, scrambling the beam coherence with a diffuser, averaging multiple measurements together. But in the end, we did not reliably resolve any temperature- or wavelength-dependent RC trends in the stroboSCAT microscope. In the process, we characterized the diode laser stability after a "cold" unlock – that is, after the lasers had been off overnight – by placing a photodiode (ThorLabs PDA100A) before the last alignment iris to monitor the beam intensity that transmitted through the beamsplitter underneath the objective (**Figure 4.17c**). Right after the laser was unlocked, it reached its spec'd 1% RMS stability within seconds but it took over an hour for the output to stabilize on longer time scales. For the pulse-to-pulse $\sim$ ps differential imaging in stroboSCAT, this long-term drift is not an issue, but for comparing differential RC images collected over the course of an hour or more, long-term laser stability is necessary. Even after letting the lasers warm up for two hours before beginning any measurements, leaving them unlocked for the entirety of the measurement, and normalizing to the PD voltage, we still observed no reliable RC trends. With the spectroscopy experiments described above, we decreased the error bar on RC from ± 0.02 in the stroboSCAT microscope to ± 0.006 in the Caltech setup and clearly resolved the trend in $RC(T, \lambda)$.

4.3.6 Comparison of the photoexcited transient spectrum and the steady state differential heating spectrum

We use the spectroSCAT arm in the stroboSCAT instrument (**Section 2.5.5**) to collect *transient* reflectance spectra in the 4L MoS_2 sample following photoexcitation with the same diode laser source (440 nm) that is used for all TMDC measurements in this chapter. The white light is generated by focusing the fundamental 1030 nm output of an ultrafast regeneratively amplified laser system into a 3 mm sapphire crystal (**Figure 2.26**). The time zero and $t = 0.1$ ns time delay spectra are shown in **Figure 4.18a**. White light fluctuations near the second harmonic (515 nm) of the fundamental add significant noise below $\lesssim$ 575 nm, completely obscuring the true transient response in this spectral regime. The change in the transient reflectance between the two spectra is in fact larger at 515 nm than at either of the exciton peak resonances where the shifts should be most pronounced. When we track the white light fluctuations over the course of the $\sim$20 min measurement, the differential contrast jumps about the zero baseline near 515 nm whereas a similarly detuned but stable spectral region near 775 nm shows a steady trend (**Figure 4.18b**). To avoid this challenge in future measurements, a more experienced white light whisperer might be able to optimize the neutral density filter and aperture before the focusing lens into the sapphire crystal to stabilize the output. The sapphire crystal could also be exchanged for an yttrium aluminum garnet (YAG) or CaF_2 crystal, although they would generate an entirely different white light spectrum.

We note that the shape and location of resonance features in the differential heating

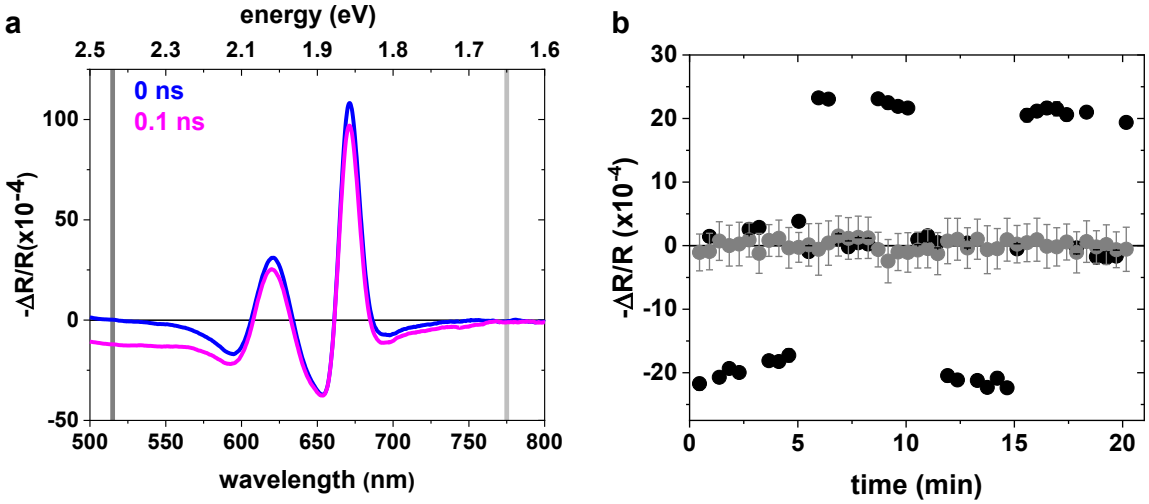

Figure 4.18: White light fluctuations dominate the transient reflectance response $\lesssim 575$ nm in 4L MoS_2. **(a)** Transient reflectance spectra collected at 0 ns (blue) and 0.1 ns (pink) time delays. While the baseline returns reliably to zero on the red side of the exciton resonances (light gray line), the baseline fluctuates drastically on the blue side of the exciton resonances (dark gray line). **(b)** Binned differential reflectance values as a function of time for 510-520 nm (black) and 770-780 nm (gray).

spectra are strikingly similar to the transient differential reflectance spectra measured after photoexcitation, suggesting that even modest sample heating dominates the transient response (**Figure 4.19**). We use the peak positions and zero crossings in each spectrum to recalibrate the spectroSCAT energy axis since it was initially calibrated using a notch filter (ThorLabs FGB67) whereas the Caltech spectrometer was more carefully calibrated using mercury and argon/neon sources. Still, the two spectra cannot be compared quantitatively. The $-\Delta R/R$ magnitude of the spectroSCAT spectrum depends on how many spatial pixels are averaged over in the rectangular region in **Figure 4.19**; the magnitude increases for decreasing bin width from the full frame height (128 pixels) down to about 13 pixels ($\sim$0.5 µm). For bin widths narrower than this, the magnitude of the transient response stays roughly the same but continues to become noisier. This cutoff likely depends on the slit width, which here was optimized by closing the slit completely, then opening it the minimum amount to produce a clean, stable spectrum. In addition, spectroSCAT measurements have contributions from both heat and excitons, both of which vary spatially (inset in **Figure 4.19**)! Furthermore, the pump was slightly smaller than the focused white light probe, which is not ideal for mitigating these spatially-dependent effects. While the spectra cannot be compared quantitatively, e.g., by subtracting the two to extract an exciton-dominated spectrum, their peak positions and relative amplitudes are strikingly similar, highlighting the importance of fully characterizing heating-induced effects to the transient response.

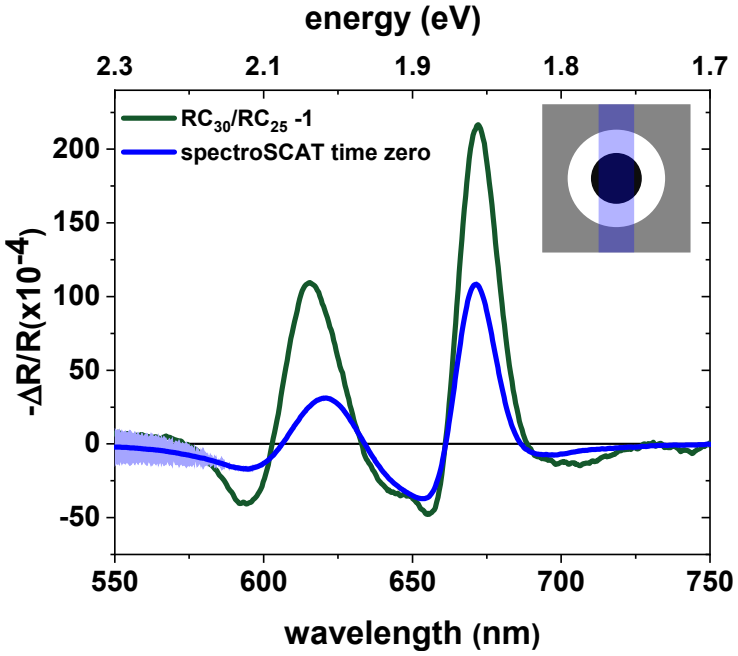

Figure 4.19: Expected differential contrast due to steady state heating by $\Delta T = 5°C$ (green) and photoexcited time-zero differential reflection spectrum (blue) averaged over a 500 nm line cut through the central excitation. Measurements are taken on the same 4L MoS_2 sample in separate instruments in the Atwater and Ginsberg groups, respectively. Shaded error bars on the spectroSCAT curve are estimated from the white light fluctuations shown in **Figure 4.18**. Inset image shows the spatial integration that occurs in a spectroSCAT measurement, which averages over a slice in the sample plane.

4.3.7 Quantitatively isolating exciton dynamics with scaled image arithmetic

With the interpretation and strategy developed above, we obtain the population dynamics and transport parameters for both heat and excitons in the encapsulated 4L MoS_2. We determine the thermal dynamics by fitting each azimuthally averaged spatial distribution of each time point in the far-detuned stroboSCAT measurement to a Gaussian function (**Figure 4.20b**). The thermal conductivity of hBN is 15× greater than in MoS_2, therefore we assume the heat transfer to hBN to be unidirectional and irreversible. We find that the integrated temperature profile has an initial fast ∼300 ps decay due to interfacial transfer to the encapsulating hBN, and then heat transfers more slowly once the temperature gradient has lessened, limited by the rate of heat diffusion in the hBN (**Figure 4.20c**). Although hBN is a good thermal conductor, its capacity to sink heat generated in MoS_2 is limited by the evolving temperature gradient between the two materials and the finite volume of hBN. If the very center ($r = 0$) of the original exciton profile (and resulting) temperature profile

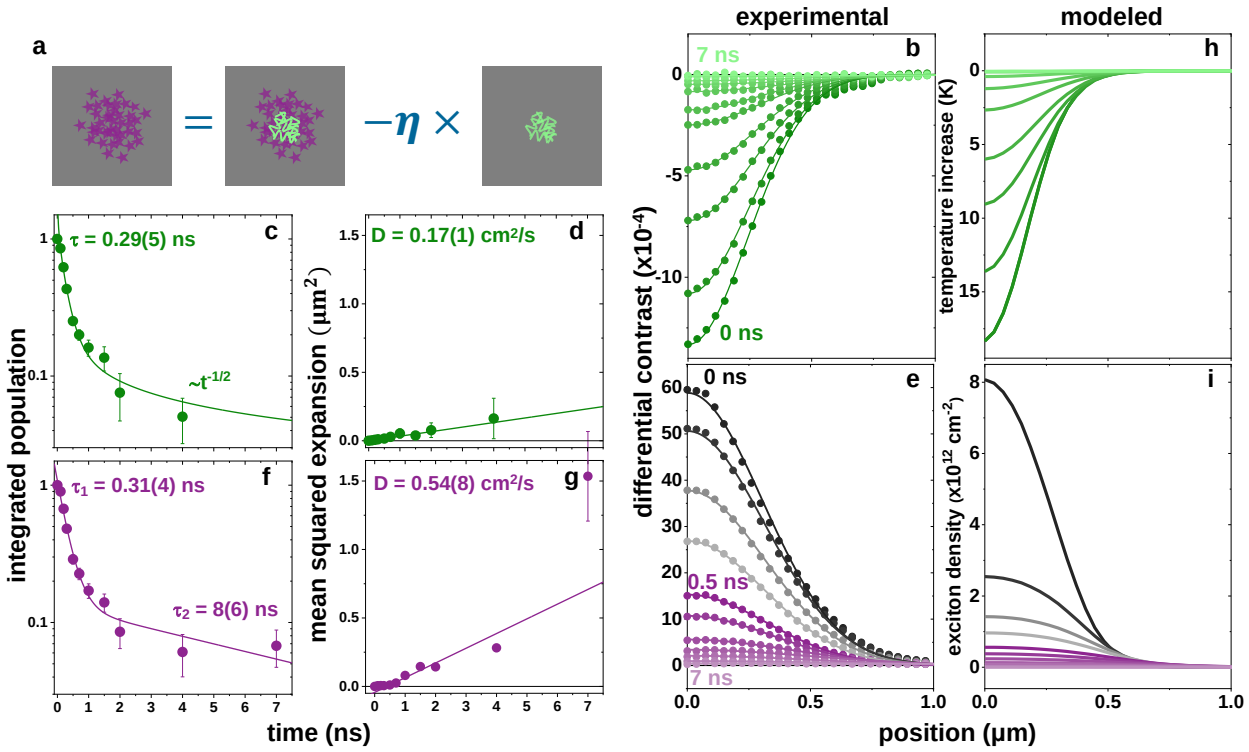

Figure 4.20: **(a)** Image arithmetic to isolate exciton distributions (purple) from thermal ones (green) when they coexist, with a scaling constant accounting for the wavelength-dependent sensitivity to optical perturbations depending on proximity to electronic resonances. **(b)** Azimuthal averages for the data shown in the bottom row of **Figure 4.6** representing thermal distributions. **(c,d)** Integrated population decay fit to a single exponential plus power law (c) and mean squared expansion fit to a line (d) for the thermal distributions in (b). **(e)** Azimuthally averaged isolated exciton profiles after scaled image subtraction of the near- and far-from-resonant datasets in **Figure 4.6**. **(f,g)** Integrated population decay fit to a biexponential (f) and mean squared expansion fit to a line starting at 0.5 ns (g) for the exciton distributions in (e). **(h,i)** Predicted thermal (h) and exciton (i) distributions from a spatiotemporal kinetic model best fit of the experimental data in (b,e).

in MoS_2 is the most critical, we ask: How does the temperature of the hBN at $r = 0$ scale as a function of time? To answer this question, we assume that (1) initially the temperature profile in hBN mimics that of the MoS_2, i.e., is Gaussian, and that (2) the temperature profile in hBN evolves according to the heat equation, i.e., standard diffusion with a mean squared expansion governed by $\sigma^2(t) - \sigma^2(0) \sim D_{\mathrm{hBN}}t$. The amplitude of a Gaussian profile that expands due to diffusion is given by

$$g(r = 0) = \frac{1}{\sigma\sqrt{2\pi}} \propto t^{-1/2}. \tag{4.25}$$

Therefore, once initial heat transfer is limited by the rate at which heat diffuses in the hBN, the rate at which the temperature lessens in the hBN will also determine the rate of interfacial thermal transfer for the MoS_2 and scale as $t^{-1/2}$ in the ∼ns time frame. We obtain an in-plane heat diffusivity in the MoS_2 of 0.17 cm^2/s, consistent with the reported lateral thermal conductivity for MoS_2 (**Figure 4.20d**) [333].

In order to quantitatively discern exciton dynamics from heat dynamics, we combine the data analysis methods and temperature-dependent RC spectroscopy measurements described above to perform frame-by-frame azimuthal profile subtraction of the near- and far-from resonant stroboSCAT datasets (**Figure 4.20a**). First, each Gaussian fit profile representing the heat population (temperature profile) in the far-detuned measurement is width- and amplitude-adjusted by a time-dependent PSF correction factor. This operation generates the *shape* of the isolated heat distribution that would have been measured with the near-resonant probe. Next, we multiply the PSF-corrected heat profiles by the above-deduced scaling factor, η, to quantitatively represent the differential contrast profile due to heating near resonance. Finally, we azimuthally average the total near-resonant stroboSCAT signal and subtract the PSF-corrected and scaled heat-only component obtained from the far-from resonant dataset. The isolated radial exciton profiles are near-Gaussian, as shown in **Figure 4.20e**. The spatially integrated exciton population dynamics fit best to a biexponential exciton decay, which we attribute to density-dependent A-M interactions that dominate at early time delays when exciton densities are higher (τ_1 = 310 ps), followed by slow nonradiative recombination of the IDE over $\tau_2 \sim 8$ nanoseconds (**Figure 4.20f**). The exciton profiles at time delays earlier than 500 ps (grayscale) do not appear to expand, potentially due to the presence of some higher-energy A excitons from partial temporal overlap of the pump and probe pulses at early time delays or other photoinduced dynamics that we cannot resolve with the ≈200 ps IRF. The extracted exciton diffusivity for ≥500 ps, once it is possible to see the profiles expanding, is 0.5 cm^2/s, in agreement with other measurements in few-layer TMDCs (**Figure 4.20g**) [49, 315, 334]. Repeating this dynamical analysis over a range of values of η from 1.4 to 7 enables an estimate of the uncertainties in the extracted diffusivities, based on uncertainty in the initial maximum sample temperature elevation that we can safely bound between 4 and 20 K.

4.3.8 Supporting experimental findings with a spatiotemporal kinetic model

We support these findings with a spatiotemporal kinetic model that describes the coupled dynamics of excitons and heat. A simple set of coupled equations captures the expansion and decay of excitons whose energy is overwhelmingly (due to very low PLQY) converted to heat via either nonradiative hot carrier relaxation following optical excitation or A-M decay:

$$\dot{N}(r,t) = D_{\mathrm{X}}(r,t)\nabla^2 N(r,t) - \frac{1}{\tau_{\mathrm{X}}}N(r,t) - R_{\text{A-M}}N^2(r,t) + G(r,t) \tag{4.26}$$

$$\dot{T}(r,t) = \alpha N^2(r,t) - \frac{1}{\tau_{\mathrm{T}}}[T(r,t) - T_0] + D_{\mathrm{T}}\nabla^2 T(r,t) + \beta N(r,t) + \gamma G(r,t). \tag{4.27}$$

Equation 4.26 describes the evolution of the exciton population, $N(r,t)$. The first term describes exciton diffusion due to the pump-induced exciton population gradient, with an exciton diffusivity of D_{X}. The second term describes single exciton recombination, where τ_{X} is the recombination lifetime. The third term describes biexciton recombination due to A-M interactions, where $R_{\text{A-M}}$ is the A-M coefficient. Finally, $G(r,t)$ describes the generation of excitons from the pump pulse [s^{-1}], which has a pulse width of 72 ps and a spatial width, σ, of 168 nm. Equation 4.27 describes the temperature or heat population, $T(r,t)$. The first term accounts for the temperature increase due to nonradiative relaxation of hot excitons that are created via A-M recombination, where $\alpha = \frac{R_{\text{A-M}}E_{\mathrm{G}}}{c}$, E_{G} is the indirect bandgap energy, and c is the specific heat. The second term describes the decay of the temperature profile back to its initial room temperature value, T_0, with a lifetime τ_{T}, and the third term describes heat diffusion with diffusivity D_{T}. The fourth term describes the temperature increase due to nonradiative single-exciton recombination, where $\beta = \frac{(1-\mathrm{PLQY})E_{\mathrm{G}}}{\tau_{\mathrm{X}}c}$. The last term describes the heat generated when excitons relax to the band edge after pump excitation, where $\gamma = \frac{E_{\mathrm{P}}-E_{\mathrm{G}}}{c}$ and E_{P} is the pump pulse energy. In addition, when propagating these equations in time, the heat decay phenomenologically transitions to a $t^{-1/2}$ scaling after 700 ps to represent thermal transfer to hBN. To fit the model to the time series of exciton profiles extracted above, along with the corresponding heat profiles obtained far-from resonance, we allow τ_{X} and D_{X} to vary only within the experimentally determined uncertainty and $R_{\text{A-M}}$ to vary within the literature estimates [335]. We approximate the indirect bandgap by the peak position of the IDE PL (1.4 eV). All other parameters are fixed by our experimentally obtained values or from literature values [25, 332].

Equations 4.26 and 4.27 were recast in natural units and expressed in matrix form for the `pdepe` function in MATLAB:

$$\begin{aligned}\frac{\partial}{\partial t}\begin{bmatrix}u_1\\u_2\end{bmatrix} = \frac{1}{r}\frac{\partial}{\partial r}\left(r\begin{bmatrix}\mathrm{A}u_2\partial_r u_1 + \mathrm{B}u_1\partial_r u_2\\ \partial_r u_2\end{bmatrix}\right)\\ + \begin{bmatrix}-\frac{\tau_T}{\tau_X}u_1 - \tau_T R_{\text{A-M}}N_0 u_1^2 + \tau_T g - (\mathrm{A}+\mathrm{B})\partial_r u_1\partial_r u_2\\ \alpha N_0 \mathrm{C}u_1^2 - (u_2 - 1) + \beta\mathrm{C}u_1 + \gamma\mathrm{C}g\end{bmatrix}\end{aligned} \tag{4.28}$$

where

$$t' \equiv t/\tau_T \tag{4.29}$$
$$r' \equiv r/\sqrt{D_T\tau_T} \tag{4.30}$$
$$u_1(r',t') \equiv N(r,t)/N_0 \tag{4.31}$$
$$u_2(r',t') \equiv T(r,t)/T_0, \text{ and} \tag{4.32}$$
$$g(r',t') \equiv G(r,t)/N_0, \tag{4.33}$$

and we define

$$\mathrm{A} \equiv \frac{\mu k_B T_0}{qD_T} \tag{4.34}$$
$$\mathrm{B} \equiv \frac{q\mu s T_0}{D_T}, \text{ and} \tag{4.35}$$
$$\mathrm{C} \equiv \frac{N_0\tau_T}{T_0}. \tag{4.36}$$

The initial conditions were set to be $N(r,0) = 0$ and $T(r,0) = 300$ K. The boundary conditions were set so that the exciton and temperature fluxes go to zero.

To model the pump pulse, which has a finite duration, we used a generating function, $G(r,t)$, which is a product of two Gaussian functions. The first is a Gaussian in space with a standard deviation of σ_r. At the center, the peak exciton density is N_0. The second is a Gaussian in time with a standard deviation of σ_t and normalized to 1. Therefore,

$$G(r,t) = N_0 \exp\left[\frac{-r^2}{2\sigma_r^2}\right] \frac{1}{\sqrt{2\pi\sigma_t^2}} \exp\left[\frac{-(t-t_0)^2}{\sigma_t^2}\right], \tag{4.37}$$

or in natural units,

$$g(r',t') = \frac{1}{\tau_T\sqrt{2\pi\sigma_t^2}} \exp\left[\frac{-r^2}{2\sigma_r^2}\right] \exp\left[\frac{-(t-t_0)^2}{\sigma_t^2}\right]. \tag{4.38}$$

Multistart optimization was performed with 500 starting points over a constrained 3-parameter space with least squares minimization to the measured heat and isolated exciton profiles. The exciton mobility and lifetime were allowed to vary over the range $15 < \mu < 22$ cm^2/V·s and $1 < \tau_X < 23$ ns, constrained by the experimentally extracted diffusivity and long decay time constants across exciton profiles extracted from $1.4 < \eta < 7$. The A-M coefficient, $R_{\text{A-M}}$, was constrained from estimated literature values to $5 \times 10^{-5} < R_{\text{A-M}} < 5 \times 10^{-2}$ cm^2/s [335]. The heat diffusivity and lifetime were fixed by the experimentally measured values. We estimate that, typical for few-layer MoS_2 where light emission from the indirect bandgap must be phonon-assisted, the PLQY is ∼1%, although we found that the peak time-zero temperature is insensitive to the value of the PLQY used.

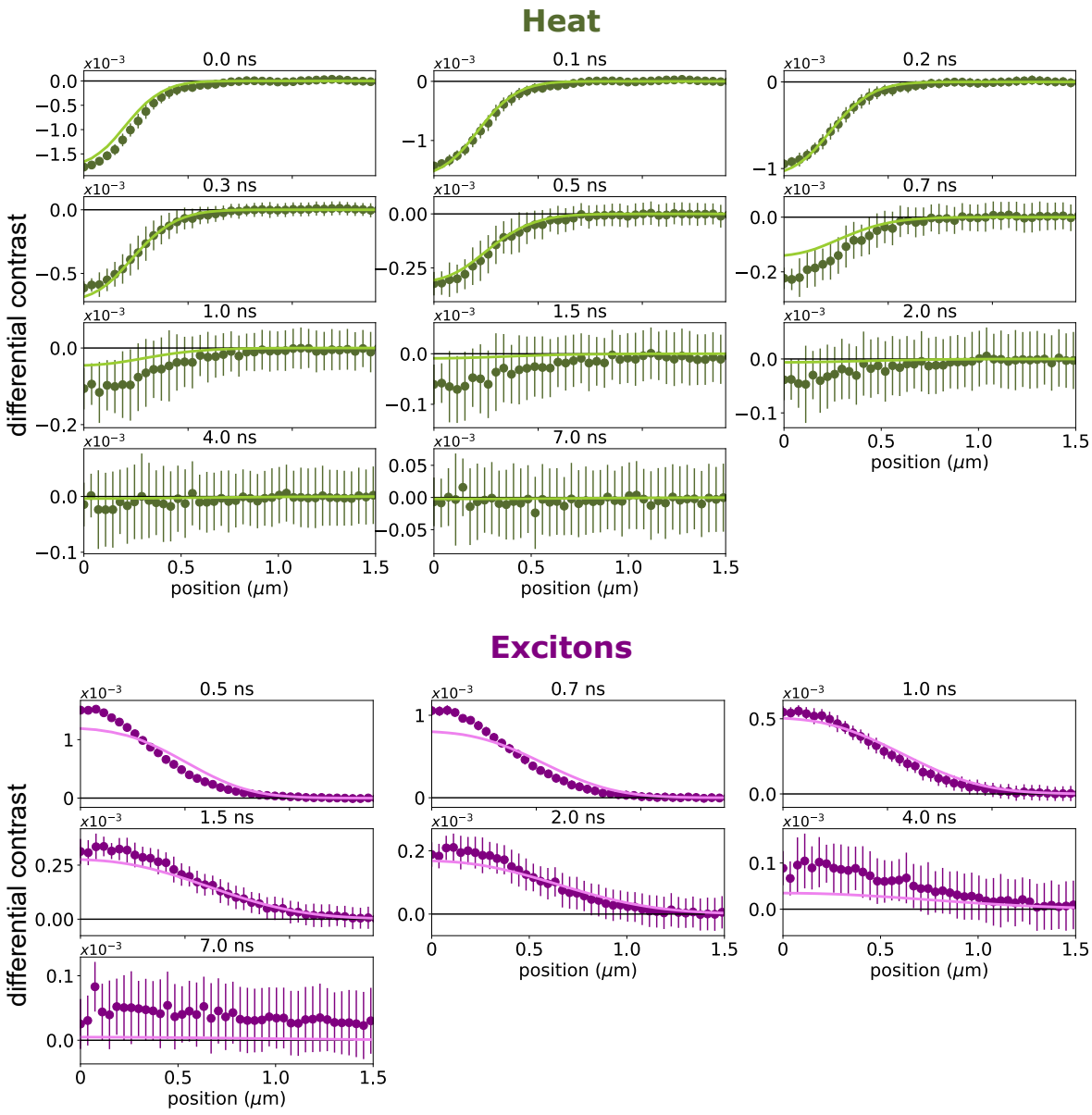

Figure 4.21: (top) Experimental far-from resonant heat profiles (dark green) with best fit from spatiotemporal model (light green). **(bottom)** Isolated experimental exciton profiles (dark purple) with best fit from spatiotemporal model (light purple).

Figures 4.20h,i and **4.21** show excellent qualitative agreement between the modeled and experimentally obtained exciton and thermal profiles. The model predicts an initial maximum exciton density of $\sim 8 \times 10^{12}$ cm^{-2}, lower than our experimental estimate based on the pump fluence and sample absorption coefficient. This discrepancy arises because the model accounts for the finite pump duration and subsequent exciton decay occurring within the experimental IRF. The predicted maximum temperature at experimental time-zero, (predominantly from exciton thermalization after above bandgap excitation), is 18 K, which is the value that is consistent with $\eta = 6.1$. To self-consistently determine the maximum temperature elevation, we extracted exciton profiles for a given value of η, then ran the spatiotemporal model optimization on the experimental exciton and heat data. If the η value predicted from the best fit maximum time-zero temperature, $\Delta T_{\text{max,fit}}$, did not agree with the value of η used to generate the exciton profiles for the fit, then we extracted a new set of exciton profiles using the η value predicted by $\Delta T_{\text{max,fit}}$ in Equation 4.23 and performed the optimization again until the η value predicted by $\Delta T_{\text{max,fit}}$ in Equation 4.23 and the η value used for the exciton profiles in the optimization agreed. The best fit $R_{\text{A-M}}$ coefficient, a parameter we cannot constrain with our experiments, is 2.6×10^{-3} cm^{-2}, which is lower than for monolayer TMDCs, but still within the expected range for multilayer TMDCs [40, 297, 317, 335]. Overall, the model supports our experimental finding that excitons diffuse slightly faster than heat, importantly enabling spatial differentiation between the two, which we described as instrumental in the differential contrast assignment above (**Section 4.3.1**).

4.3.9 Experimental and model time zero

Prior to each measurement, we characterize the pump-probe temporal overlap by tracking the differential signal rise in coarse (100 ps) and fine (10 ps) steps, as shown in the left panel of **Figure 4.22**. It is customary in pump-probe measurements to define time zero as halfway up the signal rise or to fit the signal rise and decay to an exponential function convolved with a Gaussian and set time zero as the center position of the Gaussian (solid fit lines in the left panel of **Figure 4.22**). We define time zero as the relative time delay at which the signal achieves its maximum (dashed lines in **Figure 4.22**), in part because the temporal pulse profiles are non-Gaussian due to afterpusling (**Figure 2.16**). It is straightforward to define time zero in the spatiotemporal model in an analogous way for direct comparison with experimental results (right panel in **Figure 4.22**).

4.3.10 Bare versus encapsulated measurements

In a different 4L MoS_2 sample, we compare the transient response probed near resonance when the MoS_2 is resting on the bare glass substrate and exposed to air (gold circle in **Figure 4.23**) and when it is encapsulated on both sides with hBN (green x in **Figure 4.23**). In the time zero contrast profiles measured in each region at two different pump fluences (right panel in **Figure 4.23**), the positive exciton-dominated contribution is relatively unaffected by the encapsulation. The negative thermally-dominated contribution, however, is suppressed by

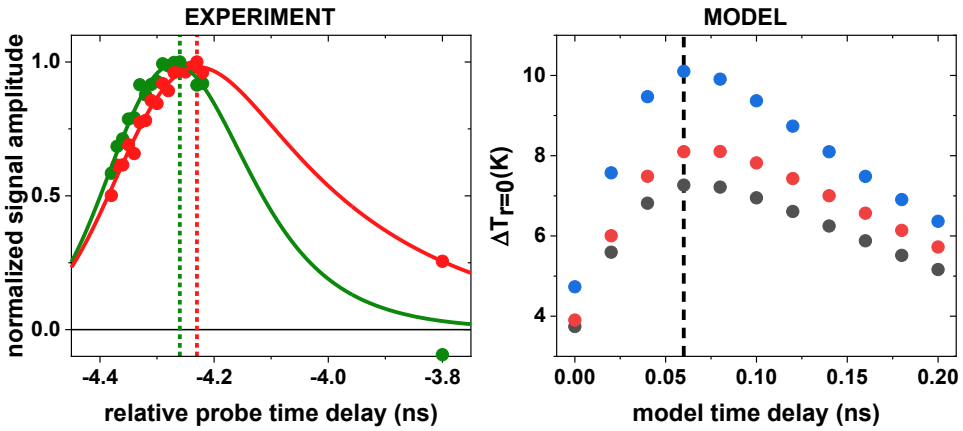

Figure 4.22: Experimental time zero **(left)** is set by measuring the integrated differential contrast about the signal rise and defining the maximum measured signal position as time zero (dashed lines). Due to the different temporal pulse profiles for each diode laser, the temporal pump-probe pulse overlap is slightly different for the 515 nm (green) versus 700 nm (red) probe. The model time zero **(right)** is determined in an analogous way by tracking the predicted temperature rise over the duration of the generation term convolved with the temporal probe PSF. We test the predicted temperature rise for several $R_{\text{A-M}}$ coefficients to check for any dependence since we cannot constrain $R_{\text{A-M}}$ with our experiments: 5×10^{-4} (gray), 1×10^{-3} (red) and 5×10^{-3} (blue) cm^2/s. Model time zero is defined as the time delay at which the maximum temperature difference is achieved (black dashed line).

$\sim$3-5$\times$ in the hBN-encapsulated sample suggesting that heat transfer to the hBN occurs faster than the time resolution of the measurement and acts as an excellent heat sink.

When we measure the full time series in the bare region under identical experimental conditions as for the hBN-encapsulated sample in **Figure 4.6**, the data exhibit the same differential contrast trends at the two probe energies – positive and negative contrast co-existence near resonance (top row in **Figure 4.24a**) and negative contrast alone far-from resonance (bottom row in **Figure 4.24a**). At the time of this measurement, the sample was nearly one year old. There is noticeable heterogeneity in the diffusion, especially in the near-resonant measurement. Although there is not a noticeable increase in scattering features in the ground state iSCAT image, it is possible that the already defect-rich surface, with intrinsic sulfur vacancy densities up to 10^{13} cm^{-2} even in exfoliated flakes [336, 337], continues to rearrange and accommodate new defects and impurities slowly over time [338]. It is known already that increased defect densities in monolayer MoS_2 impede charge transport [336, 339], although they can be useful for catalysis applications [340, 341]. The thermal decay in the bare region is similar to that in the encapsulated sample, exhibiting fast $\sim$300 ps heat transfer to the glass substrate followed by slow, diffusion-limited decay (**Figure 4.24b**). The thermal signature persists longer without encapsulation likely because glass ($\kappa_{\text{glass}} \sim 1$

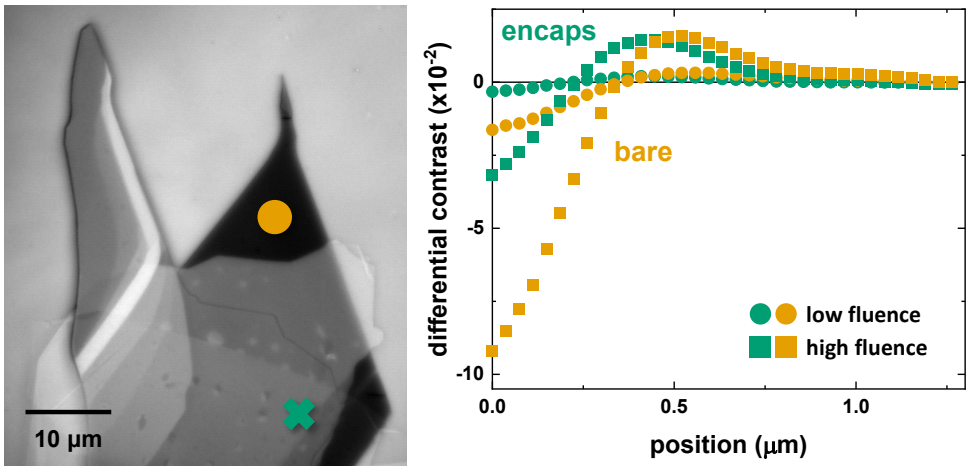

Figure 4.23: Comparison of encapsulated and unencapsulated time zero contrast in 4L MoS_2. The left reflectance contrast image shows the measured bare (gold circle) and hBN-encapsulated (green x) regions. The right plot shows the time zero radial profiles measured in each region, with "low fluence" corresponding to an exciton density of $\sim 2 \times 10^{13}$ cm^{-2} and "high fluence" corresponding to an exciton density of $\sim 10 \times 10^{13}$ cm^{-2}.

W/mK) is a very poor thermal conductor compared to hBN ($\kappa_{\text{hBN}} \gtrsim 500$ W/mK). The thermal *dynamics*, however, are quite different exhibiting a turnover in the mean squared expansion which is overall much slower than in the encapsulated sample (compare **Figure 4.24c** with **Figure 4.20d**). Perhaps the more defective bare lattice impedes not only charge but heat transport as well. For example, in disordered films of gold nanocrystals, heat transport appears subdiffusive due to nonconductive voids that must be circumvented while heat travels diffusively through contiguous regions of the film [130].

4.3.11 The Seebeck effect and exciton halos

For $1.4 < \eta < 2$, the exciton profiles extracted from the image arithmetic described above are depleted in the center forming donut- or halo-like exciton distributions (**Figure 4.25a**). Spatial exciton halos have been observed and extensively characterized by the Alexei Chernikov group at the Dresden University of Technology in monolayer WS_2 using spatially and time-resolved microphotoluminescence [111, 296, 297]. Tuning the exciton density over several orders of magnitude, they observe an evolution in the exciton profiles from Gaussian (10^8–10^9 cm^{-2}) to flat-top in the A-M–dominated regime ($10^9 - 10^{10}$ cm^{-2}) to halo-like ($10^{10} - 10^{12}$ cm^{-2}) [111]. A-M interactions flatten the Gaussian profile and inflate the effective exciton diffusivity but cannot explain the formation of exciton halos. Instead, they attribute this unconventional exciton diffusion to strong excitonic thermal gradients generated by efficient

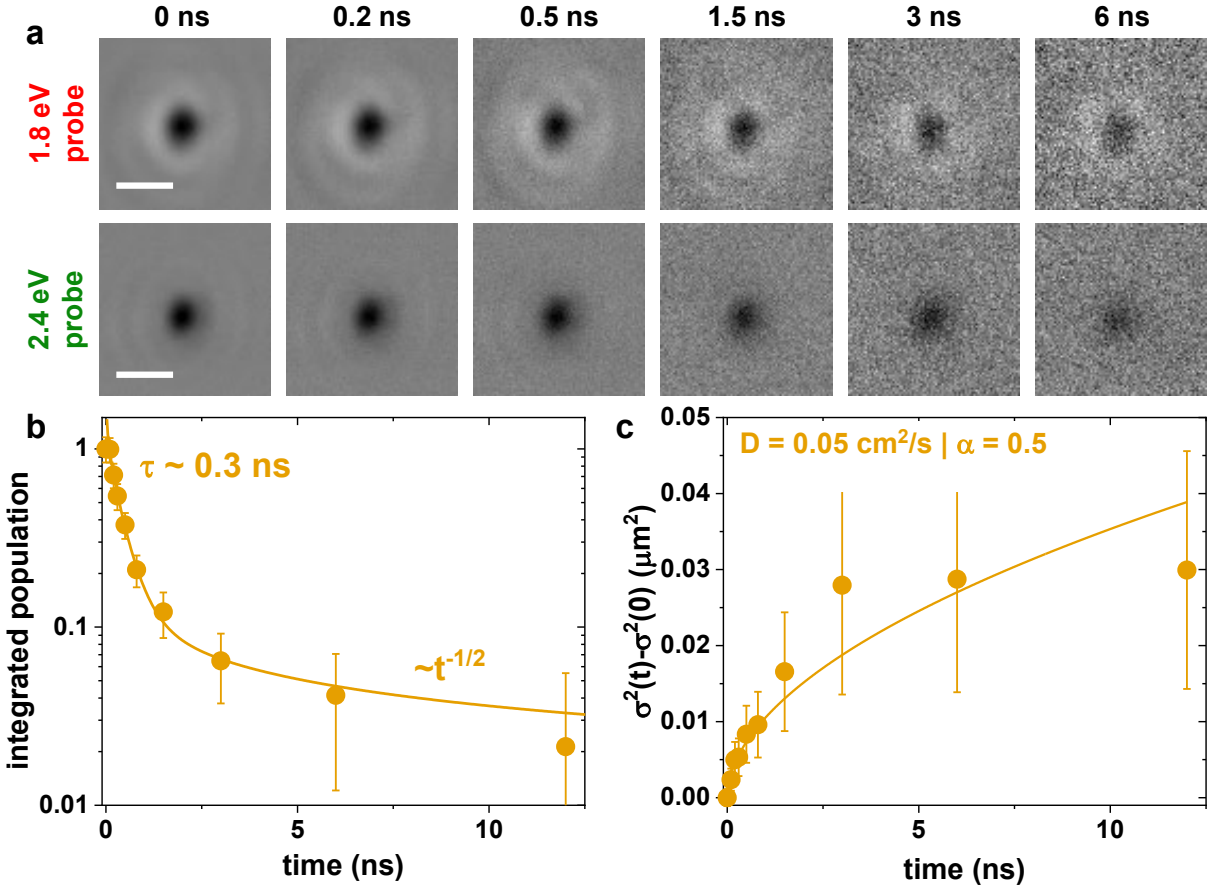

Figure 4.24: **(a)** Near-resonant (top) and far-from resonant (bottom) stroboSCAT measurements in the bare 4L MoS_2 region identified in **Figure 4.23**. **(b)** Kinetics of thermal decay from integrated areas under the 2.4 eV probe data with a fast $\tau \sim 300$ ps interfacial transfer component followed by a slower $t^{-1/2}$ transfer to the glass substrate. **(c)** Mean squared thermal expansion from Gaussian fits to the 2.4 eV probe data exhibiting subdiffusive behavior, possibly due to increased disorder in the old, exposed flake.

A-M scattering whereby the emission and reabsorption of hot optical phonons elevates the *effective* excitonic temperature to hundreds of degrees above room temperature [296]. The localized thermal gradient, ∇T, drives high kinetic energy excitons away from the hot center toward cooler regions, in addition to the driving force they experience from the spatially-dependent exciton density, ∇N (**Figure 4.25b**). This thermal drift phenomenon is also known as the Seebeck effect, an inherent material property that describes energy conversion between heat and electricity. For example, when a thermal gradient is generated across a material by heating one side, energetic electrons on the hot side have a longer mean free path than electrons on the cold side which drives electron diffusion to the cold side, inducing an electric field. When the material is incorporated into a circuit, the thermoelectric module may be used to generate power or to drive refrigeration [342]. We add this thermoelectric effect in our spatiotemporal kinetic model by adding a driving term in the exciton evolution equation due to the thermal gradient in Equation 4.26,

$$\dot{N}(r,t) = D_X \nabla^2 N(r,t) + \sigma s \nabla^2 T(r,t) - \frac{1}{\tau_X} N(r,t) - R_{\text{A-M}} N^2(r,t), \tag{4.39}$$

where $\sigma(r,t) = N(r,t) q \mu$ is the electric conductivity for exciton density N, elementary charge q, and exciton mobility μ, and S is the Seebeck coefficient, an intrinsic material parameter.

With our experimental parameters, most importantly a 72 ps pump pulse, the model does not predict spatial exciton halos even if we dramatically increase the A-M contribution to $R_{\text{A-M}} = 1$ cm^2/s, the highest observed in a 2D system [335], and include an ultrahigh Seebeck coefficient of $S = 1000$ µV/K [343] (**Figure 4.25c**). In fact, an exceedingly large Seebeck coefficient ($S > 10,000$ V/K) would be required to begin generating halo-like exciton profiles with our experimental parameters. In addition, the highest predicted temperature elevation with these parameters is $\Delta T = 20$ K. If we instead input the experimental parameters for the Chernikov measurements, most importantly the $\sim$ 100 fs pump pulse and lower heat capacity for monolayer WS_2, the model predicts halo-like exciton profiles, although they are not as pronounced as what is reported in reference [296] likely due to the lower predicted temperature elevation ($\sim$ 20 K compared to 700 K, see **Figure 4.25d**). It would appear that a phonon bottleneck is a prerequisite for generating such a pronounced nonequilibrium excitonic thermal gradient. On our measurement time scales and in our spatiotemporal model, we assume the excitons have thermalized with the lattice. It is important to note that when Chernikov et al. control the dielectric environment with hBN, they do not observe spatial exciton halos due to a reduced Coulomb interaction, less dielectric disorder and a shifted band structure, all effects that suppress A-M scattering and therefore reduce the local heating [297]. The A-M interaction is expected to be even lower in multilayer TMDC samples due to increased dielectric screening from the additional layers [344]. In addition, the instantaneous peak exciton densities are much lower in our measurements simply due to the longer diode pulse duration, suppressing A-M scattering, and therefore any out-of-equilibrium heating effects, even further. In sum, we rule out this Seebeck regime to model our observations in 4L MoS_2 and this is also consistent with the Chernikov body of work.

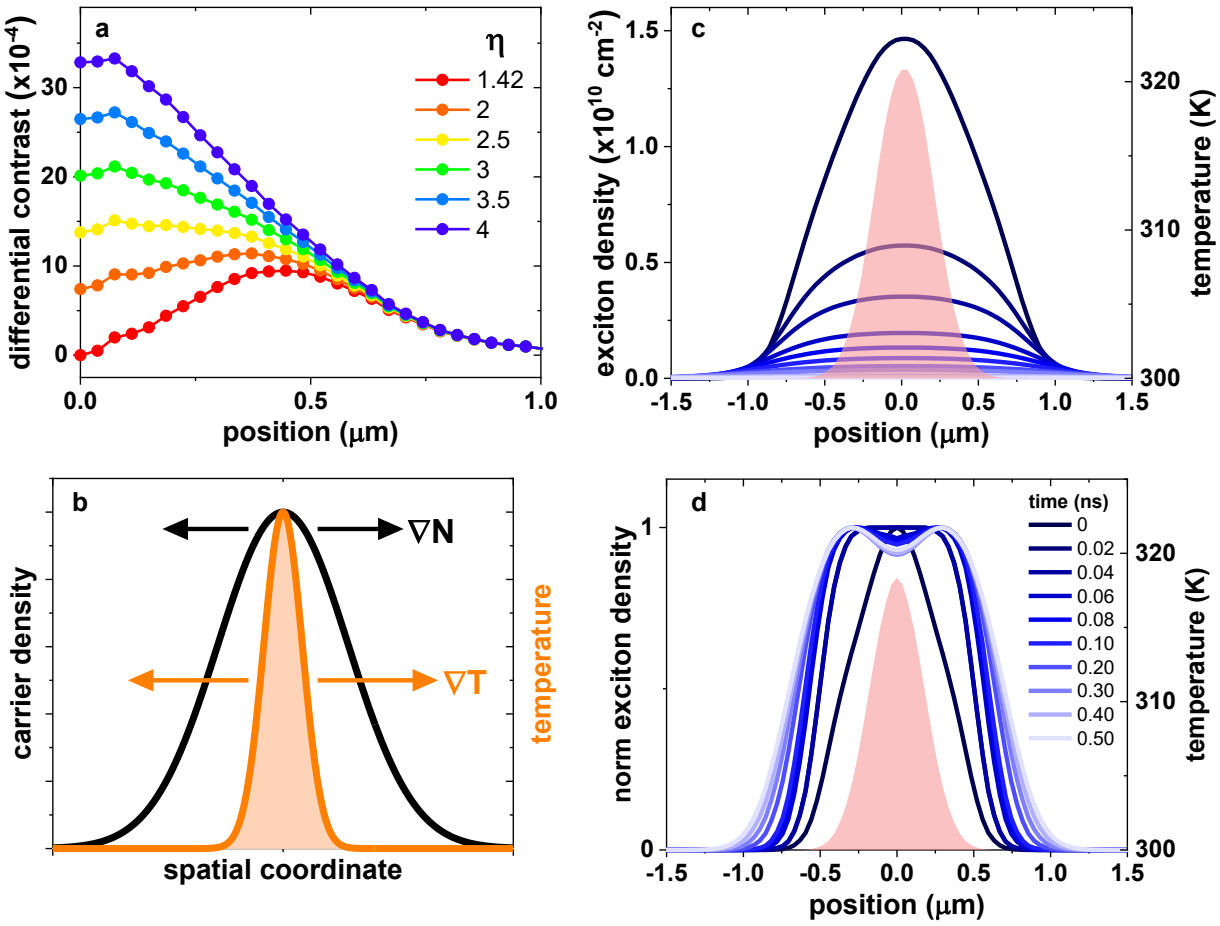

Figure 4.25: The Seebeck effect and exciton halos in TMDCs. **(a)** Time zero low-η exciton profiles starting with a minimum η value that yields positive contrast only. **(b)** In addition to photoexcited carrier gradients (black), thermal gradients (orange) may also drive exciton diffusion through a thermoelectric phenomenon known as the Seebeck effect. **(c,d)** Exciton profiles (blue) and time-zero temperature gradient (pink shaded curve) predicted with a spatiotemporal kinetic model that includes a Seebeck driving term in the exciton evolution equation for (c) Ginsberg group experimental parameters over the same time delays measured in **Figure 4.6** from 0 to 7 ns compared to (d) Chernikov group experimental parameters over the same time delays measured in Figure 4 of Perea-Causín et al. [296]. Full model parameters are listed in **Table 4.2**.

	Perea-Causín et al. [296]	This work
τ_X [ns]	0.7	4.1
D_X [cm^2/s]	0.3	0.57
$R_{A\text{-}M}$ [cm^2/s]	0.5	1.0*
σ_{pump} [nm]	174	168
t_{pump} [ps]	0.1	72
E_{pump} [eV]	2.43	2.82
E_{BG} [eV]	2.05	1.38
N_{peak} [cm^{-2}]	7×10^{12}	3.5×10^{13}
c [J/g·K]	0.3	0.4
τ_T [ns]	0.4	0.3
D_T [cm^2/s]	0.05	0.2
PLQY [%]	1	1
S [µV/K]	$1,000$	$1,000^\dagger$

Table 4.2: All model parameter values employed in two separate simulations. The right column summarizes the values either constrained or obtained via (experimentally bounded) fitting to the experimental stroboSCAT data (**Figure 4.25c**). The middle column lists the corresponding parameters taken from Perea Causín et al. [296] or estimated from the literature to reflect that the model generates "halo" profiles consistent with their experimental observations using microTRPL (**Figure 4.25d**). *Inflated from the best fit value of 0.00026 cm^2/s to generate the highest possible temperature gradient and give the best chance of generating halo profiles. †There is no significant difference in the predicted exciton profiles between using $S = 0$ or $S = 1,000$ µV/K.

4.3.12 stroboSCAT as a sensitive non-contact thermometry approach

We also wish to highlight a valuable byproduct of developing thermal sensitivity capabilities in a transient optical microscopy – namely that stroboSCAT can serve as a highly sensitive non-contact thermometry with excellent spatial resolution compared to infrared analogs. For example, based on the 18 K temperature elevation calculation in the 4L MoS_2, we reframe in **Figure 4.26** the relaxation of the temperature in **Figure 4.6** and **Figure 4.20f** to establish the sensitivity of this thermometry. **Figure 4.26a** relabels the axis of **Figure 4.20f** with the time-dependent peak temperature at the center of the heat distribution. The radial profiles of corresponding time delays, also in **Figure 4.20b**, are shown as an inset, and some example $\Delta R/R$ images are included in **Figure 4.26b**. At the longer time delays, we thus establish the ability to resolve ∼0.1 K temperature elevation. Although it is difficult to directly compare with the metrics of more conventional thermal imaging [345], this value seems on par with it and enjoys substantially higher spatial resolution. While the present data were collected by only averaging for 7 minutes per time point, we estimate, based on the

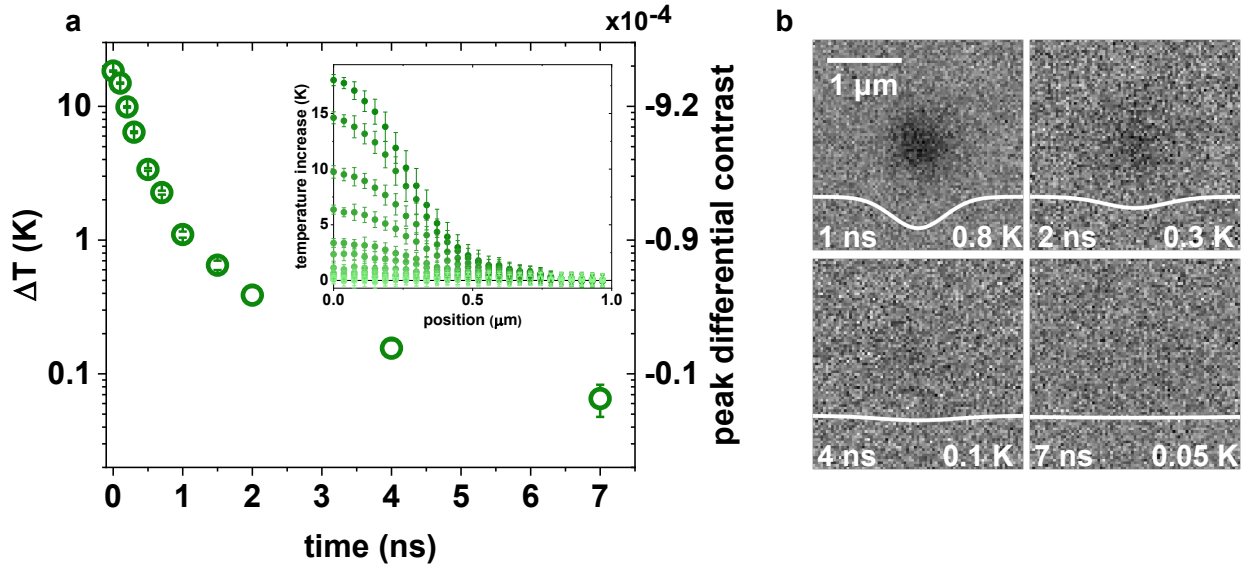

Figure 4.26: **(a)** Gaussian amplitude fit decay for the far-from resonant probe dataset. The vertical axis is calibrated using the maximum predicted sample temperature elevation from the spatiotemporal model (18 K) and the measured maximum differential contrast value. The inset shows the azimuthal averages in **Figure 4.20b** with a rescaled vertical temperature axis. Error bars represent the standard error of the mean of the azimuthal averaging. **(b)** Far-from resonant probe images labeled with the maximum temperature achieved in each frame. All images are shown on the same contrast scale. White traces are Gaussian fits to the raw azimuthally averaged data.

12-bit CMOS camera well depth and the shot noise limit, that our sensitivity should indeed be in the range of 100 mK. With increased averaging, microscope stabilization, and detector sensitivity, this limit could be pushed into the tens of mK regime, making stroboSCAT an exquisite thermometry approach with added high spatial resolution. Not only is this newfound spatially-resolved sensitivity to temperature very powerful for discerning heat and charge in photoexcited materials, but it should find great utility in thermal management characterization in the semiconductor device sector.

4.3.13 Looking towards the future: exciting extensions of this work

Regarding the toolkit that we have developed and its more general applicability, our spatio-spectro-temporal approach is able to characterize the complex, overlapping electronic and thermal system dynamics even though their contributions would be difficult to disentangle from spectroscopic data alone; discerning these dynamics in 4L MoS_2 was possible despite an

absence of strongly distinct time scales in the excitonic and thermal population dynamics. Another strategy to achieve the same result could be to use the temperature-dependence of the reflectance contrast to calibrate the response to heat at 2.4 eV, not only at 1.8 eV, where the proximity to a zero-crossing precluded this process in the current work. Careful selection of another far-from resonance probe wavelength could enable this alternative strategy for future work. As a general strategy, for each specific sample, one must carefully consider the best approach to isolate the electronic contribution to the photoexcited signal based on spectral information, as discussed here, and the extent to which the thermal and electronic diffusivities create a separation of time scales, which is minimal here but was, for example, sufficient to investigate silicon [278]. Furthermore, there are generally multiple different processes by which heat is generated that can occur on different time scales relative to the generation and evolution of electronic excitation. Regardless, the impact of heat on transient measurements is substantial in many materials, not only for few-layer TMDCs [290, 346–350]. Any type of nonradiative process, from above gap excitation, to nonlinear processes like annihilation, including Auger-Meitner effects, to 'standard' nonradiative decay, will generate heat. By measuring the photoinduced response in a reflectance geometry, the thermal response is revealed most clearly due to its superior sensitivity to the real part of the dielectric function, relative to transmission-based (or photoluminescence) measurements. Again, while it has been painstakingly investigated in semiconductor transient spectroscopy [290, 291, 351–353], which is largely performed in reflectance geometry due to the opacity of semiconductors in the visible and near-infrared parts of the spectrum, the higher sensitivity and the addition of the spatial variable that stroboSCAT affords provide additional helpful constraints to discern heat and charge. The spatial coordinate is helpful not only because of access to instantaneous spatial distributions but also to the time rate of change in the spatiotemporal evolution, which yields transport parameters such as diffusivity [117]. We therefore anticipate this newfound ability to characterize the coexistence, transport, and interplay of heat and charge in materials to be highly general and to enable a more detailed and reliable mechanistic understanding of a material's physical properties and phenomena far more broadly than in TMDCs alone.

Regarding strategies for the future, the possibility exists to interrogate materials with more than two types of energy carriers, for example, free carriers, trions and excitons, coexist together with one another and also with heat [15]. In 4L MoS_2, we probed sufficiently far from a zero crossing in the transient reflectance spectrum in all cases to avoid sign-changes in the differential contrast associated with each type of energy. In materials with additional, distinct electronic species, the combination of measuring at additional pump energies and fluences to tune the relative densities of distinct photoinduced energy carriers could enable them to be distinguished. Furthermore, a continuously tunable probe source could be leveraged to increase the signal-to-noise ratio of photoexcitations that may not appreciably modify the local dielectric function [184, 319].

We also envision a range of additional utilities of stroboSCAT in elucidating mechanisms of electron-phonon coupling and deepening our understanding of intrinsic thermal–electronic energy conversion and transport. Spatiotemporally monitoring charged photoexcitations and

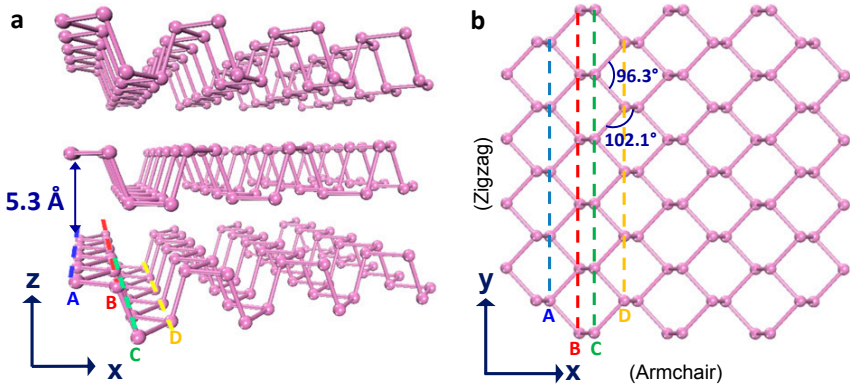

Figure 4.27: Black phosphorus lattice structure. **(a)** Side view of the BP crystal lattice. The interlayer spacing is 0.53 nm. **(b)** Top view of the lattice of single-layer BP. The bond angles are shown. The x and y directions correspond to the armchair and zigzag directions, respectively. Reprinted with permission from Reference [363].

phonons directly and simultaneously opens new doors for discovering mechanisms of electron-phonon scattering. In particular, understanding nonradiative decay pathways facilitated by traps, interfaces, defects, A-M interactions and natural background doping will elucidate design principles for engineering higher PLQY materials and directed or enhanced diffusion lengths [354–360]. Characterizing the potential interplay between heating and electronic energy flow could inform thermal management strategies by revealing the dominant factors and mechanisms that tune electron-phonon coupling. Furthermore, while thermal management aims to mitigate the impact of unwanted and deleterious heat dissipation, for example in semiconductor electronics, stroboSCAT also has the capability to directly measure transport anisotropies and thermoelectric effects in which heat is harnessed to do useful electronic work. For example, directly measuring the intrinsic Seebeck coefficient, an important factor in the intrinsic figure of merit for thermoelectrics, across different device configurations or material thicknesses may address challenges in efficiently upcycling heat loss through conversion to electricity or otherwise controlling heat flow in operating devices that suffer from poor performance due to self heating [361, 362].

4.4 stroboSCAT on intrinsic thermoelectric materials

The bandgap of black phosphorus (BP) – ranging from 1.66 eV in the single layer form, also known as phosphorene, to 0.30 eV in the bulk limit – is important for bridging the gap between gapless graphene and TMDCs, which tend to have quite large bandgaps. The in-plane anisotropies in heat and charge transport that arise from a puckered honeycomb lattice (**Figure 4.27**) are what make BP, and related materials like GeS, GeSe, ReS_2 and $ReSe_2$, quite unique. The charge effective mass along the zigzag direction is *ten times* larger

than along the armchair direction, which has ramifications for the electronic, optical, and phonon response, most importantly that charge transport is 10 times faster along the armchair direction than the zigzag direction. Longitudinal lattice vibrations, however, can more easily distort the armchair direction leading to an enhanced speed of sound and preferential thermal transport along the orthogonal and more robust zigzag direction. This results in charge and thermal transport that are not only anisotropic but that exhibit orthogonal preferred conducting directions. This scenario is ideal for thermoelectric applications where fast electron and slow thermal transport along one axis are desired. BP scores a high figure of thermoelectric merit, $ZT = S^2(\sigma/\kappa)T$, due to its intrinsic orthogonal anisotropy that enforces efficient electrical conduction (σ) along an axis with poor thermal conductance (κ) [363]. When integrated into a field-effect transistor, few-layer BP achieves record hole mobilities in Hall measurements, upwards of 5000 $\mathrm{cm^2V^{-1}s^{-1}}$ even at room temperature, likely the highest of any layered semiconductor material [364, 365].

Previous studies have spatially resolved the in-plane anisotropic hole transport in 80 nm thick BP ($D_{\mathrm{h,\ armchair}} \approx 1.3 \times 10^4$ $\mathrm{cm^2/s}$, $D_{\mathrm{h,\ zigzag}} \approx 870$ $\mathrm{cm^2/s}$) [366] and the ambipolar charge transport in 16 nm thick BP ($D_{\mathrm{a,\ armchair}} \approx 1.3 \times 10^3$ $\mathrm{cm^2/s}$, $D_{\mathrm{a,\ zigzag}} \approx 80$ $\mathrm{cm^2/s}$) [367]. We are not aware of any direct and simultaneous measurements of charge and heat transport in BP, especially atomically thin BP. Our goal was to perform such a measurement on atomically thin BP with stroboSCAT as a function of layer thickness since many material properties – such as the exciton binding energy, bandgap, electron and hole effective mass, and phonon dispersion – change appreciably over the mono- to few-layer transition. It was difficult, however, obtain a measurable signal in three- or one-layer hBN-encapsulated BP prepared by **Aidan O'Beirne** and **Henrique Bucker Ribeiro** in the **Tony Heinz** group at Stanford. Instead, we preliminarily characterized a bulk BP flake, part of the "debris" on the three-layer sample. Using a 440-640 nm pump-probe configuration, we measured the anisotropic expansion of a dark population over tens of ns that exhibits the expected anisotropy (∼2:1) for the thermal conductance [368]. The anisotropy is apparent in the data in **Figure 4.28a**, and by fitting Gaussian functions to rectangular slices parallel and perpendicular to the "fast" transport axis determined by late-time-delay images, we quantitate the anisotropic thermal transport ratio of 2.5(3):1 (**Figure 4.28b**). In the same measurement, we observe a fast-propagating positive contrast wave that quickly emanates from the center of the photoexcited signal orthogonal to the preferred thermal transport axis (**Figure 4.28c**). Within a few hundred picoseconds, it escapes the 7×7 $\mu\mathrm{m}^2$ measurement field of view. It is possible that we captured the last wisps of charge carriers diffusing along their fast axis since, using the previously measured [367] ambipolar diffusivity of $D_{\mathrm{charge}} = 1300$ $\mathrm{cm^2/s}$, charge carriers generated in the center would propagate out of the frame in ∼500 ps. There are many future directions to take these preliminary measurements such as comparing transport in GeS or GeSe with BP or measuring a 90° twisted bilayer BP sample that is predicted to have gate-tunable anisotropy [369]. Some challenges to consider are inherent to the sample (small bandgap in the few-layer to bulk limit so that enhancing the transient response by probing near resonance is not possible, difficult to fabricate pristine atomically thin samples, low differential contrast from atomically thin samples) while others could be overcome with

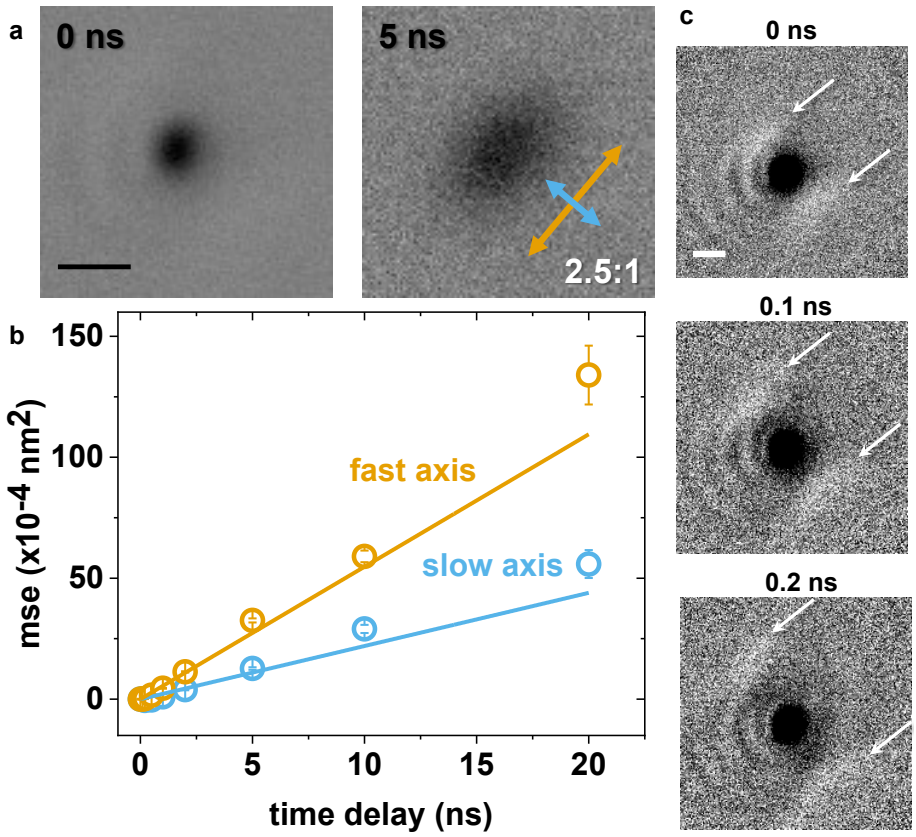

Figure 4.28: Anisotropic heat transport in black phosphorus. **(a)** Evolution of anisotropic heat transport over several ns. **(b)** Mean squared expansion along the axis parallel to fast (yellow) and slow (blue) transport with diffusion coefficients of 0.27 and 0.11 cm^2/s, respectively. **(c)** First three time points of the same data set shown in (a) with contrast re-scaled to accentuate a bright wave that emanates from the initial photoexcited spot in an orthogonal direction to the fast thermal transport axis. Scale bars are all 1 µm.

instrument improvements (faster time resolution, increased measurement stability to enable longer averaging for thinner samples). **Stephanie Hart** is currently extending these measurements into the ultrafast regime in the Ginsberg lab with exciting results that corroborate what has been described in this section. Compared to TMDCs, the research into BP and its isoelectronic materials is in its infancy. More work is needed to synthesize large, stable samples with careful surface passivation and encapsulation. But since these systems are not quite in the lime light, there are many open questions yet to be explored.

4.5 Conclusion

In conclusion, we have demonstrated the broad applicability of stroboSCAT to measure energy transport across a wide range of layered 2D systems. Whether it is mapping ILE transport in a heterobilayer, observing energy transfer across an interface of different layer thicknesses, tracking exciton transport in a metal-contacted structure with phase contrast varying with TMDC thickness or characterizing intrinsic anisotropies in thermoelectric materials, stroboSCAT is sensitive to all perturbations to the local complex refractive index following photoexcitation. To co-measure and discern the photoinduced dynamics of heat and excitons in 4L MoS_2, we use a combination of optical scattering microscopy and temperature-dependent reflectance contrast spectroscopy. This capability is a generalizable consequence of stroboSCAT's unique spatially-, spectrally-, and temporally-resolved contrast mechanism that is sensitive to any perturbation that modifies a material's local dielectric function. The spatiotemporal energy maps play a key role in identifying overlapping energetic populations with distinct contributions to the differential contrast. Our results agree with previous characterizations of few-layer MoS_2, are robust to experimental uncertainties in the estimated sample temperature elevation, and demonstrate a temperature sensitivity as good as 100 mK, ushering in a new era for spatiotemporally-resolved optical microscopy to discern charge and heat and their potential interplay. With quantitative energy-carrier-specific tracking down to few-ps time scales, directly characterizing and explaining the factors that give rise to the optoelectronic properties of a wide range of emerging semiconducting materials, including intrinsic thermoelectrics and low-dimensional devices, is now possible without having to rely on complex models or assumptions.

Chapter 5

Conclusion

The spatio-energetic landscape in many emerging semiconducting materials more closely resembles the Rocky Mountains than the rolling green hills of silicon. A nanosecond in the life of a photoexcitation, if it lives that long, is filled with collisions, re-directions and encounters with structural hurdles and energetic sinks. These inherently messy interactions are averaged over in bulk characterizations but are important to understand for developing defect-tolerant materials and directing energy flow. Stroboscopic scattering microscopy (stroboSCAT) has emerged as a technique that embraces the mayhem of nanoscale disorder, sensitively mapping all perturbations to the complex refractive index with nanometer and picosecond resolution. Its unique capabilities were essential for enabling the findings in this dissertation.

Chapter 1 provided an overview of low-dimensional and solution-processed materials, both classes of novel semiconducting materials with tunable optoelectronic properties and other emergent functionalities that make them attractive alternatives to silicon. It also introduced the microscopic mechanisms by which photoexcitations move macroscopic distances in materials and the collection of transient scattering microscopies that resolve their nanoscale energy transport properties.

Chapter 2 described the principles of light scattering and how they are leveraged in interferometric scattering microscopy (iSCAT) to sensitively image small particles. stroboSCAT, the time-resolved extension of iSCAT, opened a new range of possibilities for tracking the spatiotemporal evolution of distributions of photoexcitations. We discussed that while light scattering is the basic mechanism at the heart of all light-matter interactions, complex optical functions like the refractive index are a more suitable description for probing condensed matter systems with light. We detailed several advantages to probing in a reflection geometry including a well-defined interfacial reflection from which to measure axial transport and overwhelming sensitivity to changes in the real part of the refractive index which obviates the need for propagating assumptions through Kramers-Kronig transformations. Finally, we characterized the finer points and operation of the stroboSCAT setup.

Chapter 3 covered several case studies in which stroboSCAT resolved energy transport in both ordered and disordered semiconductors. In TIPS-Pn, exciton transport was hindered by abrupt grain boundaries. stroboSCAT also characterized the increased spot-to-spot vari-

ability in confined transport compared to unhindered transport within large grain areas. Leveraging stroboSCAT's depth-dependent phase, we observed charge carriers in a polycrystalline perovskite thin film bypassing highly resistive morphological boundaries (MBs) at the film surface by traveling deeper into the film before crossing over to a neighboring grain. Spectral interferometry emerged as an important addition to the stroboSCAT microscope for correlating image contrast phase flips with the location of MBs. Finally, in silicon, the differential phase contrast and a separation of time scales was instrumental in distinguishing overlapping heat from charge distributions.

Chapter 4 focused on stroboSCAT in low-dimensional systems including a transition metal dichalcogenide (TMDC) heterostructure and metal-contacted TMDC. In encapsulated four-layer MoS_2 where nonradiative decay pathways dominate the relaxation, excitons and heat coexist over many nanoseconds. We developed a point spread function correction to be able to subtract stroboSCAT measurements collected at different probe imaging wavelengths, where heat and excitons overlap in the near-resonant measurement but only heat was observed far from electronic resonances. Separate temperature-dependent reflectance contrast spectroscopy measurements characterized contributions due to heating alone near-resonance. In combination with a spatiotemporal model, we isolated the excitonic contribution to the stroboSCAT signal and also benchmarked stroboSCAT as a highly sensitive non-contact thermometry approach. Extensions of this work might include exploring other layered TMDCs and intrinsically thermoelectric materials.

All together, these studies highlight optical scattering as a universal, sensitive probe of photoexcitations in emerging semiconducting materials. Although the differential contrast in stroboSCAT may be difficult to decode, the reward is a glimpse into the intricate world of nanoscale energy transport and transduction. The insights gleaned from taking a closer look at all of the photoexcitations at play and the inherent structural disorder they must navigiate will deepen our understanding of their emergent functional properties and inform the design principles for next-generation optoelectronic devices.

Bibliography

(1) Cohen, M. L.; Louie, S. G., *Fundamentals of Condensed Matter Physics*; Cambridge University Press: 2016.

(2) Ashcroft, N. W.; Mermin, D. N. In *Solid State Physics*, "The Reciprocal Lattice"; Harcourt College Pulishers: 1976, pp 85–94.

(3) Kroto, H.; Fischer, J.; Cox, D., *The Fullerenes*; Pergamon: Oxford, 1993.

(4) Iijima, S. *Nature* **1991**, *354*, 56–58.

(5) Peierls, R. *Annales de l'institut Henri Poincaré* **1935**, *5*, 177–222.

(6) Landau, L. D. **1937**, *7*, 19–32.

(7) Wallace, P. R. *Physical Review* **1947**, *71*, 622–634.

(8) Slonczewski, J. C.; Weiss, P. R. *Physical Review* **1958**, *109*, 272–279.

(9) Semenoff, G. W. *Physical Review Letters* **1984**, *53*, 2449–2452.

(10) Novoselov, K. S.; Geim, A. K.; Morozov, S. V.; Jiang, D.; Zhang, Y.; Dubonos, S. V.; Grigorieva, I. V.; Firsov, A. A. *Science* **2004**, *306*, 666–669.

(11) Novoselov, K. S.; Jiang, D.; Schedin, F.; Booth, T. J.; Khotkevich, V. V.; Morozov, S. V.; Geim, A. K. *Proceedings of the National Academy of Sciences* **2005**, *102*, 10451–10453.

(12) Dimple; Jena, N.; Rawat, A.; Sarkar, A. D. *Journal of Materials Chemistry A* **2017**, *5*, 22265–22276.

(13) Novoselov, K. S.; Neto, A. H. C. *Physica Scripta* **2012**, *2012*, 014006.

(14) Chernikov, A.; Berkelbach, T. C.; Hill, H. M.; Rigosi, A.; Li, Y.; Aslan, B.; Reichman, D. R.; Hybertsen, M. S.; Heinz, T. F. *Physical Review Letters* **2014**, *113*, 076802.

(15) Wang, G.; Chernikov, A.; Glazov, M. M.; Heinz, T. F.; Marie, X.; Amand, T.; Urbaszek, B. *Reviews of Modern Physics* **2018**, *90*, 021001.

(16) Perea-Causin, R.; Erkensten, D.; Fitzgerald, J. M.; Thompson, J. J. P.; Rosati, R.; Brem, S.; Malic, E. *APL Materials* **2022**, *10*, 100701.

(17) Yu, Y.; Yu, Y.; Cai, Y.; Li, W.; Gurarslan, A.; Peelaers, H.; Aspnes, D. E.; Van de Walle, C. G.; Nguyen, N. V.; Zhang, Y.-W.; Cao, L. *Scientific Reports* **2015**, *5*, 16996.

(18) Olsen, T.; Latini, S.; Rasmussen, F.; Thygesen, K. S. *Physical Review Letters* **2016**, *116*, 056401.

(19) Cheiwchanchamnangij, T.; Lambrecht, W. R. L. *Physical Review B* **2012**, *85*, 205302.

(20) Berkelbach, T. C.; Hybertsen, M. S.; Reichman, D. R. *Physical Review B* **2013**, *88*, 045318.

(21) Raja, A.; Waldecker, L.; Zipfel, J.; Cho, Y.; Brem, S.; Ziegler, J. D.; Kulig, M.; Taniguchi, T.; Watanabe, K.; Malic, E.; Heinz, T. F.; Berkelbach, T. C.; Chernikov, A. *Nature Nanotechnology* **2019**, *14*, 832–837.

(22) Hill, H. M.; Rigosi, A. F.; Roquelet, C.; Chernikov, A.; Berkelbach, T. C.; Reichman, D. R.; Hybertsen, M. S.; Brus, L. E.; Heinz, T. F. *Nano Letters* **2015**, *15*, 2992–2997.

(23) Raja, A. et al. *Nature Communications* **2017**, *8*, 15251.

(24) Hsu, C.; Frisenda, R.; Schmidt, R.; Arora, A.; de Vasconcellos, S. M.; Bratschitsch, R.; van der Zant, H. S. J.; Castellanos-Gomez, A. *Advanced Optical Materials* **2019**, *7*, 1900239.

(25) Mak, K. F.; Lee, C.; Hone, J.; Shan, J.; Heinz, T. F. *Physical Review Letters* **2010**, *105*, 136805.

(26) Splendiani, A.; Sun, L.; Zhang, Y.; Li, T.; Kim, J.; Chim, C.-Y.; Galli, G.; Wang, F. *Nano Letters* **2010**, *10*, 1271–1275.

(27) Wang, L.; Wang, Z.; Wang, H.-Y.; Grinblat, G.; Huang, Y.-L.; Wang, D.; Ye, X.-H.; Li, X.-B.; Bao, Q.; Wee, A.-S.; Maier, S. A.; Chen, Q.-D.; Zhong, M.-L.; Qiu, C.-W.; Sun, H.-B. *Nature Communications* **2017**, *8*, 13906.

(28) Tsai, H.-S.; Huang, Y.-H.; Tsai, P.-C.; Chen, Y.-J.; Ahn, H.; Lin, S.-Y.; Lu, Y.-J. *ACS Omega* **2020**, *5*, 10725–10730.

(29) Kumar, N.; He, J.; He, D.; Wang, Y.; Zhao, H. *Journal of Applied Physics* **2013**, *113*, 133702.

(30) Shi, H.; Yan, R.; Bertolazzi, S.; Brivio, J.; Gao, B.; Kis, A.; Jena, D.; Xing, H. G.; Huang, L. *ACS Nano* **2013**, *7*, 1072–1080.

(31) Addou, R.; Colombo, L.; Wallace, R. M. *ACS Applied Materials & Interfaces* **2015**, *7*, 11921–11929.

(32) Lien, D.-H.; Uddin, S. Z.; Yeh, M.; Amani, M.; Kim, H.; Ager, J. W.; Yablonovitch, E.; Javey, A. *Science* **2019**, *364*, 468–471.

(33) Wang, W.; Sui, N.; Ni, M.; Chi, X.; Pan, L.; Zhang, H.; Kang, Z.; Zhou, Q.; Wang, Y. *The Journal of Physical Chemistry C* **2020**, *124*, 1749–1754.

(34) Amani, M. et al. *Science* **2015**, *350*, 1065–1068.

(35) Amani, M.; Taheri, P.; Addou, R.; Ahn, G. H.; Kiriya, D.; Lien, D.-H.; Ager, J. W. I.; Wallace, R. M.; Javey, A. *Nano Letters* **2016**, *16*, 2786–2791.

(36) Bretscher, H.; Li, Z.; Xiao, J.; Qiu, D. Y.; Refaely-Abramson, S.; Alexander-Webber, J. A.; Tanoh, A.; Fan, Y.; Delport, G.; Williams, C. A.; Stranks, S. D.; Hofmann, S.; Neaton, J. B.; Louie, S. G.; Rao, A. *ACS Nano* **2021**, *15*, 8780–8789.

(37) Konabe, S.; Okada, S. *Physical Review B* **2014**, *90*, 155304.

(38) Mouri, S.; Miyauchi, Y.; Toh, M.; Zhao, W.; Eda, G.; Matsuda, K. *Physical Review B* **2014**, *90*, 155449.

(39) Danovich, M.; Zólyomi, V.; Fal'ko, V. I.; Aleiner, I. L. *2D Materials* **2016**, *3*, 035011.

(40) Sun, D.; Rao, Y.; Reider, G. A.; Chen, G.; You, Y.; Brézin, L.; Harutyunyan, A. R.; Heinz, T. F. *Nano Letters* **2014**, *14*, 5625–5629.

(41) Chernikov, A.; Ruppert, C.; Hill, H. M.; Rigosi, A. F.; Heinz, T. F. *Nature Photonics* **2015**, *9*, 466–470.

(42) Steinhoff, A.; Florian, M.; Rösner, M.; Schönhoff, G.; Wehling, T. O.; Jahnke, F. *Nature Communications* **2017**, *8*, 1166.

(43) Zhao, W.; Ghorannevis, Z.; Chu, L.; Toh, M.; Kloc, C.; Tan, P.-H.; Eda, G. *ACS Nano* **2013**, *7*, 791–797.

(44) Schneider, C.; Glazov, M. M.; Korn, T.; Höfling, S.; Urbaszek, B. *Nature Communications* **2018**, *9*, 2695.

(45) Ross, J. S.; Klement, P.; Jones, A. M.; Ghimire, N. J.; Yan, J.; Mandrus, D. G.; Taniguchi, T.; Watanabe, K.; Kitamura, K.; Yao, W.; Cobden, D. H.; Xu, X. *Nature Nanotechnology* **2014**, *9*, 268–272.

(46) Ye, Y.; Wong, Z. J.; Lu, X.; Ni, X.; Zhu, H.; Chen, X.; Wang, Y.; Zhang, X. *Nature Photonics* **2015**, *9*, 733–737.

(47) Unuchek, D.; Ciarrocchi, A.; Avsar, A.; Watanabe, K.; Taniguchi, T.; Kis, A. *Nature* **2018**, *560*, 340–344.

(48) Lien, D.-H.; Amani, M.; Desai, S. B.; Ahn, G. H.; Han, K.; He, J.-H.; Ager, J. W.; Wu, M. C.; Javey, A. *Nature Communications* **2018**, *9*, 1229.

(49) Ganatra, R.; Zhang, Q. *ACS Nano* **2014**, *8*, 4074–4099.

(50) Zhang, Y.; Li, H.; Wang, L.; Wang, H.; Xie, X.; Zhang, S.-L.; Liu, R.; Qiu, Z.-J. *Scientific Reports* **2015**, *5*, 7938.

(51) Wang, H.; Zhang, C.; Rana, F. *Nano Letters* **2015**, *15*, 8204–8210.

(52) Wu, J.; Chen, Y.; Wu, J.; Hippalgaonkar, K. *Advanced Electronic Materials* **2018**, *4*, 1800248.

(53) Chow, P. C. Y.; Someya, T. *Advanced Materials* **2020**, *32*, 1902045.

(54) Simone, G.; Dyson, M. J.; Meskers, S. C. J.; Janssen, R. A. J.; Gelinck, G. H. *Advanced Functional Materials* **2020**, *30*, 1904205.

(55) Joseph, A.; Pillai, A. B.; Pulikodan, V. K.; Alexander, A.; Muhammed, R.; Namboothiry, M. A. G. *ACS Applied Electronic Materials* **2022**, *4*, 1567–1575.

(56) García de Arquer, F. P.; Armin, A.; Meredith, P.; Sargent, E. H. *Nature Reviews Materials* **2017**, *2*, 1–17.

(57) Tan, Z.-K.; Moghaddam, R. S.; Lai, M. L.; Docampo, P.; Higler, R.; Deschler, F.; Price, M.; Sadhanala, A.; Pazos, L. M.; Credgington, D.; Hanusch, F.; Bein, T.; Snaith, H. J.; Friend, R. H. *Nature Nanotechnology* **2014**, *9*, 687–692.

(58) Hoke, E. T.; Slotcavage, D. J.; Dohner, E. R.; Bowring, A. R.; Karunadasa, H. I.; McGehee, M. D. *Chemical Science* **2014**, *6*, 613–617.

(59) McMeekin, D. P.; Sadoughi, G.; Rehman, W.; Eperon, G. E.; Saliba, M.; Hörantner, M. T.; Haghighirad, A.; Sakai, N.; Korte, L.; Rech, B.; Johnston, M. B.; Herz, L. M.; Snaith, H. J. *Science* **2016**, *351*, 151–155.

(60) Diao, Y.; Lenn, K. M.; Lee, W.-Y.; Blood-Forsythe, M. A.; Xu, J.; Mao, Y.; Kim, Y.; Reinspach, J. A.; Park, S.; Aspuru-Guzik, A.; Xue, G.; Clancy, P.; Bao, Z.; Mannsfeld, S. C. B. *Journal of the American Chemical Society* **2014**, *136*, 17046–17057.

(61) Fusella, M. A.; Yang, S.; Abbasi, K.; Choi, H. H.; Yao, Z.; Podzorov, V.; Avishai, A.; Rand, B. P. *Chemistry of Materials* **2017**, *29*, 6666–6673.

(62) Tan, J. A. et al. *Advanced Functional Materials* **2023**, *33*, 2207867.

(63) Wong, C. Y.; Penwell, S. B.; Cotts, B. L.; Noriega, R.; Wu, H.; Ginsberg, N. S. *The Journal of Physical Chemistry C* **2013**, *117*, 22111–22122.

(64) Wong, C. Y.; Cotts, B. L.; Wu, H.; Ginsberg, N. S. *Nature Communications* **2015**, *6*, 5946.

(65) Wong, C. Y.; Folie, B. D.; Cotts, B. L.; Ginsberg, N. S. *The Journal of Physical Chemistry Letters* **2015**, *6*, 3155–3162.

(66) Coropceanu, V.; Cornil, J.; da Silva Filho, D. A.; Olivier, Y.; Silbey, R.; Brédas, J.-L. *Chemical Reviews* **2007**, *107*, 926–952.

(67) Takeya, J.; Yamagishi, M.; Tominari, Y.; Hirahara, R.; Nakazawa, Y.; Nishikawa, T.; Kawase, T.; Shimoda, T.; Ogawa, S. *Applied Physics Letters* **2007**, *90*, 102120.

(68) Hoffmann, R. *Angewandte Chemie International Edition in English* **1987**, *26*, 846–878.

(69) Reese, C.; Bao, Z. *Advanced Materials* **2007**, *19*, 4535–4538.

(70) Giri, G.; Park, S.; Vosgueritchian, M.; Shulaker, M. M.; Bao, Z. *Advanced Materials* **2014**, *26*, 487–493.

(71) Wade, J.; Steiner, F.; Niedzialek, D.; James, D. T.; Jung, Y.; Yun, D.-J.; Bradley, D. D. C.; Nelson, J.; Kim, J.-S. *Journal of Materials Chemistry C* **2014**, *2*, 10110–10115.

(72) Akselrod, G. M.; Deotare, P. B.; Thompson, N. J.; Lee, J.; Tisdale, W. A.; Baldo, M. A.; Menon, V. M.; Bulović, V. *Nature Communications* **2014**, *5*, 3646.

(73) Xing, G.; Mathews, N.; Sun, S.; Lim, S. S.; Lam, Y. M.; Grätzel, M.; Mhaisalkar, S.; Sum, T. C. *Science* **2013**, *342*, 344–347.

(74) Zhao, Y.; Nardes, A. M.; Zhu, K. *The Journal of Physical Chemistry Letters* **2014**, *5*, 490–494.

(75) deQuilettes, D. W.; Koch, S.; Burke, S.; Paranji, R. K.; Shropshire, A. J.; Ziffer, M. E.; Ginger, D. S. *ACS Energy Letters* **2016**, *1*, 438–444.

(76) Quan, L. N.; Rand, B. P.; Friend, R. H.; Mhaisalkar, S. G.; Lee, T.-W.; Sargent, E. H. *Chemical Reviews* **2019**, *119*, 7444–7477.

(77) Zhang, L.; Sun, C.; He, T.; Jiang, Y.; Wei, J.; Huang, Y.; Yuan, M. *Light: Science & Applications* **2021**, *10*, 61.

(78) Steirer, K. X.; Schulz, P.; Teeter, G.; Stevanovic, V.; Yang, M.; Zhu, K.; Berry, J. J. *ACS Energy Letters* **2016**, *1*, 360–366.

(79) Zhang, X.; Turiansky, M. E.; Van de Walle, C. G. *The Journal of Physical Chemistry C* **2020**, *124*, 6022–6027.

(80) Kim, G.-W.; Petrozza, A. *Advanced Energy Materials* **2020**, *10*, 2001959.

(81) Delor, M.; Slavney, A. H.; Wolf, N. R.; Filip, M. R.; Neaton, J. B.; Karunadasa, H. I.; Ginsberg, N. S. *ACS Energy Letters* **2020**, *5*, 1337–1345.

(82) Kojima, A.; Teshima, K.; Shirai, Y.; Miyasaka, T. *Journal of the American Chemical Society* **2009**, *131*, 6050–6051.

(83) Kim, J. Y.; Lee, J.-W.; Jung, H. S.; Shin, H.; Park, N.-G. *Chemical Reviews* **2020**, *120*, 7867–7918.

(84) Jeong, M.; Choi, I. W.; Go, E. M.; Cho, Y.; Kim, M.; Lee, B.; Jeong, S.; Jo, Y.; Choi, H. W.; Lee, J.; Bae, J.-H.; Kwak, S. K.; Kim, D. S.; Yang, C. *Science* **2020**, *369*, 1615–1620.

(85) Yoo, J. J.; Seo, G.; Chua, M. R.; Park, T. G.; Lu, Y.; Rotermund, F.; Kim, Y.-K.; Moon, C. S.; Jeon, N. J.; Correa-Baena, J.-P.; Bulović, V.; Shin, S. S.; Bawendi, M. G.; Seo, J. *Nature* **2021**, *590*, 587–593.

(86) Chen, J.; Yang, Y.; Dong, H.; Li, J.; Zhu, X.; Xu, J.; Pan, F.; Yuan, F.; Dai, J.; Jiao, B.; Hou, X.; Jen, A. K.-Y.; Wu, Z. *Science Advances* **2022**, *8*, eabk2722.

(87) Park, J.; Kim, J.; Yun, H.-S.; Paik, M. J.; Noh, E.; Mun, H. J.; Kim, M. G.; Shin, T. J.; Seok, S. I. *Nature* **2023**, 1–7.

(88) Berger, R. F. *Chemistry – A European Journal* **2018**, *24*, 8708–8716.

(89) Miyata, K.; Atallah, T. L.; Zhu, X.-Y. *Science Advances* **2017**, *3*, e1701469.

(90) Li, W.; Yadavalli, S. K.; Lizarazo-Ferro, D.; Chen, M.; Zhou, Y.; Padture, N. P.; Zia, R. *ACS Energy Letters* **2018**, *3*, 2669–2670.

(91) Rothmann, M. U.; Li, W.; Zhu, Y.; Bach, U.; Spiccia, L.; Etheridge, J.; Cheng, Y.-B. *Nature Communications* **2017**, *8*, 14547.

(92) Chu, Z.; Yang, M.; Schulz, P.; Wu, D.; Ma, X.; Seifert, E.; Sun, L.; Li, X.; Zhu, K.; Lai, K. *Nature Communications* **2017**, *8*, 2230.

(93) Hao, F.; Stoumpos, C. C.; Cao, D. H.; Chang, R. P. H.; Kanatzidis, M. G. *Nature Photonics* **2014**, *8*, 489–494.

(94) Slavney, A. H.; Hu, T.; Lindenberg, A. M.; Karunadasa, H. I. *Journal of the American Chemical Society* **2016**, *138*, 2138–2141.

(95) Wolf, N. R.; Connor, B. A.; Slavney, A. H.; Karunadasa, H. I. *Angewandte Chemie International Edition* **2021**, *60*, 16264–16278.

(96) Dey, A. et al. *ACS Nano* **2021**, *15*, 10775–10981.

(97) Hu, L. et al. *Nature Communications* **2021**, *12*, 466.

(98) Folie, B. D.; Tan, J. A.; Huang, J.; Sercel, P. C.; Delor, M.; Lai, M.; Lyons, J. L.; Bernstein, N.; Efros, A. L.; Yang, P.; Ginsberg, N. S. *The Journal of Physical Chemistry A* **2020**, *124*, 1867–1876.

(99) Kumar, G. S.; Sumukam, R. R.; Rajaboina, R. K.; Savu, R. N.; Srinivas, M.; Banavoth, M. *ACS Applied Energy Materials* **2022**, *5*, 1342–1377.

(100) Dou, L.; Wong, A. B.; Yu, Y.; Lai, M.; Kornienko, N.; Eaton, S. W.; Fu, A.; Bischak, C. G.; Ma, J.; Ding, T.; Ginsberg, N. S.; Wang, L.-W.; Alivisatos, A. P.; Yang, P. *Science* **2015**, *349*, 1518–1521.

(101) Mitzi, D. B.; Feild, C. A.; Harrison, W. T. A.; Guloy, A. M. *Nature* **1994**, *369*, 467–469.

(102) Smith, I. C.; Hoke, E. T.; Solis-Ibarra, D.; McGehee, M. D.; Karunadasa, H. I. *Angewandte Chemie International Edition* **2014**, *53*, 11232–11235.

(103) Stoumpos, C. C.; Cao, D. H.; Clark, D. J.; Young, J.; Rondinelli, J. M.; Jang, J. I.; Hupp, J. T.; Kanatzidis, M. G. *Chemistry of Materials* **2016**, *28*, 2852–2867.

(104) Connor, B. A.; Leppert, L.; Smith, M. D.; Neaton, J. B.; Karunadasa, H. I. *Journal of the American Chemical Society* **2018**, *140*, 5235–5240.

(105) Mao, L.; Stoumpos, C. C.; Kanatzidis, M. G. *Journal of the American Chemical Society* **2019**, *141*, 1171–1190.

(106) Miyata, A.; Mitioglu, A.; Plochocka, P.; Portugall, O.; Wang, J. T.-W.; Stranks, S. D.; Snaith, H. J.; Nicholas, R. J. *Nature Physics* **2015**, *11*, 582–587.

(107) Limmer, D. T.; Ginsberg, N. S. *The Journal of Chemical Physics* **2020**, *152*, 230901.

(108) Zhu, X.-Y.; Podzorov, V. *The Journal of Physical Chemistry Letters* **2015**, *6*, 4758–4761.

(109) Bischak, C. G.; Hetherington, C. L.; Wu, H.; Aloni, S.; Ogletree, D. F.; Limmer, D. T.; Ginsberg, N. S. *Nano Letters* **2017**, *17*, 1028–1033.

(110) Penwell, S. B.; Ginsberg, L. D. S.; Noriega, R.; Ginsberg, N. S. *Nature Materials* **2017**, *16*, 1136–1141.

(111) Kulig, M.; Zipfel, J.; Nagler, P.; Blanter, S.; Schüller, C.; Korn, T.; Paradiso, N.; Glazov, M. M.; Chernikov, A. *Physical Review Letters* **2018**, *120*, 207401.

(112) Seo, M. A.; Yoo, J.; Dayeh, S. A.; Picraux, S. T.; Taylor, A. J.; Prasankumar, R. P. *Nano Letters* **2012**, *12*, 6334–6338.

(113) Gabriel, M. M.; Kirschbrown, J. R.; Christesen, J. D.; Pinion, C. W.; Zigler, D. F.; Grumstrup, E. M.; Mehl, B. P.; Cating, E. E. M.; Cahoon, J. F.; Papanikolas, J. M. *Nano Letters* **2013**, *13*, 1336–1340.

(114) Guo, Z.; Manser, J. S.; Wan, Y.; Kamat, P. V.; Huang, L. *Nature Communications* **2015**, *6*, 7471.

(115) Rozenman, G. G.; Akulov, K.; Golombek, A.; Schwartz, T. *ACS Photonics* **2018**, *5*, 105–110.

(116) Najafi, E.; Scarborough, T. D.; Tang, J.; Zewail, A. *Science* **2015**, *347*, 164–167.

(117) Ginsberg, N. S.; Tisdale, W. A. *Annual Review of Physical Chemistry* **2020**, *71*, 1–30.

(118) Fassioli, F.; Dinshaw, R.; Arpin, P. C.; Scholes, G. D. *Journal of The Royal Society Interface* **2014**, *11*, 20130901.

(119) Ginsberg, N. S.; Cheng, Y.-C.; Fleming, G. R. *Accounts of Chemical Research* **2009**, *42*, 1352–1363.

(120) Ishizaki, A.; Fleming, G. R. *The Journal of Physical Chemistry B* **2021**, *125*, 3286–3295.

(121) Qiu, D. Y.; da Jornada, F. H.; Louie, S. G. *Physical Review Letters* **2013**, *111*, 216805.

(122) Troisi, A. *Chemical Society Reviews* **2011**, *40*, 2347–2358.

(123) Fratini, S.; Ciuchi, S.; Mayou, D.; de Laissardière, G. T.; Troisi, A. *Nature Materials* **2017**, *16*, 998–1002.

(124) Giannini, S.; Peng, W.-T.; Cupellini, L.; Padula, D.; Carof, A.; Blumberger, J. *Nature Communications* **2022**, *13*, 2755.

(125) Sneyd, A. J.; Beljonne, D.; Rao, A. *The Journal of Physical Chemistry Letters* **2022**, *13*, 6820–6830.

(126) Najafi, E.; Ivanov, V.; Zewail, A.; Bernardi, M. *Nature Communications* **2017**, *8*, 15177.

(127) Barthelemy, P.; Bertolotti, J.; Wiersma, D. S. *Nature* **2008**, *453*, 495–498.

(128) Mercadier, N.; Guerin, W.; Chevrollier, M.; Kaiser, R. *Nature Physics* **2009**, *5*, 602–605.

(129) Bulchandani, V. B.; Karrasch, C.; Moore, J. E. *Proceedings of the National Academy of Sciences* **2020**, *117*, 12713–12718.

(130) Utterback, J. K.; Sood, A.; Coropceanu, I.; Guzelturk, B.; Talapin, D. V.; Lindenberg, A. M.; Ginsberg, N. S. *Nano Letters* **2021**, *21*, 3540–3547.

(131) Seitz, M.; Meléndez, M.; Alcázar-Cano, N.; Congreve, D. N.; Delgado-Buscalioni, R.; Prins, F. *Advanced Optical Materials* **2021**, *9*, 2001875.

(132) Bohren, C. F.; Huffman, D. R., *Absorption and Scattering of Light by Small Particles*; John Wiley & Sons Inc.: 1998.

(133) Van de Hulst, H., *Light Scattering by Small Particles*; Dover: 1981.

(134) Van De Hulst, H. C. *Physica* **1949**, *15*, 740–746.

(135) Newton, R. G. *American Journal of Physics* **1976**, *44*, 639–642.

(136) Griffiths, D. J. In *Introduction to Quantum Mechanics*, 2nd ed., "Phase Shifts"; Pearson Prentice Hall: 2005, pp 405–407.

(137) Littlejohn, R. G. "Notes 36: Introduction to Time-Independent Scattering Theory and Scattering from Central Force Potentials" `https://bohr.physics.berkeley.edu/classes/221/notes/introscatt.pdf`.

(138) Rayleigh, L. *The London, Edinburgh, and Dublin Philosophical Magazine and Journal of Science* **1871**, *41*, 107–120.

(139) Nave, R. Hyperphysics: Blue Sky `http://hyperphysics.phy-astr.gsu.edu/hbase/atmos/blusky.html`.

(140) Petty, G. W., *A First Course in Atmospheric Radiation*, 2nd; Sundog Publishing: 2006.

(141) Skolnik, M., *Introduction to Radar Systems*, 3rd; McGraw-Hill Education: 2002.

(142) Griffiths, D. J. In *Introduction to Electrodynamics*, 4th ed., "Electric Fields in Matter"; Pearson: 2013, pp 167–204.

(143) Lambert, B. "An illustration of the frequency response of various dielectric mechanisms in terms of the real and imaginary parts of the permittivity." `https://commons.wikimedia.org/wiki/File:Dielectric_responses.svg`.

(144) Feynman, R. P. In *The Feynman Lectures on Physics*, Leighton, R. B., Sands, M., Eds., New Millennium Edition, "Chapter 31: The Origin of the Refractive Index"; Basic Books: 2011; Vol. 1.

(145) Dresselhaus, M. "Solid State Physics Part II: Optical Properties of Solids" `http://web.mit.edu/6.732/www/opt.pdf`.

(146) Bennett, B.; Soref, R.; Del Alamo, J. *IEEE Journal of Quantum Electronics* **1990**, *26*, 113–122.

(147) Dresselhaus, M. 5.4 Direct Interband Transitions in "Solid State Physics Part II: Optical Properties of Solids", `http://web.mit.edu/6.732/www/opt.pdf`.

(148) Cohen, M. L.; Louie, S. G. In *Fundamentals of Condensed Matter Physics*, "9.4 Interband optical transitions in semiconductors and insulators"; Cambridge University Press: 2016, pp 196–201.

(149) Peyghambarian, N.; Koch, S. W.; Mysyrowicz, A. In *Introduction to Semiconductor Optics*, "13-5 Bandgap Renormalization"; Prentice Hall: 1993, pp 330–333.

(150) Haug, H.; Koch, S. W. In *Quantum Theory of the Optical and Electronic Properties of Semiconductors*, 4th ed., "Optical Properties of a Quasi-Equilibrium Electron-Hole Plasma"; World Scientific Publishing: Singapore, pp 283–296.

(151) Wolff, P. A. *Physical Review* **1962**, *126*, 405–412.

(152) Pogna, E. A. A.; Marsili, M.; De Fazio, D.; Dal Conte, S.; Manzoni, C.; Sangalli, D.; Yoon, D.; Lombardo, A.; Ferrari, A. C.; Marini, A.; Cerullo, G.; Prezzi, D. *ACS Nano* **2016**, *10*, 1182–1188.

(153) Park, Y.; Han, S. W.; Chan, C. C. S.; Reid, B. P. L.; Taylor, R. A.; Kim, N.; Jo, Y.; Im, H.; Kim, K. S. *Nanoscale* **2017**, *9*, 10647–10652.

(154) Liu, F.; Ziffer, M. E.; Hansen, K. R.; Wang, J.; Zhu, X. *Physical Review Letters* **2019**, *122*, 246803.

(155) Qiu, Z. et al. *Science Advances* **2019**, *5*, eaaw234.

(156) Ashcroft, N. W.; Mermin, D. N. In *Solid State Physics*, "The Drude Theory of Metals"; Harcourt College Pulishers: 1976, pp 1–25.

(157) Yu, P. Y.; Cardona, M. In *Fundamentals of Semiconductors*, 4th ed., "Free-Carrier Absorption in Doped Semiconductors"; Springer: 2010, pp 306–310.

(158) Dresselhaus, M. Chapter 2: Drude Theory–Free Carrier Contribution to the Optical Properties in "Solid State Physics Part II: Optical Properties of Solids", `http://web.mit.edu/6.732/www/opt.pdf`.

(159) Ahrenkiel, R. K.; Ahrenkiel, S. P. In *Theory and Methods of Photovoltaic Material Characterization*; Materials and Energy, Vol. 13, "Free Carrier Absorption"; World Scientific Publishing: 2018, pp 207–218.

(160) Henry, C. H.; Logan, R. A.; Bertness, K. A. *Journal of Applied Physics* **1981**, *52*, 4457–4461.

(161) Soref, R.; Bennett, B. *IEEE Journal of Quantum Electronics* **1987**, *23*, 123–129.

(162) Sabbah, A. J.; Riffe, D. M. *Physical Review B* **2002**, *66*, 165217.

(163) Ndebeka-Bandou, C.; Carosella, F.; Ferreira, R.; Wacker, A.; Bastard, G. *Semiconductor Science and Technology* **2014**, *29*, 023001.

(164) Hagan, D. E.; Nedeljkovic, M.; Cao, W.; Thomson, D. J.; Mashanovich, G. Z.; Knights, A. P. *Optics Express* **2019**, *27*, 166–174.

(165) Rosei, R.; Lynch, D. W. *Physical Review B* **1972**, *5*, 3883–3894.

(166) Varshni, Y. P. *Physica* **1967**, *34*, 149–154.

(167) O'Donnell, K. P.; Chen, X. *Applied Physics Letters* **1991**, *58*, 2924–2926.

(168) Went, C. "Optical Properties of Solids" `https://github.com/corawent/fundamentals/blob/master/optical-properties.ipynb`.

(169) Sakurai, J. In *Advanced Quantum Mechanics*, 1st, "Dispersion Relations and Causality"; Addison Wesley: 1982, pp 62–63.

(170) Cahill, K. In *Physical Mathematics*, "Complex-variable theory"; Cambridge University Press: 2013, pp 207–208.

(171) Ashoka, A.; Tamming, R. R.; Girija, A. V.; Bretscher, H.; Verma, S. D.; Yang, S.-D.; Lu, C.-H.; Hodgkiss, J. M.; Ritchie, D.; Chen, C.; Smith, C. G.; Schnedermann, C.; Price, M. B.; Chen, K.; Rao, A. *Nature Communications* **2022**, *13*, 1437.

(172) Hecht, E. In *Optics*, "The Fresnel Equations"; Addison-Wesley: 1998, pp 109–121.

(173) Price, M. B.; Butkus, J.; Jellicoe, T. C.; Sadhanala, A.; Briane, A.; Halpert, J. E.; Broch, K.; Hodgkiss, J. M.; Friend, R. H.; Deschler, F. *Nature Communications* **2015**, *6*, 8420.

(174) Yang, Y.; Yang, M.; Moore, D. T.; Yan, Y.; Miller, E. M.; Zhu, K.; Beard, M. C. *Nature Energy* **2017**, *2*, 1–7.

(175) Pasanen, H. P.; Vivo, P.; Canil, L.; Abate, A.; Tkachenko, N. *Physical Chemistry Chemical Physics* **2019**, *21*, 14663–14670.

(176) Sorenson, S. A.; Patrow, J. G.; Dawlaty, J. M. *The Journal of Physical Chemistry C* **2016**, *120*, 7736–7747.

(177) Ichimura, K.; Yoshizawa, M.; Matsuda, H.; Okada, S.; Ohsugi, M. M.; Nakanishi, H.; Kobayashi, T. *The Journal of Chemical Physics* **1993**, *99*, 7404–7416.

(178) Jackson, J., *Classical Electrodynamics*; John Wiley & Sons Inc.: 1998.

(179) Yang, Y.; Yan, Y.; Yang, M.; Choi, S.; Zhu, K.; Luther, J. M.; Beard, M. C. *Nature Communications* **2015**, *6*, 7961.

(180) Chen, X.; Wang, K.; Beard, M. C. *Physical Chemistry Chemical Physics* **2019**, *21*, 16399–16407.

(181) Ashoka, A.; Gauriot, N.; Girija, A. V.; Sawhney, N.; Sneyd, A. J.; Watanabe, K.; Taniguchi, T.; Sung, J.; Schnedermann, C.; Rao, A. *Nature Communications* **2022**, *13*, 5963.

(182) Volkmer, A.; Cheng, J.-X.; Sunney Xie, X. *Physical Review Letters* **2001**, *87*, 023901.

(183) Cheng, J.-X.; Volkmer, A.; Xie, X. S. *JOSA B* **2002**, *19*, 1363–1375.

(184) Xu, D.; Mandal, A.; Baxter, J. M.; Cheng, S.-W.; Lee, I.; Su, H.; Liu, S.; Reichman, D. R.; Delor, M. *arXiv* **2022**, DOI: 10.48550/arXiv.2205.01176.

(185) Kim, J.; Zhao, H.; Hou, S.; Khatoniar, M.; Menon, V.; Forrest, S. R. *Physical Review Applied* **2020**, *14*, 034048.

(186) Abbe, E. *Archiv für Mikroskopische Anatomie* **1873**, *9*, 413–468.

(187) Rayleigh, L. *The London, Edinburgh, and Dublin Philosophical Magazine and Journal of Science* **1879**, *8*, 261–274.

(188) Heeger, D. "Signals, Linear Systems, and Convolution" https://www.cns.nyu.edu/~david/handouts/convolution.pdf.

(189) Gaskill, J. D. In *Linear Systems, Fourier Transforms, and Optics*, "Chapter 6: Convolution"; Wiley-Interscience: 1978.

(190) Goodman, J. In *Introduction to Fourier Optics*, "Section 2.3: Linear Systems"; Roberts and Company Publishers: 2004.

(191) Taylor, R. W.; Sandoghdar, V. *Nano Letters* **2019**, *19*, 4827–4835.

(192) Taylor, R. W.; Sandoghdar, V., *Label-Free Super-Resolution Microscopy*; Astratov, V., Ed.; Biological and Medical Physics, Biomedical Engineering, "Interferometric Scattering (iSCAT) Microscopy and Related Techniques"; Springer International Publishing: Cham, 2019; 25-65.

(193) Young, G.; Kukura, P. *Annual Review of Physical Chemistry* **2019**, *70*, 301–322.

(194) Lindfors, K.; Kalkbrenner, T.; Stoller, P.; Sandoghdar, V. *Physical Review Letters* **2004**, *93*, 037401.

(195) Ortega-Arroyo, J.; Kukura, P. *Physical Chemistry Chemical Physics* **2012**, *14*, 15625–15636.

(196) Gingell, D.; Todd, I. *Biophysical Journal* **1979**, *26*, 507–526.

(197) Lemineur, J.-F.; Wang, H.; Wang, W.; Kanoufi, F. *Annual Review of Analytical Chemistry* **2022**, *15*, 57–82.

(198) Krishnan, M.; Mojarad, N.; Kukura, P.; Sandoghdar, V. *Nature* **2010**, *467*, 692–695.

(199) Kukura, P.; Celebrano, M.; Renn, A.; Sandoghdar, V. *Nano Letters* **2009**, *9*, 926–929.

(200) Naser, H.; Shanshool, H. M.; Hassan, S. F.; Dheyab, A. B. *MAPAN* **2019**, *34*, 289–294.

(201) Born, M.; Wolf, E., *Principles of Optics: Electromagnetic Theory of Propagation, Interference and Diffraction of Light*, 7th ed.; Cambridge University Press: Cambridge, 1999.

(202) Feng, S.; Winful, H. G. *Optics Letters* **2001**, *26*, 485–487.

(203) Boyd, R. W. *JOSA* **1980**, *70*, 877–880.

(204) Jacobsen, V.; Stoller, P.; Brunner, C.; Vogel, V.; Sandoghdar, V. *Optics Express* **2006**, *14*, 405–414.

(205) Holanová, K.; Vala, M.; Piliarik, M. *Optics & Laser Technology* **2019**, *109*, 323–327.

(206) Ortega Arroyo, J.; Andrecka, J.; Spillane, K. M.; Billington, N.; Takagi, Y.; Sellers, J. R.; Kukura, P. *Nano Letters* **2014**, *14*, 2065–2070.

(207) Piliarik, M.; Sandoghdar, V. *Nature Communications* **2014**, *5*, 4495.

(208) Liebel, M.; Hugall, J. T.; van Hulst, N. F. *Nano Letters* **2017**, *17*, 1277–1281.

(209) Young, G. et al. *Science* **2018**, *360*, 423–427.

(210) Dahmardeh, M.; Mirzaalian Dastjerdi, H.; Mazal, H.; Köstler, H.; Sandoghdar, V. *Nature Methods* **2023**, *20*, 442–447.

(211) Plakhotnik, T.; Palm, V. *Physical Review Letters* **2001**, *87*, 183602.

(212) Wolpert, C.; Dicken, C.; Atkinson, P.; Wang, L.; Rastelli, A.; Schmidt, O. G.; Giessen, H.; Lippitz, M. *Nano Letters* **2012**, *12*, 453–457.

(213) Karrai, K.; J. Warburton, R. *Superlattices and Microstructures* **2003**, *33*, 311–337.

(214) Amos, L. A.; Amos, W. B. *Journal of Cell Science* **1991**, *1991*, 95–101.

(215) Ignatovich, F. V.; Novotny, L. *Physical Review Letters* **2006**, *96*, 013901.

(216) Berciaud, S.; Cognet, L.; Blab, G. A.; Lounis, B. *Physical Review Letters* **2004**, *93*, 257402.

(217) Boyer, D.; Tamarat, P.; Maali, A.; Lounis, B.; Orrit, M. *Science* **2002**, *297*, 1160–1163.

(218) Ortega Arroyo, J.; Cole, D.; Kukura, P. *Nature Protocols* **2016**, *11*, 617–633.

(219) Utterback, J. K.; King, A. J.; Belman-Wells, L.; Larson, D. M.; Hamerlynck, L. M.; Weber, A. Z.; Ginsberg, N. S. *ACS Energy Letters* **2023**, 1785–1792.

(220) Trueb, J. T.; Avci, O.; Sevenler, D.; Connor, J. H.; Ünlü, M. S. *IEEE Journal of Selected Topics in Quantum Electronics* **2017**, *23*, 394–403.

(221) Dulin, D.; Barland, S.; Hachair, X.; Pedaci, F. *PLOS ONE* **2014**, *9*, e107335.

(222) Schnedermann, C.; Sung, J.; Pandya, R.; Verma, S. D.; Chen, R. Y. S.; Gauriot, N.; Bretscher, H. M.; Kukura, P.; Rao, A. *The Journal of Physical Chemistry Letters* **2019**, *10*, 6727–6733.

(223) Gitomer, S. J.; Jones, R. D.; Begay, F.; Ehler, A. W.; Kephart, J. F.; Kristal, R. *The Physics of Fluids* **1986**, *29*, 2679–2688.

(224) Alén, B.; Bickel, F.; Karrai, K.; Warburton, R. J.; Petroff, P. M. *Applied Physics Letters* **2003**, *83*, 2235–2237.

(225) Guenther, T.; Lienau, C.; Elsaesser, T.; Glanemann, M.; Axt, V. M.; Kuhn, T.; Eshlaghi, S.; Wieck, A. D. *Physical Review Letters* **2002**, *89*, 057401.

(226) Schnedermann, C.; Lim, J. M.; Wende, T.; Duarte, A. S.; Ni, L.; Gu, Q.; Sadhanala, A.; Rao, A.; Kukura, P. *The Journal of Physical Chemistry Letters* **2016**, *7*, 4854–4859.

(227) Piland, G.; Grumstrup, E. M. *The Journal of Physical Chemistry A* **2019**, *123*, 8709–8716.

(228) Cole, D.; Young, G.; Weigel, A.; Sebesta, A.; Kukura, P. *ACS Photonics* **2017**, *4*, 211–216.

(229) Brokmann, X.; Coolen, L.; Hermier, J.-P.; Dahan, M. *Chemical Physics* **2005**, *318*, 91–98.

(230) Sowa, Y.; Steel, B. C.; Berry, R. M. *Review of Scientific Instruments* **2010**, *81*, 113704.

(231) Sheng, R.; Ho-Baillie, A.; Huang, S.; Chen, S.; Wen, X.; Hao, X.; Green, M. A. *The Journal of Physical Chemistry C* **2015**, *119*, 3545–3549.

(232) Jacoboni, C.; Canali, C.; Ottaviani, G.; Alberigi Quaranta, A. *Solid-State Electronics* **1977**, *20*, 77–89.

(233) Shanks, H. R.; Maycock, P. D.; Sidles, P. H.; Danielson, G. C. *Physical Review* **1963**, *130*, 1743–1748.

(234) Shi, D. et al. *Science* **2015**, *347*, 519–522.

(235) Hill, A. H.; Smyser, K. E.; Kennedy, C. L.; Massaro, E. S.; Grumstrup, E. M. *The Journal of Physical Chemistry Letters* **2017**, *8*, 948–953.

(236) Anthony, J. E.; Brooks, J. S.; Eaton, D. L.; Parkin, S. R. *Journal of the American Chemical Society* **2001**, *123*, 9482–9483.

(237) Giri, G.; Verploegen, E.; Mannsfeld, S. C. B.; Atahan-Evrenk, S.; Kim, D. H.; Lee, S. Y.; Becerril, H. A.; Aspuru-Guzik, A.; Toney, M. F.; Bao, Z. *Nature* **2011**, *480*, 504–508.

(238) Chen, J.; Tee, C. K.; Shtein, M.; Anthony, J.; Martin, D. C. *Journal of Applied Physics* **2008**, *103*, 114513.

(239) Zhu, H.; Miyata, K.; Fu, Y.; Wang, J.; Joshi, P. P.; Niesner, D.; Williams, K. W.; Jin, S.; Zhu, X.-Y. *Science* **2016**, *353*, 1409–1413.

(240) Wan, Y.; Guo, Z.; Zhu, T.; Yan, S.; Johnson, J.; Huang, L. *Nature Chemistry* **2015**, *7*, 785–792.

(241) Zhu, T.; Wan, Y.; Guo, Z.; Johnson, J.; Huang, L. *Advanced Materials* **2016**, *28*, 7539–7547.

(242) Folie, B. D.; Haber, J. B.; Refaely-Abramson, S.; Neaton, J. B.; Ginsberg, N. S. *Journal of the American Chemical Society* **2018**, *140*, 2326–2335.

(243) Rivnay, J.; Jimison, L. H.; Northrup, J. E.; Toney, M. F.; Noriega, R.; Lu, S.; Marks, T. J.; Facchetti, A.; Salleo, A. *Nature Materials* **2009**, *8*, 952–958.

(244) Greuter, F.; Blatter, G. *Semiconductor Science and Technology* **1990**, *5*, 111–137.

(245) Yun, J. S.; Ho-Baillie, A.; Huang, S.; Woo, S. H.; Heo, Y.; Seidel, J.; Huang, F.; Cheng, Y.-B.; Green, M. A. *The Journal of Physical Chemistry Letters* **2015**, *6*, 875–880.

(246) Reid, O. G.; Yang, M.; Kopidakis, N.; Zhu, K.; Rumbles, G. *ACS Energy Letters* **2016**, *1*, 561–565.

(247) deQuilettes, D. W.; Vorpahl, S. M.; Stranks, S. D.; Nagaoka, H.; Eperon, G. E.; Ziffer, M. E.; Snaith, H. J.; Ginger, D. S. *Science* **2015**, *348*, 683–686.

(248) deQuilettes, D. W.; Jariwala, S.; Burke, S.; Ziffer, M. E.; Wang, J. T.-W.; Snaith, H. J.; Ginger, D. S. *ACS Nano* **2017**, *11*, 11488–11496.

(249) Tian, W.; Cui, R.; Leng, J.; Liu, J.; Li, Y.; Zhao, C.; Zhang, J.; Deng, W.; Lian, T.; Jin, S. *Angewandte Chemie International Edition* **2016**, *55*, 13067–13071.

(250) Ciesielski, R.; Schäfer, F.; Hartmann, N. F.; Giesbrecht, N.; Bein, T.; Docampo, P.; Hartschuh, A. *ACS Applied Materials & Interfaces* **2018**, *10*, 7974–7981.

(251) MacDonald, G. A.; Yang, M.; Berweger, S.; Killgore, J. P.; Kabos, P.; Berry, J. J.; Zhu, K.; DelRio, F. W. *Energy & Environmental Science* **2016**, *9*, 3642–3649.

(252) Snaider, J. M.; Guo, Z.; Wang, T.; Yang, M.; Yuan, L.; Zhu, K.; Huang, L. *ACS Energy Letters* **2018**, *3*, 1402–1408.

(253) Saliba, M.; Correa-Baena, J.-P.; Grätzel, M.; Hagfeldt, A.; Abate, A. *Angewandte Chemie International Edition* **2018**, *57*, 2554–2569.

(254) Yoo, J. J.; Shin, S. S.; Seo, J. *ACS Energy Letters* **2022**, *7*, 2084–2091.

(255) Berry, J. et al. *Advanced Materials* **2015**, *27*, 5102–5112.

(256) Stranks, S. D.; Eperon, G. E.; Grancini, G.; Menelaou, C.; Alcocer, M. J. P.; Leijtens, T.; Herz, L. M.; Petrozza, A.; Snaith, H. J. *Science* **2013**, *342*, 341–344.

(257) Tress, W. *Advanced Energy Materials* **2017**, *7*, 1602358.

(258) Baffou, G.; Bon, P.; Savatier, J.; Polleux, J.; Zhu, M.; Merlin, M.; Rigneault, H.; Monneret, S. *ACS Nano* **2012**, *6*, 2452–2458.

(259) Wu, B.; Nguyen, H. T.; Ku, Z.; Han, G.; Giovanni, D.; Mathews, N.; Fan, H. J.; Sum, T. C. *Advanced Energy Materials* **2016**, *6*, 1600551.

(260) Schneider, C. A.; Rasband, W. S.; Eliceiri, K. W. *Nature Methods* **2012**, *9*, 671–675.

(261) Schindelin, J. et al. *Nature Methods* **2012**, *9*, 676–682.

(262) Vincent, L.; Soille, P. *IEEE Transactions on Pattern Analysis and Machine Intelligence* **1991**, *13*, 583–598.

(263) Najman, L.; Schmitt, M. *IEEE Transactions on Pattern Analysis and Machine Intelligence* **1996**, *18*, 1163–1173.

(264) Lotufo, R.; Falcao, A. In *Mathematical Morphology and its Applications to Image and Signal Processing*, Goutsias, J., Vincent, L., Bloomberg, D. S., Eds.; Computational Imaging and Vision, "The Ordered Queue and the Optimality of the Watershed Approaches"; Springer US: Boston, MA, 2000, pp 341–350.

(265) Lombardot, B. "Interactive Watershed" `https://imagej.net/plugins/interactive-watershed`.

(266) Yakunin, S.; Sytnyk, M.; Kriegner, D.; Shrestha, S.; Richter, M.; Matt, G. J.; Azimi, H.; Brabec, C. J.; Stangl, J.; Kovalenko, M. V.; Heiss, W. *Nature Photonics* **2015**, *9*, 444–449.

(267) Glassbrenner, C. J.; Slack, G. A. *Physical Review* **1964**, *134*, A1058–A1069.

(268) Jellison, G. E.; Burke, H. H. *Journal of Applied Physics* **1986**, *60*, 841–843.

(269) Neamen, D., *Semiconductor Physics and Devices*; McGraw-Hill: Boston, MA, 2002.

(270) Rosling, M.; Bleichner, H.; Jonsson, P.; Nordlander, E. *Journal of Applied Physics* **1994**, *76*, 2855–2859.

(271) Zhao, H. *Applied Physics Letters* **2008**, *92*, 112104.

(272) Kroemer, H. *IEEE Transactions on Electron Devices* **1978**, *25*, 850–850.

(273) Sze, S., *Physics of Semiconductor Devices*; Wiley: New York, 1981.

(274) Li, C.-M.; Sjodin, T.; Dai, H.-L. *Physical Review B* **1997**, *56*, 15252–15255.

(275) Zhou, J.-J.; Park, J.; Timrov, I.; Floris, A.; Cococcioni, M.; Marzari, N.; Bernardi, M. *Physical Review Letters* **2021**, *127*, 126404.

(276) Lu, I.-T.; Zhou, J.-J.; Park, J.; Bernardi, M. *Physical Review Materials* **2022**, *6*, L010801.

(277) Green, M. A. *Solar Energy Materials and Solar Cells* **2008**, *92*, 1305–1310.

(278) Delor, M.; Weaver, H. L.; Yu, Q.; Ginsberg, N. S. *Nature Materials* **2020**, *19*, 56–62.

(279) Celebrano, M.; Kukura, P.; Renn, A.; Sandoghdar, V. *Nature Photonics* **2011**, *5*, 95–98.

(280) Merryweather, A. J.; Schnedermann, C.; Jacquet, Q.; Grey, C. P.; Rao, A. *Nature* **2021**, *594*, 522–528.

(281) Wang, F.; Wu, Y.; Hybertsen, M. S.; Heinz, T. F. *Physical Review B* **2006**, *73*, 245424.

(282) Uddin, S. Z.; Higashitarumizu, N.; Kim, H.; Yi, J.; Zhang, X.; Chrzan, D.; Javey, A. *ACS Nano* **2022**, *16*, 8005–8011.

(283) Das, S. et al. *Nature Electronics* **2021**, *4*, 786–799.

(284) Cahill, D. G.; Braun, P. V.; Chen, G.; Clarke, D. R.; Fan, S.; Goodson, K. E.; Keblinski, P.; King, W. P.; Mahan, G. D.; Majumdar, A.; Maris, H. J.; Phillpot, S. R.; Pop, E.; Shi, L. *Applied Physics Reviews* **2014**, *1*, 011305.

(285) Yalon, E.; Aslan, B.; Smithe, K. K. H.; McClellan, C. J.; Suryavanshi, S. V.; Xiong, F.; Sood, A.; Neumann, C. M.; Xu, X.; Goodson, K. E.; Heinz, T. F.; Pop, E. *ACS Applied Materials & Interfaces* **2017**, *9*, 43013–43020.

(286) Sood, A.; Sievers, C.; Shin, Y. C.; Chen, V.; Chen, S.; Smithe, K. K. H.; Chatterjee, S.; Donadio, D.; Goodson, K. E.; Pop, E. *ACS Nano* **2021**, *15*, 19503–19512.

(287) Gabourie, A. J.; Köroğlu, Ç.; Pop, E. *Journal of Applied Physics* **2022**, *131*, 195103.

(288) Zheng, W.; McClellan, C. J.; Pop, E.; Koh, Y. K. *ACS Applied Materials & Interfaces* **2022**, *14*, 22372–22380.

(289) He, J.; Tritt, T. M. *Science* **2017**, *357*, eaak9997.

(290) Cooper, J. K.; Reyes-Lillo, S. E.; Hess, L. H.; Jiang, C.-M.; Neaton, J. B.; Sharp, I. D. *The Journal of Physical Chemistry C* **2018**, *122*, 20642–20652.

(291) Ruppert, C.; Chernikov, A.; Hill, H. M.; Rigosi, A. F.; Heinz, T. F. *Nano Letters* **2017**, *17*, 644–651.

(292) Waxler, R.; Cleek, G. *J Res Natl Bur Stand A Phys Chem* **1973**, *77A*, 755–763.

(293) Fan, T. Y.; Daneu, J. L. *Applied Optics* **1998**, *37*, 1635–1637.

(294) Handa, T.; Tahara, H.; Aharen, T.; Kanemitsu, Y. *Science Advances* **2019**, *5*, eaax0786.

(295) Li, Y.; Chernikov, A.; Zhang, X.; Rigosi, A.; Hill, H. M.; van der Zande, A. M.; Chenet, D. A.; Shih, E.-M.; Hone, J.; Heinz, T. F. *Physical Review B* **2014**, *90*, 205422.

(296) Perea-Causín, R.; Brem, S.; Rosati, R.; Jago, R.; Kulig, M.; Ziegler, J. D.; Zipfel, J.; Chernikov, A.; Malic, E. *Nano Letters* **2019**, *19*, 7317–7323.

(297) Zipfel, J.; Kulig, M.; Perea-Causín, R.; Brem, S.; Ziegler, J. D.; Rosati, R.; Taniguchi, T.; Watanabe, K.; Glazov, M. M.; Malic, E.; Chernikov, A. *Physical Review B* **2020**, *101*, 115430.

(298) Goodman, A. J.; Lien, D.-H.; Ahn, G. H.; Spiegel, L. L.; Amani, M.; Willard, A. P.; Javey, A.; Tisdale, W. A. *The Journal of Physical Chemistry C* **2020**, *124*, 12175–12184.

(299) Lo Gerfo M., G.; Bolzonello, L.; Bernal-Texca, F.; Martorell, J.; van Hulst, N. F. *The Journal of Physical Chemistry Letters* **2023**, *14*, 1999–2005.

(300) Cui, Q.; Ceballos, F.; Kumar, N.; Zhao, H. *ACS Nano* **2014**, *8*, 2970–2976.

(301) Grumstrup, E. M.; Gabriel, M. M.; Cating, E. E. M.; Van Goethem, E. M.; Papanikolas, J. M. *Chemical Physics* **2015**, *458*, 30–40.

(302) Hill, A. H.; Kennedy, C. L.; Massaro, E. S.; Grumstrup, E. M. *The Journal of Physical Chemistry Letters* **2018**, *9*, 2808–2813.

(303) Block, A.; Liebel, M.; Yu, R.; Spector, M.; Sivan, Y.; García de Abajo, F. J.; van Hulst, N. F. *Science Advances* **2019**, *5*, eaav8965.

(304) Liu, Q.; Wei, K.; Tang, Y.; Xu, Z.; Cheng, X.; Jiang, T. *Advanced Science* **2022**, *9*, 2105746.

(305) Guzelturk, B. et al. *ACS Nano* **2020**, *14*, 4792–4804.

(306) Geim, A. K.; Grigorieva, I. V. *Nature* **2013**, *499*, 419–425.

(307) Velický, M.; Toth, P. S. *Applied Materials Today* **2017**, *8*, 68–103.

(308) Rivera, P.; Schaibley, J. R.; Jones, A. M.; Ross, J. S.; Wu, S.; Aivazian, G.; Klement, P.; Seyler, K.; Clark, G.; Ghimire, N. J.; Yan, J.; Mandrus, D. G.; Yao, W.; Xu, X. *Nature Communications* **2015**, *6*, 6242.

(309) Miller, B.; Steinhoff, A.; Pano, B.; Klein, J.; Jahnke, F.; Holleitner, A.; Wurstbauer, U. *Nano Letters* **2017**, *17*, 5229–5237.

(310) Calman, E. V.; Fogler, M. M.; Butov, L. V.; Hu, S.; Mishchenko, A.; Geim, A. K. *Nature Communications* **2018**, *9*, 1895.

(311) Jauregui, L. A. et al. *Science* **2019**, *366*, 870–875.

(312) Jiang, Y.; Chen, S.; Zheng, W.; Zheng, B.; Pan, A. *Light: Science & Applications* **2021**, *10*, 72.

(313) Schaibley, J. R.; Yu, H.; Clark, G.; Rivera, P.; Ross, J. S.; Seyler, K. L.; Yao, W.; Xu, X. *Nature Reviews Materials* **2016**, *1*, 1–15.

(314) Purdie, D. G.; Pugno, N. M.; Taniguchi, T.; Watanabe, K.; Ferrari, A. C.; Lombardo, A. *Nature Communications* **2018**, *9*, 5387.

(315) Kumar, N.; Cui, Q.; Ceballos, F.; He, D.; Wang, Y.; Zhao, H. *Nanoscale* **2014**, *6*, 4915–4919.

(316) Kato, T.; Kaneko, T. *ACS Nano* **2016**, *10*, 9687–9694.

(317) Yuan, L.; Wang, T.; Zhu, T.; Zhou, M.; Huang, L. *The Journal of Physical Chemistry Letters* **2017**, *8*, 3371–3379.

(318) Cordovilla Leon, D. F.; Li, Z.; Jang, S. W.; Cheng, C.-H.; Deotare, P. B. *Applied Physics Letters* **2018**, *113*, 252101.

(319) Su, H.; Xu, D.; Cheng, S.-W.; Li, B.; Liu, S.; Watanabe, K.; Taniguchi, T.; Berkelbach, T. C.; Hone, J. C.; Delor, M. *Nano Letters* **2022**, *22*, 2843–2850.

(320) Went, C. M.; Wong, J.; Jahelka, P. R.; Kelzenberg, M.; Biswas, S.; Hunt, M. S.; Carbone, A.; Atwater, H. A. *Science Advances* **2019**, *5*, eaax6061.

(321) Ni, Z. H.; Wang, H. M.; Kasim, J.; Fan, H. M.; Yu, T.; Wu, Y. H.; Feng, Y. P.; Shen, Z. X. *Nano Letters* **2007**, *7*, 2758–2763.

(322) Castellanos-Gomez, A.; Agraït, N.; Rubio-Bollinger, G. *Applied Physics Letters* **2010**, *96*, 213116.

(323) Byrnes, S. J. *arXiv* **2020**, DOI: 10.48550/arXiv.1603.02720.

(324) McCreary, K. M.; Hanbicki, A. T.; Sivaram, S. V.; Jonker, B. T. *APL Materials* **2018**, *6*, 111106.

(325) Liu, J.; Leng, J.; Wang, S.; Zhang, J.; Jin, S. *The Journal of Physical Chemistry Letters* **2019**, *10*, 97–101.

(326) Byrnes, S. tmm: Simulate light propagation in multilayer thin and/or thick films using the fresnel equations and transfer matrix method. Version 0.1.8, http://pypi.python.org/pypi/tmm.

(327) Song, B.; Gu, H.; Fang, M.; Chen, X.; Jiang, H.; Wang, R.; Zhai, T.; Ho, Y.-T.; Liu, S. *Advanced Optical Materials* **2019**, *7*, 1801250.

(328) Lee, S.-Y.; Jeong, T.-Y.; Jung, S.; Yee, K.-J. *physica status solidi (b)* **2019**, *256*, 1800417.

(329) Li, X.; Zhu, H. *Journal of Materiomics* **2015**, *1*, 33–44.

(330) Yu, Y.; Yu, Y.; Li, G.; Puretzky, A. A.; Geohegan, D. B.; Cao, L. *Science Advances* **2020**, *6*, eabb4823.

(331) Uddin, S. Z.; Kim, H.; Lorenzon, M.; Yeh, M.; Lien, D.-H.; Barnard, E. S.; Htoon, H.; Weber-Bargioni, A.; Javey, A. *ACS Nano* **2020**, *14*, 13433–13440.

(332) Volovik, L. S.; Fesenko, V. V.; Bolgar, A. S.; Drozdova, S. V.; Klochkov, L. A.; Primachenko, V. F. *Soviet Powder Metallurgy and Metal Ceramics* **1978**, *17*, 697–702.

(333) Yan, R.; Simpson, J. R.; Bertolazzi, S.; Brivio, J.; Watson, M.; Wu, X.; Kis, A.; Luo, T.; Hight Walker, A. R.; Xing, H. G. *ACS Nano* **2014**, *8*, 986–993.

(334) Liu, H.; Wang, C.; Zuo, Z.; Liu, D.; Luo, J. *Advanced Materials* **2020**, *32*, 1906540.

(335) Uddin, S. Z.; Rabani, E.; Javey, A. *Nano Letters* **2021**, *21*, 424–429.

(336) Hong, J. et al. *Nature Communications* **2015**, *6*, 6293.

(337) Vancsó, P.; Magda, G. Z.; Pető, J.; Noh, J.-Y.; Kim, Y.-S.; Hwang, C.; Biró, L. P.; Tapasztó, L. *Scientific Reports* **2016**, *6*, 29726.

(338) Pető, J.; Ollár, T.; Vancsó, P.; Popov, Z. I.; Magda, G. Z.; Dobrik, G.; Hwang, C.; Sorokin, P. B.; Tapasztó, L. *Nature Chemistry* **2018**, *10*, 1246–1251.

(339) Song, S. H.; Joo, M.-K.; Neumann, M.; Kim, H.; Lee, Y. H. *Nature Communications* **2017**, *8*, 2121.

(340) Tsai, C.; Li, H.; Park, S.; Park, J.; Han, H. S.; Nørskov, J. K.; Zheng, X.; Abild-Pedersen, F. *Nature Communications* **2017**, *8*, 15113.

(341) Hu, J. et al. *Nature Catalysis* **2021**, *4*, 242–250.

(342) Ge, Z.-H.; Zhao, L.-D.; Wu, D.; Liu, X.; Zhang, B.-P.; Li, J.-F.; He, J. *Materials Today* **2016**, *19*, 227–239.

(343) Ye, T.; Wang, X.; Li, X.; Qingyu Yan, A.; Ramakrishna, S.; Xu, J. *Journal of Materials Chemistry C* **2017**, *5*, 1255–1260.

(344) Yuan, L.; Huang, L. *Nanoscale* **2015**, *7*, 7402–7408.

(345) Adhikari, S.; Spaeth, P.; Kar, A.; Baaske, M. D.; Khatua, S.; Orrit, M. *ACS Nano* **2020**, *14*, 16414–16445.

(346) Terazima, M.; Hara, T.; Hirota, N. *The Journal of Physical Chemistry* **1993**, *97*, 13668–13672.

(347) Lukianova-Hleb, E. Y.; Lapotko, D. O. *Nano Letters* **2009**, *9*, 2160–2166.

(348) Tong, L.; Liu, Y.; Dolash, B. D.; Jung, Y.; Slipchenko, M. N.; Bergstrom, D. E.; Cheng, J.-X. *Nature Nanotechnology* **2012**, *7*, 56–61.

(349) Smolin, S. Y.; Choquette, A. K.; Wang, J.; May, S. J.; Baxter, J. B. *The Journal of Physical Chemistry C* **2018**, *122*, 115–123.

(350) Liu, B.; Menon, V. M.; Sfeir, M. Y. *APL Photonics* **2021**, *6*, 016103.

(351) Panzer, M. A.; Shandalov, M.; Rowlette, J. A.; Oshima, Y.; Chen, Y. W.; McIntyre, P. C.; Goodson, K. E. *IEEE Electron Device Letters* **2009**, *30*, 1269–1271.

(352) Zhu, J.; Tang, D.; Wang, W.; Liu, J.; Holub, K. W.; Yang, R. *Journal of Applied Physics* **2010**, *108*, 094315.

(353) Pennathur, A. K.; Tseng, C.; Dawlaty, J. M. *The Journal of Physical Chemistry C* **2022**, *126*, 4593–4600.

(354) Lu, C.-P.; Li, G.; Mao, J.; Wang, L.-M.; Andrei, E. Y. *Nano Letters* **2014**, *14*, 4628–4633.

(355) Wang, H.; Zhang, C.; Rana, F. *Nano Letters* **2015**, *15*, 339–345.

(356) Chow, C. M.; Yu, H.; Jones, A. M.; Schaibley, J. R.; Koehler, M.; Mandrus, D. G.; Merlin, R.; Yao, W.; Xu, X. *npj 2D Materials and Applications* **2017**, *1*, 1–6.

(357) Shree, S.; Semina, M.; Robert, C.; Han, B.; Amand, T.; Balocchi, A.; Manca, M.; Courtade, E.; Marie, X.; Taniguchi, T.; Watanabe, K.; Glazov, M. M.; Urbaszek, B. *Physical Review B* **2018**, *98*, 035302.

(358) Li, L.; Carter, E. A. *Journal of the American Chemical Society* **2019**, *141*, 10451–10461.

(359) Li, L.; Lin, M.-F.; Zhang, X.; Britz, A.; Krishnamoorthy, A.; Ma, R.; Kalia, R. K.; Nakano, A.; Vashishta, P.; Ajayan, P.; Hoffmann, M. C.; Fritz, D. M.; Bergmann, U.; Prezhdo, O. V. *Nano Letters* **2019**, *19*, 6078–6086.

(360) Rosser, D.; Fryett, T.; Ryou, A.; Saxena, A.; Majumdar, A. *npj 2D Materials and Applications* **2020**, *4*, 1–6.

(361) Dresselhaus, M. S.; Dresselhaus, G.; Sun, X.; Zhang, Z.; Cronin, S. B.; Koga, T. *Physics of the Solid State* **1999**, *41*, 679–682.

(362) Kim, S. E.; Mujid, F.; Rai, A.; Eriksson, F.; Suh, J.; Poddar, P.; Ray, A.; Park, C.; Fransson, E.; Zhong, Y.; Muller, D. A.; Erhart, P.; Cahill, D. G.; Park, J. *Nature* **2021**, *597*, 660–665.

(363) Ling, X.; Wang, H.; Huang, S.; Xia, F.; Dresselhaus, M. S. *Proceedings of the National Academy of Sciences* **2015**, *112*, 4523–4530.

(364) Long, G.; Maryenko, D.; Shen, J.; Xu, S.; Hou, J.; Wu, Z.; Wong, W. K.; Han, T.; Lin, J.; Cai, Y.; Lortz, R.; Wang, N. *Nano Letters* **2016**, *16*, Publisher: American Chemical Society, 7768–7773.

(365) Xia, F.; Wang, H.; Hwang, J. C. M.; Neto, A. H. C.; Yang, L. *Nature Reviews Physics* **2019**, *1*, 306–317.

(366) Liao, B.; Zhao, H.; Najafi, E.; Yan, X.; Tian, H.; Tice, J.; Minnich, A. J.; Wang, H.; Zewail, A. H. *Nano Letters* **2017**, *17*, 3675–3680.

(367) He, J.; He, D.; Wang, Y.; Cui, Q.; Bellus, M. Z.; Chiu, H.-Y.; Zhao, H. *ACS Nano* **2015**, *9*, 6436–6442.

(368) Fei, R.; Faghaninia, A.; Soklaski, R.; Yan, J.-A.; Lo, C.; Yang, L. *Nano Letters* **2014**, *14*, 6393–6399.

(369) Cao, T.; Li, Z.; Qiu, D. Y.; Louie, S. G. *Nano Letters* **2016**, *16*, 5542–5546.

(370) Barker, A. J.; Sadhanala, A.; Deschler, F.; Gandini, M.; Senanayak, S. P.; Pearce, P. M.; Mosconi, E.; Pearson, A. J.; Wu, Y.; Srimath Kandada, A. R.; Leijtens, T.; De Angelis, F.; Dutton, S. E.; Petrozza, A.; Friend, R. H. *ACS Energy Letters* **2017**, *2*, 1416–1424.

(371) Lee, C.; Yan, H.; Brus, L. E.; Heinz, T. F.; Hone, J.; Ryu, S. *ACS Nano* **2010**, *4*, 2695–2700.

(372) Liang, L.; Meunier, V. *Nanoscale* **2014**, *6*, 5394–5401.

(373) Niu, Y.; Gonzalez-Abad, S.; Frisenda, R.; Marauhn, P.; Drüppel, M.; Gant, P.; Schmidt, R.; Taghavi, N. S.; Barcons, D.; Molina-Mendoza, A. J.; De Vasconcellos, S. M.; Bratschitsch, R.; Perez De Lara, D.; Rohlfing, M.; Castellanos-Gomez, A. *Nanomaterials* **2018**, *8*, 725.

(374) Cushing, S. K.; Zürch, M.; Kraus, P. M.; Carneiro, L. M.; Lee, A.; Chang, H.-T.; Kaplan, C. J.; Leone, S. R. *Structural Dynamics* **2018**, *5*, 054302.

(375) Harb, M.; Ernstorfer, R.; Dartigalongue, T.; Hebeisen, C. T.; Jordan, R. E.; Miller, R. J. D. *The Journal of Physical Chemistry B* **2006**, *110*, 25308–25313.

(376) Wunderlich, B. In *Encyclopedia of Materials: Science and Technology*, Buschow, K. H. J., Cahn, R. W., Flemings, M. C., Ilschner, B., Kramer, E. J., Mahajan, S., Veyssière, P., Eds., "Thermal Analysis"; Elsevier: Oxford, 2001, pp 9134–9141.

(377) Tro, N. J. In *Chemistry: A Molecular Approach*, 2nd ed., "Measuring Delta E for Chemical Reactions: Constant-Volume Calorimetry"; Prentice Hall: 2010, pp 246–248.

(378) Boas, M. L., *Mathematical Methods in the Physical Sciences*, 3rd ed.; John Wiley and Sons Ltd.: 2006; 444-448.

(379) Abramowitz, M.; Stegun, I., *Handbook of Mathematical Functions*; National Bureau of Standards: Washington, DC, 1972.

Appendix A

Sample preparation

A.1 General sample requirements for stroboSCAT measurements

A.1.1 Sample substrates

All substrates are 22×22 mm or 24×50 mm VWR #1.5 glass coverslips (thickness 0.16-0.19 mm), but can be smaller. Every substrate is subjected to an extensive cleaning procedure as follows: 15 min sonication in a 2% Hellmanex solution in NANOpure deionized water, followed by several quick rinses in NANOpure deionized water; 15 min sonication in NANOpure deionized water; 10 min sonication in acetone; 10 min sonication in isopropyl alcohol; immediately dried under a flow of filtered nitrogen; and finally cleaned with an O_2 plasma for 3 minutes in a reactive ion etch chamber. For substrates that are too small to span the sample stage, they may be mounted onto a larger 25×50 mm coverslip with epoxy or extended with nail polish-adhered coverslip "wings" (**Figure 2.24**).

A.2 Sample preparation for materials in Chapter 3

A.2.1 Metal-halide perovskite single crystals

Methylammonium lead bromide ($MAPbBr_3$) single crystals were prepared according to a published procedure using antisolvent vapor diffusion [234]. Briefly, a 1:1 molar ratio, 0.2 M solution of $PbBr_2$/MABr was prepared in N,N-dimethylformamide (DMF). The solution was then filtered using a 0.2 µm PTFE syringe filter. 2 mL were placed in a clean 4 mL vial, which was placed inside a larger scintillation vial filled with dichloromethane. The large vial was sealed and crystals were left to grow for 1 week, resulting in hyperrectangular crystals of dimensions ∼3×3×1 mm. $CsPbBr_3$ single crystals were grown using antisolvent vapor diffusion according to a published procedure [239]. The same procedure as that described for $MAPbBr_3$ was used, with a 1:1 molar ratio, 0.04 M solution of $PbBr_2$/CsBr in DMF

and using nitromethane as antisolvent. The crystals were left to grow for 3 weeks, resulting in large hyperrectangular crystals of dimensions $\sim 20\times2\times2$ mm, which were cleaved before mounting on substrates for measurements.

A.2.2 Metal-halide perovskite thin films

$MAPbBr_3$ polycrystalline films were prepared by dissolving MABr and $Pb(Ac)_2$ in a 3:1 molar ratio in DMF with a final concentration of 0.5 M. The solution was spin-cast at 2000 rpm for 60 seconds. The films were subsequently annealed for 5 minutes at 100°C [114].

$MAPbI_3$ polycrystalline films were prepared by using different published processing routes described briefly below:

- $Pb(Ac)_2$ precursor films [370] were prepared by dissolving MAI and $Pb(Ac)_2$ in a 3:1 molar ratio in DMF for a final concentration of 0.5 M. The solution was spin-cast at 2000 rpm for 60 seconds. The films were subsequently annealed for 5 minutes at 100°C.
- PbI_2 precursor films [114] were prepared by dissolving MAI and PbI_2 at a 1:1 molar ratio at 200 mg/mL in DMF. The solution was spin-cast at 2000 rpm for 30 seconds. The films were subsequently annealed for 20 minutes at 100°C.
- $PbCl_2$ precursor films [247] were prepared by dissolving MAI and PbCl2 at a 3:1 molar ratio with final concentrations of 2.64 M and 0.88 M, respectively. The solution was spin-cast at 2000 rpm for 60 seconds. The films were subsequently left to dry for 30 minutes at room temperature in the glovebox, followed by annealing at 90°C for 150 minutes.

A.2.3 TIPS-pentacene

TIPS-pentacene was dissolved in toluene at 5mg/mL and filtered through a 0.45 µm polytetrafluoroethylene (PTFE) filter. The substrates were treated by leaving to soak overnight in a petri dish with a solution of 190 µL TPS in 100 mL toluene, then rinsed with toluene and dried prior to deposition. The TIPS-pentacene solution was then spin-cast at 250 rpm, and then solvent-vapor annealed at 60°C in a toluene-saturated atmosphere for 24 hours.

A.2.4 Silicon

Silicon wafers were prime-grade p-type, boron-doped wafers purchased from WaferNet Inc., used without further modification. The wafer may be cut with a diamond scribe to fit in the sample stage directly. The immersion oil droplet placed on the objective or silicon wafer must be large enough to span the working distance of the objective (0.14 mm) where the glass substrate would otherwise be. An alternative option is to cut a smaller piece of silicon wafer and image it through a clean glass substrate with a little bit of immersion oil between the imaged wafer surface and glass substrate for index matching. For this sample configuration,

it is also much easier to find the sample focus if the oil droplet on the bottom of the substrate extends beyond the opaque silicon wafer fragment so that its spread becomes obvious when it comes into contact with the objective as the sample stage is lowered (**Figure A.1**). It is also possible, however, to roughly center a larger wafer fragment over the objective and lower the sample into focus while imaging on the camera, which is the method currently being used in the lab.

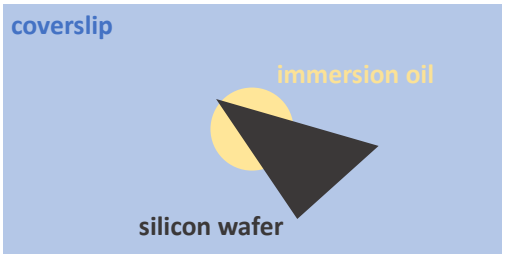

Figure A.1: Silicon-oil-coverslip sample configuration with immersion oil extending beyond the narrow wafer fragment.

A.2.5 Reagents

All reagents were used as received without further purification. Methylammonium bromide (MABr, GreatCell Solar); methylammonium iodide (MAI, GreatCell Solar); Cesium bromide (CsBr, Alfa Aesar); lead bromide ($PbBr_2$, Alfa Aesar); lead iodide (PbI_2, Alfa Aesar); lead chloride ($PbCl_2$, Alfa Aesar); lead acetate trihydrate ($Pb(Ac)_2$, Sigma-Aldrich); 6,13-Bis(triisopropylsilylethynyl)pentacene (TIPS- Pentacene, Sigma-Aldrich); Trichloro(phenethyl)silane (TPS, Sigma-Aldrich); poly(methyl methacrylate) (PMMA, Mw = 120,000, Sigma-Aldrich). All solvents are purchased from Sigma-Aldrich.

A.2.6 Sample handling

All samples apart from Silicon and halide perovskite single crystals are prepared in a sealed glovebox with nitrogen atmosphere and with <2ppm O_2 and H_2O. Once prepared, the samples are sealed between two substrates using epoxy (EPO-TEK OG159-2) in the glovebox to protect them from water and oxygen exposure during measurements. For atomic force microscopy measurements on thin films, another sample is prepared consecutively under the same conditions and using the same solution, but is not sealed between the two substrates and is measured immediately after preparation. Single crystals are all grown at ambient conditions. Once the crystals are grown, they are brought into the glovebox, placed on clean substrates, and 200 µL of a 30 mg/mL solution of PMMA in chloroform (mixed at 50° for 15-30 min or until fully dissolved) is dropcast on the crystals to keep them in place and prevent exposure to oxygen and moisture during measurements.

A.3 Sample preparation for materials in Chapter 4

We use the hot pick-up technique to fabricate hBN-encapsulated few-layer MoS_2 heterostructures on coverglass [314]. Briefly, hBN and MoS_2 are exfoliated onto 285 nm of thermally oxidized SiO_2 on Si. We make stamps consisting of PDMS covered with a thin film of the thermoplastic polymer polycarbonate (PC). Using these stamps, we first pick up the top hBN, then the desired MoS_2 flake, and then the bottom hBN, all at 50°C. We deposit the stack onto #1.5 coverglass, which serves as the substrate for all stroboSCAT measurements, at 180°C, and then dissolve the PC in chloroform.

We characterize the hBN-encapsulated MoS_2 sample using optical microscopy, Raman spectroscopy, and atomic force microscopy (AFM). The 4L MoS_2 flake measured in **Section 4.3** is outlined in blue in **Figure A.2a,b**. The AFM image in **Figure A.2b** shows that our sample has large ($> 7\times7$ µm), homogeneous, bubble-free areas, which are ideal for measuring in stroboSCAT. The separation between the two MoS_2 Raman peaks demonstrates that these samples are 4 layers thick **Figure A.2c,d** [371–373]. The hBN layer between the MoS_2 flake and glass substrate is thin enough ($\sim$5 nm) to allow easy optical access to the MoS_2 layer within the 1.4 NA objective's depth of field.

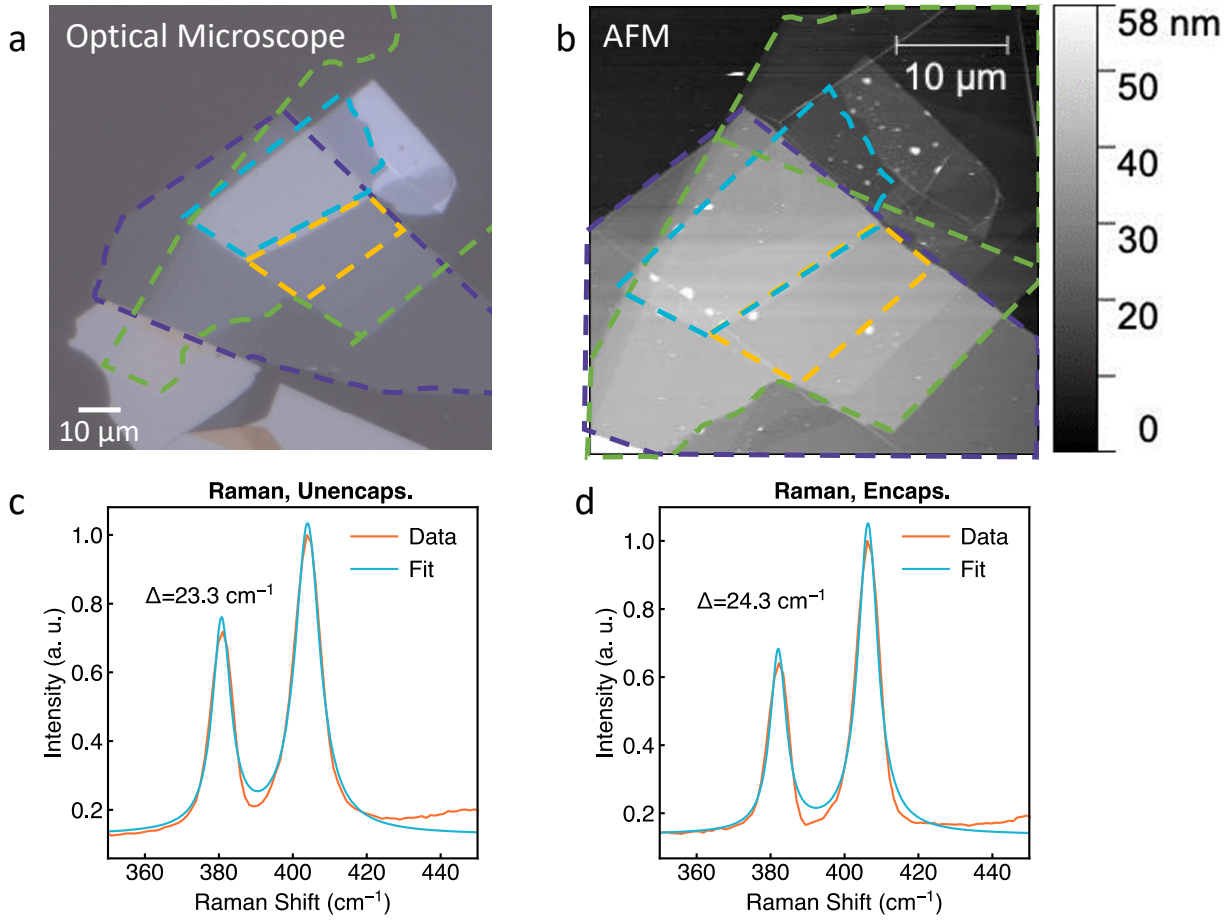

Figure A.2: **(a)** Optical microscope image of hBN-encapsulated MoS_2 where blue outline is 4L MoS_2, yellow outline is 1L MoS_2, green outline is substrate-adjacent hBN and purple outline is air-adjacent hBN. **(b)** Atomic force microscopy scan of sample used to identify hBN thicknesses. **(c, d)** Raman spectroscopy of out-of-plane A_{1g} mode in pre-encapsulated (c) and post-encapsulated (d) region, demonstrating a shift that corresponds to an MoS_2 thickness of 4 layers.

Appendix B

Useful calculations

B.1 Carrier density

Calculating the expected carrier density (cm^{-3} or cm^{-2}) for a stroboSCAT measurement requires one measurement in the lab (described below), knowledge of experimental parameters (laser wavelength, repetition rate, pulse width, beam diameter) and the sample's complex refractive index.

The first step is to calculate the energy density incident on the sample. In the lab, we measure the incident beam power with a ThorLabs microscope slide power sensor (S175C) by spanning the sensor over the sample stage, centered above the objective. (In a future sample stage iteration that accommodates standard $1'' \times 3''$ slides, the power sensor could be slotted into the stage directly.) Note that most semiconductors have indices of refraction higher than that of air ($n_{\text{air}} = 1$) or glass ($n_{\text{glass}} = 1.5$), so the measured light transmission through a bare coverslip or the exposed objective is slightly higher than what would reach the sample experimentally, although this is usually a small effect that may be ignored. For example, ∼4% of the incident light will be reflected at a glass-air interface compared to ∼20% at a MoS_2-glass interface due to a higher impedance mismatch ($n_{MoS_2} \sim 4$). From this direct measurement of power, the incoming beam fluence (energy per unit area per pulse) may be calculated:

$$\text{fluence } [\text{J/cm}^2] = \frac{\text{laser power } [\text{J/s}]}{\text{repetition rate } [\text{s}^{-1}] \times \text{beam area } [\text{cm}^2]}. \tag{B.1}$$

An aside on Gaussian beam width conventions

Gaussian beams have a transverse (to the direction of propagation) intensity, $I(r)$, that is typically described by the following equation

$$I(r) = \frac{2P}{\pi w^2} e^{-2r^2/w^2}, \tag{B.2}$$

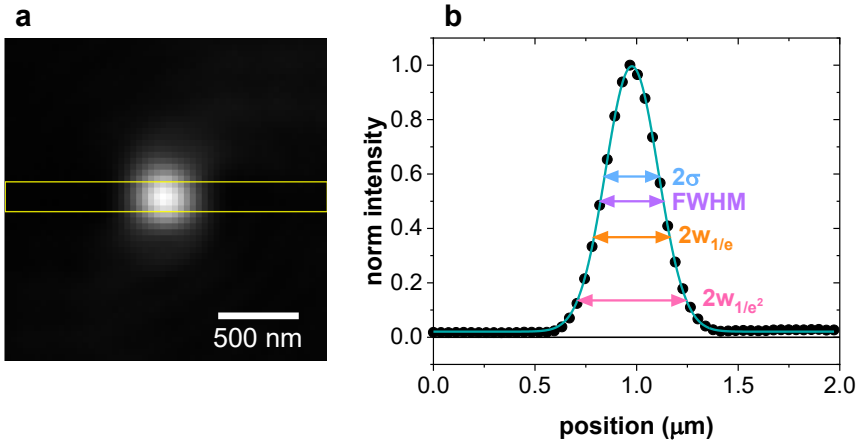

Figure B.1: **(a)** Pump beam profile reflected from a glass coverslip. **(b)** Gaussian fit to the region boxed in yellow (a) with associated Gaussian beam width conventions for comparison.

where P is the total beam power and w is the radius of the beam when its intensity drops to $1/e^2$ ($\sim$13.5%) of its maximum value. A common definition for the beam area then is simply $A = \pi w^2$ in which about 86% of the laser power is contained.

Other conventions for beam widths include the $1/e$ width, where the electric field strength drops to $\sim$37% of its maximum value, and the full width at half maximum (FWHM), where the intensity drops to 50% of its maximum value. The $1/e$ width is used to define the maximum possible exposure to a laser beam in the ANSI laser safety standard. In practice, after imaging the reflected beam profile, you may fit a standard Gaussian distribution, $G(r) \propto \exp -r^2/2\sigma^2$, with characteristic width, σ (**Figure B.1**). The following equations may be used to convert the standard deviation to any of these other width conventions:

$$w_{1/e^2} = 2\sigma \tag{B.3}$$

$$w_{1/e} = (2/\sqrt{2})\sigma \approx 1.414\sigma \tag{B.4}$$

$$\text{FWHM} = 2\sqrt{2\ln 2}\sigma \approx 2.355\sigma \tag{B.5}$$

From the beam fluence (Equation B.1), the photon density may be calculated

$$\text{photon density } [\text{cm}^{-2}] = \frac{\text{fluence } [\text{J/cm}^2]}{\text{energy per photon } [\text{J}]}, \tag{B.6}$$

where Planck's constant is used to convert the incident light frequency or wavelength to energy ($E = \text{h}\nu = \text{hc}/\lambda$).

Finally, the carrier density may be calculated in a few different ways.

Case #1, Very thin samples: If the absorbing material is so thin that incident light is reflected at its boundaries and may bounce back through the material multiple times, effectively enhancing the absorption, a transfer-matrix calculation may be used to estimate the fraction of incident photons that are actually absorbed, f:

$$\text{carrier density } [\text{cm}^{-2}] = \text{photon density } [\text{cm}^{-2}] \times f. \tag{B.7}$$

Case #2, Thicker samples: More commonly, the imaginary part of the refractive index, k, or the sample absorption coefficient, $a = 4\pi k/\lambda$, are known and may be used to calculate the volumetric carrier density:

$$\text{carrier density } [\text{cm}^{-3}] = \text{photon density } [\text{cm}^{-2}] \times a[\text{cm}^{-1}]. \tag{B.8}$$

The area carrier density may be calculated using the sample thickness, z, or the microscope depth of field (300 nm), whichever is smaller:

$$\text{carrier density } [\text{cm}^{-2}] = \text{carrier density } [\text{cm}^{-3}] \times z[\text{cm}]. \tag{B.9}$$

Finally, the carrier density should be multiplied by $1 - R = T$, the fraction of light that is transmitted to the material after partial reflection at the substrate-sample interface. All together, from the measured incident laser power to the area carrier density, the calculation is

$$\text{carrier density } [\text{cm}^{-2}] = \frac{T \times \text{laser power } [\text{J/s}] \times a\ [\text{cm}^{-1}] \times z\ [\text{cm}]}{\text{repetition rate } [\text{s}^{-1}] \times \text{beam area } [\text{cm}^2] \times \text{energy per photon } [\text{J}]} \tag{B.10}$$

or, when a transfer-matrix calculation (**Section B.4**) is used to estimate the fraction of incident photons absorbed, az may be replaced with that fraction. Equation B.10 may be more compactly expressed as

$$\Delta N = \frac{TFaz}{h\nu}, \tag{B.11}$$

where N is the carrier density [cm^{-2}], F is the laser fluence, and ν is the optical frequency of the pump pulse. Note that az is a first-order approximation using a Taylor series expansion of the Beer-Lambert law: $I(z)/I_0 = e^{-OD} = e^{-az} \approx 1 - az + (az)^2/2$ where $I(z)$ is the light intensity at depth z, I_0 is the incident light intensity, and OD is the optical density. So $1 - I(z)/I_0 = 1 - e^{-az} \approx az$ is the light intensity that is absorbed after propagating through depth z, valid when az is small.

In the case where the sample is thinner than the penetration depth ($1/a$) and the objective depth of field (300 nm), Equation B.10 may be modified [374, 375]:

$$\Delta N = (1 - R_1)\ \frac{F}{h\nu}\ az(1 + R_2 e^{-az}), \tag{B.12}$$

where R_1 is the reflectance from the glass-sample interface and R_2 is the reflectance from the sample-air interface. The second term accounts for additional absorption from back-reflections at the top sample surface. The transfer-matrix method should account for this effect as well, but it can be convenient to have a simple equation on hand too.

There are several other useful quantities one may wish to calculate from the incident beam power and other experimental parameters:

$$\text{peak power [W]} = \frac{\text{laser power [J/s]}}{\text{repetition rate [s}^{-1}\text{]} \times \text{pulse width [s]}} \tag{B.13}$$

$$\text{power density [W/cm]}^2 = \frac{\text{fluence [J/cm}^2\text{]}}{\text{pulse width [s]}} \tag{B.14}$$

$$\text{carriers per pulse} = \text{carrier density [cm}^{-2}\text{]} \times \text{beam area [cm}^2\text{]} \tag{B.15}$$

$$\text{average carrier separation [cm]} = \frac{1}{\sqrt[3]{\text{carrier density [cm}^{-3}\text{]}}} = \frac{1}{\sqrt{\text{carrier density [cm}^{-2}\text{]}}} \tag{B.16}$$

Note that to calculate a **peak** fluence at the center of the carrier distribution, the fluence calculated with the the chosen beam width convention, $(1/e^2, 1/e, \text{FWHM})$, must be multiplied by the corresponding factor, $(e^2, e, 2$, respectively). For example, if the calculated $1/e^2$ fluence was 35 µJ/cm^2, the peak fluence would be $35 \times e^2 = 260$ µJ/cm^2. The peak fluence can be used to calculate the peak carrier density, peak power density, minimum carrier separation, etc., and is often important to calculate when nonlinear effects like Auger-Meitner recombination are possible and would acquire a spatial dependence due to the spatially-dependent carrier distribution.

B.2 Calorimetry

Calorimetry is the act of measuring changes in the state variables of a body for the purpose of deriving the heat transfer associated with changes of its state due, for example, to chemical reactions, physical changes, or phase transitions under specified constraints [376]. Calorimetry used in the context of this dissertation typically refers to quantifying the amount of heat released or absorbed during a reaction by measuring temperature changes in a thermally isolated chamber [377]. For example, this is how the caloric content of food is determined. Maybe you burned potato chips or marshmallows in your high school chemistry class. In the context of light-matter interactions, and light absorption in particular, we use "calorimetry" to refer to the calculated temperature increase from the conversion of light energy into heat

or a temperature increase in a light-absorbing material. Knowing the material's absorption properties, such as a or k, specific heat capacity, c, and mass density, ρ, the calculation is performed as follows:

B.2.1 Method #1: Using the definition of heat capacity

The heat capacity, C, represents how much energy, ΔQ, must be supplied to a material to raise its temperature by ΔT:

$$C = \frac{\Delta Q}{\Delta T}. \tag{B.17}$$

Note that Q can be heat that is dissipated from any original form of energy - thermal, electrical, chemical, solar. The more familiar form of this equation in calorimetry uses the specific heat capacity, ($c = C/m$), an intensive property

$$Q = mc\Delta T, \tag{B.18}$$

where m is the mass of the material. In practice, the material thickness, z, and density, ρ, are known. To put an upper bound on the temperature increase in a material due to light absorption, $\Delta T_{\max}$, we assume if there is no emission that all absorbed photons are converted to heat, i.e., nonradiative relaxation pathways completely dominate and no absorbed photons escape via light emission. In addition, we use the peak fluence or peak carrier density to calculate the peak temperature attained:

$$\Delta T_{\max} = \frac{Q}{mc} = \frac{\text{peak fluence} \cdot \text{fraction of photons absorbed}}{\rho z c}. \tag{B.19}$$

Note that Equation B.19 does not factor in the spatial profile of the laser pulse, however, by calculating the maximum temperature change in the center of the excitation profile and using the known Gaussian pulse profile in space, the corresponding temperature increase spatial map, $\Delta T(x, y)$, may be constructed. For 4-layer MoS_2 and the measurements described in **Chapter 4**, the maximum predicted temperature increase at the center of the 440 nm excitation spot is:

$$\Delta T_{\max} = \frac{260\ \mu\text{J/cm}^2 \cdot 0.06}{5\ \text{g/cm}^3 \cdot 0.65 \times 10^{-7}\ \text{cm/layer} \cdot 4\ \text{layers} \cdot 0.4\ \text{J/g K}} = 30\ \text{K}. \tag{B.20}$$

B.2.2 Method #2: Unit analysis, with c in friendly units

Alternatively, using unit conversion, the heat capacity [332] may be expressed in units, [eV/(cm^{2}K)], that are more conducive to experimental parameters. (Special thanks to **Dipti Jasrasaria** for introducing me to this useful Rabani group calculation!) For example, in the same 4-layer MoS_2 case described above:

$$c = 15.22\,\frac{\text{cal}}{\text{mol K}} \cdot \frac{2.611\ \times 10^{19}\,\text{eV}}{\text{cal}} \cdot \frac{\text{mol}}{160.07\,\text{g}} \cdot \frac{5.06\,\text{g}}{\text{cm}^3} \cdot \frac{0.65 \times 10^{-7}\,\text{cm}}{\text{layer}} \cdot 4\,\text{layers} \\ = 3.27 \times 10^{12}\,\text{eV cm}^{-2}\,\text{K}^{-1}. \tag{B.21}$$

Used in conjunction with the peak carrier density, N_{peak}, and incident pump energy, E_{pump}, this formulation yields a straightforward calculation for ΔT_{max}:

$$\Delta T_{\text{max}} = N_{\text{peak}} E_{\text{pump}}/c = \frac{3.5 \times 10^{13}}{\text{cm}^2} \cdot 2.8\ \text{eV} \cdot \frac{\text{cm}^2\ \text{K}}{3.27 \times 10^{12}\ \text{eV}} = 30\ \text{K}. \tag{B.22}$$

This formula is also useful for calculating the expected temperature increase due to relaxation to the band edge or thermalization, ΔT_{therm}. For example, in 4-layer MoS_2, about 40% of the absorbed energy is converted to heat through relaxation to the direct band edge, ($E_{\text{D}} = 1.8$ eV), and an additional 10% by relaxation to the lowest-energy indirect band edge, ($E_{\text{ID}} = 1.4$ eV):

$$\Delta T_{\text{therm,D}} = N_{\text{peak}}(E_{\text{pump}} - E_{\text{direct}})/c = 0.36\Delta T_{\text{max}} = 11\ \text{K},\ \text{and} \tag{B.23}$$

$$\Delta T_{\text{therm,ID}} = N_{\text{peak}}(E_{\text{pump}} - E_{\text{indirect}})/c = 0.5\Delta T_{\text{max}} = 15\ \text{K}. \tag{B.24}$$

B.3 Products and convolutions of Gaussians

The convolution of two Gaussians is also Gaussian, a property known as "self-similarity," and the variance of the result of such a convolution is the sum of the variances of the constituting Gaussians. Here, we perform the derivations, in all gory detail, that lead to these conclusions in order to explain further and to understand their limitations and extensions.

Consider two two-dimensional Gaussian probability distribution functions (PDFs)

$$g_1(x,y) = \frac{1}{2\pi\sigma_1^2}\, e^{-\frac{(x^2+y^2)}{2\sigma_1^2}}\ \text{and}\ g_2(x,y) = \frac{1}{2\pi\sigma_2^2}\, e^{-\frac{(x^2+y^2)}{2\sigma_2^2}}, \tag{B.25}$$

where

$$\int_{-\infty}^{\infty}\int_{-\infty}^{\infty} g_1(x,y)\,\mathrm{d}x\,\mathrm{d}y = \int_{-\infty}^{\infty}\int_{-\infty}^{\infty} g_2(x,y)\,dx\,dy = 1. \tag{B.26}$$

The convolution of these two functions is defined as

$$g_1 \otimes g_2 = \int_{-\infty}^{\infty}\int_{-\infty}^{\infty} g_1(x-u, y-v) g_2(x,y)\,\mathrm{d}u\,\mathrm{d}v. \tag{B.27}$$

Since it is not always easy to evaluate convolution integrals in real space, we invoke the convolution theorem [378] and perform the calculation in reciprocal space:

$$g_1(x,y) \otimes g_2(x,y) = F^{-1}[F(g_1(x,y))F(g_2(x,y))], \tag{B.28}$$

where F is the Fourier transform

$$F(g(x,y)) = \int_{-\infty}^{\infty}\int_{-\infty}^{\infty} g(x,y)\, e^{-2\pi i(mx+ny)}\,\mathrm{d}x\,\mathrm{d}y, \tag{B.29}$$

and F^{-1} is the inverse Fourier transform:

$$F^{-1}(F(m,n)) = \int_{-\infty}^{\infty}\int_{-\infty}^{\infty} F(m,n)\, e^{2\pi i(mx+ny)}\,\mathrm{d}x\,\mathrm{d}y. \tag{B.30}$$

The Fourier transform of $g_1(x,y)$ is given by

$$F(g_1) = \frac{1}{2\pi\sigma_1^2}\int_{-\infty}^{\infty} e^{-\frac{x^2}{2\sigma_1^2}}\, e^{-2\pi imx}\,\mathrm{d}x \int_{-\infty}^{\infty} e^{-\frac{y^2}{2\sigma_1^2}}\, e^{-2\pi iny}\,\mathrm{d}y. \tag{B.31}$$

Using Euler's formula $e^{i\theta} = \cos\theta - i\sin\theta$, we can re-write Equation B.31 as:

$$F(g_1) = \frac{1}{2\pi\sigma_1^2}\int_{-\infty}^{\infty} e^{-\frac{x^2}{2\sigma_1^2}}[\cos 2\pi mx - i\sin 2\pi mx]\,\mathrm{d}x \int_{-\infty}^{\infty} e^{-\frac{y^2}{2\sigma_1^2}}[\cos 2\pi ny - i\sin 2\pi ny]\,\mathrm{d}y. \tag{B.32}$$

The terms in $\sin x$ and $\sin y$ are odd, and therefore their integral over all space is zero, leaving:

$$F(g_1) = \frac{1}{2\pi\sigma_1^2}\int_{-\infty}^{\infty} e^{-\frac{x^2}{2\sigma_1^2}}\cos 2\pi mx\,\mathrm{d}x \int_{-\infty}^{\infty} e^{-\frac{y^2}{2\sigma_1^2}}\cos 2\pi ny\,\mathrm{d}y. \tag{B.33}$$

We pull out our handy dandy integral table [379] and find the result of the standard integral:

$$\int_{-\infty}^{\infty} e^{-ax^2}\cos 2kx\,\mathrm{d}x = \sqrt{\frac{\pi}{a}}e^{-\frac{k^2}{a}}. \tag{B.34}$$

With $a = 1/2\sigma_1^2$ and $k = \pi m$ or $k = \pi n$, the integrals in Equation B.33 may be evaluated:

$$F(g_1) = e^{-2\pi\sigma_1^2(m^2+n^2)}. \tag{B.35}$$

This is yet another Gaussian PDF in (m,n), i.e., the Fourier transform of a Gaussian PDF is another Gaussian PDF, another self-similarity! The Fourier transform of $g_2(x,y)$ will yield a similar expression, and so putting it all together:

$$F(g_1)F(g_2) = e^{-2\pi\sigma_1^2(m^2+n^2)}\, e^{-2\pi\sigma_2^2(m^2+n^2)} = e^{-2\pi(\sigma_1^2+\sigma_2^2)(m^2+n^2)}. \tag{B.36}$$

This result, comparing with Equation B.35, is the Fourier transform of a Gaussian PDF with width

$$\sigma_{g_1 \otimes g_2} = \sqrt{\sigma_1^2 + \sigma_2^2}. \tag{B.37}$$

And since the Fourier transform is invertible,

$$F^{-1}[F(g_1)F(g_2)] = \frac{1}{2\pi(\sigma_1^2 + \sigma_2^2)}\, e^{-\frac{x^2+y^2}{2(\sigma_1^2+\sigma_2^2)}}. \tag{B.38}$$

Note that the area under a convolution is equal to the product of the areas under the functions:

$$\begin{aligned} \int_{-\infty}^{\infty} (g_1 \otimes g_2)\, \mathrm{d}x &= \int_{-\infty}^{\infty} \left[\int_{-\infty}^{\infty} g_1(u) g_2(x-u)\, \mathrm{d}u \right] \mathrm{d}x \\ &= \int_{-\infty}^{\infty} g_1(u) \left[\int_{-\infty}^{\infty} g_2(x-u)\, \mathrm{d}x \right] \mathrm{d}u \\ &= \left[\int_{-\infty}^{\infty} g_1(u)\, \mathrm{d}u \right] \left[\int_{-\infty}^{\infty} g_2(x)\, \mathrm{d}x \right]. \end{aligned} \tag{B.39}$$

Therefore, convolving an arbitrary function with a point spread function represented by a Gaussian PDF preserves the area under the arbitrary function.

In the case where one of the Gaussian functions in the convolution is not normalized and has an arbitrary amplitude, N,

$$g_N(x,y) = N e^{-\frac{x^2+y^2}{2\sigma_N^2}}, \tag{B.40}$$

the convolution of $g_N(x,y)$ with normalized PDF $g_1(x,y)$ is given by:

$$g_N(x,y) \otimes g_1(x,y) = \frac{N\sigma_N^2}{\sigma_N^2 + \sigma_1^2}\, e^{-\frac{x^2+y^2}{2(\sigma_N^2+\sigma_1^2)}}. \tag{B.41}$$

The area of a 2D Gaussian with amplitude N and width σ_N is given by $2\pi N\sigma_N^2$. Using the standard Gaussian integral

$$\int_{-\infty}^{\infty} e^{-ax^2}\, \mathrm{d}x = \sqrt{\frac{\pi}{a}}, \tag{B.42}$$

we find that the area under $g_N(x,y)$ is preserved in the convolution with a PDF:

$$\begin{aligned}\int_{-\infty}^{\infty}\int_{-\infty}^{\infty} g_N(x,y)\otimes g_1(x,y) &= \frac{N\sigma_N^2}{\sigma_N^2+\sigma_1^2}\int_{-\infty}^{\infty} e^{-\frac{x^2}{2(\sigma_N^2+\sigma_1^2)}}\,\mathrm{d}x\int_{-\infty}^{\infty} e^{-\frac{y^2}{2(\sigma_N^2+\sigma_1^2)}}\,\mathrm{d}y \\ &= \frac{N\sigma_N^2}{\sigma_N^2+\sigma_1^2}\sqrt{2\pi(\sigma_N^2+\sigma_1^2)}^2 \\ &= 2\pi N\sigma_N^2 \\ &= \int_{-\infty}^{\infty}\int_{-\infty}^{\infty} g_N(x,y).\end{aligned} \tag{B.43}$$

Key takeaways

- The convolution of two Gaussian functions with widths σ_1 and σ_2 is also a Gaussian function with width $\sigma_{1\otimes 2} = \sqrt{\sigma_1^2+\sigma_2^2}$
- The area under a convolution of two Gaussians is equal to the product of the areas under the Gaussians: $A_{1\otimes 2} = A_1 A_2$
- Convolution with a PDF (normalized Gaussian) preserves the area under the original function.

B.4 Transfer-matrix method

Consider a plane wave incident on an interface between two materials, like a glass coverslip and a thin semiconducting film. The relevant electric field values are the incident amplitude, E_i, the reflected amplitude, E_r, and the transmitted amplitude, E_t. The ratio of the reflected and incident amplitude is called the *reflection coefficient*, r. The ratio of the transmitted and incident amplitude is called the *transmission coefficient*, t. In the geometrical optics approximation for light propagation, the Fresnel equations relate r and t to the index of refraction of the two materials that form the interface and the angle of the incident light relative to the surface normal. The equations are derived by applying the boundary conditions for the electric and magnetic field [172]. For s-polarized light (electric field polarized parallel to the plane of the interface), r and t are given by:

$$r_s = \frac{E_r}{E_i} = \frac{n_i\cos\theta_i - n_t\cos\theta_t}{n_i\cos\theta_i + n_t\cos\theta_t} \text{ and} \tag{B.44}$$

$$t_s = \frac{E_t}{E_i} = \frac{2n_i\cos\theta_i}{n_i\cos\theta_i + n_t\cos\theta_t}, \tag{B.45}$$

where n_i, n_t are the refractive index in the incident medium and transmitting medium, respectively, and θ_i, θ_t are the angles measured from the surface normal to the incident and transmitting plane waves, respectively. The reflectance, R, and transmittance, T, quantify

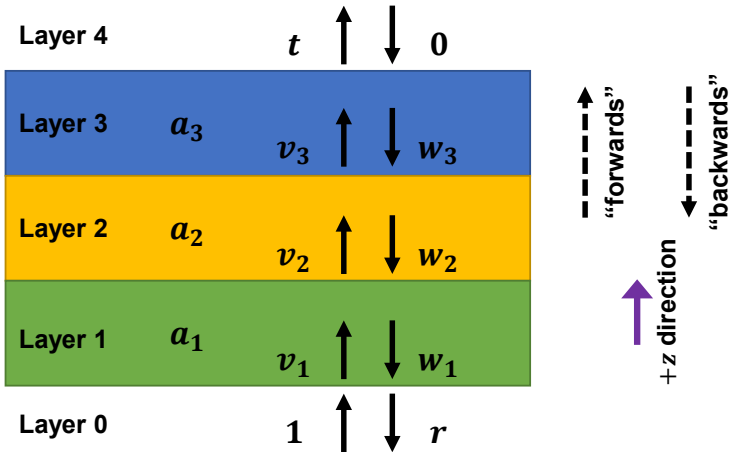

Figure B.2: The transfer-matrix method on an $N = 5$ stack of 3 finite layers between two semi-infinite non-absorbing layers yields the forward (v_n) and backward (w_n) electric field amplitudes and absorbed light fraction (a_n) in each layer along with the overall reflection (r) and transmission (t) coefficients.

the fraction of incident power that is reflected by or transmitted across the interface and are given by the square of the reflection and transmission amplitude coefficients, respectively. For normally incident s-polarized light:

$$R_s \equiv |r_s|^2 = \left|\frac{n_i - n_t}{n_i + n_t}\right|^2 \text{ and} \tag{B.46}$$

$$T_s \equiv |t_s|^2 = \left|\frac{2n_i}{n_i + n_t}\right|^2 = 1 - R_s. \tag{B.47}$$

Note that this does not (yet) account for attenuation of the electric field due to light absorption. It only describes the reflected or transmitted field amplitudes or power right on either side of the interface.

If there happened to be a counter-propagating plane wave coming from the other side of the interface, say going from material 2→1 instead of 1→2, we can use the principle of superposition to express the forward (E_f) and backward (E_b) propagating field amplitudes:

$$E_{b1} = E_{f1} r_{12} + E_{b2} t_{21} \tag{B.48}$$

$$E_{f2} = E_{f1} t_{12} + E_{b2} r_{21} \tag{B.49}$$

where t_{12}, r_{12} are the transmission and reflection coefficients going from layer 1 to 2.

We use the "tmm" Python software package to implement the transfer-matrix calculation [323, 326]. The package is available from PyPI (`https://pypi.org/project/tmm/`). The

Jupyter notebook below was originally written by **Cora Went** with slight modifications by me. To run, it requires λ, n, k for each layer in a separate excel spreadsheet.

```
import numpy as np
import pandas as pd
import matplotlib.pyplot as plt
import scipy.io
from scipy.interpolate import interp1d
from tmm import coh_tmm, absorp_in_each_layer, color
```

```
# load n,k data as a pandas dataframe with
# different materials as csv sheets
# then convert to dictionary with sheet name as key,
# data arrays as lambda (nm), n, k
def read_excel_sheets(xls_path):
    xl = pd.ExcelFile(xls_path, engine='openpyxl')
    df = pd.DataFrame()
    new_dict = {}
    for idx, name in enumerate(xl.sheet_names):
        sheet = xl.parse(name, skiprows=1)
        new_dict[name] = sheet.to_dict(orient='split')
    return new_dict

nkdata_raw = read_excel_sheets('nkdata.xlsx')
```

```
# list of materials (sheet names) in stack,
# ***bottom to top*** in the order that light would pass through them
mat_list = np.array(["layer1","layer2","layer3"])

# list of layer thicknesses in nm, start and end with inf
d_list = np.array([np.inf,thickness1,thickness2,thickness3,np.inf])

# list of wavelengths
ldas = np.arange(400,800,1).reshape(-1,1)

# polarization
pol = "s"

# incident angle
theta = 0;
```

```
# interpolate nk data
nkdata = {}
for mat in mat_list:
    raw = nkdata_raw[mat+"_raw"]
    n_raw = interp1d(raw[:,0],raw[:,1],fill_value="extrapolate")
    k_raw = interp1d(raw[:,0],raw[:,2],fill_value="extrapolate")
    n = n_raw(ldas/1000)
    k = k_raw(ldas/1000)
    nkdata[mat] = np.column_stack((ldas,n,k))
```

```
# wavelength for Fresnel coefficient calculation
wl = wavelength

# initialize all matrices
R = np.zeros(np.shape(ldas))
T = np.zeros(np.shape(ldas))
A = np.zeros(np.shape(ldas))
a_layer = np.zeros((np.size(ldas),np.size(mat_list)))

# loop over all wavelengths
i = 0
for lda in ldas:
    # initialize n_list, index
    n_list = np.ones(np.size(d_list), dtype=complex)
    j = 0

    # calculate n,k at this wavelength for each material, populate n_list
    for mat in mat_list:
        j += 1
        nk = nkdata[mat]
        n_list[j] = nk[i,1]+nk[i,2]*1j

    # TMM
    coh_tmm_data = coh_tmm(pol, n_list, d_list, theta, lda)

    # absorption in each layer
    a = absorp_in_each_layer(coh_tmm_data)

    # add to arrays
    R[i,0] = coh_tmm_data["R"]
    T[i,0] = coh_tmm_data["T"]
    A[i,0] = 1- coh_tmm_data["R"]-coh_tmm_data["T"]
    a_layer[i,:] = a[1:np.size(mat_list)+1]

    # calculate Fresnel coefficients at specific wavelength
    if lda==wl:
        vw_list = coh_tmm_data["vw_list"]
        kz_list = coh_tmm_data["kz_list"]
        delta_n = d_list[1:-1]*kz_list[1:-1]
        # propagate v and w to the end of each layer
        vw_list[1:-1,0] = vw_list[1:-1,0]*np.exp(delta_n*1j)
        # v will decrease, w will increase (absorption)
        vw_list[1:-1,1]=vw_list[1:-1,1]*np.exp(delta_n*-1j)
        vw_list[0]=[1,coh_tmm_data["r"]]
        vw_list[-1]=[coh_tmm_data["t"],0]

        vw_amp = np.square(np.absolute(vw_list))
        total_R = coh_tmm_data["R"]
        total_T = coh_tmm_data["T"]
```

```
    i += 1
```

```
print('At wavelength ', wl, ' nm:')

# forward and backward amplitudes (columns, respectively)
# in each layer (rows)
# at a particular wavelength!
df_amps = pd.DataFrame({'|r|_f': np.round(np.abs(vw_list[:,0]),3),
                        '|r|_b': np.round(np.abs(vw_list[:,1]),3)})
print(df_amps)

# forward and backward phases
df_phase = pd.DataFrame({'phi_f': np.round(np.angle(vw_list[:,0]),3),
                         'phi_b': np.round(np.angle(vw_list[:,1]),3)})
print(df_phase)

# forward and backward *squared* amplitudes
df_intensity = pd.DataFrame({'R_f': np.round(vw_amp[:,0],3),
                             'R_b': np.round(vw_amp[:,1],3)})
print(df_intensity)

print('\n Total reflection coefficient, R = ', total_R)
print('\n Total transmission coefficient, T = ', total_T)
print('\n Estimated absorption fraction = ', 1-(total_T+total_R))
```

```
# plotting
fig,ax = plt.subplots(figsize=(10,7.5))

i = 0
for mat in mat_list:
    ax.plot(ldas, a_layer[:,i], label = "$"+mat+"$",linewidth=3)
    i += 1

ax.set_xlabel("Wavelength (nm)",size=18,fontweight='bold')
ax.set_ylabel("Absorption",size=18,fontweight='bold')
ax.legend(loc="upper right",fontsize=14)
ax.set_title("Simulated Absorption",size=22,fontweight='bold')
ax.tick_params(labelsize='14')
ax.set_xlim([400,800])
ax.set_ylim([0,1])
```

```
# find absorption at particular wavelength (indexed from 0=400 nm)
# in particular layer a_layer[wavelength,layer]
absorption=np.sum(a_layer[lda_index,layer_index])
print(absorption)
```

B.5 Azimuthally averaged profile function in Python

```
# data = NxN image array
# center = (x,y) pixel center
# len = length of azimuthal profile,
# preferably odd for Simpson's rule calculation
def azimuthal_profile(data, center, len):
    # remember, indices in python are row, column
    y,x = np.indices((data.shape))
    # calculate the radius from center of each pixel
    r = np.sqrt((x - center[0])**2 + (y - center[1])**2)
    # round to integer value
    r = r.astype(np.int)

    # weight each radius by its corresponding pixel value
    tbin = np.bincount(r.ravel(), data.ravel())
    # number of pixels in each radius bin
    nr = np.bincount(r.ravel())
    # normalize radial values by the number of pixels
    # that were in each radii bin
    azim_profile = tbin / nr
    # crop to a shorter profile, skipping first pixel
    azim_profile_crop = azim_profile[1:len]

    return azim_profile_crop
```